How better water splitters could make green hydrogen practical p. 354

Behavioral design of training can improve diversity of hiring p. 364

Stretchy organic solar cells p. 381

Science

$15
24 JANUARY 2025
science.org
AAAS

MANIFOLD MALES

Genetic orchestration of breeding morphs in ruffs

pp. 358 & 406

LIFE AT THE INTERFACE OF SCIENCE + ENGINEERING

lecture series

Dr. Phillip A. Sharp
Nobel Laureate
Institute Professor Emeritus, MIT

10th Anniversary Lecture
Discovery in Life Sciences: Biotechnology and Convergence with Engineering

Friday, February 14, 2025 | 1:00 PM
Boston, MA | Hynes Convention Center

Future convergence of medical science with physical and engineering sciences empowered by the computational and AI technology holds promise of continued progress in addressing critical societal challenges. Join us at the AAAS Annual Meeting for the 10th anniversary lecture of *Life at the Interface of Science + Engineering*!

Phillip A. Sharp is an Institute Professor Emeritus at MIT and member of the Department of Biology and the Koch Institute for Integrative Cancer Research. His research interests have centered on the molecular biology of gene expression relevant to cancer, and the mechanisms of RNA splicing. In 1977, his research provided the first indications of "discontinuous genes". This discovery fundamentally changed scientists' understanding of gene structure and was recognized by a 1993 Nobel Prize in Physiology or Medicine.

UNIVERSITY AT ALBANY

Rensselaer

Lecture series established through the generosity of Dr. Marlene Belfort and Dr. Georges Belfort.

CONTENTS

354
Electrolyzers are key to the green hydrogen dream.

24 JANUARY 2025 • VOLUME 387 • ISSUE 6732

NEWS

IN BRIEF

IN DEPTH

350
Exiting WHO on day one

PHOTOS: (TOP TO BOTTOM): FABIAN STRAUCH/DPA VIA ALAMY; EVAN VUCCI/AP PHOTO

FEATURES

INSIGHTS

PERSPECTIVES

ON THE COVER

A breeding ruff male (*Calidris pugnax*) in alert posture scans the breeding area for mating opportunities at Liminka Bay, Finland. Ruff males deploy one of three mating tactics that differ in aggressive and courtship behaviors.

Differences in aggression between tactics are tied to concentrations of circulating androgens, which are modulated by the actions of a single gene. See pages 358 and 406. *Photo: Jari Peltomäki/Finnature*

SCIENCE (ISSN 0036-8075) is published weekly on Friday, except last week in December, by the American Association for the Advancement of Science, 1200 New York Avenue, NW, Washington, DC 20005. Periodicals mail postage (publication No. 484460) paid at Washington, DC, and additional mailing offices. Domestic individual membership, including subscription (12 months): $165 ($74 allocated to subscription). Domestic institutional subscription (51 issues): $2865; Foreign postage extra: Air assist delivery: $135. First class, airmail, student, and emeritus rates on request. Canadian rates with GST available upon request, GST #125488122. Publications Mail Agreement Number 1069624. **Printed in the U.S.A.**
Change of address: Allow 4 weeks, giving old and new addresses and 8-digit account number. **Postmaster:** Send change of address to AAAS, P.O. Box 96178, Washington, DC 20090–6178. **Single-copy sales:** $15 each plus shipping and handling available from backissues.science.org; bulk rate on request. **Authorization to reproduce** material for internal or personal use under circumstances not falling within the fair use provisions of the Copyright Act can be obtained through the Copyright Clearance Center (CCC), www.copyright.com. The identification code for *Science* is 0036-8075. *Science* is indexed in the *Reader's Guide to Periodical Literature* and in several specialized indexes.

EDITORIAL

Citizen of science

Alan I. Leshner
is chief executive officer emeritus of the American Association for the Advancement of Science and former executive publisher of *Science*.
alan.i.leshner@gmail.com

H. Holden Thorp
is Editor-in-Chief of the *Science* journals.
hthorp@aaas.org

Floyd Bloom, who died on 8 January, was a towering figure in both neuroscience and the scientific community as a whole. As Editor-in-Chief of *Science* from 1995 to 2000, he presided over a transformative period in which the journal embraced the digital age, expanding its reach and impact while advocating for open access and the sharing of data. His groundbreaking contributions to neuropharmacology and the understanding of neurotransmitters were only part of his legacy. Through his leadership, mentorship, and pioneering research, Bloom left an indelible mark on the scientific world, one that continues to inspire new generations.

Early on, Bloom's research helped establish the roles of monoamines, particularly norepinephrine, as transmitters in the brain. He and colleagues went on to lead the way in combining anatomical, physiological, and pharmacological tools to elucidate the function of neurotransmitters at the cellular level. He was a coauthor of his field's defining textbook, *The Biochemical Basis of Neuropharmacology*. Bloom's work earned him many awards and prizes, as well as election to such organizations as the National Academy of Sciences, the National Academy of Medicine (then the Institute of Medicine), the American Academy of Arts and Sciences, and the American Philosophical Society. In 1976–1977, Bloom served as one of the first presidents of the Society for Neuroscience. He also was president of the American College of Neuropsychopharmacology and of the American Association for the Advancement of Science (AAAS, the publisher of *Science*). He served as Editor-in-Chief of *Science* and of *Brain Research*. Bloom's ability to translate complex science into accessible language made him a popular witness before US Congressional committees and an emissary to the broader public.

> **"...Bloom left an indelible mark on the scientific world..."**

Recognizing the potential of information and computer technologies for accelerating scientific progress, he was one of the planners of the National Institutes of Health's Human Brain Project in the 1990s, a forerunner of the current BRAIN Initiative, which is developing new technologies to advance neuroscience knowledge and application. He cofounded the company Neurome, Inc. to accelerate therapeutic development for neurodegenerative diseases.

As Editor-in-Chief of *Science*, Bloom brought the journal into the electronic age. He saw value in digitizing prior content to increase its use and impact. His team also created four complementary online publications: *Science* OnLine (which eventually became what is now the online version of *Science*), *Science*'s Next Wave, *Science* News on the Web, and *Science*'s Signal Transduction Knowledge Environment (which became *Science Signaling*). Bloom also saw technology as a vehicle for making data more easily accessible, whether by sharing it more broadly or through moving toward more open access policies for scientific publications. To quote his last *Science* editorial, "The technology *Science* seeks for our readers and authors is meant to organize information into wisdom, reveal important puzzles to solve, and draw new insights creatively. Seek with us." It is breathtaking to think of the explosion in electronic enhancements to scientific publishing that he lived to see after he wrote these words.

Bloom is remembered for his generosity and graciousness as a friend, mentor, and colleague. He had an extraordinary memory for people and events, a wonderful sense of humor, and what seemed to be a permanent smile on his face. He was born in Minneapolis, MN, and was an undergraduate at Southern Methodist University. He then earned an MD from Washington University in St. Louis. He was married for over 40 years to physician-scientist Jody Corey-Bloom. Until 2005, he was chair of the Department of Neuropharmacology at the Scripps Research Institute. When he died, he was professor emeritus in the Molecular and Integrative Neuroscience Department at Scripps. He previously was director of Behavioral Neurobiology at the Salk Institute and chief of the Laboratory of Neuropharmacology at the National Institute of Mental Health. Bloom trained a large number of students and postdoctoral researchers, many of whom have gone on to become leaders in government, industry, and academia. In 2005, when some colleagues decided to create a scientific "Bloom Family Tree," it included about 1000 scientists. The leadership rosters of the Society for Neuroscience and the American College of Neuropharmacology have been filled with individuals who are Bloom's scientific offspring.

Floyd Bloom epitomized the notion of a citizen of science—someone who does significant scientific work and is dedicated to advancing the broader enterprise and its contributions to society. We are all beneficiaries of his exemplary citizenship.

–Alan I. Leshner and H. Holden Thorp

10.1126/science.adw0373

NEWS

> “The markets and the economy are decarbonising and regardless of who is in the White House, this cannot be stopped.”
>
> **Alicia Pérez-Porro** of the Centre for Ecological Research and Forestry Applications in Spain, commenting to the Science Media Centre on President Donald Trump withdrawing the United States from the Paris climate accord.

IN BRIEF

Edited by
Jeffrey Brainard

ROCKET SCIENCE

Blue Origin emerges as competitor to SpaceX

The heavy-lift New Glenn rocket, developed by Blue Origin, Amazon founder Jeff Bezos's space company, reached orbit on its first attempt last week. The flight from Cape Canaveral, Florida, helps establish the company as a credible competitor to SpaceX, which now dominates the launch industry. Larger than SpaceX's Falcon 9 rocket—but smaller than its Starship—New Glenn (shown) is roughly the size of the Saturn V of Apollo Moon mission fame and promises to lower the cost of sending large science missions to space. Like SpaceX's current rockets, its lower stage is designed to be reusable, although the first attempt to land the booster, on an ocean barge, failed. Blue Origin plans to fly the rocket up to eight more times this year, primarily to launch satellites for Amazon's satellite internet provider, Project Kuiper. It will eventually be a key component of the company's NASA contract to provide a lunar lander for astronauts by decade's end.

L.A. research facilities spared

DISASTERS | The fires that spread destruction across the Los Angeles region this month and killed at least 27 people have spared two famed scientific facilities: NASA's Jet Propulsion Laboratory (JPL), which has spearheaded planetary missions and astronomy efforts, and the historic Mount Wilson Observatory. But the area's Eaton blaze destroyed an estimated 9000 buildings in Altadena and Pasadena, California. At least 200 JPL employees lost homes, and about 100 more were displaced after fire damaged their dwellings. As the Eaton fire grew, JPL evacuated staff and temporarily moved some operations to a backup operations center off site. As firefighters

PHOTO: JOHN RAOUX/AP

continued battling blazes in the area this week, the JPL facility remained closed; managers plan to reopen it on 27 January. At the Mount Wilson Observatory, where Edwin Hubble discovered the universe was expanding, firefighters stopped flames as they approached the edge of a parking lot. The facility also narrowly escaped the 2020 Bobcat wildfire, after which managers improved fire protections. Now used mostly for public outreach, it hosts the Center for High Angular Resolution Astronomy array, six telescopes operated by Georgia State University.

A COVID-19 pardon and ban

PUBLIC HEALTH | One day before leaving office, former President Joe Biden issued a preemptive pardon to Anthony Fauci, former director of the U.S. National Institute of Allergy and Infectious Diseases (NIAID), to head off possible prosecution by President Donald Trump. Fauci, who led NIAID for 38 years before retiring in 2022, has drawn the ire of Republicans for supporting pandemic public health measures and for favoring the view that SARS-CoV-2 had a natural origin. He also testified before Congress that bat virus experiments funded by NIAID at the Wuhan Institute of Virology (WIV) in China did not fit the federal definition of gain-of-function research that makes dangerous human viruses more risky. Republicans who think WIV created SARS-CoV-2 disagree, and some wanted Fauci to be charged with perjury. Separately, on 17 January conservation biologist Peter Daszak and the nonprofit EcoHealth Alliance, which held the NIAID grant that funded the WIV studies, were formally debarred for 5 years by the Department of Health and Human Services from receiving federal funds. EcoHealth had fired Daszak as president as of 6 January.

Early supernovae seeded dust

COSMOLOGY | A type of supernova produced by giant stars may have been a major source of the dust particles from which other stars and planets in the young universe formed, new research indicates. The finding, supported by data from the JWST space telescope, provides an alternative to the theory that the dust mostly came from aging, cooling stars over millions of years, an idea many astronomers find implausible. At last week's annual meeting of the American Astronomical Society, a research team said it examined spectra recorded by JWST of four supernovae that exploded a few hundred million years ago; they found large clumps of dust emitting wavelengths of light characteristic of aluminum, silicate, and carbon dust, the ingredients of future planets. When the researchers compared the spectrum of one supernova with its spectrum recorded 15 years earlier by a different telescope, they found that additional silicate dust equal to 10% of the mass of our Sun had accumulated around the supernova.

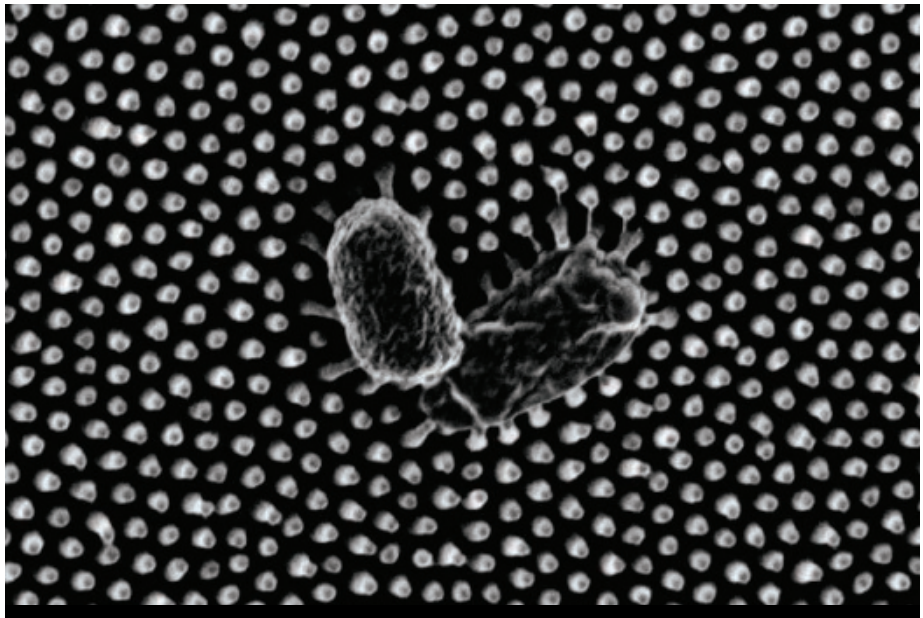

PHOTO: YUTAO CHEN; BECKMAN INSTITUTE/UNIVERSITY OF ILLINOIS URBANA-CHAMPAIGN

BIOPHYSICS

Cicada wings' surprising superpower: killing microbes

Every 13 or 17 years, cicadas emerge from the ground across the eastern United States en masse, producing a deafening din to attract mates. The thumb-sized insects also possess a lesser known, potentially beneficial trait: Their wings can kill bacteria. This month at the annual meeting of the Society for Integrative and Comparative Biology, a team reported discovering the mechanism: microscopic pillars that bend and rupture pathogens' cell membrane (shown), a strategy that could control infections in medical tubing and implants, for example. The researchers used polystyrene to fabricate platforms with "nanopillars" as tall as those on cicada wings—about 300 nanometers—and covered them with a common bacterium, *Pseudomonas*, which can cause pneumonia. The nanopillars killed about 98% of the microbes, on par with bleach, a common disinfectant. They cost more than disinfectants but, in contrast, do not corrode devices or harm the environment.

Herbicide tied to low birthweight

AGRICULTURE | The largest study of the herbicide glyphosate in the United States, where use has increased 750% since the advent of biotech crops, has found that babies in rural counties are now born slightly earlier and with below-average weight. These changes, although small, could result in more than $1 billion of health care costs nationwide each year, the researchers estimate. For the most vulnerable infants, in historically disadvantaged groups, the effect on birthweight is 12 times greater than for the least at risk. The study, published 14 January in the *Proceedings of the National Academy of Sciences*, did not directly measure individual exposure to glyphosate, a weakness. The U.S. Environmental Protection Agency is expected to complete a reevaluation of the compound by next year.

U.S. cancer institute head leaves

LEADERSHIP | Kimryn Rathmell, who directed the U.S. National Cancer Institute (NCI), stepped down this week after submitting her resignation to the incoming administration of President Donald Trump. During her 13-month tenure, Rathmell, a physician-scientist who studies kidney cancer, launched an ongoing initiative to study the rise in cancers in young adults and completed an analysis of disparities in cancer care. Although the president appoints the director of NCI, part of the National Institutes of Health, several past directors have stayed on for awhile in a new administration. Trump is considering at least two candidates for the job, *The Cancer Letter* reports.

IN DEPTH

ENERGY

Private fusion firms put bold claims to the test

Amid skepticism, companies bet that speed and innovation can realize fusion's promise

By **Daniel Clery**

Will this be the year private companies start to transform nuclear fusion from an interminable scientific puzzle into a profitable technology for producing carbon-free energy? So far, most of the dozens of efforts backed by venture capital have not gotten beyond computer predictions and small-scale prototypes. But this year, several firms will debut large new machines that, they say, will soon coax a roiling ionized gas to fusion-friendly temperatures. In theory, these bigger testbeds could even produce more heat than they use to spark fusion—a threshold known as breakeven.

"Fusion is a happening thing," says physicist Michel Laberge, founder of Canada's General Fusion, one of the startups. In the next year or two, "I think quite a few people will achieve sort of breakeven-ish numbers."

To physicists who have labored for decades in government-funded labs to make fusion work, such timetables appear wildly optimistic, likely driven more by the needs of investors than by scientific reality. "There has been no machine in my lifetime that you've turned on and it immediately performed. Never," says Steven Cowley, director of the Princeton Plasma Physics Laboratory, the United States's premier fusion lab.

Investors—and the world—will be watching keenly to see which view is right.

Fusion melds atomic nuclei to produce a larger nucleus, releasing energy in the process. But because the positively charged nuclei fiercely repel each other, sustaining the process requires intense heat and pressure, like that at the cores of stars or in a nuclear explosion. To spark controlled fusion, physicists heat isotopes of hydrogen until they form an ionized plasma, which starts to fuse at about 100 million degrees Celsius.

So far, despite billions of dollars and decades of effort, only the U.S.-based National Ignition Facility (NIF), which crushes and heats tiny capsules of fusion fuel with powerful lasers, has achieved breakeven. Other government-funded efforts have focused on doughnut-shaped devices called tokamaks that confine plasma with powerful magnets and heat it with microwaves and particle beams. ITER, a giant tokamak under construction in France that won't start operation until next decade, is poised to become the standard bearer for that approach.

Governments are still backing fusion—the United Kingdom announced £410 million for fusion research last week. But the slow pace of those efforts and the demand for carbon-free energy as climate change warms the world has prompted many researchers to seek a faster, privately financed route. The Fusion Industry Association reported having 45 members in 2024, which had collectively raised more than $7 billion in funding.

The startups hope that speedy, iterative development typical of industry will let them steal a march on government efforts. General Fusion aims to "incrementally improve very quickly, to iterate on our plan, to learn, and to move on to get results," says nuclear engineer Megan Wilson, the company's chief strategy officer.

PHOTO: ERIK ANDERSEN/GENERAL FUSION

A reactor vessel (left) and plasma injector (right) come together for General Fusion's debut in February.

Some firms aim to make smaller, cheaper tokamaks or close cousins called stellarators, using cutting-edge technologies such as high-temperature superconductors and machine learning. Others have resurrected previously abandoned techniques, such as the field-reversed configuration (FRC), a spinning smoke ring of plasma that briefly confines itself through a magnetic field it creates.

FRCs were discovered in the 1950s, but the plasma rings only lasted microseconds. National labs and universities made them more durable in the decades after, but the work ran out of steam. Undaunted, General Fusion has used some of its $340 million in backing to develop a plasma injector that puffs an FRC ring 2 meters across into a reaction chamber. There a shock wave initiated by pistons that strike the outer wall of the reaction chamber quickly crushes the ring to one-tenth of its original size, heating it to millions of degrees.

General Fusion's new machine, dubbed LM26, will debut next month in Vancouver, Canada, and start compressing plasma in March, with a goal to get to 100 million degrees Celsius—fusion temperature—by the end of the year, Laberge says. But LM26 will compress deuterium, not the deuterium-tritium mix required for energy generation. An actual fusion-capable reactor from the company wouldn't be ready until at least the 2030s, Laberge says—and would require much more investment.

A more secretive company, Helion, based near Seattle, is carrying out initial tests on its latest FRC-based machine, which was reportedly completed in the last few months. Known as Polaris, it simultaneously fires FRC rings from both ends of an elongated reaction chamber so they merge in the chamber's center, heating and compressing the plasma. A powerful magnet encircling the chamber compresses the FRC further until fusion starts in the fuel, a mixture of deuterium and tritium.

"The ultimate goal of Polaris is to show that we can create some electricity from fusion," says Helion spokesperson Jessie Barton. Most fusion power plant designs envision tapping the heat of fusion to boil water and drive a turbine. But in Polaris, the heat will cause the plasma to swell and push back against the force of the magnets, generating electricity via induction.

Cowley is not convinced of the promise of FRCs. "The problem with [FRCs] is that they are unstable, they're so unstable in most experiments that they don't confine very well either," he says. But Helion is confident: It signed an agreement with Microsoft to provide it with power by 2029. A power plant sited somewhere in Washington state would supply 50 megawatts. "The next machine that we build will be that power plant," Barton says.

A highly publicized fusion spin out from the Massachusetts Institute of Technology is taking a more conventional approach: a compact tokamak reactor called SPARC, which it will assemble this year. Although the machine, from Commonwealth Fusion Systems (CFS), is much smaller than ITER's tokamak, less than 5 meters in diameter compared to ITER's 16.4 meters, it is supposed to achieve similar performance for a fraction for ITER's cost, which is in excess of $25 billion. One factor: CFS is relying, for the first time in the fusion field, on high-temperature superconductors to make extra-strong magnets.

The superconducting material is a brittle ceramic, hard to make into wire and wind into the coils needed for electromagnets, so CFS uses a steel tape spray-coated with the superconductor. Over several years, the company has developed ways to wind and weave those tapes into the two types of magnets they need. "We've now built and demonstrated both of the key technologies for SPARC," says CFS physicist Alex Creely.

This year, the company will assemble its machine's 32 magnets. "On our current schedule, we're looking to begin operations in 2026 and get net energy in 2027," Creely says. Last month, CFS announced it had signed an agreement with Dominion Energy of Virginia to build a prototype power plant in Chesterfield County in the early 2030s.

Cowley is skeptical of the timetable. Superconducting tape has never been formed into such powerful magnets, and he suspects CFS will struggle to achieve the fields required. "I actually don't think that we'll see anything from anybody this coming year."

Other companies, using technologies with varying levels of maturity, have also set aggressive schedules. But fusion has a habit of confounding the best laid plans. Cowley points out that NIF struggled to make any significant reactions when it opened in 2009 and spent more than a decade refining its techniques to reach fusion ignition.

Michl Binderbauer, CEO of TAE Technologies, another FRC-focused effort that hopes to debut its new machine in 2026 or 2027, knows a lot is riding on the private, pioneering efforts. "What I hope doesn't happen is that one of us catastrophically implodes or fails and it kind of sucks the wind out of the whole industry." ■

INFECTIOUS DISEASES

Mpox drug wins approval in Japan—but it doesn't work

Europe previously approved tecovirimat for mpox, based on animal data; the U.S. has stockpiled it for smallpox

By **Jon Cohen**

On 2 January, Japan's regulatory agency issued a news release that startled some scientists: It had approved the antiviral drug tecovirimat, also known as TPOXX, for the treatment of mpox and two cousins, smallpox and cowpox.

No treatments exist for mpox, a painful and sometimes fatal disease now raging in sub-Saharan Africa, and tecovirimat initially looked promising: It prevented death in monkeys given lethal doses of mpox and smallpox virus. The European Union and the United Kingdom both approved it in 2022, during an earlier epidemic of mpox in men who have sex with men (MSM). At the time, the drug had been shown to be safe in humans, but no efficacy data existed. Until recently mpox was a rare disease limited to remote African villages, which made large, placebo-controlled trials difficult.

But in the past 6 months, two such studies have definitively shown tecovirimat doesn't work in people infected with either of the two clades of mpox virus. "To approve it now is very confusing," says Jason Zucker, an infectious disease specialist at Columbia University who co-led one of the trials, the Study of Tecovirimat for Human Mpox (STOMP), which enrolled mostly MSM on four continents. "I am very curious to read studies used by Japanese [regulators] to approve it," adds epidemiologist Placide Mbala of the Democratic Republic of the Congo's (DRC's) National Institute of Biomedical Research, who helped run the other trial, named PALM007. That study, in children and adults in the DRC, also found no benefit.

It's unclear what moved Japan's Pharmaceuticals and Medical Devices Agency to approve the drug in the face of negative data.

The agency told *Science* it "does not answer any questions regarding specific products." In a press release, the drug's manufacturer, U.S.-based SIGA Technologies, said Japan's decision was based on favorable results from 15 clinical trials that together enrolled 800 people—although all were healthy volunteers, meaning those trials could only measure safety and how the body processes the drug, not efficacy. In an email, SIGA told *Science* the agency also considered the PALM007 results, but the STOMP data "were not available at the time of their review."

The findings from the two trials could cause the European drug agencies to reverse their decision. And some argue they should even lead the U.S. Food and Drug Administration (FDA) to revisit a 2018 approval of the drug against smallpox, a potential bioterror threat, because the mechanism of action is the same for both viruses. (FDA has not approved the drug for mpox.)

A nurse in Kamituga, Democratic Republic of the Congo, applies disinfectant to a child's mpox rash.

Tecovirimat blocks the interaction between cellular proteins and a surface protein common to orthopoxviruses, which in turn disrupts the formation of new virus particles. The studies showing it works in monkeys led to FDA's approval for smallpox. Because that disease was eradicated decades ago, the agency relied on the Animal Rule, which allows for the approval of drugs against national security threats when efficacy trials are unethical or unfeasible. By now the U.S. government has invested more than $600 million in 1.5 million doses of tecovirimat for the country's Strategic National Stockpile.

The European Medicines Agency (EMA) and the U.K.'s Medicines & Healthcare products Regulatory Agency (MHRA) in 2022 approved the drug for the three poxviruses under "exceptional circumstances."

But tecovirimat fell flat in the real world. In PALM007, which enrolled 600 people, skin lesions did not heal any faster in people getting the drug, the National Institute of Allergy and Infectious Diseases (NIAID) announced in August 2024. Mortality was 1.7% whether people got the drug or the placebo. PALM007 also showed no impact on virus levels in blood, in lesions, and in the throat.

STOMP's results, revealed by NIAID in December 2024, were more dire still: The lack of efficacy was so clear that NIAID pulled the plug on the study when it had enrolled 75% of the targeted 719 participants. "This is pretty convincing evidence that when used alone, it's not going to be efficacious," says study chair Timothy Wilkin, a clinician at the University of California, San Diego.

But in an August 2024 statement about PALM007, SIGA CEO Diem Nguyen said the company was "highly encouraged" by the results and claimed some preliminary analyses of the trial data suggest tecovirimat "offers potential benefit" to patients with severe disease and those who sought treatment early. NIAID biostatistician Lori Dodd discounts those hints. "[The] observed differences were small and did not satisfy standard criteria for statistical significance," she says.

The reasoning behind regulatory approvals is often difficult to understand, says John Rizk, who is working on a Ph.D. in pharmacology at the University of Maryland and coauthored a November 2024 report in *Drugs* on mpox therapeutics and vaccines and their regulatory status. Still, he says, "This Japan approval was a shocker to me."

When EMA approved tecovirimat, it said it would review that decision after new studies reported results. Marco Cavaleri, who heads EMA's office of biological health threats and vaccines, says the agency "will scrutinize" the data from both trials and an ongoing study in Brazil, Switzerland, and Argentina. As for Japan's approval, "it looks a bit strange at this point in time," Cavaleri says. MHRA told *Science* it annually reviews all drug authorizations made under the "exceptional circumstances" provision. Rizk says the European agencies should at least issue a "dear doctor" letter to notify clinicians about the PALM007 and STOMP findings.

What the new data mean for tecovirimat as a smallpox treatment is unclear. In a statement sent to *Science*, FDA notes the drug's failure to speed healing in the mpox trials does not mean it will be ineffective against smallpox. If the drug ever is used to treat smallpox in humans, FDA will try to obtain data from studies. SIGA says the monkey studies suggest it will work against smallpox because they "accurately recapitulate" how that virus sickens and kills people.

But Wilkin says FDA should reconsider its approval for smallpox. "We felt that we needed a therapy in case there was a bioterrorist attack," he says. "But I would not feel comfortable counting on its efficacy." ■

GLOBAL HEALTH

'Cataclysmic:' Experts decry U.S. departure from WHO

Trump's decision to leave would be a financial blow to the agency and "isolate" the U.S. from health intelligence

By **Gretchen Vogel**

After he was sworn in as the 47th U.S. president on 20 January, Donald Trump signed an executive order many global health experts had feared, withdrawing the United States from the World Health Organization (WHO). Trump claims the U.N.'s health agency mishandled the COVID-19 pandemic and other global health crises, has failed to adopt needed reforms, and demands "unfairly onerous payments" from the U.S.

Trump started the process to quit WHO once before, in July 2020, during his first presidential term. Because the withdrawal process takes a year, President Joe Biden was able to reverse the decision when he took office in January 2021.

Now, Trump has a real chance to part ways with WHO, although there are likely to be at least some diplomatic efforts to keep the U.S. on board. WHO "regrets the announcement," it said in response to the decision. "We hope the United States will reconsider, and we look forward to engaging in constructive dialogue to maintain the partnership between the USA and WHO, for the benefit of the health and well-being of millions of people around the globe." Only one other U.N. member country—Liechtenstein—is not part of WHO.

Science examined what the departure, if Trump goes through with it, will mean for the U.S., WHO, and the broader global health community.

Q: What will a U.S. withdrawal mean for WHO?

A: The consequences could be dramatic. Beyond its membership dues of roughly $110 million annually, the U.S. is one of the biggest voluntary donors, contributing $1.1 billion in 2022 and 2023 combined. All

PHOTO: J. COHEN/*SCIENCE*

told, the country provides about one-fifth of WHO's budget. Other members might make up some of the difference, as they did when Trump slashed U.S. contributions during his first term. But European countries are facing other challenges, such as stagnating economies and pressure to increase defense spending, says Ilona Kickbusch, a global health expert at the Graduate Institute of International and Development Studies. Voices skeptical of WHO are also proliferating within the European Union, she says, and might be emboldened to reduce funding if the U.S. leaves.

A U.S. departure will also sever WHO's ties to world-class U.S. agencies such as the Centers for Disease Control and Prevention (CDC) and the Food and Drug Administration (FDA), which currently provide guidance to WHO on a range of topics—and receive crucial information in return. Leaving "would isolate the CDC from a lot of intelligence that is crucial for our global security," says virologist Marion Koopmans, who studies emerging infectious diseases at Erasmus Medical Center in the Netherlands.

Q: How else might the U.S. be affected?

A: In past years, much of the money contributed by the U.S. went toward responding to outbreaks and other emergencies. Losing those funds will restrict WHO's ability to react quickly, says Jeremy Konyndyk, president of Refugees International, who advises WHO on its emergency response system. That would be a bad deal for the U.S., he says, because WHO does work no other organization currently does. There were several Ebola outbreaks during Trump's first term, Konyndyk notes, and because WHO activated its emergency response, "we didn't need to deploy the U.S. military. We didn't need to spend a billion dollars of U.S. funding to get that under control."

Koopmans agrees a departure will leave the U.S. more vulnerable: "Our best defense is global collaboration and data sharing."

Q: What does the decision mean for Americans who work for or with WHO?

A: The executive order directs the Secretary of State and the Office of Management and Budget to "recall and reassign United States Government personnel or contractors working in any capacity with the WHO." Each year, many dozens of employees from CDC, FDA, and other federal agencies are deployed to both the Geneva headquarters and to crisis areas on behalf of WHO, notes Lawrence Gostin, an expert in national and global health law at Georgetown University. U.S. citizens who are employed by WHO directly can stay, at least for now. This includes, for example, epidemiologist Maria van Kerkhove, director of WHO's Department of Epidemic and Pandemic Preparedness and Prevention, who became the agency's face during the COVID-19 pandemic. U.S. citizens will likely also be able to serve on influential advisory boards such as the Strategic Advisory Group of Experts on Immunization. Members of such boards do not represent countries but are chosen for their expertise, Gostin notes.

It's not clear what will happen to so-called WHO collaborating centers, of which the U.S. hosts 72, more than any other country. Designated by WHO as world-leading in their field, such centers provide analysis and advice to the organization. (Gostin, for example, heads the WHO Collaborating Center on National and Global Health Law.) They have to be reauthorized by both WHO headquarters and the White House every 4 years.

Q: What does Trump's decision mean for U.S. influence on global health?

A: The country will lose its voice at the World Health Assembly, an annual meeting of member states that elects the director-general, reviews and approves WHO's budget, and sets policies on issues such as disease eradication, tobacco control, and vaccine equity. China would likely take on a much larger role, Konyndyk says: "If your true concern is that WHO is captured by China, then removing the U.S. from the equation just seals the deal."

Q: Would the U.S. also withdraw from the Pan American Health Organization (PAHO)?

A: PAHO, which has played a key role in many public health successes in the Western Hemisphere, was founded in 1902 as the International Sanitary Bureau, long before WHO was created, but it has served as WHO's regional office for the Americas since 1949. It's not clear whether withdrawal from WHO would automatically mean leaving PAHO, which has its headquarters in Washington, D.C., just a few blocks from the White House.

Q: Could the U.S. Congress block a withdrawal?

A: The U.S. joined WHO through a joint act of Congress in 1948. As a result, Congress may need to weigh in on a withdrawal, Gostin says. "When Congress has joined something, then you typically need Congress to support a presidential decision to leave it," he says. The Republicans' slim majority in both chambers means a few dissenters might be able to block Trump's move.

Q: Might Trump reconsider?

A: The administration could still try to use the threat of departure as a bargaining chip to force significant reforms—some of which might actually be good, Gostin says: "If Trump does a deal to make the WHO more resilient, robust, and accountable, he would be doing the U.S. a favor and the world a favor." Remaining a member would enable Trump to push for a candidate he likes as successor to WHO Director-General Tedros Adhanom Ghebreyesus, whose term ends in 2027.

If instead Trump goes through with the plan to withdraw, Gostin says, "It's a cataclysmic decision for WHO and world health. But it's even more damaging to America's national interests and security." ■

PHOTO: JIM WATSON VIA GETTY IMAGES

Donald Trump signs his decision to pull out of WHO, one of many of executive orders issued on Inauguration Day.

BIOMEDICINE

Misreported meals skew nutrition research data

Survey-based studies linking diet patterns to health may be fatally flawed, paper suggests

By **Catherine Offord**

Is coffee good for you? What about chocolate? Scientists trying to answer these questions often look for links between what people say they eat and the health conditions they develop later in life. But a study published last week in *Nature Food* shows just how unreliable that approach may be.

With the help of a technique that measures people's energy expenditure, researchers derived an equation to assess the accuracy of responses in dietary surveys. They found that more than half the records in widely used nutritional survey databases such as the U.S. National Health and Nutrition Examination Survey (NHANES) are likely wrong because people underreport what they consumed. The results call into question the thousands of studies that have used these data sets to link particular diets to human health, the authors claim.

Although the findings are not surprising to many experts, they say the paper represents the best attempt yet to quantify the problem, and underscores the need for better measures of what people eat. "If you want to try and set policy around food based on this type of data, then obviously your policy is fundamentally flawed to some extent," says Gary Frost, a nutritionist and dietician at Imperial College London.

Nutritional epidemiology studies typically ask people to keep a food diary or complete questionnaires about their intake in recent hours, weeks, or months. Biostatisticians have long warned that people can misremember or be reluctant to cop to what they consume.

Some have proposed ways to mitigate the problem—by eliminating data from participants who report intakes below the minimum for human survival, for example—but others insist it's time to give up on these surveys altogether. "This [sort of data] is so bad, it's not even worth using," says David Allison, an obesity researcher and biostatistician at the Indiana University School of Public Health-Bloomington.

A rigorous, if expensive, way to detect misreporting is using the doubly labeled water (DLW) technique, in which participants drink water labeled with heavy versions of oxygen and hydrogen and scientists test for these elements in urine samples over the following days. Because oxygen, but not hydrogen, is used to make carbon dioxide that is exhaled as the body burns calories, the relative amounts of these elements in urine reflect how much energy a person has used.

Studies employing the DLW technique alongside food questionnaires have found people typically use more energy than they report consuming—indicating they are either undereating, or, more likely, underreporting. Analyses of several hundred participants in the U.K.'s National Diet and Nutrition Survey (NDNS) have put the discrepancy at about 30%.

In the *Nature Food* study, researchers used more than 6000 existing DLW measurements from people between ages 4 and 96 to derive an equation that predicts a person's energy expenditure based on characteristics such as sex, age, and bodyweight. Then they applied this equation to thousands of records in NHANES and NDNS and looked for discrepancies between predicted expenditure and reported intake. For NHANES, more than 50% of adults' reported intakes fell below the range predicted by the equation, whereas in NDNS, more than 60% did. Some diets, such as those with more reported protein, showed greater discrepancies than others.

People tend to underreport how much they eat, creating a challenge for researchers trying to link diet to health.

The results suggest that "many studies of nutritional epidemiology that try to link dietary exposures to disease outcomes are founded on really dodgy data," says biologist and study co-author John Speakman of the University of Aberdeen and the Shenzhen Institute of Advanced Technology.

The findings are significant given the large number of studies that rely on NHANES data, says Samantha Kleinberg, a computer scientist at the Stevens Institute of Technology. Researchers can apply the new equation to check their own data sets, she says—though it may perform poorly for people with unusual energy requirements, such as athletes or pregnant people, and only detects misreporting indirectly.

Others are more critical. Walter Willett, a nutritional epidemiologist at the Harvard T. H. Chan School of Public Health, calls the study "flawed." DLW measurements don't offer a precise view of energy intake, he says: They fluctuate in a person over time and are sensitive to physical activity. He argues that misreporting is not severe enough to distort diet-disease links in well-conducted studies.

In a statement, the U.S. National Center for Health Statistics, which oversees NHANES, says underreporting in dietary surveys is well recognized, and its data are nevertheless "valuable and important." It adds that NHANES "takes important measures to ensure high data quality" and provides tutorials for researchers about how to analyze the data.

Dietary surveys remain the best data available, says Lindsay Jaacks, a nutritional epidemiologist at the University of Edinburgh. She adds that DLW studies don't reveal what people omit from survey responses. "We don't know if the 'missing' food and drink is ultraprocessed food or fruit or lunch meat or yogurt or sugary milky coffees."

Many researchers are developing methods to wean nutritional epidemiology off questionnaires, or at least complement them. Emerging techniques include photographic food diaries, where participants snap each meal and researchers estimate its content, and wearable cameras or motion and audio sensors to track consumption. Frost's team and others are also working to identify biomarkers in urine that could reveal how much of a particular food someone has eaten.

None of these methods are ready for largescale rollout. But equations like the one published last week could at least help nutritional epidemiologists evaluate the impact of misreporting on their research, Frost says. He hopes more innovations will follow. "We've got to move on," he says. "We've got to try and use new technologies to do better." ■

COMBINED PHOTO: SEFA OZEL/SHUTTERSTOCK

Canadian Prime Minister Justin Trudeau will leave office in March.

PHOTO: COLE BURSTON/*THE NEW YORK TIMES* VIA REDUX

SCIENCE POLICY

Canadian science girds for shift

Conservative Party expected to win elections later this year

By **Brian Owens**

Justin Trudeau's announcement earlier this month that he will step down as Canada's prime minister opens the way for a change of government that could have major implications for science. Many research advocates have seen Trudeau's Liberal government, which has been in power since 2015, as an ally. Now, they are anxious about what a government led by the Conservative Party, which is widely expected to win national elections later this year, will mean for issues ranging from climate change to science funding.

"One of the dominant narratives is that [the Conservatives] want to balance the deficit, so this is not the time to be asking for new money," says Sarah Laframboise, executive director of the science advocacy group Evidence for Democracy. "We should expect to see cuts."

Many scientists welcomed the Liberal Party's 2015 election victory. Running on a platform that promised to "value science and treat scientists with respect," Trudeau unseated Conservative Stephen Harper, who had served as prime minister since 2006 and had drawn harsh criticism from Canada's research community. Scientists had protested Harper's decisions to prevent government researchers from speaking to the press, cut funding for basic research, and cancel Canada's long-form census, among other actions. Trudeau's government quickly reversed course, reinstating the census, adopting a governmentwide scientific integrity policy that gave researchers greater freedom to speak to the press and the public, and enacting a large boost to research funding in 2018. Trudeau also appointed a dedicated science minister and chief scientific adviser.

Strains did develop, however. The government appeared to believe it had accomplished its science goals and began taking the community's support for granted, Laframboise says. "We got a lot of quick, visible wins," she says. "But some of these have lapsed or fallen off the radar."

The Liberal government did not sustain the 2018 funding boost, for example, and didn't respond to requests to increase federal stipends for graduate students until 2024. In 2019, it folded the science minister's position into another portfolio and many government departments have not fully implemented their scientific integrity policies. And ambitious plans to create a capstone organization to improve coordination among the nation's main science funding agencies have gone nowhere. "We don't have a national vision for science and research," Laframboise says.

Researchers give Trudeau higher marks on health policy. One highlight was Canada's response to the COVID-19 pandemic, says Jim Woodgett, senior scientist at the Lunenfeld-Tanenbaum Research Institute at Mount Sinai Hospital. Canada's death rate, for example, was lower than in the United States, the United Kingdom, and Sweden. Woodgett credits the government's embrace of expert panels on infectious diseases and vaccines, which provided rapid, actionable advice. "It was quite remarkable," Woodgett says. "I think that saved more than 100,000 lives."

The Trudeau government was also effective in curbing greenhouse gas emissions, says Kathryn Harrison, a policy specialist at the University of British Columbia. "Since the 1990s every government made bold promises and issued plans. But they never implemented any of the most effective measures and emissions kept going up," she says. "Trudeau's was the first federal government that moved from promising to actually adopting policies."

Those policies included revising the process for assessing the environmental impact of major development projects, regulating methane emissions, setting clean electricity and fuel efficiency standards, and putting a price on carbon emissions. Those steps helped halt the rise in Canada's emissions. However, the country "is not currently on track to meet our 2030 emissions targets, but we could be close," Harrison says. She does fault Trudeau for encouraging Canada's export of fossil fuels, such as by approving new shipping terminals for natural gas and expanding an oil pipeline.

A new Conservative government, expected to be led by longtime politician Pierre Poilievre, is likely to weaken or kill some of Trudeau's climate policies. For example, a cap on emissions from the oil and gas sector that has not yet been finalized is likely dead. And Poilievre has pledged to scrap carbon fees charged to consumers, though related levies on industry—a powerful tool for lowering emissions—could survive, Harrison says.

A Conservative government's science policies are less clear. Rick Perkins, the Conservative shadow science minister, did not respond to a request for comment. But Conservative leaders have traditionally put a priority on applied, not basic, research. It may fall to researchers to advocate for ongoing support for fundamental research, Woodgett says. "It's incumbent on scientists to continue to make the case for investment, and we've got to be delivering value for that investment," he says.

But advocacy is becoming risky business for scientists in Canada, Laframboise warns. Scientists who speak out on issues such as drug safety, diversity initiatives, and climate action face increasingly personal attacks, particularly from Conservative members of Parliament. Many say they are now scared of going public, Laframboise says. "These are polarizing conversations," she says. "We don't live in a world where sharing a piece of evidence is neutral, we're engaging in a process that is already polarized."

Just how fractious Canada's politics will be won't become clearer until later this year. The Liberal Party will choose its new leader and prime minister on 9 March. A federal election must then be held no later than October, but could come sooner. ■

Brian Owens is a journalist in St. Stephen, Canada.

THE PARTING OF WATER

A green hydrogen plant in Puertollano, Spain, is Europe's largest.

Green hydrogen is key to decarbonizing the world. But the costly, finicky devices that make it need dramatic improvement

By **Robert F. Service**

For the moment, production at North America's largest plant making hydrogen with renewable energy stinks. At SoHyCal's facility near Fresno, California, manure from more than 7000 cows at the Bar 20 dairy ranch is channeled to a covered lagoon, where bacteria convert much of it to methane-rich biogas that's run through fuel cells to generate electricity. Some of that power is shunted to SoHyCal's electrolyzer, a railcar-size device that splits water into hydrogen and oxygen gas. The result: about 300 kilograms of "green" hydrogen a day, which is used to power a pair of Fresno city buses and a smattering of local hydrogen-fueled cars.

This year, the plant will start to draw extra power from nearby solar farms, boosting output to 1 ton of hydrogen per day, says Pedro Pajares, who runs the U.S. offshoot of H2B2, the Spanish firm behind the project. But as for scaling up beyond that, Pajares says, "I have worries."

Hydrogen is often touted as the future of green energy, and the allure is clear. When burned or run through a fuel cell, the fuel produces water as exhaust, not carbon dioxide (CO_2). It is energy-rich enough to drive semitrailer trucks, cargo ships, and other heavy-duty vehicles that are tough to power with batteries. And for many industrial processes requiring high-temperature reactions, such as fertilizer production and steel manufacturing, hydrogen is basically the only alternative to fossil fuels, says Kathy Ayers, a water electrolysis expert at Nel Hydrogen, a Norwegian electrolyzer producer. "Low-carbon hydrogen is absolutely essential if we are going to address the climate crisis."

But if the scale of SoHyCal is any indication, that future remains a long way off. According to the International Energy Agency, the world needs to churn out more than 300 million tons of green hydrogen annually if it is to have a shot at limiting global warming to 1.5°C by 2050. Yet today, operating green hydrogen plants, mostly in Europe and China, produce just 1 million tons per year. "There is a big mismatch," Pajares says.

Production is meager not because hydrogen is some exotic energy source. Manufacturers already produce some 97 million tons of it, largely to make fertilizer and refine oil. But almost all of it comes from steam methane reforming, which is far from green. It uses high-pressure steam to break apart methane—the main ingredient in natural gas—into CO_2 and hydrogen. Every year, the process spews roughly 1 billion tons of CO_2 into the atmosphere—equivalent to Japan's emissions—to make so-called gray hydrogen.

Green hydrogen comes instead from electrolyzers powered by renewable electricity. As at SoHyCal, the devices turn out relatively small volumes of hydrogen at high prices. But governments worldwide have begun a push to scale up green hydrogen production. Earlier this month, for example, the U.S. Department of the Treasury finalized a $3 per kilogram tax credit for producers of green hydrogen. Meanwhile, researchers are trying to drive down the cost of electrolyzers—which accounts for roughly one-third of the cost of green hydrogen—and boost their efficiency. The U.S. Department of Energy (DOE) alone set aside $1 billion this decade to improve electrolyzer technology. "The money is there," Ayers says. "The issue is can we actually get systems installed."

At SoHyCal's hydrogen plant near Fresno, California, biogas from manure powers fuel cells, which supply green electricity to electrolyzers.

The cost of green hydrogen has already dropped this past decade from about $10 per kilogram of hydrogen (equivalent to $10 per 3.5 liters of gasoline) to about $5 per kilogram today. In 2021, DOE launched an "Earthshot" program aiming to drop the price to $2 per kilogram in 2026 and $1 per kilogram by 2031, at which point it could compete with gray hydrogen. Among DOE's targets: reducing the need for costly precious metal catalysts in many electrolyzers, improving the membranes at the core of the devices to enable faster and safer hydrogen production, and finding designs that work better with the variable electricity supply from solar and wind farms. "There is a lot of innovation coming," says Shannon Boettcher, an electrolyzer expert at the University of California, Berkeley. "The trend is very similar to the march of progress in photovoltaics and wind power."

Making better, cheaper electrolyzers is not the only hurdle green hydrogen faces, Boettcher says. Hydrogen cannot be chilled and compressed easily, so it requires large pipelines and storage facilities. And powering the electrolyzers needed to make 300 million tons of hydrogen a year would require more than a terawatt of cheap renewable electricity, more than all the solar and wind power currently installed worldwide. "A lot of things have to come together," Boettcher says.

THE CHEMISTRY OF SPLITTING WATER is the easy part. It was first done by English scientists more than 230 years ago. By the 1890s, engineers in France had built an electrolysis plant to produce hydrogen for military airships. A few decades after that, hundreds of such plants, mostly powered by hydroelectric dams, were producing hydrogen to make ammonia fertilizer. But with the advent of steam methane reforming in the 1930s, the cost of making hydrogen plummeted. Green hydrogen was replaced with gray.

Today, multiple electrolyzer technologies are vying to turn the hydrogen market green again. The most common and commercially mature version is known as an alkaline water electrolyzer (AWE). It works a bit like a battery. Two electrodes separated by a porous membrane are immersed in water containing an electrolyte that encourages the movement of ions. Green electricity fed to the negatively charged cathode splits water molecules into hydrogen molecules and negatively charged hydroxide ions. The hydroxide ions are drawn through the membrane to the positively charged anode, where they react to form oxygen and a smaller amount of water. The membrane slows the commingling of the hydrogen and oxygen, which could otherwise combine explosively. Dozens of such cells are stacked side by side to create the overall electrolyzer.

An AWE's main advantage is that the catalysts that coat the electrodes to speed up the water splitting can be cheap, such as nickel and stainless steel. But the approach

PHOTOS: H2B2 USA; (OPPOSITE PAGE) ANGEL GARCIA/BLOOMBERG VIA GETTY IMAGES

has limitations. If the supplied current drops sharply, as can happen with intermittent renewable energy sources, extra hydrogen can diffuse across the membrane to the oxygen-producing anode, creating an explosion hazard. Another problem: An AWE's electrodes typically can only handle relatively small currents. That means the electrodes must be large and, despite the cheap catalysts, costly to make significant amounts of hydrogen.

Innovative tweaks could help. In a standard AWE, for example, the produced gases tend to form bubbles on the electrodes, which impede the splitting of additional water molecules. But in 2022, Gerhard Swiegers, a chemist at the University of Wollongong, and his colleagues came up with a new design that relies on a membrane with a capillary design that wicks water and electrolyte from the bottom of the cell up to electrodes on either side. Because the electrodes aren't submerged in liquid, bubbles are no longer a concern. The design also allows the gases to be shunted off as soon as they are produced, reducing the risk of explosion.

Swiegers co-founded the startup Hysata, which has built lab-scale prototypes that demonstrate the superior efficiency of the capillary membranes. Whereas most AWEs require 50 to 53 kilowatt hours (kWh) of electricity to produce 1 kilogram of hydrogen, Hysata's devices only need 41.5 kWh—already beating an efficiency goal set for 2050 by the International Renewable Energy Agency. "This is a giant leap in performance," says Hysata's CEO, Paul Barrett. In May 2024, the company announced it had raised $111 million to scale up the technology.

IF THE ALKALINE CELL is the current king of electrolyzer technology, then the proton exchange membrane (PEM) is the teenage challenger. In PEM cells, the action is reversed, beginning not at the cathode, but at the anode, which pulls electrons off water molecules to split them into oxygen molecules and protons. The protons travel through a membrane to the cathode where they meet up with electrons supplied by renewable electricity to create hydrogen molecules.

The key difference from AWEs is the membrane. It isn't a porous separator, but a dense, solid polymer, made up of spaghetti-like molecules with chemical appendages that readily transfer protons across the membrane like a bucket brigade. The membrane requires no liquid electrolyte and reduces hydrogen crossover. On top of all that, PEM designs can typically handle larger and more variable currents. That translates to smaller, potentially cheaper electrolyzers that can produce the same amount of hydrogen.

Unlocking green hydrogen

Electrolyzers can use green electricity to split water molecules into oxygen and hydrogen gas. All three major designs resemble a battery, with a pair of electrodes separated by a membrane. They can be expensive to build and inefficient, requiring 50–60 kilowatt hours of electricity per kilogram of hydrogen. Three main types are vying to boost efficiency and lower costs.

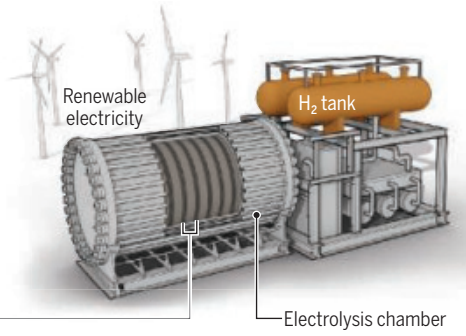

Electrolysis cell section

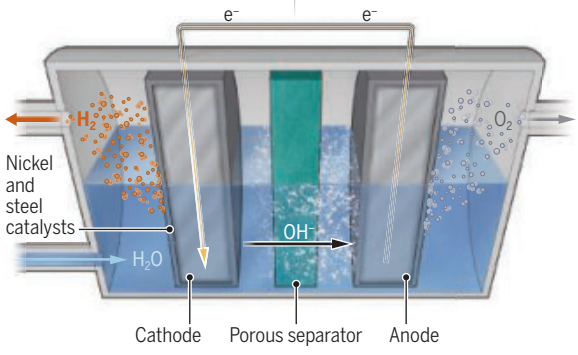

Alkaline water

Alkaline water electrolyzers (AWEs) have been around for more than a century. But commercial interest has prompted recent improvements.

PROS
- Mature technology
- Cheap catalysts
- Low capital costs

CONS
- Moderate efficiency, therefore large
- Can produce explosive gas mixtures
- Don't work well with fluctuating current

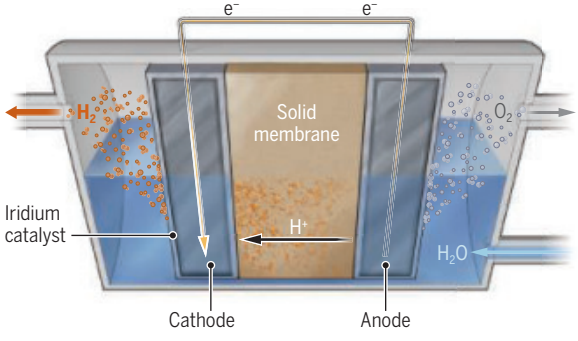

Proton exchange membrane (PEM)

Also decades old, PEM devices send ions in the opposite direction from AWEs, across a solid rather than a porous membrane.

PROS
- Higher efficiency, therefore smaller
- Work better with fluctuating current
- Work better with high currents

CONS
- Typically require costly iridium catalysts
- Membranes use "forever chemicals"
- Often higher capital costs

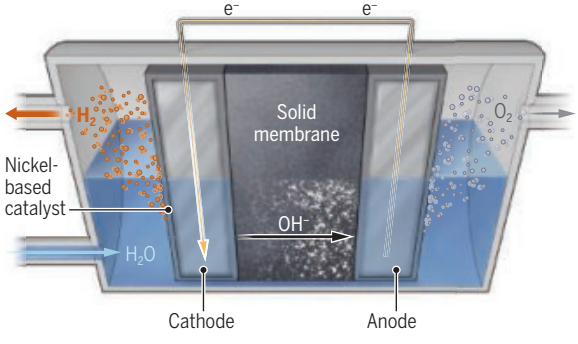

Anion exchange membrane

The latest technology, this electrolyzer combines features of both older designs and could lower costs. But it still must prove durable for decades.

PROS
- Doesn't require iridium
- Efficiency could be high
- No "forever chemicals" in membranes

CONS
- Rapid membrane degradation
- May degrade with fluctuating currents
- High current operation unproven

But PEM electrolyzers also have their downsides. Higher electrical power ravages most metal catalysts. Further corrosion comes from the protons, which create highly acidic hot spots. To withstand these conditions, PEM electrodes are coated in durable catalysts made with iridium—an extremely rare metal that's twice as costly as gold. "There is not sufficient iridium to grow [the industry]," says Pelayo García de Arquer, an electrolyzer expert at the Institute of Photonic Sciences (ICFO) in Barcelona, Spain. To make matters worse, the membranes are typically made from fluoropolymers—so-called PFAS materials that persist in the environment and are being phased out in many countries.

Many groups are devising novel PEM membranes without fluorine, as well as electrodes that require less iridium. PEM cells usually rely on iridium oxide (IrO_2). But recent theoretical work suggests the iridium in another compound, IrO_3, is more reactive, potentially allowing chemists to

GRAPHIC: A. FISHER/*SCIENCE*

use smaller quantities. Ryuhei Nakamura and his colleagues at the RIKEN Center for Sustainable Resource Science synthesized IrO_3 and sprinkled it on top of a manganese oxide electrode coating, using just 4% of the iridium normally needed for PEM devices. Their electrolyzer churned out hydrogen at essentially the same rate as top IrO_2 devices with no signs of degradation for more than 3000 hours, the team reported last year in *Science* (10 May 2024, p. 666). "We are already working with companies to scale this up," Nakamura says.

Other PEM researchers are looking to increase the durability and catalytic efficiency of cheaper metals such as cobalt and tungsten, hoping to replace iridium altogether. In June 2024, García de Arquer and his colleagues reported that pretreating a cobalt-tungsten catalyst in a basic solution helped shield it from acidic degradation and stabilized the metals in a more catalytically active arrangement. The upshot: The catalyst's output jumped fivefold, to nearly that of iridium oxide. "We have the highest current density and highest stability for noniridium catalysts," says co-author Lu Xia, also at ICFO. Boettcher calls the results "quite remarkable" but notes the researchers still need to show the alternative catalysts can match iridium's ability to handle high electrical currents.

Both the cobalt-tungsten catalyst and RIKEN's IrO_3 version still have a lot to prove. To be commercially viable, water-splitting electrodes need to last about 10 years, and neither catalyst has been tested for more than a few months. "There could be some pixie dust that comes along, and this may be it," Swiegers says of the new options. But for now, "iridium seems to be the only material that works long term with PEM."

LONG-TERM DURABILITY is also the main challenge for a third kind of water splitter, anion exchange membrane (AEM) electrolyzers. These emerging devices attempt to blend the best features of AWE and PEM designs. Like AWEs, they ferry hydroxide ions produced at the cathode through a membrane to the anode, and they do not need precious metal catalysts or a fluorine-based membrane. But like PEM devices, AEMs use solid membranes, designed to conduct hydroxide ions rather than protons. The combination could make them cheaper and able to handle the variable electricity supply from renewables.

The problem is that the oxygen-forming catalysts at the anode also promote reactions that "chew through" the membranes, causing them to break down in weeks or months, says Paul Kempler, a chemical engineer at the University of Oregon. But many labs are exploring ways to boost membrane durability. Germany-based Enapter, for example, spikes the water with liquid electrolyte, creating an environment that prevents corrosion. Enapter CEO Jürgen Laakmann believes the tweak will enable membranes to last for a decade. "Our stacks will last as long as other stacks," he predicts.

Boettcher's group has its own strategy for protecting the membrane: coating the anode with a thin layer of hafnium oxide. The coating allows hydroxide ions passing through the membrane to reach the anode, but, because it is an insulator, it blocks the electrical charges that tear apart the membrane. In the 16 February 2024 issue of *ACS Energy Letters*, Boettcher's team reported the hafnium oxide layer dramatically slowed membrane degradation. He calls the results "preliminary" but says that if the strategy works on a commercial scale, "this is a home run technology."

Hydrogen bubbles from an electrolyzer. Hundreds of millions of tons a year will be needed to meet climate targets.

GREEN HYDROGEN will need multiple home runs. Perhaps the biggest challenge the industry faces is the price of electricity, which makes up roughly two-thirds of the cost of green hydrogen, says Bryan Pivovar, who heads electrolyzer research at the U.S. National Renewable Energy Laboratory. Without subsidies, a price of $1 per kilogram for green hydrogen is impossible at today's electricity prices, no matter how cheap the electrolyzers get, Pivovar says. To reach $1 per kilogram, renewable electricity costs will need to fall by a factor of 10, according to a DOE green hydrogen road map. "We are reliant on the solar, wind, and utility industries to get the price of electricity down," Ayers says.

Green hydrogen needs not only cheap electricity, but heaps more of it. The DOE road map says meeting a U.S. target of producing 30 million tons by 2030 will require installing some 200 gigawatts of fresh renewable energy capacity, nearly double the installed U.S. solar capacity today.

Even if all that happens, and green hydrogen starts to be copiously produced, manufacturers will face the challenge of storing it and shipping it to customers. For existing hydrogen users, such as oil refineries, shipping and storage already adds at least $2 per kilogram to the cost of the gas, according to a December 2024 analysis in *Joule* by Harvard University's Roxana Shafiee and Daniel Schrag. So, unless those costs drop as well—or green hydrogen factories can be located close to customers—prospects for ubiquitous green hydrogen are dim. "Hydrogen may be the best way to decarbonize some sectors of the economy," Schrag says. "But it's a lot more expensive than people are portraying."

For now, all those realities help explain why SoHyCal is only bubbling out enough hydrogen to fuel two city buses. But Pajares believes green hydrogen has momentum. His company has already inked an agreement to launch a similar demonstration facility in Michigan this year and has six other U.S. plants on the drawing board. "Green hydrogen is not a commodity yet," Pajares says. But, he thinks, "it's finally here to stay." ■

PHOTO: IMAGO VIA ZUMA PRESS

INSIGHTS

PERSPECTIVES

EVOLUTION

Adaptations in surprising places

Testosterone is controlled while it circulates in the bloodstream

By **Kimberly A. Rosvall**

Imagine a power plant that produces electricity for all parts of a town. If the school needs more power than an empty store, for example, there need to be multiple adjustments across the grid. This electric grid is analogous to the physiological system in vertebrates that supports the flow of steroid hormones from gonads to target tissues. On page 406 of this issue, Loveland *et al.* (*1*) describe the biological equivalent of a step-down transformer within the power lines that keeps the town running when demands differ among end users. Working on a particular bird species, the authors connect testosterone-mediated adaptation in reproductive traits to a single gene with an unexpected pattern of expression in the brain, gonads, and the blood itself. These findings change what we know about how hormone levels can be controlled and how hormone-mediated traits evolve.

In humans and most other vertebrates, testosterone is produced in the gonads (the testes in males), where it supports sperm production. Testosterone also travels in the bloodstream, affecting tissues that express testosterone-binding androgen receptors. This influences a range of traits, such as behavior, body size, and ornamentation. These multiple pleiotropic effects of testosterone can promote evolutionary change, but they can also impede evolution if the shifting of multiple traits at once introduces costly trade-offs (*2*, *3*). By analogy, it may be disastrous to pump high power throughout a town regardless of the needs of the end users. The power grid problem can be controlled by decreasing production at the power plant or installing step-down transformers at the end user to lower the voltage to usable levels. In vertebrates, this typically amounts to reducing testosterone production in the gonads or decreasing expression of androgen receptors in target tissues, respectively.

Loveland *et al.* studied the charismatic ruff (*Calidris pugnax*), a shorebird with an impressive degree of variation among males with respect to sexually selected behavioral and physical traits (*4*). "Independent" males sport showy plumage and aggressively defend a display territory, where they court females. "Satellite" males are slightly less showy and less aggressive. They display alongside the more dominant independents and gain mates opportunistically. "Faeder" males look

Department of Biology, Indiana University, Bloomington, IN, USA. Email: krosvall@iu.edu

PHOTO: JARI PELTOMÄKI/FINNATURE

Male ruffs have two nonaggressive morphs, including the satellite (shown) and faeder, both of which have evolved lower testosterone through enzymatic changes in the brain, testes, and blood.

like females; they are smaller, drabber, and lack the veritable mane of feathers around their necks. Thus, they are able to blend in with females to avoid aggression from other males. This allows them to mate covertly.

Testosterone has been considered a potential driver of this trait variation, and indeed, independents have much higher testosterone levels than the other morphs (*4*). However, there is no gene for testosterone (it is not a gene product), and so it has been hard to pin down exactly how testosterone-mediated traits come about through genetic evolution.

In vertebrates, testosterone is generated by a multienzyme pathway that converts cholesterol into certain prohormones that eventually transform into active steroids such as testosterone or its close cousin estradiol. Classically, these gonadally sourced sex steroids are considered the point of origin for many traits, especially behavior. Castrated chickens don't strut or fight but do so after a testes transplant (*5*). Comparative analyses link steroid levels in the blood to diverse traits across vertebrates (*6*). Behavioral differences are thought to stem from neural sensitivity to those hormones (*7*, *8*), particularly in the brain.

Loveland *et al.* observed that the ruff morphs do not differ in expression of the genes encoding the sex steroid receptors (androgen and estrogen receptors) or in those encoding enzymes involved in testosterone production. Instead, the morphs differ in both sequence and expression of 17-beta hydroxysteroid dehydrogenase 2 (*HSD17B2*), a gene that encodes an enzyme that inactivates testosterone. The new gene variants (or derived *HSD17B2* alleles) originated from separate chromosomal rearrangements, which occurred 3.8 million and 0.07 million years ago for faeders and satellites, respectively (*4*). Loveland *et al.* connect this single gene to morph differences in testosterone through multiple causal inferences. They modeled enzyme structure and affinity to testosterone, and tests in cultured cells showed that the derived forms of HSD17B2 convert testosterone to an inactive metabolite at least twice as fast as the original version of the enzyme. The authors also compared *HSD17B2* sequences to those of other shorebird species and identified traces of past natural selection favoring the new variants in ruffs.

For the faeders and satellites, high levels of derived *HSD17B2* gene expression were found in six behaviorally salient areas of the brain, which suggests that inactivation of testosterone explains the distinctive behaviors of these morphs. Most unexpectedly, the enzyme's transcript was detected in the ruffs' blood too. Nonaggressive morphs have three orders of magnitude more *HSD17B2* expression than independents. This is presumably critical to how satellites and faeders achieve less testosterone in circulation than independents (*4*) but have high testosterone in the testes, the latter of which is needed for sperm production. In essence, the power plant is generating a lot of power. But, the power line itself (the bloodstream) is acting as a step-down transformer, dialing down the testosterone before it can do much outside the gonads.

The findings of Loveland *et al.* point to what may be an emerging "rule of life" for hormone-mediated traits or possibly all complex traits—in evolution, each problem has many possible solutions. Endocrine systems can be modified in nearly endless ways to generate behavioral diversity (*9*), including adaptations outside the brain (*10*, *11*). Lineages can use distinct genomic architecture for externally similar traits (*12*, *13*). Even the same trait can be regulated in different ways in males versus females (*14*) or in summer versus winter (*15*). That blood is not expected to circulate steroid-modifying enzymes like HSD17B2 underscores that a multi-tissue "organismal" approach to understanding trait evolution is needed. Comparative approaches across diverse species are also key because nature has had billions of years to generate diverse solutions to all kinds of problems. We can harness this history of adaptation, leveraging diversity across the tree of life to develop and test new biological rules, including those that may lie outside the canon of how we think adaptations (such as the ruff's distinct morphs) are built. When we inevitably encounter a result that defies expectations, it creates an exciting opportunity to ask why. ■

REFERENCES AND NOTES

1. J. L. Loveland, *Science* **387**, 406 (2025).
2. E. D. Ketterson, J. W. Atwell, J. W. McGlothlin, *Integr. Comp. Biol.* **49**, 365 (2009).
3. G. Kinsler, Y. Li, G. Sherlock, D. A. Petrov, *PLOS Biol.* **22**, e3002848 (2024).
4. C. Küpper *et al.*, *Nat. Genet.* **48**, 79 (2016).
5. A. A. Bertold, *Arch. Anat. Physiol. Wissenschr. Med.* **1849**, 42 (1849).
6. J. F. Husak *et al.*, *Evolution* **75**, 1003 (2021).
7. K. A. Rosvall *et al.*, *Proc. Biol. Sci.* **279**, 3547 (2012).
8. J. R. Merritt *et al.*, *Proc. Natl. Acad. Sci. U.S.A.* **117**, 21673 (2020).
9. K. A. Rosvall, *Horm. Behav.* **146**, 105246 (2022).
10. N. Niepoth *et al.*, *Nature* **629**, 1082 (2024).
11. J. B. Pease *et al.*, *Proc. Natl. Acad. Sci. U.S.A.* **119**, e2119671119 (2022).
12. S. E. Lipshutz *et al.*, bioRxiv 10.1101/2024.02.13.580205 (2024).
13. R. Greenway *et al.*, *Curr. Biol.* **34**, 4968 (2024).
14. K. A. Rosvall, A. B. Bentz, E. M. George, *Horm. Behav.* **123**, 104565 (2020).
15. G. E. Demas, K. M. Munley, A. M. Jasnow, *Trends Endocrinol. Metab.* **34**, 799 (2023).

10.1126/science.adv1194

CELL BIOLOGY

Decoding lysosome communication

Lysosome interaction with other organelles may be linked to pulmonary hypertension

By **Soni Savai Pullamsetti**[1,2,3] *and* **Rajkumar Savai**[1,2,3]

Pulmonary arterial hypertension (PAH; group 1 pulmonary hypertension) is a fatal disease characterized by increased pressure in the pulmonary artery and extensive remodeling of all three vascular layers (endothelium, smooth muscle, and adventitia) of the pulmonary arterial wall (*1*). Dysfunction of the artery's endothelium plays a central role in the development and progression of PAH, but the underlying mechanisms are not fully understood. On page 376 of this issue, Harvey *et al.* (*2*) report that disrupted activity of lysosomes correlates with altered sterol metabolism in these cells, vascular inflammation, and disease severity. Furthermore, the study raises the question of how lysosomes communicate with different organelles in a cell in health and disease. Interactions between organelles are important for cellular homeostasis (*3*, *4*) and when dysregulated can lead to cardiovascular disease, metabolic disorders, and cancer (*5*). Understanding the mechanisms of organelle communication could inform new preventive and therapeutic strategies for numerous conditions.

The lysosome is a membrane-bound organelle that is the central cellular hub for macromolecule catabolism, recycling, and signaling. The organelle therefore plays a crucial role in cellular metabolism as well as in regulating immune responses by processing antigens that activate immune cells (*6*). Disturbances in these functions can lead to the accumulation of undigested or partially digested macromolecules in the lysosomes or to impaired transport of molecules out of

[1]Institute for Lung Health (ILH), Justus Liebig University, Giessen, Germany. [2]Max Planck Institute for Heart and Lung Research, Bad Nauheim, Germany. [3]Department of Internal Medicine, Justus Liebig University, Giessen, Germany. Email: soni.pullamsetti@mpi-bn.mpg.de

the lysosome. This can result in a lysosomal storage phenotype and disease. Lysosomal dysfunction has been studied primarily in the context of inherited lysosomal storage disorders (LSDs), which are often associated with neurodegenerative, cardiac, and pulmonary abnormalities (*6*). In particular, rare, recessive, and loss-of-function genetic mutations that lead to LSDs are linked to pulmonary vascular disease. This includes mutations in subunits of vacuolar H^+ adenosine triphosphatase (V-ATPase), a proton pump that acidifies intracellular vesicles such as lysosomes. These mutations lead to impaired lysosomal acidification and cause the PAH observed in LSDs such as Gaucher disease, Niemann-Pick disease, and Fabry disease (*7*).

Harvey *et al.* discovered that a specific mutation in the gene encoding nuclear receptor coactivator 7 (NCOA7) results in a deficiency of the receptor in pulmonary arterial endothelial cells and, consequently, an LSD phenotype and PAH. The authors noted that patients with this deficiency had poorer survival among patients with PAH. Harvey *et al.* determined that NCOA7 binds to V-ATPase in pulmonary arterial endothelial cells and promotes lysosomal acidification and sterol processing. NCOA7 deficiency disrupted sterol metabolism in the lysosomes of these cells, leading to the accumulation of oxysterol and bile acids. These metabolites were associated with worsened mortality in PAH and drove the immune activation of human PAH endothelial cells and mice deficient for endothelial Ncoa7 or exposed to an inflammatory bile acid (see the figure).

Lysosomal dysfunction can involve various mechanisms to manifest the phenotypes seen in autoimmune and cardiovascular diseases. For example, in Gaucher disease, lysosome dysfunction in neuronal cells is associated with the activation of mammalian target of rapamycin complex 1 (mTORC1), a protein complex that localizes to the membrane of the endoplasmic reticulum (ER), where it regulates protein synthesis and protein stress responses (*7*). In atherosclerosis, defective lysosomal degradation in macrophages causes lipid accumulation in the organelle and activation of stress responses in mitochondria and the ER. It also activates the inflammasome, a protein complex that turns on the production of proinflammatory cytokines (*8*). The findings of Harvey *et al.* suggest that interorganelle interactions with lysosomes also occur in vascular endothelial cells to coordinate metabolism and immune function.

What is the nature of interactions between lysosomes and other organelles? Beyond physical interaction through membrane contact sites (*3*), fatty acid metabolism may be a means of interorganelle communication. Free fatty acids generated in the lysosome can be exported to mitochondria, where they are oxidized, a process associated with cellular immune responses (*9*). Fatty acid oxidation supports the production of acetyl–coenzyme A (acetyl-CoA), α-ketoglutarate (α-KG), and oxaloacetate. Acetyl-CoA and α-KG are further transported to the nucleus, where they regulate gene expression through histone acetylation and methylation, respectively (*10*). Therefore, it is plausible that the lysosomal dysregulation observed by Harvey *et al.* affects mitochondrial fatty acid oxidation, which in turn affects histone methylation in the nucleus. This dysregulation contributes to the altered epigenetic profiles observed in endothelial cells and also other vascular cells in PAH (*11*). In support of this concept, acetyl-CoA, a precursor of fatty acids and cholesterol, regulates smooth muscle cell proliferation in the pulmonary arterial wall in PAH. This could be reversed by inhibiting adenosine triphosphate (ATP) citrate lyase, an enzyme that produces oxaloacetate

Communication hub

Fatty acids generated in the lysosome may be a means of communication among organelles. In vascular endothelial cells, lysosomal dysfunction associated with a deficiency in the protein NCOA7 may trigger changes in the mitochondria and nucleus that lead to pulmonary arterial hypertension.

Healthy conditions

The nuclear receptor NCOA7 also controls the acidification of lysosomes, a condition needed for sterol metabolism. The resulting fatty acids are oxidized in mitochondria, with potential effects on gene expression and cellular homeostasis.

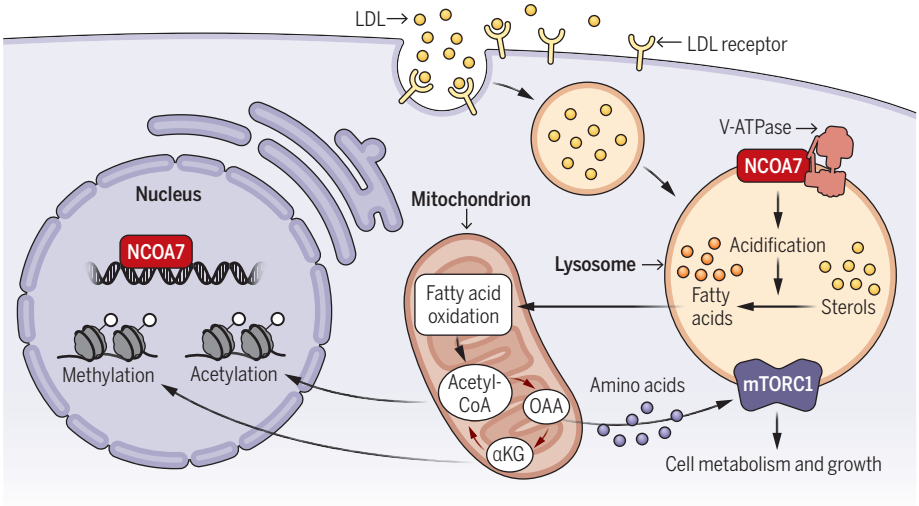

Pulmonary arterial hypertension

When NCOA7 is deficient in lysosomes, fatty acid production and downstream effects decrease. This leads to the production of proinflammatory factors that may underlie disease severity.

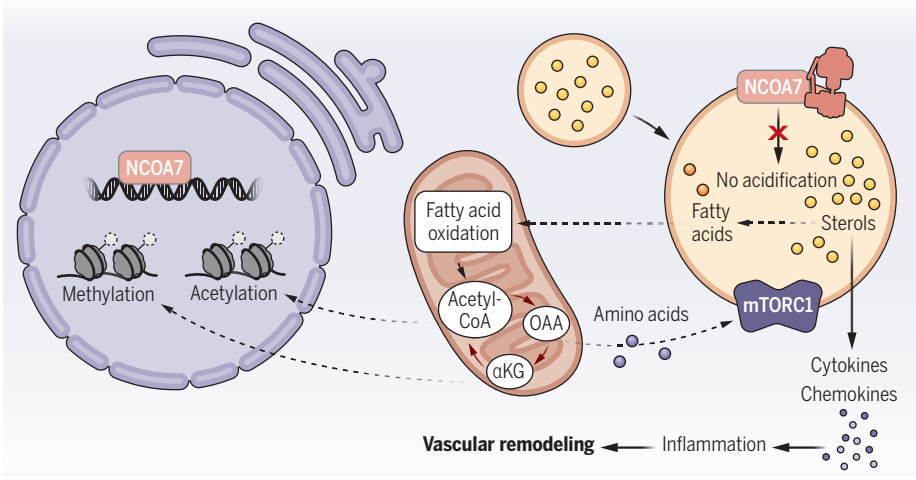

Acetyl-CoA, acetyl–coenzyme A; αKG, α-ketoglutarate; LDL, low-density lipoprotein; mTORC1, mammalian target of rapamycin complex 1; NCOA7, nuclear receptor coactivator 7; OAA, oxaloacetate; V-ATPase, vacuolar H^+ adenosine triphosphatase.

GRAPHIC: K. HOLOSKI/*SCIENCE*

and acetyl-CoA, molecules that not only affect cell metabolism but also regulate histone acetylation and gene expression in the nucleus (*12*). Thus, it is plausible that dysregulation of sterol metabolism in lysosomes perturbs acetyl-CoA levels, disrupting sterol synthesis and histone acetylation in the nucleus, leading to vascular cell abnormalities. The as-yet-unknown functional role of oxaloacetate in mitochondria may be to influence lysosomes by regulating amino acid metabolism and the mTORC1 pathway in vascular cells (*13*).

The findings of Harvey *et al.* suggest that lysosomal dysfunction might be reversed by activators of NCOA7, and this may be broadly effective in conditions beyond PAH across health and disease. Furthermore, a combination of genomic and metabolomic testing for NCOA7 and oxysterols could offer an advance in diagnosis and prognosis. Other approaches include agents that boost lysosomal acidification, supplement lysosomal proteases (cathepsins), and block mTOR signaling (*14*). Targeting the interorganelle interactions that underlie lysosomal dysfunction with metabolic and epigenetic modulators could be another avenue for therapeutic exploitation. Studies of other vascular beds and organs suggest a tissue-specific and vessel type–specific immunomodulatory role for certain subtypes of vascular endothelial cells (*15*). Whether these particular cells promote an immune response or immune tolerance in PAH remains to be elucidated. Important questions are how these endothelial cell subpopulations can be identified, what interactions take place between the organelles in these cells, and how the interactions can be therapeutically altered. ■

REFERENCES AND NOTES

1. C. Guignabert *et al.*, *Eur. Respir. J.* **64**, 2401095 (2024).
2. L. D. Harvey *et al.*, *Science* **387**, eadn7277 (2025).
3. Y. Zhang *et al.*, *Cell Death Discov.* **9**, 51 (2023).
4. R. S. Kuna *et al.*, *Sci. Adv.* **9**, eadf0138 (2023).
5. S. Patergnani, S. Marchi, B. Delprat, M. R. Wieckowski, *Front. Cell Dev. Biol.* **9**, 678307 (2021).
6. E. Uribe-Carretero, V. Rey, J. M. Fuentes, I. Tamargo-Gómez, *Biology* **13**, 34 (2024).
7. A. Jezela-Stanek, J. Chorostowska-Wynimko, A. Tylki-Szymańska, *Clin. Respir. J.* **14**, 422 (2020).
8. F. Bonacina *et al.*, *Nat. Rev. Cardiol.* (2024).
9. S. C. Huang *et al.*, *Nat. Immunol.* **15**, 846 (2014).
10. X. Li *et al.*, *Nature* **622**, 619 (2023).
11. P. Chelladurai *et al.*, *Sci. Transl. Med.* **14**, eabe5407 (2022).
12. Y. Grobs *et al.*, *Sci. Transl. Med.* **16**, eado7824 (2024).
13. P. Jouandin *et al.*, *Science* **375**, eabc4203 (2022).
14. M. Cao, X. Luo, K. Wu, X. He, *Signal Transduct. Target. Ther.* **6**, 379 (2021).
15. J. Amersfoort, G. Eelen, P. Carmeliet, *Nat. Rev. Immunol.* **22**, 576 (2022).

ACKNOWLEDGMENTS

The authors acknowledge support from the Institute for Lung Health, European Research Council Consolidator Grant (866051).

10.1126/science.adv1201

GRAPHIC: N. BURGESS/*SCIENCE*

OPTICS

Chirality à la carte

Light drives a fast switching between achiral and chiral states in a crystal

By **Carl P. Romao**[1] *and* **Dominik M. Juraschek**[2]

Chirality—the inability of an object to be superposed onto its mirror image—is important to biological, chemical, and physical processes. For example, amino acids and sugars found in all living organisms are chiral, bearing a specific handedness (left or right) that affects the reactivity of the molecule. Crystals can also have inherent chirality and exist as a pair of two distinct states that are mirror images of one another (enantiomers). Chirality of crystals is intimately connected to electromagnetic properties and dictates how light interacts with a material (*1*). However, modifying chirality in solids is challenging because it requires structural rearrangement. On page 431 in this issue, Zeng *et al.* (*2*) report that light-driven vibrational motions of atoms produce chirality in an achiral material on a picosecond timescale. This is not only desirable for advanced optoelectronic devices but also creates opportunities to explore complex physical phenomena in solids.

Two different forms of chirality exist: geometric and motion-based (*3*). A helical object, such as a screw, has geometric chirality in which the object cannot be superposed onto itself after a rotation followed by a reflection (no rotoreflection symmetry). By contrast, motion-based chirality can exist in systems that have an achiral geometry (its mirror image is identical to the original). When an achiral object spins or rotates in a helical pattern, its mirror image is no longer symmetric because of the motion, making the dynamical system chiral. For example, circularly polarized light that spins around its direction of propagation exhibits motion-based chirality. This phenomenon is described by a combination of translational and rotational motions and hence by the linear and angular momentum of an entity.

[1]Section of Solid State and Theoretical Inorganic Chemistry, Institute of Inorganic Chemistry, Eberhard Karls University Tübingen, Tübingen, Germany. [2]Department of Applied Physics and Science Education, Eindhoven University of Technology, Eindhoven, Netherlands. Email: d.m.juraschek@tue.nl

Driving chirality on demand

Polarized light can cause achiral crystals to exhibit phonon chirality with distinct handedness. Circularly polarized light can generate synchronized atomic motion in a solid to generate chiral phonons. Zeng *et al.* experimentally demonstrate that linearly polarized light can displace atoms to produce geometrically chiral phonons in an achiral boron phosphate crystal.

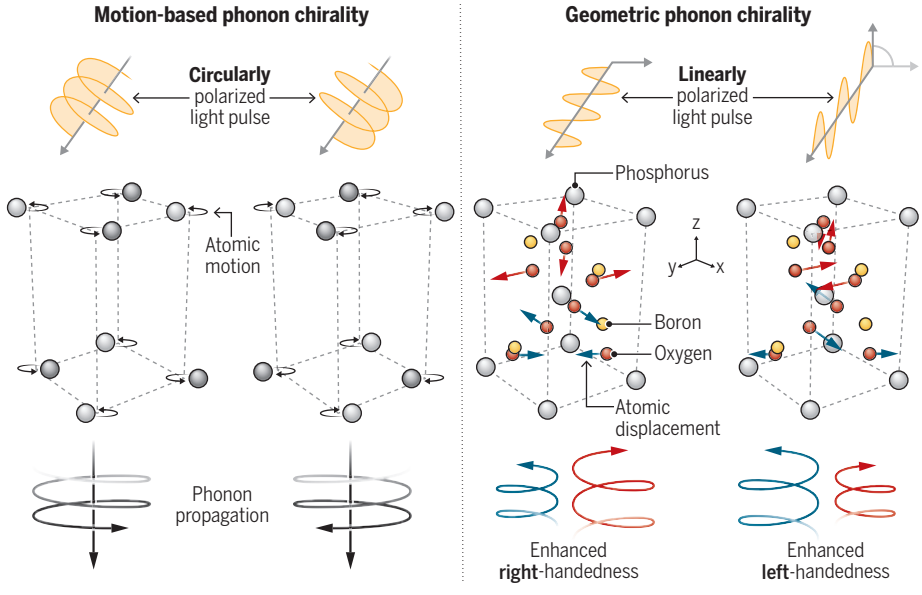

Motion-based chirality is also found in elementary excitations that arise when a material is excited to a state away from its equilibrium, such as phonons (collective vibrational motions of the atoms). "Chiral phonons" carry an angular momentum associated with rotational atomic motion and can couple to incident light and the electronic state of a solid (*4*). For example, circularly polarized light can generate synchronized rotation of atoms in a solid. These atoms then act as tiny electromagnetic coils and produce a magnetic field on the nanoscale, which could be used in magnetic memory devices (*5*). Given these observations, the question of whether phonons can also exhibit geometric chirality remains to be answered.

Zeng *et al*. observed an introduction of geometric chirality in the achiral insulator boron phosphate upon irradiation with terahertz pulses. Displacement patterns of phonons in any achiral material can temporarily transform its structure to a chiral one. This type of phonon mode, called "geometric chiral phonon," breaks the symmetry of a crystal not by atomic motion, but by the instantaneous displacement of the atoms (*6*). However, it is challenging to move the average positions of the atoms away from their equilibrium positions. A simple atomic vibration transforms the crystal back and forth between the two enantiomeric states, and the crystal remains in its original achiral state on average. To resolve this, nonlinear interactions between phonons have been proposed to shift a crystal into either of the enantiomeric states (*6*).

Zeng *et al*. used pump-probe measurements with a femtosecond time resolution to experimentally demonstrate this effect of nonlinear interactions, also known as phononic rectification, and the generated chirality. In this approach, the first beam of light (pump) excites phonons in a boron phosphate crystal to cause atomic vibration followed by the second beam (probe), which investigates the sample's response. When the phonons were excited by the pump beam, the authors observed a rotation of the polarized probe beam. This polarization rotation, which is also called optical activity, is direct proof of light-induced chirality in a solid. To explain the light-induced chirality effect, Zeng *et al*. investigated the crystal structure of boron phosphate. Without light, the material was in an achiral state in which the crystal had equal sizes of right- and left-handed chiral structural units. Nonlinear excitation of geometric chiral phonons enhanced a specific chiral structural unit while suppressing the other (see the figure). This produced an enantiomeric state with a distinct handedness in the material. Zeng *et al*. further demonstrated selective generation of enantiomeric states in the boron phosphate crystal by changing the polarization of the pump beam, which produced opposite rotations of the probe beam.

Although the light-induced chirality of boron phosphate has only a short lifetime, the mechanism presented by Zeng *et al*. could be used to drive long-lasting transitions between achiral and chiral states in various materials (*7*–*9*). This could bring intriguing physical phenomena in a broad range of achiral crystals, such as polarized electron spin and phonon angular momentum currents, which have been primarily observed in chiral solids (*10*–*12*).

"This suggests that light-induced geometric chirality could be a universal effect..."

Chirality of molecules and supramolecular assemblies has been modified using circularly polarized light (*13*). The study of Zeng *et al*. goes beyond small molecules and experimentally demonstrates light-induced geometric chirality in a crystal. This suggests that light-induced geometric chirality could be a universal effect and directly applicable to hybrid systems, such as molecular crystals and surface chemical reactions. As detection (*14*) and quantification (*15*) techniques advance, the method of Zeng *et al*. could be used to provide fast switching between chirality states to control electromagnetic states of a solid and achieve ultrafast information storage and processing. ■

REFERENCES AND NOTES

1. R. Winkler, U. Zülicke, arxiv:2405.20940 (2024).
2. Z. Zeng *et al*., *Science* **431**, 431 (2025).
3. L. D. Barron, *J. Am. Chem. Soc*. **108**, 5539 (1986).
4. T. Wang, H. Sun, X. Li, L. Zhang, *Nano Lett*. **24**, 4311 (2024).
5. C. P. Romao, D. M. Juraschek, *Nature* **628**, 505 (2024).
6. C. P. Romao, D. M. Juraschek, *ACS Nano* **18**, 29550 (2024).
7. T. Hayashida, K. Kimura, D. Urushihara, T. Asaka, T. Kimura, *J. Am. Chem. Soc*. **143**, 3638 (2021).
8. M. Fava, E. McCabe, A. H. Romero, E. Bousquet, arXiv:2405.12696 (2024).
9. S. Zhang, K. Luo, T. Zhang, *npj Comput. Mater*. **10**, 264 (2024).
10. B. P. Bloom, Y. Paltiel, R. Naaman, D. H. Waldeck, *Chem. Rev*. **124**, 1950 (2024).
11. K. Kim *et al*., *Nat. Mater*. **22**, 322 (2023).
12. K. Ohe *et al*., *Phys. Rev. Lett*. **132**, 056302 (2024).
13. N. P. Huck, W. F. Jager, B. de Lange, B. L. Feringa, *Science* **273**, 1686 (1996).
14. D. Ayuso, A. F. Ordonez, O. Smirnova, *Phys. Chem. Chem. Phys*. **24**, 26962 (2022).
15. A. Inda, R. Oiwa, S. Hayami, H. M. Yamamoto, H. Kusunose, *J. Chem. Phys*. **160**, 184117 (2024).

10.1126/science.adv0319

NEUROSCIENCE

Expanding the brain's terrain for reward

A previously unknown region in the brainstem controls dopamine activity

By **Sten Grillner**

The neurotransmitter dopamine is central to most aspects of behavior in vertebrates, including humans, affecting mood, learning, and decision-making. The dopamine-releasing neurons in the brain's ventral tegmental area (VTA) are controlled by other brain structures that are activated in different contexts in which a rewarding stimulus is identified (*1*–*3*). The targets of VTA neurons include the striatum, prefrontal cortex, amygdala, and hippocampus. On page 379 of this issue, Zichó *et al*. (*4*) report that neurons in the subventricular tegmental nucleus (SVTg) of the mammalian brainstem exert prominent control of dopamine neuron activity to reduce anxiety in a reward situation. Activation of these neurons in the mouse inhibited the lateral habenula, a brain region associated with depression. The findings suggest that neurons in the brainstem may play a role in disorders such as anxiety and depression.

Most neurons in the brain circuits that influence dopamine release are spontaneously active during resting conditions. This applies to the SVTg, the lateral habenula, and the dopamine neurons in the VTA. From a control point of view, this is an advantage because the activity of a given type of neuron can be both up- and down-regulated by different inputs. Thus, inhibition of the SVTg leads to a disinhibition of the lateral habenula, thereby increasing inhibition of dopamine neurons and decreasing release of dopamine in the VTA.

What is the behavioral impact of the SVTg? Zichó *et al*. found that when this region of the mouse brain was stimulated (optogenetically) during a place preference test, mice preferred the stimulated chamber. Moreover, the next day when there was no stimulation, the mice still preferred the

Department of Neuroscience, Karolinska Institutet, Stockholm, Sweden. Email: sten.grillner@ki.se

chamber in which they were stimulated the day before. Clearly, the activation had a behavioral effect and resulted in a remembered preference. Activating neuronal projections from the orbitofrontal cortex (in the prefrontal cortex) to the SVTg had a similar effect to that of activating the SVTg directly (see the figure). In another context, mice tended to have a fear of an open field, but SVTg activation reduced this behavior. The activation of SVTg can therefore be regarded as being anxiolytic (anxiety reducing).

Zichó *et al*. also noted that mice appeared to perceive activation of the SVTg as a positive event. Each time the animals poked their nose into a specific opening, the SVTg was optogenetically stimulated, and the animals would actively seek to be stimulated. Such self-stimulation for a reward has been observed with other parts of the dopamine system (*5*). Furthermore, the mice remembered from one day to the next which nose port to select.

What happens in the SVTg in a real reward situation, outside of experimental optogenetic activation? Zichó *et al*. showed in an anxiety-inducing situation (water deprivation) that when mice were given droplets of water with sugar dissolved, SVTg neurons became activated within a few hundred milliseconds after consumption as a direct result of the reward. What about reward prediction? The authors observed that if mice were taught that they would receive a reward 2 seconds after exposure to a specific signal, the animals could predict that the reward was coming ahead of the actual reward, fitting the classical definition of reward prediction (*3*). All experiments were performed on mice but based on the common expression of a marker molecule. Zichó *et al*. concluded that the SVTg also exists in rats, macaques, and humans, and presumably can be considered a conserved hub at least in mammals.

There are several structures that, in addition to the SVTg, influence the activity in dopamine neurons. For instance, striosomes comprise a specific compartment of the striatum that contains two types of GABA-mediated striatal projection neurons (SPNs)—those expressing D1 dopamine receptors that inhibit dopamine neurons directly and those bearing D2 receptors that project to other GABA-mediated neurons in the globus pallidus externa. GABA (γ-aminobutyric acid) is the primary inhibitory neurotransmitter in the brain. When activated, these GABA-mediated neurons target and disinhibit dopamine neurons in the VTA (*6*). The striosomes can also act through an excitatory relay onto the lateral habenula, together with input from the prefrontal cortex and the SVTg (*7*). The lateral habenula also receives input from the hypothalamus and cortex (*8*) and is an evolutionarily conserved structure (*7, 9*). There are also direct inputs from brainstem circuits such as the pedunculopontine nucleus that directly target the dopamine neurons. It is, however, clear from the study of Zichó *et al*. that the SVTg provides a substantial input that affects dopamine neurons under the experimental conditions used in their study.

Dopamine control in the brain

A complex network of neuronal pathways across different brain regions controls the activity of dopamine-releasing neurons in the mammalian brain. Blue indicates GABA-releasing, inhibitory neurons (GABA, γ-aminobutyric acid); red indicates glutamate-releasing, excitatory neurons; purple indicates dopamine-releasing neurons. Black arrows indicate additional input, whether excitatory or inhibitory.

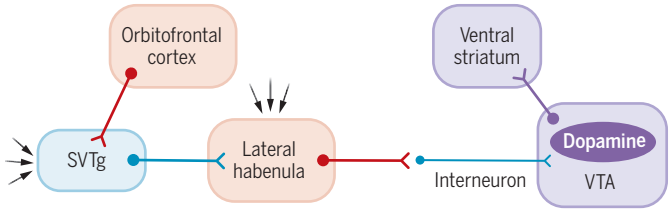

A new circuit
The subventricular tegmental nucleus (SVTg) of the brainstem (in mice) contains neurons that control dopamine release from neurons in the ventral tegmental area (VTA). The ventral striatum is a major target region receiving those dopamine signals.

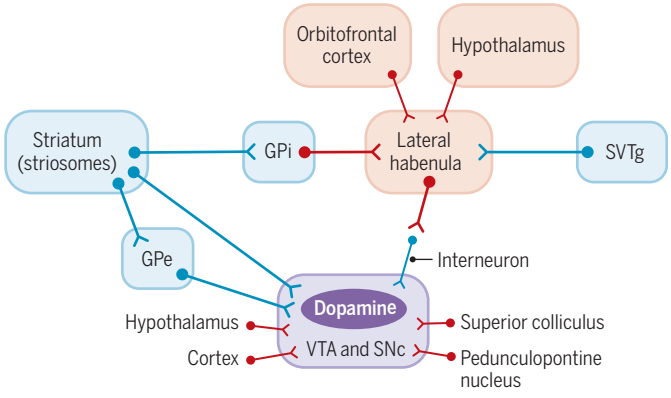

The wider dopamine circuit in the brain
A complex circuit controls dopamine release from the VTA and susbstantia nigra pars compacta (SNc). This network includes neurons (striosomes) in the striatum. One neuron type inhibits dopamine neurons directly and a second signals through globus pallidus externa (GPe) neurons to stimulate dopamine release. Striosomes also inhibit excitatory neurons in globus pallidus interna (GPi) that target the lateral habenula.

The overall activity of the brain's dopamine neurons is shaped by a system of complementary networks. Notably, dopamine neurons are not one entity but rather are subdivided into at least seven subpopulations that project to partially overlapping striatal and cortical areas. These subtypes can most likely be selectively activated under different behavioral situations. The overall design of the circuits that control dopamine activity is, however, organized in a similar way with input and projection patterns in all vertebrates investigated, from the lamprey to mammals (*10–12*). Now a new member, the SVTg in the brainstem, has been added.

The SVTg appears to have all the classical elements of dopamine control and is likely a major contributor to the regulation of dopamine neurons in mammals, including humans. It should be noted, however, that the experiments of Zichó *et al*. involved dopamine-producing neurons in the VTA. The neurotransmitter is also released by neurons within the substantia nigra pars compacta, regions of the brain that project preferentially to the dorsal striatum and have been implicated in different aspects of behavior and the control of movement (*13*). Whether the SVTg also affects this region is thus an open question. ■

GRAPHIC: K. HOLOSKI/*SCIENCE*

REFERENCES AND NOTES

1. A. M. Graybiel, A. Matsushima, *Annu. Rev. Neurosci.* **46**, 359 (2023).
2. A. Klaus, J. Alves da Silva, R. M. Costa, *Annu. Rev. Neurosci.* **42**, 459 (2019).
3. W. Schultz, *Curr. Biol.* **27**, R369 (2017).
4. K. Zichó *et al.*, *Science* **387**, eadr2191 (2025).
5. M. E. Olds, J. L. Fobes, *Annu. Rev. Psychol.* **32**, 523 (1981).
6. I. Lazaridis *et al.*, *Curr. Biol.* **34**, 5263 (2024).
7. M. Stephenson-Jones *et al.*, *Nature* **539**, 289 (2016).
8. I. Lazaridis *et al.*, *Mol. Psychiatry* **24**, 1351 (2019).
9. M. Stephenson-Jones, O. Floros, B. Robertson, S. Grillner, *Proc. Natl. Acad. Sci. U.S.A.* **109**, E164 (2012).
10. S. Grillner, B. Robertson, *Curr. Biol.* **26**, R1088 (2016).
11. S. Grillner, B. Robertson, *Handbook of Dopamine*, S. Cragg, M. Walton, Eds. (Elsevier, 2024).
12. B. Robertson *et al.*, *PLOS ONE* **7**, e35642 (2012).
13. M. Watabe-Uchida, L. Zhu, S. K. Ogawa, A. Vamanrao, N. Uchida, *Neuron* **74**, 858 (2012).

Acknowledgments
The author thanks B. Robertson and acknowledges support from the Swedish Research Council (VR-M-2021-01995) and from European Union Horizon 2020 no. 101147319 (EBRAINS 2.0 Project).

10.1126/science.adv1207

POLICY FORUM

DIVERSITY

Behaviorally designed training leads to more diverse hiring

A field experiment provides a promising proof of concept

By **Cansın Arslan[1], Edward H. Chang[2], Siri Chilazi[3], Iris Bohnet[3,4], Oliver P. Hauser[1,5]**

Many organizations have shown interest in increasing the diversity of their workforces for various reasons. Collectively, they have spent millions of dollars and countless employee hours on diversity training. Yet, there is little empirical evidence that such training increases diversity in organizations (*1*, *2*). Diversity training may be ineffective because it is commonly implemented in ways that are not conducive to changing behavior: It takes place far in advance of consequential decisions and tends to be generic and not specific to the behaviors that organizations may want to affect (e.g., hiring). Results of our large-scale field experiment in a global telecommunications and engineering firm show that behaviorally designed diversity training can influence hiring decisions. This training increased the short-listing of women and nonnational applicants and increased the hiring of nonnational applicants relative to business as usual. This proof of concept demonstrates that new approaches to diversity training can deliver results.

Although meta-analyses have found that diversity training can help people acquire knowledge about diversity issues (*3*), previous studies of the typical diversity trainings conducted in organizations have found largely null effects on behavior (*4*, *5*). As such, for organizations interested in increasing diversity, it might be reasonable to conclude that diversity training does not work, so they should instead invest their resources into other sorts of diversity initiatives.

But if training as thus far implemented has been largely ineffective, it is important to ask why. Research on decision-making may offer some clues: Past studies have shown that timeliness is critical for behavioral interventions (*6*), that effects of prejudice-reduction interventions can decay quickly (*7*), that the decision context and appropriate authority figures matter for behavior change (*8*), and that making diversity salient can spur equity-enhancing decisions (*9*, *10*). Yet in practice, organizational diversity trainings are typically created without following principles of behavioral design (*11*). As a result, employees often participate in generic diversity training at onboarding or as part of an annual process, without regard to when con-

Training was sent to hiring managers before they selected candidates to interview.

PHOTO: MAVO/ISTOCKPHOTO

[1]Department of Economics, University of Exeter Business School, Exeter, UK. [2]Harvard Businesss School, Boston, MA, USA. [3]Harvard Kennedy School, Cambridge, MA, USA. [4]Harvard Radcliffe Institute, Cambridge, MA, USA. [5]Institute for Data Science and Artificial Intelligence, University of Exeter, Exeter, UK. Email: o.hauser@exeter.ac.uk

sequential workplace decisions—such as hiring and promotions—occur, and the content may span myriad topics without focusing on specific decisions.

The company with which we partnered was interested in encouraging managers to hire more people from underrepresented groups. To have the best chance to accomplish this goal, the diversity training drew on principles of behavioral design (*11*). First, the training was timely: Hiring managers were asked to watch a 7-min diversity training video immediately before short-listing candidates (i.e., selecting whom to interview). Second, the content was tailored to hiring decisions: The training told managers to base their assessment on skills and to think about how to maximize the collective intelligence of their team. It also asked managers to reflect on what perspectives and characteristics were missing on their teams. Third, the training invoked appeals to authority and accountability: The video featured two senior executives of the company discussing these topics. Finally, the training explicitly affirmed that the company valued diversity and inclusion (e.g., by telling managers, "We want to be an organization that reflects the diversity of our society, both today and in the future. Try to bring someone into the team with a background, experience, or perspective that is currently underrepresented").

In addition to the diversity training, in accordance with the company's recommendation, the field experiment also included another condition featuring a version of the training that did not explicitly mention diversity but focused on team effectiveness instead (hereafter referred to as the "effectiveness training"). This condition allowed us to explore an alternative framing that did not make diversity explicit, potentially assuaging concerns around reactance to explicit diversity trainings (*12*). The content of the effectiveness training was similar to that of the diversity training (e.g., it was of similar length, it included the same senior executives, and the timing of the delivery—i.e., before short-listing candidates—was the same), but it instead framed hiring people with different perspectives and backgrounds as being beneficial for team effectiveness, as opposed to making any explicit references to diversity or inclusion. For example, the effectiveness training (versus the diversity training) asked managers to "reflect on what's needed for the role but also what's needed to build a more effective [versus diverse] team" and invited them to consider "building a high-performing [versus inclusive] culture," respectively. Comparing these two conditions allowed us to isolate the effect of making salient both diversity and the company's commitment to diversity in the training.

To test the effects of these different trainings, all hiring managers at the company (80% men; listing job vacancies across 110 countries) were randomly assigned to one of three conditions before raising a job requisition: the diversity training condition, the effectiveness training condition, or the no-treatment ("business-as-usual") control condition [see fig. S1 in the supplementary materials (SM) for a depiction of our study design].

Prior research suggests that interventions perceived as controlling or constraining can lead to backlash or reactance (*12*). Thus, watching the video was voluntary. In addition, we conducted intention-to-treat analyses (i.e., we analyzed hiring decisions for all 10,433 job requisitions raised by 3385 managers in the experimental time frame of July 2022 through December 2022, regardless of whether the hiring manager watched the video), thereby avoiding self-selection issues and increasing the generalizability of our results. For additional information about the experimental conditions, the sample, our analysis strategy, and robustness checks, see the SM. Unless noted otherwise, all analyses were preregistered (AsPredicted no. 101182).

We examined the effects of the diversity training on who was short-listed and who was hired. It was 12% (3.0 percentage points) more likely for a woman to be on the short list in the diversity training condition relative to the control condition [$P = 0.008$; 95% confidence interval (CI) (0.008, 0.053)] (see the figure). However, we did not see significant effects of the diversity training on the likelihood that a woman was hired relative to the control condition ($P = 0.100$). The likelihood of short-listing and hiring female applicants in the effectiveness training condition was not significantly different from the control condition ($P = 0.088$ and $P = 0.238$, respectively) or the diversity training condition ($P = 0.394$ and $P = 0.662$, respectively). For a breakdown of results, see table S2 in the SM.

We preregistered our intent to examine effects of the treatment on race or ethnicity if the data were available. Collecting such data can be complicated for a multinational company because in some countries it is illegal to collect race or ethnicity data, whereas in others it is uncommon for people to disclose such information. In the end, the engineering firm could only make the nationality of job applicants available to us. A higher representation of nonnationals and women was part of its internal equity, diversity, and inclusion (EDI) goals. Thus, we conducted non-preregistered analyses of whether a nonnational—that is, a job candidate who is a national of a country that is different from the country of the job opening—was short-listed or hired (using the same preregistered regression specifications and controls). It was 13% (2.7 percentage points) more likely for a nonnational to be on the short list in the

A proof of concept that diversity training can work

The likelihoods that a female, nonnational, or female nonnational applicant was short-listed or was hired were highest in the diversity training condition. Likelihood estimates of conditions included preregistered control variables and fixed effects. Error bars represent 95% confidence intervals. See the supplementary materials for further details.

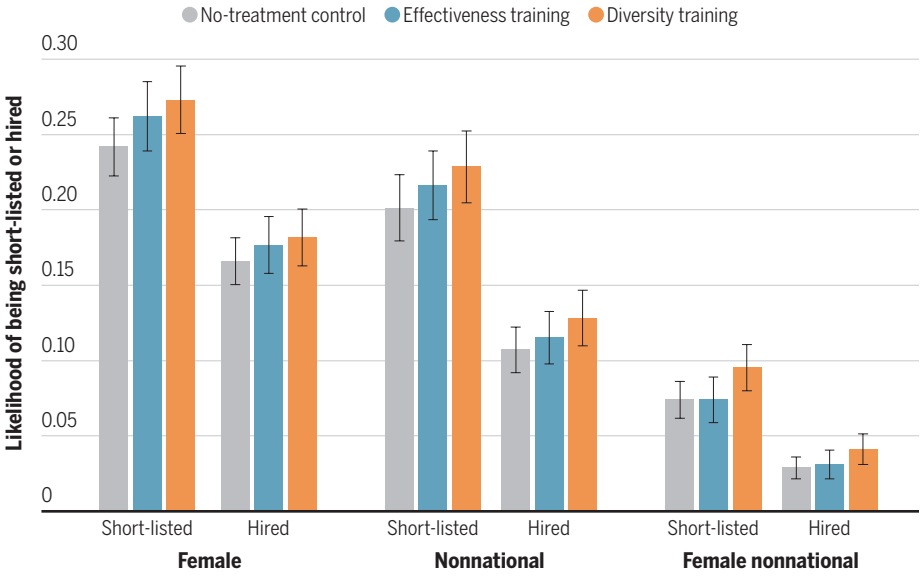

GRAPHIC: V. PENNEY/*SCIENCE*

diversity training condition relative to the control condition [P = 0.024; 95% CI (0.004, 0.051)] (see the figure). The diversity training also increased the likelihood that a nonnational was hired by 20% (2.1 percentage points) relative to the control condition [P = 0.025; 95% CI (0.003, 0.040)]. Again, the rates of short-listing and hiring nonnationals in the effectiveness training condition were not significantly different from the control condition (P = 0.213 and P = 0.362, respectively) or the diversity training condition (P = 0.294 and P = 0.173, respectively).

In further non-preregistered analyses, we also examined treatment effects on the short-listing and hiring of people from multiple underrepresented groups—in our case, female nonnationals. It was 28% (2.1 percentage points) more likely for a female nonnational to be on the short list in the diversity training condition relative to the control condition [P = 0.007; 95% CI (0.006, 0.037)] (see the figure). The diversity training also increased the likelihood that a female nonnational applicant was hired by 41% (1.2 percentage points) relative to the control condition [P = 0.018; 95% CI (0.002, 0.023)]. The increase in short-listing in the diversity training condition was also significantly higher relative to the effectiveness training condition [P = 0.010; 95% CI (0.005, 0.037)], but it was not significant for hiring (P = 0.055). The effectiveness training condition was not significantly different with respect to short-listing and hiring relative to the control condition (P = 0.973 and P = 0.652, respectively).

The findings for nonnationals were not just driven by Europeans moving around Europe or Canadians being hired in the US. In further non-preregistered analyses, we found similar results when examining whether applicants from the Global South were shortlisted or hired (see table S3 in the SM).

We also conducted various heterogeneity analyses to explore potential moderators. We found that the effects of diversity training were generally larger in higher-income countries (see table S4 in the SM), in countries that have higher levels of gender equality (see table S5 in the SM), and in the wealthy and relatively gender-equal headquarters country of the company (see tables S6 to S8 in the SM). We did not find significant moderation by individual characteristics of the manager, such as manager gender or seniority (see tables S9 and S10 in the SM). These results suggest that there is considerable variation in response to diversity training by country and cultural context but not by individual factors.

The results of this field experiment show that a behaviorally designed diversity training can lead to consequential behavior change. Although the effect sizes on hiring were at times small in absolute terms, they were often large in relative terms (e.g., it was 114% more likely for a female nonnational candidate to be hired in the headquarters country in the diversity training condition versus the control condition), which reflects low baseline rates of hiring members of historically underrepresented groups. In addition, our results were stronger in the headquarters country, where societal gender equality is high. It is plausible that diversity interventions work better when aligned with cultural norms (*3*) or that our intervention brought about higher levels of conformity among managers closer to the center of the organization. By contrast, the effectiveness training did not significantly affect short-listing or hiring compared with the control and did significantly worse for short-listing outcomes compared with the diversity training when looking at female nonnationals, consistent with past research showing that making diversity salient can spur equity-enhancing decisions (*9*, *10*).

"...success relies on carefully considered design choices and the decision context."

Because our goal was to test a behaviorally designed diversity training that consisted of many differences compared with past trainings—including diversity salience, timeliness, task specificity, and the delivery by an organizational authority figure—we are unable to single out the specific active ingredient that led to the observed behavior change. It is possible that any, all, or some combination of these factors were necessary to see our effects, and future research should experimentally isolate each of these factors. Our approach also made salient that managers were expected to contribute to an "organization that reflects the diversity of our society," and, as such, managers may have reweighted the decision criteria ahead of their short-listing and hiring decisions or simply complied with a request from a senior leader (*13*).

The current research is a proof of concept that diversity training can work to change the diversity of hires, but its success relies on carefully considered design choices and the decision context. Although the outcome of interest in this study was demographic representation, we cannot exclude the possibility that the trainings also affected other outcomes, such as team performance, job satisfaction, or turnover.

Going forward, we hope that researchers, policy-makers, and organizational leaders will invest in rigorous randomized controlled trials (*14*) to study when and how diversity training can be implemented in ways that lead to actual behavior change across a wide range of relevant organizational outcomes. Such evidence might be particularly important at a time when the merits and impacts of diversity initiatives are debated. Many organizations have committed to broadening their representation and want to access the full range of the talent pool. Our research offers a practical tool for leaders interested in changing behavior to meet this commitment. ■

REFERENCES AND NOTES

1. A. Kalev, F. Dobbin, E. Kelly, *Am. Sociol. Rev.* **71**, 589 (2006).
2. E. L. Paluck, R. Porat, C. S. Clark, D. P. Green, *Annu. Rev. Psychol.* **72**, 533 (2021).
3. K. Bezrukova, C. S. Spell, J. L. Perry, K. A. Jehn, *Psychol. Bull.* **142**, 1227 (2016).
4. E. H. Chang *et al.*, *Proc. Natl. Acad. Sci. U.S.A.* **116**, 7778 (2019).
5. C. K. Lai, J. A. Lisnek, *Psychol. Sci.* **34**, 424 (2023).
6. J. Austin, S. O. Sigurdsson, Y. S. Rubin, *Environ. Behav.* **38**, 140 (2006).
7. C. K. Lai *et al.*, *J. Exp. Psychol. Gen.* **145**, 1001 (2016).
8. R. B. Cialdini, N. J. Goldstein, *Annu. Rev. Psychol.* **55**, 591 (2004).
9. E. H. Chang, E. L. Kirgios, A. Rai, K. L. Milkman, *Manage. Sci.* **66**, 2752 (2020).
10. E. L. Kirgios, A. Rai, E. H. Chang, K. L. Milkman, *Nat. Hum. Behav.* **6**, 383 (2022).
11. I. Bohnet, S. Chilazi, *Make Work Fair: Data-Driven Design for Real Results* (Harper Collins, 2025); https://www.harpercollins.com/products/make-work-fair-iris-bohnetsiri-chilazi.
12. F. Dobbin, D. Schrage, A. Kalev, *Am. Sociol. Rev.* **80**, 1014 (2015).
13. J. Axt, J. To, *J. Pers. Soc. Psychol. Rev.* 10.1177/10888683241244829 (2024).
14. O. P. Hauser, E. Linos, T. Rogers, *Res. Organ. Behav.* **37**, 185 (2017).
15. C. Arslan, E. H. Chang, S. Chilazi, I. Bohnet, O. P. Hauser, Code and data access instructions for "Behaviorally designed training leads to more diverse hiring," Dryad (2025); https://doi.org/10.5061/dryad.9cnp5hqvt.

ACKNOWLEDGMENTS

All code for replication and information about how to request access to the proprietary dataset can be found in the SM as well as at Dryad (*15*). The authors are grateful to the global telecommunications and engineering company that allowed them to study these research questions and to MoreThanNow, a behavioral science consultancy that assisted the company with the implementation of the randomized controlled trial. The authors thank, in particular, J. Elfer, K. Wright, and G. Lindemann for the trial implementation as well as E. Kirgios, K. Milkman, and A. Duckworth for feedback on the manuscript. Neither the field partner nor MoreThanNow had any role in the data analysis, the publishing decision, or the manuscript preparation. The research team did not receive any compensation for their involvement in this study, neither from the global telecommunications and engineering company nor from MoreThanNow. O.P.H. has previously been involved in paid consulting work for MoreThanNow on other projects (unrelated to the global telecommunications and engineering company), and all members of the research team serve as unpaid academic advisors to MoreThanNow. O.P.H. acknowledges funding from the UKRI Future Leaders Fellowship (MR/T020253/1).

SUPPLEMENTARY MATERIALS

science.org/doi/10.1126/science.ads5258

10.1126/science.ads5258

BOOKS *et al.*

Anatomical studies seeking to define sex and gender often lead to more questions than answers.

HUMAN ANATOMY

In search of the female form

Bodies have long resisted easy categorization

By **Tara Mulder**

Breasts, clitoris, hymen, womb—do these parts make a woman? In *Immaculate Forms*, historian Helen King shows how, throughout (mostly) Western history, these four parts have both defined and complicated femaleness.

King identifies medicine and its uneasy companion, religion, as the main constructors and gatekeepers of sexed bodies. Consequently, many of her sources are medical and religious texts and images. But she also references anthropological writings; cultural productions, including artwork, poetry, novels, movies, and magazine articles; and cultural ephemera, from ancient Greece and Rome to today.

"People have always altered the raw material of bodies," maintains King. Sometimes these alterations have taken expected forms: breast enlargements or reductions, mastectomies and hysterectomies for health or gender affirmation, and clitoridectomies to curtail masturbatory impulses. But sometimes these alterations have been surprising. In the early 19th century, Princess Marie Bonaparte, great-grandniece of Napoleon, underwent voluntary surgery to have her clitoris moved closer to her vaginal opening. Her request came from research she herself had conducted, which showed that women with more than two and a half centimeters between their clitoris and vaginal opening had a difficult time "reach[ing] orgasm from vaginal sex."

Immaculate Forms: A History of the Female Body in Four Parts
Helen King
Basic Books, 2025.
480 pp.

King refuses to write either a narrative of progress "toward a 'now' in which we know pretty much all there is to know" or a romanticized story of lost wisdom. Neither would be accurate. Instead, her history is one that loops forward and back around, goes off on tangents, drops the thread, and picks it up again.

We can see this looping in the repeating history of "discovering" the clitoris. Ancient Greek medical writers knew about the clitoris; they called it the "nymph" or the "myrtle berry." But, in 1559, Italian anatomist Matteo Realdo Colombo announced that he had "discovered" the clitoris—with his little finger, no less. Then, again, in 1998, urologist Helen O'Connell announced her discovery of the full, interior clitoris—a large erectile organ extending beneath the labia. But anatomy books from the late 19th century had shown this same thing. It was textbooks from the mid-20th century that depicted the clitoris as merely a little bud at the top of the vulva.

In her 40 years of working on the history of the female body, King has toppled more than one beloved yet erroneous hypothesis. In her 2013 book, *The One-Sex Body on Trial*, she mounted an eviscerating offensive against Thomas Laqueur's evocative theory of a premodern "one-sex" body. She similarly challenged Rachel Maines's story of the development of the vibrator as a cure for hysteria, critiquing both Maines's flawed thesis and her subpar research methods.

King is meticulous and prolific. She has written with equal erudition and care about the ancient, medieval, and early modern periods. She brings this range and expertise to *Immaculate Forms*—plus more than a little humor. I laughed out loud when I read that, to her, an ancient Roman breast votive looks "very much like a baked potato."

But sometimes King's precision gets in her way. There is a famous drawing of a uterus from anatomist Andreas Vesalius's 1543 *On the Fabric of the Human Body*. As she has before, King here takes Laqueur to task for labeling this image "vagina as penis"—part of his evidence for the "one-sex" body. But King points out that, in Vesalius's text, this image is "clearly labeled as a womb," not a penis. Laqueur, she contends, is forcing an anachronistic, modern interpretation onto the image. But the thing is, this image, which includes the vagina as well as the uterus, looks exactly like a penis. Here, King's insistence on exactness does not help her reader understand what a penile-looking vagina/uterus is doing in a 16th-century anatomy text.

At times, too, this book could have used more organization. In the part on the hymen, King argues that, as important as the hymen has been throughout history, it has never been clear whether it is real or not. After reading the chapter, I was still left wondering whether the hymen is real or not (which perhaps was King's point). But I would have liked a bit more scaffolding as I navigated this challenging material.

King's care, however, pays off in her thoughtful and inclusive attention to ambiguously and trans-sexed bodies. One of the book's main points is that repeatedly, throughout history and despite the best efforts of medicine, religion, and culture, binaries fall apart. "Femaleness" is not always clear, and it is not always distinguishable from "maleness." *Immaculate Forms* is a masterful achievement born from an impressive and influential career. ■

The reviewer is at the Department of Classical and Ancient Near Eastern Studies, University of Wisconsin–Madison, Madison, WI, USA. Email: tlmulder@wisc.edu

10.1126/science.adu3681

SCIENCE AND SOCIETY

Scientists as advocates

A sociologist rejects the notion that science is inherently apolitical, urging scholars to join the public square

Citizen Scholar: Public Engagement for Social Scientists
Philip N. Cohen
Columbia University Press, 2025. 312 pp.

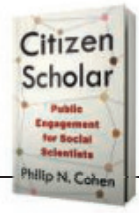

By **Jonathan Wai**

Sociologist Philip Cohen's new book, *Citizen Scholar: Public Engagement for Social Scientists*, argues that we need more scholars to join the public square. He is open about his personal political commitments as a "progressive who favors liberal social policies" and argues that more scientists should be up front about theirs, rejecting the idea that academics are inherently apolitical. "Others might say my public political pronouncements undermine not just my science but the reputation of sociology as a whole," he writes. "I can't prove they're wrong. But I think the roles of citizen and scholar are ultimately compatible."


Marine conservationist Aristide Takoukam Kamla (left) engages with tourists in Dizangue, Cameroon.

Cohen begins the book by discussing his personal experience using social media to engage with broad audiences during the COVID-19 pandemic. Twitter (now X) is where Cohen got his start on social media, although he has since left the platform. In its prime, he argues, academics, journalists, and political types all engaged with one another on Twitter and thus reached multiple audiences. So far, he has not seen this replicated on other platforms.

The reviewer is at the Department of Education Reform and Department of Psychology, University of Arkansas, Fayetteville, AR, USA. Email: jwai@uark.edu

Here, he reminds scholars to read more widely than they might otherwise be inclined, listen to and learn from people in other fields and the broader public, focus on contributing something unique to the conversation, collaborate, and ensure that their efforts contribute to new knowledge. Cohen argues that a citizen scholar's workflow should focus not just on disseminating information but also on integrating broad sources of new information in a way that informs subsequent scholarship. This strategy echoes earlier models for building better theories that are more replicable and robust (*1*).

Next, Cohen argues that descriptive research has much to offer public policy [for a similar argument, see (*2*)], as many stakeholders are unlikely to appreciate complicated graphs and statistics. "Descriptive empirical work sets research agendas, shapes media narratives, and informs students and the public," he insists.

The book emphasizes open scholarship and open science, arguing that transparency and accountability are important to advancing science. Here, Cohen probes the inherent tension between leaving one's politics at the laboratory door and the need to be a spokesperson for one's area of expertise.

Next, he addresses peer review, observing that "in a recent year, there were almost 14 million peer reviews of research articles conducted, requiring sixty-nine million hours." He argues that, despite its flaws, peer review is important because it is a way for the public to know that information has been vetted by experts. Cohen includes in this discussion an argument in favor of public review of articles that have already been published as a means to debunk and call out flawed scholarship.

Marketing is something all academics do. Most of us engage with our field peers—in the past, people ordered "offprints" of their work and mailed the articles to colleagues—but increasingly, if we want to be cited and have a major impact, we need others to at least scan our work too. Cohen argues that social media is useful in this regard and that, for better or worse, it is now an important tool for scholarship and career advancement. When scholars choose not to engage in such forums, he reminds readers, others will fill the void.

"I want to urge a more open attitude toward an activist orientation," Cohen writes. Silence is not acceptable for the type of citizen scholar he envisions—a vision that is seemingly at odds with the traditional academic values of institutional and personal neutrality (*3*).

Cohen concludes by introducing readers to the public engagement "pentagulation," which he defines as an interplay between peer review, open scholarship, one's personal website, their social media, and interactions with the news media. Here he provides tips on how to engage with the public and how to maximize the impact of one's scholarship.

Should academic scientists be openly political? Or should they instead focus their efforts on reducing the likelihood of their personal values biasing their research? When might public engagement do more harm and when might it do more good (*4*, *5*)? Cohen's position is firm—our values are inherently inseparable from our science, and we must act accordingly. ■

REFERENCES AND NOTES

1. P. E. Meehl, *J. Consult. Clin. Psychol.* **46**, 806 (1978).
2. J. Gerring, *Br. J. Polit. Sci.* **42**, 721 (2012).
3. "Report on the university's role in political and social action" (Univ. of Chicago, 1967); https://provost.uchicago.edu/reports/report-universitys-role-political-and-social-action.
4. N. Hall, *Genome Biol.* **15**, 424 (2014).
5. S. Martinez-Conde, *J. Neurosci.* **36**, 2077 (2016).

10.1126/science.adv2036

PHOTO: DANIEL BELOUMOU OLOMO/AFP VIA GETTY IMAGES

ANNOUNCING THE 2024

Swanson Award Winners


PHOTO BY TOM COOK

Dr. Andreas Madlung
DISTINGUISHED PROFESSOR OF BIOLOGY, UNIVERSITY OF PUGET SOUND
Lynwood W. Swanson Scientific Research Award

Dr. Lynwood Swanson
TRUSTEE EMERITUS, M.J. MURDOCK CHARITABLE TRUST

Dr. Samuel Fey
ASSOCIATE PROFESSOR OF BIOLOGY, REED COLLEGE
Lynwood W. Swanson Promise for Scientific Research Award

We are honored to recognize the scientific accomplishments of these esteemed researchers.

〈 **Scan the QR code to learn more about the winners**

College Science Research
A MURDOCK TRUST PROGRAM

M.J. Murdock
CHARITABLE TRUST

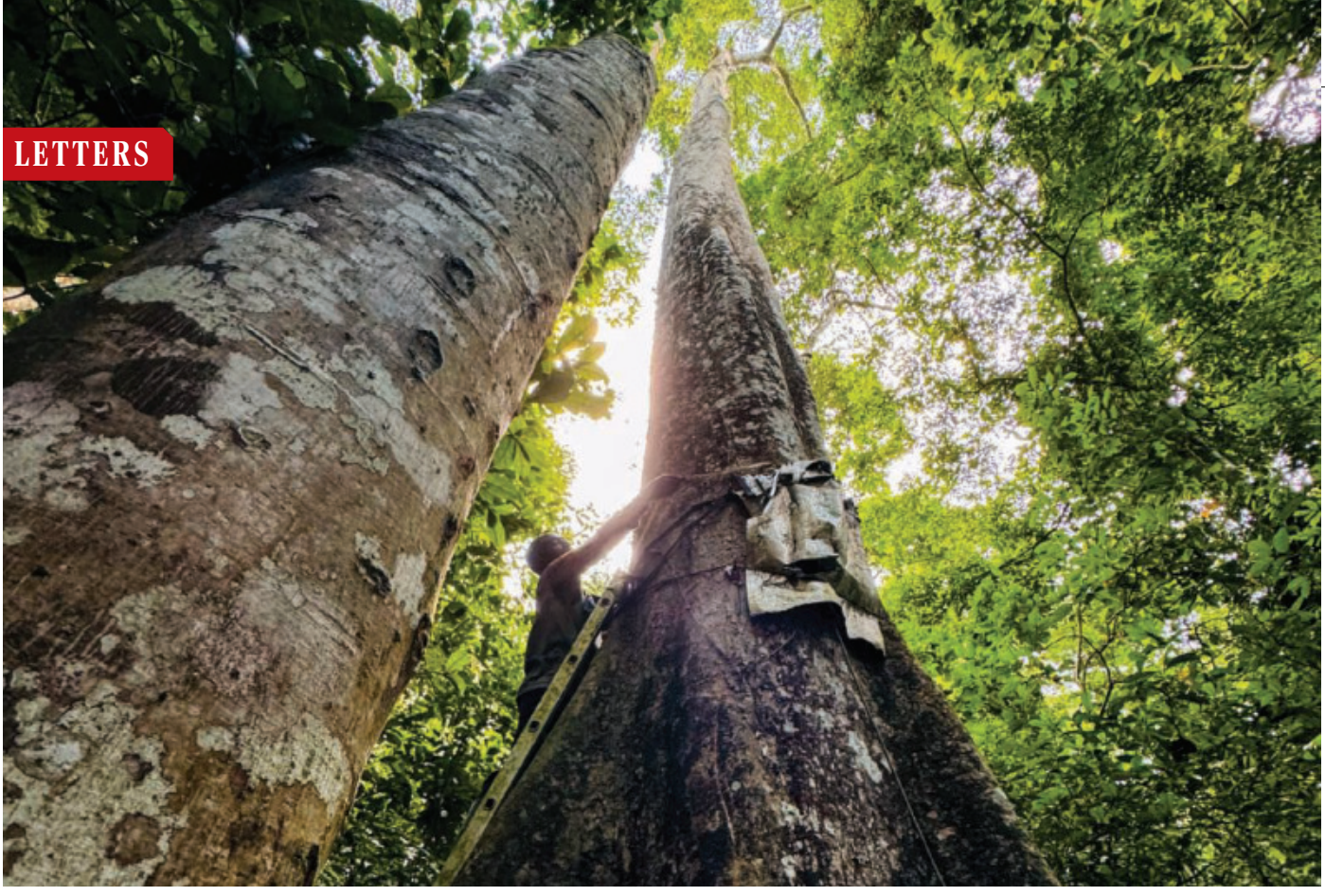

Incorporating measurements from individual trees, such as those taken by this scientist in Ghana, can increase the accuracy of forest carbon estimates.

PHOTO: DR. NEHA HUNKA

Edited by **Jennifer Sills**

Editorial Expression of Concern

In the 4 June 2010 issue, *Science* published the Report "FCHo proteins are nucleators of clathrin-mediated endocytosis" by W. M. Henne *et al.* (*1*). The editors and authors have been made aware of potential data integrity issues in several figures. We are alerting readers to this concern while we work with the institution and the authors to determine an appropriate course of action.

H. Holden Thorp
Editor-in-Chief, *Science*

REFERENCES AND NOTES

1. W. M. Henne *et al.*, *Science* **328**, 1281 (2010).

10.1126/science.adv6429

Spatial resolution for forest carbon maps

Forests are central to climate solutions (*1*), and transparent and accurate data on forest carbon stocks and fluxes are critical for scientists and decision-makers. Satellite-based forest carbon maps have recently proliferated from public agencies such as NASA and the private sector. These maps have tended toward ever-higher spatial resolutions. However, higher spatial resolutions increase the uncertainties of carbon maps, rendering products at very high spatial resolution largely meaningless for forest carbon monitoring.

Many new satellites can resolve fine features on the landscape, and even some individual trees outside forests (*2*), but this resolution (0.3 to 5 m) is too high for mapping forest carbon. Forest carbon has a natural resolution constraint: the size of an individual tree. To create these maps, tree data from the ground are required because there is no direct measure of tree carbon nor any way to accurately divide trees into smaller components from space (*3*). Typically, a plot the size of some desired mapping resolution is created in a forest, within which trees are measured and converted to carbon estimates, summed, and combined with satellite data to develop statistical models used to map forest carbon. It is not possible to map (or validate) forest carbon with meaningful accuracy at resolutions higher than the area of the forest plot data used to create a map (*4*).

Because most carbon in a forest is stored in large trees (*5*–*7*), map resolutions should at minimum exceed the crown diameter of a typical large tree, which ranges from about 10 m for temperate forests to about 20 m for tropical forests (*8*). To minimize other sources of uncertainty that increase at high resolution (*9*, *10*), forest plots that include many trees should be at least 0.25 ha (50 m) and ideally 1 ha (100 m) in tropical forests (*11*) and at least 0.1 ha in boreal and temperate forests (*12*). Maps should not be downscaled to higher spatial resolutions given that a map's values and uncertainties are only meaningful at their original resolution.

By adhering to these resolution guidelines, map users can make informed decisions about the data used to monitor forests as nature-based climate solutions, and map producers can make useful maps. Any satellite-based product should undergo rigorous and transparent validation before it is used for operational monitoring, including the generation of forest-based carbon credits. Without aligning forest carbon map resolution with forest plot data, we cannot accurately quantify carbon in the forest or in the trees.

Laura Duncanson[1]*, Neha Hunka[1], Tommaso Jucker[2], John Armston[1], Nancy Harris[3], Lola Fatoyinbo[4], Christopher A. Williams[5], Jeff W. Atkins[6,7], Brett Raczka[8], Shawn Serbin[4], Michael Keller[9], Ralph Dubayah[1], Chad Babcock[10], Mark A. Cochrane[11], Andrew Hudak[12], George C. Hurtt[1],

Paul M. Montesano[13], L. Monika Moskal[14], Taejin Park[15], Sassan Saatchi[16,17], Carlos A. Silva[18], Hao Tang[19], Rodrigo Vargas[20], Aaron Weiskittel[21], Konrad Wessels[22], Scott J. Goetz[23]

[1]Geographical Sciences, University of Maryland, College Park, MD, USA. [2]School of Biological Sciences, University of Bristol, Bristol, UK. [3]World Resources Institute, Washington, DC, USA. [4]NASA Goddard Space Flight Center, Greenbelt, MD, USA. [5]Graduate School of Geography, Clark University, Worcester, MA, USA. [6]US Department of Agriculture (USDA) Forest Service, Southern Research Station, New Ellenton, SC, USA. [7]Department of Biology, Virginia Commonwealth University, Richmond, VA, USA. [8]Computational and Information Systems Lab, Data Assimilation Research Section, National Center for Atmospheric Research, Boulder, CO, USA. [9]International Institute of Tropical Forestry, USDA Forest Service, Rio Piedras, PR, USA. [10]Forest Resources Department, University of Minnesota, St. Paul, MN, USA. [11]University of Maryland Center for Environmental Science, Frostburg, MD, USA. [12]Rocky Mountain Research Station, USDA Forest Service, Moscow, ID, USA. [13]NASA Goddard Space Flight Center, ADNET Systems, Greenbelt, MD, USA. [14]School of Environmental and Forest Sciences, University of Washington, WA, USA. [15]Bay Area Environmental Research Institute, Moffett Field, CA, USA. [16]NASA Jet Propulsion Laboratory, California Institute of Technology, Pasadena, CA, USA. [17]CTrees, Pasadena, CA, USA. [18]Forest Biometrics, Remote Sensing and Artificial Intelligence Lab (SilvaLab), School of Forest, Fisheries, and Geomatics Science, University of Florida, Gainesville, FL, USA. [19]Department of Geography, National University of Singapore, Singapore. [20]Department of Plant and Soil Sciences, University of Delaware, Newark, DE, USA. [21]Center for Research on Sustainable Forests, University of Maine, Orono, ME, USA. [22]Geography and Geoinformation Science, George Mason University, Fairfax, VA, USA. [23]School of Informatics, Computing and Cyber Systems, Northern Arizona University, Flagstaff, AZ, USA.
*Corresponding author.
Email: lduncans@umd.edu

REFERENCES AND NOTES

1. P. Friedlingstein *et al.*, *Earth Syst. Sci. Data* **14**, 4811 (2022).
2. C. Tucker *et al.*, *Nature* **615**, 80 (2023).
3. J. Chave *et al.*, *Surv. Geophys.* **40**, 863 (2019).
4. L. Duncanson *et al.*, *Surv. Geophys.* **40**, 979 (2019).
5. V. Meyer *et al.*, *Biogeosciences* **15**, 3377 (2018).
6. J. A. Lutz *et al.*, *Glob. Ecol. Biogeogr.* **27**, 849 (2018).
7. J. W. F. Slik *et al.*, *Glob. Ecol. Biogeogr.* **22**, 1261 (2013).
8. T. Jucker *et al.*, *Glob. Chang. Biol.* **28**, 5254 (2022).
9. S. G. Zolkos, S. J. Goetz, R. Dubayah, *Remote Sens. Environ.* **128**, 289 (2013).
10. M. Réjou-Méchain *et al.*, *Surv. Geophys.* **40**, 881 (2019).
11. L. Duncanson *et al.*, in *Good Practices for Satellite-Derived and Product Validation*, L. Duncanson *et al.*, Eds. (2021), p. 236.
12. G. W. Frazer, S. Magnussen, M. A. Wulder, K. O. Niemann, *Remote Sens. Environ.* **115**, 636 (2011).

10.1126/science.adt6811

Tanzania's effective trophy hunting laws

In their Letter "Stop elephant hunting in Tanzania borderlands" (19 July 2024, p. 265), J. Poole *et al.* object to recent killings of elephants by trophy hunters on the grounds that the targeted animals were important to population sustainability and were part of a long-term research study in Kenya. Although we agree that this elephant population is crucial to species conservation, we consider only collared elephants to be under study, not the entire subpopulation or all elephants monitored, and we do not agree that the handful of elephants killed by trophy hunters puts the population at risk. Poole *et al.* also suggest that Tanzania should make exceptions to the United Nations (UN) Principle of Permanent Sovereignty over Natural Resources, essentially ceding management of the elephant population to Kenya, but the UN principle has no exceptions and applies universally and equally, unless a bilateral agreement has been established and agreed upon by partner states.

Trophy hunting in Tanzania is well-regulated and complies with the Convention on International Trade in Endangered Species of Wild Fauna and Flora (CITES). Tanzania's conservative annual quota of 50 elephants (*1*) for trophy hunting represents less than 0.1% of the country's elephant population (*2*). Between 2018 and 2023, only 38 elephant bulls were hunted in Tanzania (*3*), instead of the approved quota by CITES of 300 elephants for the 6 years. Trained wildlife officers, professional hunters, and village game scouts accompany trophy hunters and identify appropriate targets on the basis of age and sex (*4*). Hunters are permitted to kill only males with tusks that weigh at least 20 kg or measure at least 160 cm (*2*). Although killing animals wearing collars or otherwise marked for research is not formally prohibited, the accompanying professionals are trained to understand the importance of avoiding such animals as targets.

Poole *et al.* argue that the targeted "super tuskers" are important to population growth, but most mature bulls sire offspring starting at about 25 years old (*5*), and most super tuskers (elephants with tusks that weigh more than 45 kg each) are between 45 and 55 years old (*6*) and are nearing the end of their natural life cycle of about 70 years (*7*). Therefore, elephants approved as hunting targets have likely already been breeding for at least 20 years. If not hunted, such elephants are often killed in human-elephant conflicts (*8*). Given that males gain in dominance rank as they age (*9*), old bulls prevent young bulls from breeding effectively. Therefore, trophy hunting allows young bulls to breed earlier, contributing to increased genetic diversity (*5*).

Trophy hunting benefits conservation and community development (10, 11). Revenue from trophy hunting accounts for 55.5% of the money that the Tanzania Wildlife Management Authority invests in conservation (12), whereas photographic tourism accounts for only 21.1% (12), Special Wildlife Investment Concession Areas (SWICA) account for 12.9%, and other sources (such as sport fishing, resident hunting, and the Tourism Development Levy) account for 10.5% (12).

Elephants that are part of research studies provide important data for conservation and management, including information about reducing human-elephant conflicts. To help protect elephants under research, researchers in Kenya and Tanzania could alert one another when research elephants with GPS collars or known body markers (such as a broken or single tusk) move into another country. By sharing knowledge, countries can jointly monitor research elephants and save them from trophy hunters. Cross-border coordination framework laws have successfully improved cross-border biodiversity management in the Maasai Mara–Serengeti ecosystem (13).

Julius Keyyu[1]*, Robert Fyumagwa[2], Eblate Mjingo[1], Dos Santos Silayo[3], Emmanuel Masenga[1], Victor Kakengi[1], Alfan Rija[4], Jafari Kideghesho[5]

[1]Tanzania Wildlife Research Institute, Arusha, Tanzania. [2]Wildlife Conservation Initiative, Arusha, Tanzania. [3]Tanzania Forest Services, Dodoma, Tanzania. [4]Sokoine University of Agriculture, Chuo Kikuu, Morogoro, Tanzania. [5]College of African Wildlife Management, Moshi, Tanzania.
*Corresponding author.
Email: julius.keyyu@tawiri.or.tz

REFERENCES AND NOTES

1. CITES, Export quotas, United Republic of Tanzania (2024); https://cites.org/eng/resources/quotas/export_quotas?field_country_target_id=197&field_species_target_id=Loxodonta+africana&field_specimens_target_id=&field_date_value%5Bmin%5D=2017-01-01&field_date_value%5Bmax%5D=2024-12-31.
2. A. L. Lobora *et al.*, Eds, "Tanzania Elephant Management and Action Plan 2023-2033" (Ministry of Natural Resources and Tourism, United Republic of Tanzania, 2023).
3. "Elephant hunting in Tanzania: A perspective of transboundary ecosystem" (Ministry of Natural Resources and Tourism, United Republic of Tanzania, 2024); https://www.tawiri.or.tz/elephant-hunting-in-tanzania-a-transboundary-ecosystem-perspective_2024/.
4. "The Wildlife Conservation (Tourist Hunting) Regulations, 2015" (United Republic of Tanzania, Government notice no. 414, 2015); https://www.tawa.go.tz/storage/app/uploads/public/631/705/8b0/6317058b0c071118827416.pdf.
5. H. B. Rasmussen *et al.*, *Behav. Ecol.* **19**, 9 (2008).
6. "Meet Tsavo's Super Tuskers. A profile on Africa's giants" (Tsavo Trust, 2024); https://tsavotrust.org/meet-tsavos-super-tuskers-a-profile-on-africas-giants/#.
7. P. C. Lee, L. F. Bussière, C. E. Webber, J. H. Poole, C. J. Moss, *Biol. Lett.* **9**, 20130011 (2013).
8. C. R. B. Allen, L. J. N. Brent, T. Motsentwa, M. N. Weiss, D. P. Croft, *Sci. Rep.* **10**, 13996 (2020).
9. J. H. Poole, *Anim. Behav.* **37**, 140 (1989).
10. V. K. Muposhi, E. Gandiwa, P. Bartels, S. M. Makuza, *Int. J. Biodivers.* **2016**, 8763980 (2016).
11. P. A. Lindsey, G. A. Balme, P. J. Funston, P. H. Henschel, L. T. B. Hunter, *Conserv. Lett.* **9**, 296 (2016).
12. Tanzania Wildlife Management Authority (TAWA), "Report of the Controller and Auditor General on the Financial and Compliance Audit for the Financial Year ended 30 June 2023" (National Audit Office, United Republic of Tanzania, 2024); https://www.tawa.go.tz/storage/app/uploads/public/66c/494/665/66c4946658644109241619.pdf.
13. P. Shah, G. O. Krhoda, *Int. J. Sci. Res. Innov. Technol.* **5**, 26 (2018).

10.1126/science.adr8801

A path to US Tribal energy sovereignty

Native American Tribal lands are extraordinarily rich with energy and mineral resources. A rapidly changing energy system, increasing energy demand, and energy-related national security imperatives present Tribes with a generational economic opportunity. If the federal government respects Tribal sovereignty, resource extraction and related projects such as natural gas development, power plants, and data centers on Tribal lands can help create economic prosperity. Tribes could benefit from choosing to become better networked and integrated into domestic and global supply chains.

Despite making up only 2% of the US land base, Tribal lands contain 50% of US uranium reserves (*1*) and enough wind and solar energy generation potential to produce $75 billion in project investment (*2*). Nearly all US reserves of critical minerals needed to manufacture batteries, wind turbines, and electric motors are on or near Tribal reservations, including 97% of nickel, 89% of copper, and 79% of lithium (*3*).

A statue stands on Southern Ute Indian Tribal lands, home to sophisticated natural gas operations.

Centuries of violence, colonialism, and systematic oppression by the federal government have deeply eroded Tribal sovereignty and trust (*4*). Laws such as the 1887 Dawes Act stripped land from Tribes, and the legacy of energy and mining on Tribal lands is rife with financial exploitation, human rights abuses, broken treaties, and dire environmental and health impacts (*5*, *6*). Although poverty and education levels have begun to improve in some cases, the pace and scale of these changes remain insufficient (*7*).

Tribes electing to engage in energy and mineral development on their lands face challenges with roots in these historical injustices. Bureaucracy and outdated federal regulations hinder Tribes' ability to invest efficiently and effectively and impede their access to wider markets. Because scientific and economic resource analyses of Tribal lands are sparse, Tribes are often unaware of the scale of their opportunities. Limited organizational and technical capacity constrain Tribes' ability to develop new projects and access government funds (*8*). Many Tribes lack the necessary administrative capabilities, institutions, and technically trained workforces to fully use the energy resources on their own lands (*8*).

To improve relationships and support vibrant Tribal societies, US federal and state governments must center Tribal communities' desires, acknowledge historical injustices (*9*), and support Tribes as they address skill gaps and expand workforces and infrastructure. Tribes must have the right to lead development projects and ensure that jobs and economic opportunities remain within Tribal communities (*10*–*12*). In addition, Tribes must be empowered to apply their expertise, values, and traditional knowledge to resource development and infrastructure development.

Although challenges remain, collaborating to pursue mutually beneficial aspirations represents an important opportunity to improve relations between the US government and Tribal Nations. As an example, producing and refining critical minerals in Indian Country could support US energy and security goals as well as provide Tribal Nations and people with enhanced sovereignty and increased economic well-being. Development and incorporation into domestic and global supply chains (*13*) would give Tribes access to substantial revenue streams outside of gaming and tied to the modern economy. Tribes might then choose to invest their earnings and capital into a diverse portfolio and take advantage of wider economic opportunities.

Shane Seibel[1], Richard Luarkie[2], Daniel Cardenas[3], Cody Mayer[4], Ramon Sanchez[5], Matt Dannenberg[5], Bazile Minogiizhigaabo Panek[6], Albert Bond[7], Zane Gordon[7], Demi Morishige[1], Kourtney Hadrick[1], Graham Stahnke[1], Robert Fofrich[8], Steve Davis[9], Richard Tallman[4], Brooke Bowser[4], Morgan D. Bazilian[4]*

[1]Southern Ute Indian Tribe Growth Fund, Ignacio, CO, USA. [2]Emerging Equities Solutions Group, Casa Blanca, NM, USA. [3]National Tribal Energy Association, Riverton, WY, USA. [4]Payne Institute for Public Policy, Colorado School of Mines, Golden, CO, USA. [5]Alliance for Tribal Clean Energy, Washington, DC, USA. [6]Good Sky Guidance, Ashland, WI, USA. [7]US Department of the Interior, Bureau of Indian Affairs, Division of Energy and Mineral Development, Denver, CO, USA. [8]Institute of the Environment and Sustainability, University of California, Los Angeles, CA, USA. [9]Earth System Science, Stanford University, Stanford, CA, USA.
*Corresponding author.
Email: mbazilian@mines.edu

REFERENCES AND NOTES

1. S. Regan, T. L. Anderson, "The Energy Wealth of Indian Nations" (George W. Bush Institute, 2014).
2. A. Milbrandt, D. Heimiller, P. Schwabe, "Techno-Economic Renewable Energy Potential on Tribal Lands" (National Renewable Energy Laboratory, 2018).
3. S. Block, "Mining Energy-Transition Metals: National Aims, Local Conflicts" (MSCI, 2021).
4. L. C. Jantarasami *et al.*, "Tribes and Indigenous Peoples," in *Impacts, Risks, and Adaptation in the United States: Fourth National Climate Assessment, Volume II*, D. R. Reidmiller *et al.*, Eds. (US Global Change Research Program, 2018), pp. 572–603.
5. A. H. Merjian, *Gonzaga Law Rev.* **46**, 609 (2010).
6. J. R. Owen *et al.*, *Nat. Sustain.* **6**, 203 (2023).
7. C. Wilkerson, C. Farha, "Oklahoma Tribal Area Economies: Rising Incomes, Falling Poverty" (Federal Reserve Bank of Kansas City, 2025).
8. M. Amoah *et al.*, *Extr. Ind. Soc.* **20**, 101557 (2024).
9. D. Raimi, A. Davicino, *Energy Res. Soc. Sci.* **107**, 103324 (2024).
10. M. Lopez, *Nat. Resour. Environ.* **34**, 53 (2020).
11. Energy Policy Act of 1992, as amended, 25 USC § 3502 (1992).
12. Indian Mineral Development Act of 1982, as amended, under 25 USC § 2106 (1982).
13. A. Kung *et al.*, *J. Energy Nat. Resour. Law* **40**, 413 (2022).

10.1126/science.adt7820

PHOTO: MORGAN D. BAZILIAN

RESEARCH

IN *SCIENCE* JOURNALS

Edited by **Michael Funk**

Artist's depiction of optically induced chirality in a crystal

PHOTO: ZENG *ET AL.*

NONLINEAR PHONONICS

Optically induced chirality

Chirality is a topological property of a material and is usually fixed when the material is prepared. A material is chiral (or achiral) and remains so for all temperatures and thermodynamics conditions. A right-handed chiral state cannot be easily switched to a left-handed one. Zeng *et al*. identified a class of materials with compensated staggered chirality in which left- and right-handed chiral forms coexist within the same unit cell (see the Perspective by Romao and Juraschek). Application of ultrafast laser pulses induced a nonlinear excitation of the phonon modes, favoring the enhancement of one staggered chiral state over the other. Such light-induced chirality could be used to explore nonequilibrium physics in topological and correlated systems. — Ian S. Osborne *Science* p. 431, 10.1126/science.adr4713; see also p. 361, 10.1126/science.adv0319

BIODIVERSITY

Avoiding harms from climate mitigation

Nature-based solutions are increasingly part of the strategy for achieving net zero carbon emissions to curb climate change. However, promoting tree growth in previously forested areas (reforestation) or unforested areas (afforestation) and planting bioenergy crops may help or harm biodiversity in the process. Smith *et al*. modeled projected vertebrate biodiversity responses to these land use changes in 2050. Although both strategies had positive effects on biodiversity by reducing climate change, local effects through habitat conversion were much stronger. Because most modeled species inhabit forests, forest growth had a mean positive effect, whereas bioenergy cropping had a mean negative effect. Reforestation can benefit many vertebrates, but models suggest that for most nonforest areas, doing nothing is better for biodiversity than afforestation or bioenergy cropping. —Bianca Lopez

Science p. 420, 10.1126/science.adm9485

METALLURGY

High-strength alloys that can still stretch

The techniques used to make ultrastrong alloys typically leave them unable to undergo much strain, thus making them brittle rather than ductile. Yan *et al*. found an exception to this pattern in alloys primarily based on vanadium, cobalt, and nickel with additions of aluminum, tungsten, copper, and boron that show a yield stress up to 2.6 gigapascals and 10% strain before fracturing. The authors attribute the different behavior to a combination of short-range ordering that is segregated near the grain boundaries and the formation of $L1_2$ particles less than 10 nanometers in size that are dispersed in the grain interiors. —Marc S. Lavine

Science p. 401, 10.1126/science.adr4917

IMMUNOLOGY

Divide to conquer the antibody pool

Antibodies, which are produced by B cells known as plasma cells, play a central role in adaptive immunity. MacLean *et al*. used mouse models to understand the cellular processes underpinning how cells producing high-affinity antibodies against a pathogen dominate the plasma cell population. After immunization, B cells capable of producing

high-affinity antibodies proliferated more than those that would produce low-affinity antibodies. The proliferation was associated with the extent of help received from T follicular helper cells, but it was not dependent on sustained cell-cell interactions. Rather, plasma cells could retain their proliferative advantage outside of germinal center structures, with signals from the cytokine interleukin-21 promoting cell division. —Sarah H. Ross

Science p. 413, 10.1126/science.adr6896

SOLAR CELLS

Stretchy and efficient organic blends

Stretchable organic solar cells for powering wearable devices have been achieved by blending a ductile donor semiconductor polymer with a plasticizing small-molecule acceptor to overcome the inherent brittleness of the photoactive components. Wang *et al*. have shown that the acceptor actually enhances ductility in the blend and maintains electron mobility despite its lack of crystallinity. Devices achieved a power conversion efficiency of greater than 16% and could maintain 80% of that efficiency at 80% strain. —Phil Szuromi

Science p. 381, 10.1126/science.adp9709

REPRODUCTION

Y are these genes necessary?

The mammalian Y chromosome is small, but it contains multiple gene families that are thought to play a role in spermatogenesis and are implicated in fertility defects. To systematically examine their functions, Subrini *et al*. used CRISPR-Cas9 to generate 13 different mouse models with deletions in individual Y chromosome genes and gene combinations implicated in human infertility. The authors then characterized the effects of each of their mutants on spermatogenesis, X-Y pairing, and other aspects of meiosis and the testis transcriptome. This study provides valuable insights into the functions of key genes on the Y chromosome, and the mouse models are a resource for further research in this area. —Yevgeniya Nusinovich

Science p. 393, 10.1126/science.ads6495

NEURODEGENERATION

Tainted connections

The "amyloid cascade model" of Alzheimer's disease suggests that plaques of amyloid beta (Aβ) precede and trigger other pathological changes such as the spread of abnormal tau protein. However, how amyloid pathology influences tau pathology remains incompletely understood. Roemer-Cassiano *et al*. analyzed Aβ and tau positron emission tomography and functional magnetic resonance imaging from the Alzheimer's Disease Neuroimaging Initiative and found that the spread of tau is in part mediated by Aβ-related increases in connectivity between tau epicenters and brain regions that are vulnerable to tau accumulation. —Daniela Neuhofer

Sci. Transl. Med. (2025) 10.1126/scitranslmed.adp2564

NEURODEGENERATION

Biotin for brain health

Manganese is essential for various cell functions, but chronic exposure causes a neurodegenerative condition with symptoms resembling Parkinson's disease. Lai *et al*. developed an adult fly model of manganese-induced Parkinsonism and found that altered metabolism of biotin (also known as vitamin B_7) mediated the metal's neurotoxicity. Manganese exposure reduced the amount of "free" or bioavailable biotin, which resulted in neuronal loss and mitochondrial and lysosomal dysfunction in the brain and impaired motor function. Supplementing the flies' diet with biotin alongside manganese exposure prevented these effects. These cellular effects were reproduced in cultured human dopaminergic neurons. —Leslie K. Ferrarelli

Sci. Signal. (2025) 10.1126/scisignal.adn9868

IN OTHER JOURNALS

Edited by **Corinne Simonti** *and* **Jesse Smith**

COGNITION

"More" "Food"

For decades, researchers have been exploring the ability of nonhuman animals to learn to communicate in human ways. Although research continues across species, augmented interspecies communication devices (i.e., button soundboards) have proliferated among animal owners, especially those with dogs. Bastos *et al.* used a large database of data collected by such owners to explore whether buttons pushed by pet dogs reflect more than just imitation or a "Clever Hans" effect. Across more than 150 dogs, button pushes were revealed to be nonaccidental, nonrandom, and not imitations of their owners' pushes, demonstrating deliberate efforts by the dogs. Further, specific category combinations were more common than would be expected by chance, particularly those related to food, play, their own names, and want. —Sacha Vignieri *Sci. Rep.* (2024) 10.1038/s41598-024-79517-6

Dogs, like Bunny here, may use soundboards deliberately, not just to mimic their owners.

PHOTOS: RUTH FREMSON/THE NEW YORK TIMES/REDUX

IMMUNOLOGY

Gut microbiota instruct lung immunity

The microbes found within the gut play an important role in mammalian health by influencing networks of immune cells throughout the body. Burrows *et al*. investigated how *Tritrichomonas musculis*, a species of protozoa that can form part of the commensal microbiome of mice, affected immune responses within the lungs. After transfer and colonization of *T. musculis* within the gut, type 2 innate lymphoid cells relocated from the intestine to the lung, where they interacted with B cells and $CD4^+$ T cells to promote elevated numbers of eosinophils in the airways. These changes in lung immune cells were correlated with increased pathology in response to lung

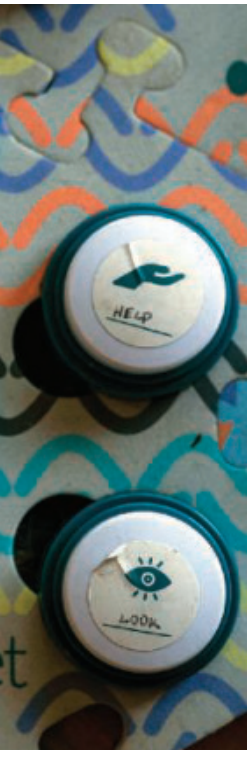

inflammation induced by house dust mite and bolstered protection against *Mycobacterium tuberculosis*. —Sarah H. Ross

Cell (2024)
10.1016/j.cell.2024.11.020

OPTOELECTRONICS

High-speed optical modulators on silicon

Enabling greater data rates over our communication networks will require the development of high-speed optical modulators with low power consumption and low cost. Although materials such as thin-film lithium niobate or indium phosphide platforms are fast and efficient, their costs are high. Wang *et al.* show that thin lithium tantalate is a stronger contender in terms of cost because it is compatible with silicon-based integrated photonics and can thus take advantage of the cost-saving, large-scale volume fabrication capability of the microelectronics industry. The authors demonstrate a 100-gigahertz integrated optical modulator that can support transmission rates exceeding 400 gigabits per second, showing that a lithium tantalate–based platform is a highly promising option for next-generation communications network transceivers. —Ian S. Osborne

Optica (2024)
10.1364/OPTICA.537730

MODEL ORGANISMS

Tagging crickets by CRISPR

To expand functional genetic studies in understudied insects, Matsuoka *et al.* established CRISPR/Cas9 genome-editing techniques in the two-spotted cricket, *Gryllus bimaculatus*. This hemimetabolous insect serves as a contrast to traditional model organisms such as *Drosophila melanogaster*. The study demonstrates successful gene knock-out and knock-in methods targeting genes such as *Ultrabithorax* (*Gb-Ubx*). The researchers achieved high efficiency in mutating target genes, with 47.4% of injected crickets transmitting mutations to offspring. Targeting *Gb-Ubx*, they observed phenotypic changes in leg development, showcasing the potential of this technique for functional genetic studies. This approach increases the viability of *G. bimaculatus* as a model for investigating gene function across diverse insect species. —Di Jiang

Development (2025)
10.1242/dev.199746

CHEMISTRY

Confined carbons in water

Aqueous reactions of carbon dioxide (CO_2) are closely linked to Earth's carbon cycle and have implications for carbon capture and sequestration. However, it is challenging to capture the underlying mechanisms of these processes in the high-pressure and high-temperature conditions found in many geological environments. Li *et al.* combined ab initio molecular dynamic simulations with Markov state modeling and unsupervised machine learning to elucidate the complex reaction pathways of CO_2 in supercritical water. In contrast to bulk solutions that favored carbonation reactions between CO_2 and water, extreme special confinement of aqueous CO_2 solution promoted anomalous stabilization of pyrocarbonate ions, a critical intermediate for converting CO_2 to carbonic acid. This could improve our understanding of carbon reactions in aqueous geofluids. —Sumin Jin

Proc. Natl. Acad. Sci. U.S.A. (2024)
10.1073/pnas.2406356121

CONSERVATION

Galápagos dog control

Dogs have been abandoned on the Galápagos archipelago throughout its history of human contact, causing great harm to its endemic fauna. Spatola *et al.* conducted a genomic analysis of the current dog population of Isabel and Santa Cruz islands to investigate the impact of dog culling introduced in the 1980s. No genetic bottlenecks signaling that that the culling was effective were observed. Instead, despite legislation, it appears that there has been a more recent influx of dogs from South America, boosting the feral population. Targeted fertility control seems to be the only possible tool left that might effectively reduce the pressure of introduced canids on the Galápagos' fragile ecosystems. —Caroline Ash

Curr. Biol. (2025)
10.1016/j.cub.2024.10.079

PHYSICS

Emergent flow

Hydrodynamics is usually associated with the macroscopic properties of systems with many interacting particles. How big does a system have to be to exhibit hydrodynamic behavior? To address this question, Brandstetter *et al.* studied the dynamics of interacting ^{6}Li atoms confined to two dimensions. For a system of only 10 atoms, the researchers observed the signatures of so-called elliptic flow: Starting from an initial elliptic density distribution, the axes of the ellipsis flipped during the expansion of the system. This observation was contingent on the presence of interactions and suggests the emergence of fluid-like behavior in this few-fermions system. —Jelena Stajic

Nat. Phys. (2025)
10.1038/s41567-024-02705-8

RESEARCH ARTICLE SUMMARY

VASCULAR BIOLOGY

Lysosomal dysfunction and inflammatory sterol metabolism in pulmonary arterial hypertension

Lloyd D. Harvey, Mona Alotaibi, Yi-Yin Tai, Ying Tang, Hee-Jung J. Kim, Neil J. Kelly, Wei Sun, Chen-Shan C. Woodcock, Sanya Arshad, Miranda K. Culley, Wadih El Khoury, Rong Xie, Yassmin Al Aaraj, Jingsi Zhao, Neha Hafeez, Rashmi J. Rao, Siyi Jiang, Vinny Negi, Anna Kirillova, Dror Perk, Annie M. Watson, Claudette M. St. Croix, Donna B. Stolz, Ji Young Lee, Mary Hongying Cheng, Manling Zhang, Samuel Detmer, Edward Guzman, Rajith S. Manan, Rajan Saggar, Kathleen J. Haley, Aaron B. Waxman, Satoshi Okawa, Tae-Hwi Schwantes-An, Michael W. Pauciulo, Bing Wang, Amy Webb, Caroline Chauvet, Daniel G. Anderson, William C. Nichols, Ankit A. Desai, Robert Lafyatis, Mehdi Nouraie, Haodi Wu, Jeffrey G. McDonald, Susan Cheng, Ivet Bahar, Thomas Bertero, Raymond L. Benza, Mohit Jain, Stephen Y. Chan*

INTRODUCTION: Vascular inflammation regulates endothelial cell (EC) pathophenotypes, particularly in pulmonary arterial hypertension (PAH). Dysregulation of lysosomal activity and cholesterol metabolism causes inflammation, but their relevance to PAH is unclear.

RATIONALE: Lysosomal acidification depends on vacuolar H^+ adenosine triphosphatases (V-ATPases). Nuclear receptor coactivator 7 (NCOA7) binds to V-ATPases to control lysosomal function and is up-regulated in human ECs under proinflammatory stimuli and in PAH lung tissue. However, a mechanism that connects NCOA7 to vascular disease remains undefined.

RESULTS: In pulmonary arterial ECs and in PAH, cytokine induction of NCOA7 preserved lysosomal acidification and served as a homeostatic brake to constrain inflammation. Conversely, NCOA7 deficiency promoted lysosomal dysfunction and production of proinflammatory oxysterols and bile acids that immunoactivated ECs. Mice deficient for endothelial *Ncoa7* or exposed to the bile acid 7α-hydroxy-3-oxo-4-cholestenoic acid displayed worsened EC immunoactivation and more severe PAH. In humans, an unbiased, metabolome-wide association study (n = 2756 PAH patients) identified a plasma signature of the same NCOA7-dependent oxysterols and bile acids that was associated with PAH mortality ($P < 1.1 \times 10^{-6}$). Supporting a genetic predisposition to NCOA7 deficiency in genome-edited, inducible pluripotent stem cell–derived ECs, the intronic single-nucleotide polymorphism (SNP) rs11154337 in *NCOA7* regulated NCOA7 expression, lysosomal acidification, oxysterol and bile acid production, and EC immunoactivation. SNP rs11154337 was associated with PAH severity through 6-min walk distance and mortality in discovery [n = 93 patients, P = 0.009; hazard ratio (HR) = 0.54, 95% confidence interval (CI) (0.34–0.86)] and validation [n = 630 patients, $P = 2 \times 10^{-4}$; HR = 0.49, 95% CI (0.34–0.71)] cohorts. Using computational modeling of small-molecule binding to NCOA7, we synthesized an activator of NCOA7 that promoted lysosomal activity, abrogated oxysterol generation, prevented EC immunoactivation, and reversed rodent PAH.

CONCLUSION: We established a genetic and metabolic paradigm that links lysosomal biology and oxysterol and bile acid processes to EC inflammation and PAH, thus carrying implications for diagnostic and therapeutic development. ■

The list of author affiliations is available in the full article online.
*Corresponding author. Email: chansy@pitt.edu
Cite this article as L. D. Harvey *et al.*, *Science* **387**, eadn7277 (2025). DOI: 10.1126/science.adn7277

S READ THE FULL ARTICLE AT
https://doi.org/10.1126/science.adn7277

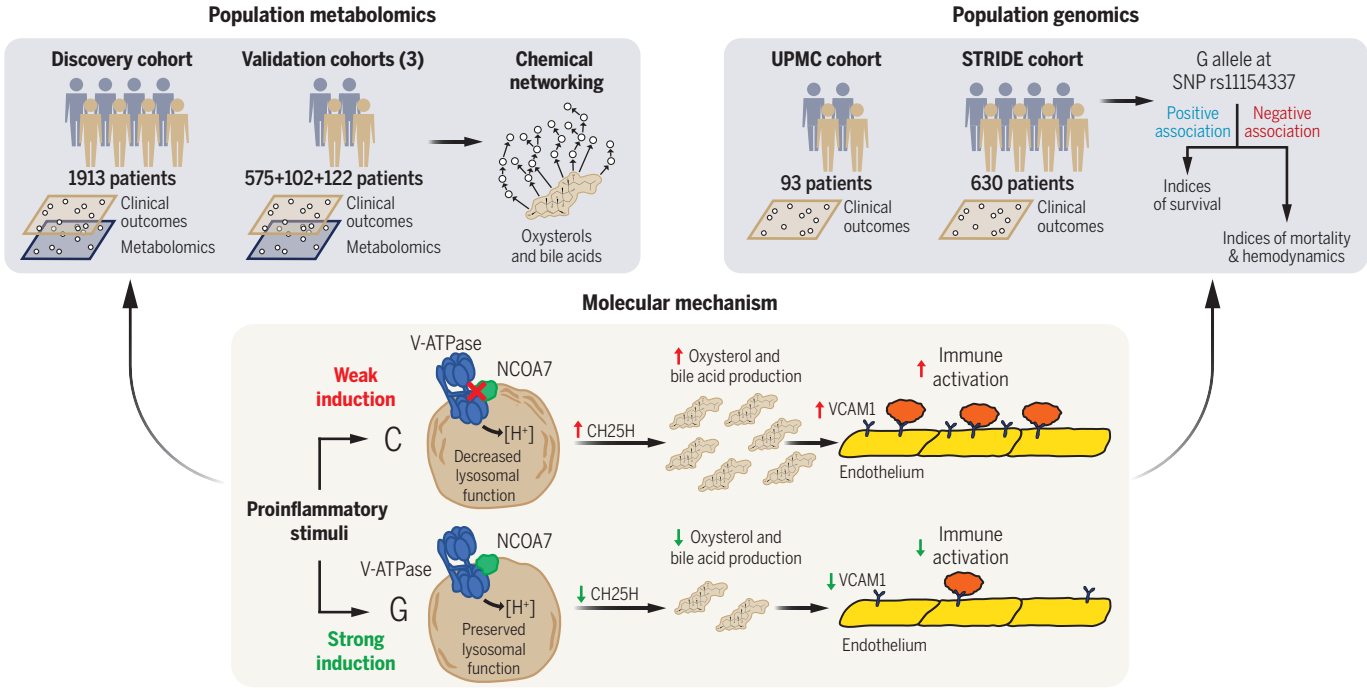

Multidimensional analyses of genomic and metabolomic datasets in combination with experimental validation define a SNP-dependent role for NCOA7 in lysosomal activity, oxysterol and bile acid production, endothelial immunoactivation, and the development of PAH. UPMC, University of Pittsburgh Medical Center; STRIDE, Sitaxsentan To Relieve Impaired Exercise; CH25H, cholesterol 25-hydroxylase; VCAM1, vascular cellular adhesion molecule 1.

RESEARCH ARTICLE SUMMARY

DIRECTED EVOLUTION

Rapid in silico directed evolution by a protein language model with EVOLVEpro

Kaiyi Jiang†, Zhaoqing Yan†, Matteo Di Bernardo†, Samantha R. Sgrizzi, Lukas Villiger, Alisan Kayabolen, B. J. Kim, Josephine K. Carscadden, Masahiro Hiraizumi, Hiroshi Nishimasu, Jonathan S. Gootenberg*‡, Omar O. Abudayyeh*‡

INTRODUCTION: Protein engineering is a critical tool in basic biology and medicine, but current methods have multiple shortcomings. Directed evolution is labor intensive, can get trapped in local maxima, and is not compatible with complex objectives. In silico optimization with protein language models (PLMs) has some power to predict functional mutations but often fails to substantially improve function. Emerging generative methods have shown progress in engineering simple objectives, such as binding, but cannot generalize to improve diverse protein functions. We introduce EVOLVEpro, a protein engineering method that combines PLMs with few-shot active learning on a regression model to augment experimental directed evolution. EVOLVEpro rapidly improves protein activity with sparse experimental data, overcoming limitations of current directed evolution and in silico protein engineering approaches.

RATIONALE: Protein language models, trained across broad sequence diversity, learn emergent properties from natural protein evolution, but the relationship between model representation and protein activities is unclear. We hypothesized that iterative experiments could rapidly elucidate the relationship between PLM embeddings and desired protein functions or attributes, enabling directed optimization of proteins towards desired goals. EVOLVEpro interprets PLMs embeddings through a top-layer regression model, learning the relationship between sequence and experimentally determined activities through an iterative active learning process. The lightweight random forest regression model can optimize multiple protein properties simultaneously during iterative rounds of testing with as few as 10 experimental data points per round, enabling complex multiobjective evolution campaigns and minimal experimental setup.

RESULTS: EVOLVEpro outperformed zero-shot methods in benchmarks across 12 deep mutational scanning datasets, including epitope binding, nucleic acid binding, and enzyme catalysis. We used EVOLVEpro to engineer six different proteins with diverse applications. We improved the binding affinity two monoclonal antibodies by up to 40-fold, the indel formation activity of a miniature CRISPR nuclease by fivefold, the insertion efficiency of a prime editor by twofold, the integration efficiency of a serine integrase by fourfold, and the transcription fidelity and mRNA quality of a T7 RNA polymerase by 100-fold. We found that EVOLVEpro predictions are substantially different and superior to predictions by the base layer alone, underscoring the importance of PLM interpretation by regressors and experimental data. EVOLVEpro-nominated mutations are distinctive from an evolutionary perspective, insightful from a structural analysis perspective, and based on iteration through position-specific hypotheses explored across rounds of evolution.

CONCLUSION: With high success rates at improving protein function, EVOLVEpro is advantageous relative to existing protein engineering methods. The model requires minimal initial knowledge of the target protein and can optimize over multiple objectives that would otherwise be inaccessible to typical directed evolution approaches. These features make EVOLVEpro well-suited for the engineering of challenging proteins for both basic biology and translational applications. The lack of correlation between base PLM and EVOLVEpro predictions demonstrates the need for interpretation of foundational models through the lens of experimentation and suggests that further hybrid approaches combining in silico and experimental methods will increase our capacity to engineer and understand protein function landscapes across the diversity of life. ■

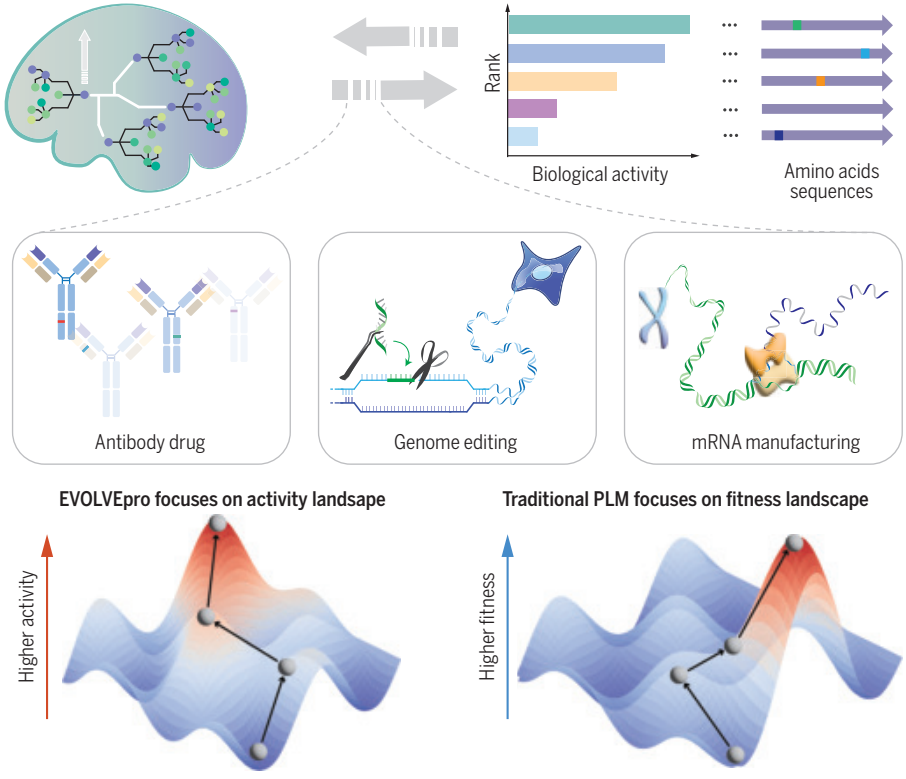

EVOLVEpro learns activity landscape for rapid in silico protein engineering. EVOLVEpro explores functional landscapes rather than fitness landscapes, engineering diverse proteins, such as monoclonal antibodies, genome editing machinery, and mRNA-producing enzymes, to high levels of activity.

The list of author affiliations is available in the full article online.
*Corresponding author. Email: omar@abudayyeh.science (O.O.A.); jgoot@mit.edu (J.S.G.)
†These authors contributed equally to this work.
‡These authors contributed equally to this work.
Cite this article as K. Jiang *et al.*, *Science* **387**, eadr6006 (2025). DOI: 10.1126/science.adr6006

READ THE FULL ARTICLE AT
https://doi.org/10.1126/science.adr6006

RESEARCH ARTICLE SUMMARY

MICROBIOLOGY

Highly multiplexed spatial transcriptomics in bacteria

Ari Sarfatis†, Yuanyou Wang†, Nana Twumasi-Ankrah, Jeffrey R. Moffitt*

INTRODUCTION: Many population-level bacterial phenomena are driven by the heterogeneous decisions made by single cells, with rare phenotypes playing critical roles in behaviors such as stress response, antibiotic resistance, and pathogenesis. In parallel, many bacterial behaviors occur in complex, often structured environments not well approximated by the test tube. In this light, image-based approaches to single-cell transcriptomics, with their ability to provide transcriptome-wide gene expression within individual cells in the context of native environments, have tremendous promise for the study of a diversity of microbial questions. Unfortunately, these methods have yet to be applied to bacteria.

RATIONALE: The central challenge is the massive density of RNAs within bacterial cells. Image-based approaches to single-cell transcriptomics require the resolution of fluorescent signals from individual RNA molecules to identify them, yet the density of RNAs within bacterial cells can be multiple orders of magnitude too high for the resolution of individual molecules with conventional microscopy. In this study, we addressed this challenge by developing a bacterially optimized expansion microscopy toolbox that allows the tunable expansion of individual bacterial cells up to ~1000-fold in volume. We then combined these expansion methods with multiplexed error-robust fluorescence in situ hybridization (MERFISH) to create an image-based single-cell transcriptomics method, which we call bacterial-MERFISH, capable of resolving large fractions of the bacterial transcriptome within single cells in a diversity of environments.

RESULTS: We benchmarked bacterial-MERFISH in log-phase *Escherichia coli* cells and demonstrated the ability to expand cells either ~50-fold or ~1000-fold in volume, which, in turn, allowed the profiling of up to 80% of the *E. coli* transcriptome in single cells. Through measurements of 97, 1057, or 1930 operons, we demonstrated that bacterial-MERFISH is accurate and sensitive and has high throughput. To demonstrate its discovery potential, we first applied bacterial-MERFISH to study the response of *E. coli* to a switch in carbon source from glucose to xylose. We found a notably heterogeneous response, with individual *E. coli* cells progressively exploring a variety of carbon-utilization operons before expressing those associated with the utilization of xylose. We next leveraged the subcellular resolution of bacterial-MERFISH to map the intracellular organization of the *E. coli* transcriptome. We discovered a diversity of spatial patterns that are globally shaped by both the genome and proteome organization. Finally, we used bacterial-MERFISH to profile the spatial adaptation of a human gut commensal, *Bacteroides thetaiotaomicron* (*B. theta*), to the mouse colon. We found that *B. theta* adjusts its gene expression over micrometer-scale lengths, likely in response to the local availability of dietary or host-derived polysaccharides.

CONCLUSION: Collectively, these measurements demonstrate that bacterial-MERFISH is a high-performance single-cell transcriptomic method for bacteria. Given its combination of sensitivity, multiplexing, throughput, and spatial resolution, we anticipate that bacterial-MERFISH will be a powerful tool for exploring diverse microbiology questions across a range of length scales, including intracellular organization, specialization within biofilms, dynamics of antibiotic-resistant persisters, host-microbe interactions during pathogenesis, and interbacterial dynamics within complex microbial communities. ■

The list of author affiliations is available in the full article online.
*Corresponding author. Email: jeffrey.moffitt@childrens.harvard.edu
†These authors contributed equally to this work.
Cite this article as A. Sarfatis *et al.*, *Science* **387**, eadr0932 (2025). DOI: 10.1126/science.adr0932

READ THE FULL ARTICLE AT
https://doi.org/10.1126/science.adr0932

Bacterial-MERFISH profiles thousands of operons in single cells in a range of environments. Bacterial-MERFISH overcomes the substantial density of bacterial mRNAs with an optimized expansion microscopy toolbox that provides up to ~1000-fold volumetric expansion of individual cells. MERFISH then charts the expression of large fractions of the transcriptome in hundreds of thousands of cells, providing insight into bacterial single-cell heterogeneity, the intracellular organization of the transcriptome, and the adaptation of bacteria to micrometer-scale niches in the gut.

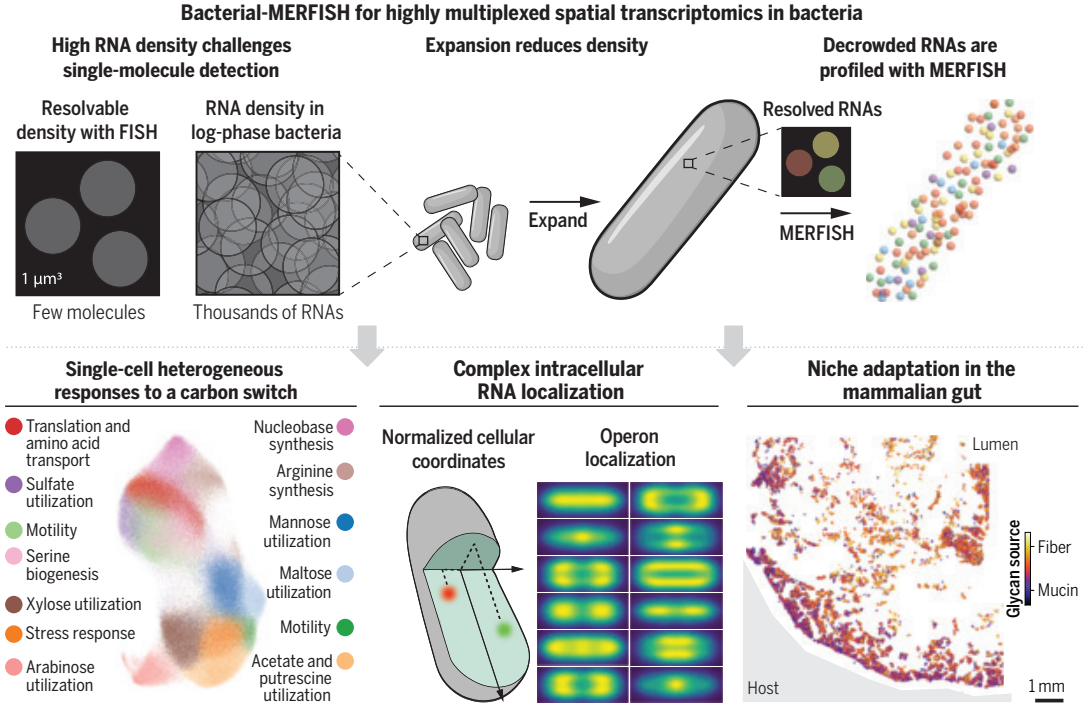

RESEARCH ARTICLE SUMMARY

NEUROSCIENCE

Identification of the subventricular tegmental nucleus as brainstem reward center

Krisztián Zichó, Boldizsár Zsolt Balog, Réka Z. Sebestény, János Brunner, Virág Takács, Albert M. Barth, Charlotte Seng, Áron Orosz, Manó Aliczki, Hunor Sebők, Eva Mikics, Csaba Földy, János Szabadics, Gábor Nyiri*

INTRODUCTION: Reward processing in the brain is essential for guiding goal-directed behavior, shaping motivational states, and regulating mood. This process involves evaluating and predicting the affective valence of stimuli (their intrinsic quality as either good or bad), a function supported by an evolutionarily ancient subcortical neural network. Dopamine release from the ventral tegmental area (VTA) plays a central role in decision-making, adaptive behaviors, and facilitating memory formation, by linking rewards to actions that yield positive outcomes. The ventral tegmental area is tightly regulated by the lateral habenula (LHb), a critical hub for assessing and predicting the emotional value of stimuli and mediating responses to negative experiences. The balanced activity of the LHb-ventral tegmental area axis is therefore crucial for memory formation, prediction, and the maintenance of mental health.

RATIONALE: Negative events strongly activate the LHb, but its overactivation can contribute to anxiety and depression, underscoring the importance of precise regulation. Conversely, inhibiting LHb activity signals positive valence and has shown therapeutic potential in treating depression, as evidenced by the effects of deep brain stimulation and ketamine. Despite decades of research, the primary inhibitory inputs to the LHb remain incompletely understood. In this study, we identified a previously uncharacterized brainstem nucleus beneath the fourth ventricle, which we named the subventricular tegmental nucleus (SVTg). This nucleus provides abundant inhibitory innervation to the LHb. To investigate the role of the SVTg in reward processing, we employed a multidisciplinary approach, including cell type-specific viral tracing, monosynaptic rabies tracing, single-cell RNA sequencing, in vivo and in vitro electrophysiology, fiber photometry, and optogenetic behavioral experiments.

RESULTS: We discovered that the SVTg is a γ-aminobutyric acid (GABA)-ergic inhibitory nucleus receiving inputs from regions involved in valence, salience, and memory processing. The SVTg provides the largest purely inhibitory inputs to the LHb and inhibits several other brain regions linked to negative experiences (Fig. A). The SVTg is activated by reward and reward-predicting cues (Fig. B) but not by neutral environmental stimuli, and it can regulate reward location memory. SVTg stimulation induced a positive motivational state, place preference, reduced anxiety, and triggered reward-related dopamine release in the nucleus accumbens, highlighting its role in reward processing. When given the opportunity, mice self-stimulated the SVTg (Fig. C), suggesting its role in reward-seeking behavior. Conversely, SVTg suppression caused place aversion and increased fear. Associational cortices, including the anterior cingulate and other prefrontal cortical regions, target the SVTg. The orbitofrontal cortex (OFC) signals positive valence through the SVTg, whereas serotonergic neurotransmission activates it through distinct mechanisms. Precisely timed SVTg activity prevents excessive fear responses. Our genetic analysis identified selective protein markers for the SVTg, enabling its localization in the brainstem across mice, rats, monkeys, and humans.

CONCLUSION: Our study identifies the SVTg as a GABAergic inhibitory brainstem reward center that integrates inputs from prefrontal cortical and subcortical regions to process affective valence. It controls several brain areas associated with negative emotional states, including the LHb. The SVTg plays a critical role in continuously regulating the brain's valence circuitry, signaling reward and preventing overactivation of aversion circuits during negative events. Given its evolutionary conservation across species, understanding the function and potential dysfunction of the mammalian SVTg may provide valuable insights into emotional and fear-related disorders such as anxiety, depression, and possibly addiction. ■

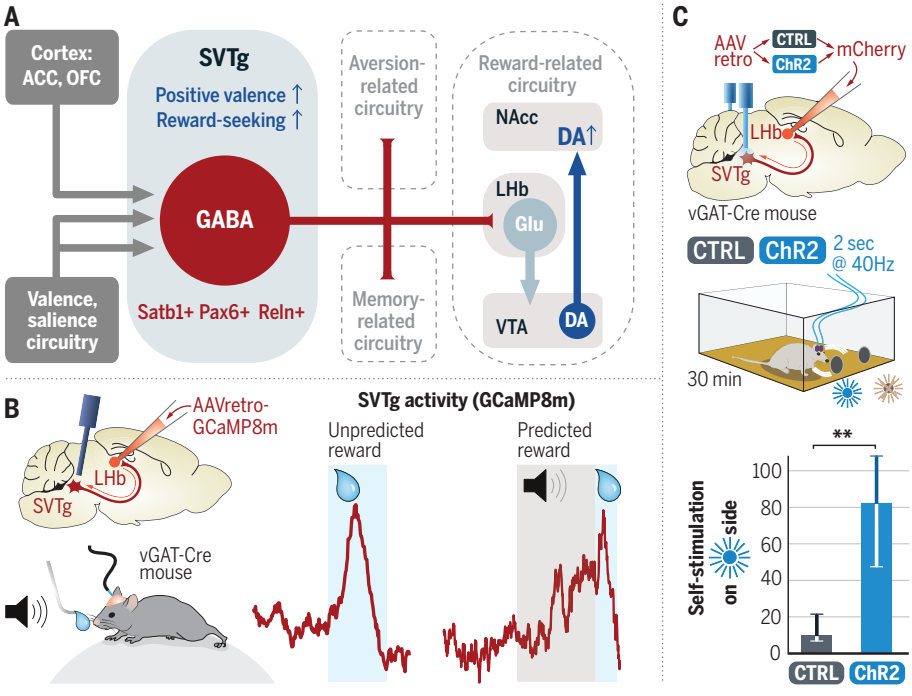

SVTg, a brainstem reward center. (**A**) SVTg GABAergic neurons promote positive valence by inhibiting LHb and other aversion-related nuclei. ACC, anterior cingulate cortex; DA, dopamine; Glu, glutamatergic; NAcc, nucleus accumbens. (**B**) The SVTg of awake mice are activated by unpredicted and predicted reward. AAVretro, retrogradely adeno-associated viruses; vGAT, vesicular GABA transporter. (**C**) Mice optogenetically self-stimulated their SVTg (with light-sensitive ChR2), compared with control (CTRL) mice. Medians and interquartile ranges.

The list of author affiliations is available in the full article online.
*Corresponding author. Email: nyiri.gabor@koki.hun-ren.hu
Cite this article as K. Zichó *et al.*, *Science* **387**, eadr2191 (2025). DOI: 10.1126/science.adr2191

READ THE FULL ARTICLE AT
https://doi.org/10.1126/science.adr2191

RESEARCH ARTICLE SUMMARY

OCEAN CARBON

Antarctic krill vertical migrations modulate seasonal carbon export

A. J. R. Smith*, S. Wotherspoon, L. Ratnarajah, G. R. Cutter, G. J. Macaulay, B. Hutton, R. King, S. Kawaguchi, M. J. Cox

INTRODUCTION: Antarctic krill (*Euphausia superba*) is among the most abundant animals on the planet (between 117 and 379 million tonnes). Krill play a vital role in the biological carbon pump—a biologically driven mechanism that sequesters carbon to the deep ocean—by consuming phytoplankton in the upper water column and producing fast-sinking fecal pellets which sink to the seafloor. Sinking particles, including carbon-rich fecal pellets, are vulnerable to degradation through fragmentation, reingestion, dissolution into the surrounding seawater, or bacterial remineralization. This means that not all of the material consumed by krill in the upper ocean is exported to deeper depths, and some of the consumed carbon is returned to the upper ocean. Vertical migration, a behavior common to krill and many zooplankton and fish species worldwide, is believed to increase the efficiency of the biological carbon pump by actively transporting particulate organic carbon consumed by organisms in the upper ocean directly into the mesopelagic zone (waters deeper than 200 m) with minimal degradation.

RATIONALE: Active acoustic techniques using ship-based echosounders are commonly used to observe vertical migration patterns. However, when observing krill and zooplankton, sound attenuation restricts these observations to the upper 250 m of the water column. Moreover, impenetrable Antarctic sea ice prevents access by ships to important krill habitats in winter, limiting the seasonal resolution of vertical migration observations. A lack of observational data means that few global climate models include vertical migration as a mechanism for carbon export or models rely on broad assumptions with little exploration into seasonal variability. The exclusion of vertical migrations has been suggested to have considerable influence on the accuracy of carbon export estimates by global climate models. Using echosounder observations from a seafloor lander in East Antarctica coupled with a numerical model, we explore how observed patterns in vertically migrating krill contribute to the total particulate organic carbon flux across a full year.

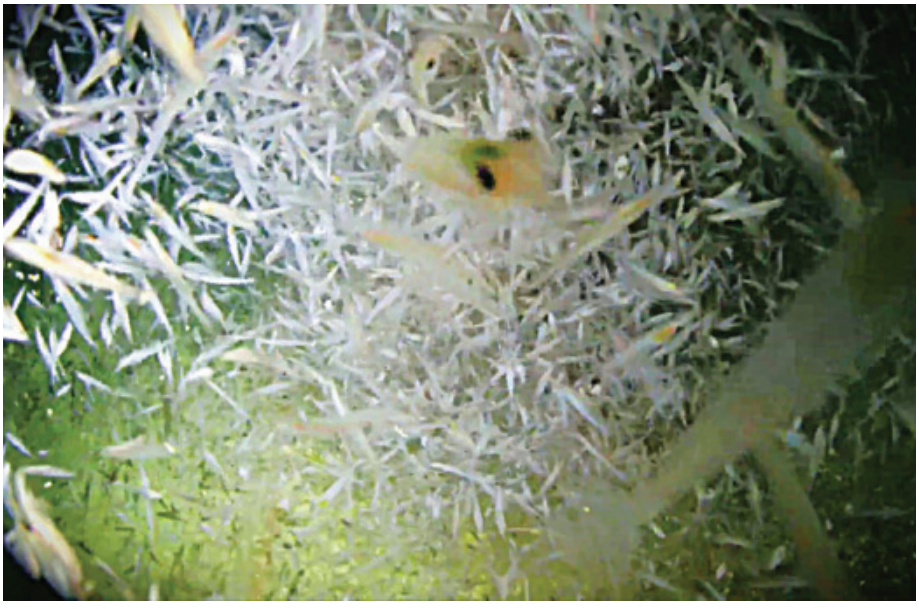

Lights, camera, krill. East Antarctic mooring reveals hidden behavior of Antarctic krill on the seafloor with acoustic observations used to explore year-round vertical migration patterns and particulate organic carbon sequestration by this important species.

RESULTS: An upward-looking echosounder positioned at 385-m depth on the continental shelf of Prydz Bay provided full water column high-resolution observations of krill density and depth every 7 min for a full year. Video camera footage captured Antarctic krill swarming around lights on the lander close to the seafloor with fecal pellets produced at depth. Over the year of observations, one-quarter of the krill population participated in vertical migrations between shallower epipelagic waters (<200 m) into deeper mesopelagic waters (>200 m). Krill were observed to typically complete one full cycle of vertical migration per day, and the amplitude of these migrations were highly seasonal. In summer, vertical migrations were restricted to the upper 100 m, giving krill an opportunity to graze on the phytoplankton. The greatest fraction of krill migrating into mesopelagic waters occurred in winter (when surface primary productivity was lowest), where krill performed full water column migrations from the surface to the seabed. Consequently, nonmigrating krill exported 8.4 mg C m^{-2} day^{-1} from sinking fecal pellets released in the upper water column, whereas migrating krill injected considerably less particulate organic carbon (1.3 mg C m^{-2} day^{-1}) into the mesopelagic zone over a full year. Carbon injection by migrating krill was highly seasonal, with the largest contributions to carbon flux in winter (when a greater proportion of migrating krill were present), but overall vertical migration contributed less than 10% of the total krill particulate organic carbon flux.

CONCLUSION: Our observations show high seasonal variability in krill diel vertical migration patterns with almost no migration occurring into the mesopelagic during summer. Modeling results suggest that previous estimates of carbon injection by migrating krill, which are based on assumed rather than observed vertical migration behavior, have been overestimated and that the Antarctic krill migrant pump has a minor contribution to particulate organic carbon export. This contradicts established theories on the value of vertical migration to the biological carbon pump. However, increased attention is required to resolve changes to krill grazing behaviors and attenuation processes such as bacterial remineralization that are likely to affect carbon export and potentially influence the effect of vertical migration on the downward flux of carbon to deep waters. ■

The list of author affiliations is available in the full article online.
*Corresponding author. Email: abigail.smith@utas.edu.au
Cite this article as A. J. R. Smith *et al.*, *Science* **387**, eadq5564 (2025). DOI: 10.1126/science.adq5564

READ THE FULL ARTICLE AT
https://doi.org/10.1126/science.adq5564

PHOTO: AUSTRALIA ANTARCTIC DIVISION

RESEARCH ARTICLES

SOLAR CELLS

Mechanically robust and stretchable organic solar cells plasticized by small-molecule acceptors

Zhenye Wang[1]†, Di Zhang[1]†, Lvpeng Yang[1]†, Omar Allam[2,3], Yerun Gao[1], Yang Su[2], Meichen Xu[1], Songmin Mo[4], Qinghe Wu[4]*, Zhi Wang[1], Junfeng Liu[1], Jiayi He[1], Rui Li[1], Xingwang Jia[1], Zhilin Li[1], Long Yang[1], Mark D. Weber[2], Yu Yu[1], Xinliang Zhang[1], Tobin J. Marks[5,6], Natalie Stingelin[2], Josh Kacher[2], Seung Soon Jang[2]*, Antonio Facchetti[2,5,6]*, Ming Shao[1]*

Emerging wearable devices would benefit from integrating ductile photovoltaic light-harvesting power sources. In this work, we report a small-molecule acceptor (SMA), also known as a non–fullerene acceptor (NFA), designed for stretchable organic solar cell (*s*-OSC) blends with large mechanical compliance and performance. Blends of the organosilane-functionalized SMA BTP-Si4 with the polymer donor PNTB6-Cl achieved a power conversion efficiency (PCE) of >16% and ultimate strain (ε_u) of >95%. Typical SMAs suppress OSC blend ductility, but the addition of BTP-Si4 enhances it. Although BTP-Si4 is less crystalline than other SMAs, it retains considerable electron mobility and is highly miscible with PNTB6-Cl and is essential for enhancing ε_u. Thus, *s*-OSCs with PCE > 14% and operating normally under various deformations (>80% PCE retention under an 80% strain) were demonstrated. Analysis of several SMA-polymer blends revealed general molecular structure–miscibility–stretchability relationships for designing ductile blends.

Wearable optoelectronic devices (e-wearables) comprising stretchable transistors (*1*–*3*), displays (*4*–*6*), and sensors (*7*–*11*) remaining operational under mechanical deformations are of great interest. Their powering components occupy a large physical space of these devices and limit overall conformability and robustness. Organic solar cells (OSCs), comprising donor and acceptor semiconductor blends, are promising power sources for e-wearables given their mechanical flexibility and stretchability, light weight, and solution processability (*12*–*15*). State-of-the-art rigid OSCs on glass have achieved power conversion efficiencies (PCEs) surpassing 20% (*16*–*19*). However, stretchable OSCs (*s*-OSCs) adhering to arbitrary surfaces require accommodating much larger deformations (strain ε > 30%) than bending have rarely been reported (*20*–*22*).

Developing ductile organic photoactive blends remains challenging for several reasons. Polymer donors have a π-conjugated backbone and strong intermolecular π-π interactions, promote light absorption or hole transport and crystallinity, but suppress ductility (*23*). Bulk heterojunction (BHJ) photoactive layers consist of the donor and acceptor, and the interactions of donor and acceptor also determine film properties. However, all existing small-molecular acceptors (SMAs), including fullerenes, non–fullerene acceptors, and polymerized SMAs (P-SMAs), are brittle (ultimate strain ε_u < 5%) (*24*, *25*).

Various insulating [i.e., polydimethylsiloxane (PDMS) and styrene ethylene butylene styrene (SEBS)] (*26*–*28*) and ductile semiconducting (*29*–*32*) polymers have been incorporated as a ternary component to increase blend ε_u values. Although photoactive materials design has historically emphasized increasing PCE, the focus has recently expanded to enhancing mechanical properties (*33*–*35*). Unfortunately, to date, the greatest stretchability for high-performance blends remains <33% (*33*–*36*). Aside from lacking intrinsic stretchable photoactive blends, the efficiency of current *s*-OSCs lags far behind those of rigid and bendable devices (*37*, *38*), and, despite pioneering progress (*25*, *39*), simultaneously achieving efficient (PCE > 10%) and mechanically stretchable (ε_u > 30%) *s*-OSCs remains an unsolved challenge.

In this work, we report a new organosilane-functionalized SMA (BTP-Si4) blended with a ductile polymer donor (PNTB6-Cl) for stretchable blend films and solar cells (structures, Fig. 1A). Equally as notable, comparison of traditional (e.g., Y6-like) and new (BTP-Si4–like) SMA families provides new understanding of the interplay between photoactive material molecular structure, donor-acceptor miscibility, achievable mechanical properties, and performance under deformation.

Materials and photovoltaic performance in rigid solar cells

We first compared the properties of BTP-Si4 and Y6 blends with the ductile donor polymer PNTB6-Cl (Fig. 1A). Their synthesis, optical absorption, and energetic characteristics are reported in the supplementary materials (figs. S1 to S3 and table S1). BTP-Si4 has the same conjugated core-IDC end groups of Y6 but is *N*-functionalized with a (4-butyl)diheptyl(methyl)silyl substituent. BTP-Si4 single-crystal structure (Fig. 1B) indicated formation of three packing types, typical of high-efficiency SMAs. However, because of the elongated and bulky *N*-sidechains, BTP-Si4 exhibited a larger core-core π-π stacking distance of 3.57 Å (type III) than Y6 (3.36 Å), which suppressed excessive aggregation. The synergistic effect of branching and extension of BTP-Si4 sidechain combined with silane incorporation balanced SMA aggregation and three-dimensional (3D) charge transport (*40*, *41*) as well as optimized the miscibility with the donor polymer for simultaneously enhancing ductility and device efficiency.

We first evaluated the photovoltaic performance of rigid OSCs (Fig. 1C and table S2). The control PNTB6-Cl:Y6 device exhibited a PCE of 15.7 ± 0.14% (PCE_{max} = 15.9%), whereas that of the PNTB6-Cl:BTP-Si4 device was slightly increased to 16.2 ± 0.13% (PCE_{max} = 16.4%). Despite short-circuit current (J_{sc}) suppression, increased open-circuit voltage (V_{oc}) by ~0.05 V and fill factor (FF) contributed to PCE enhancement. The integrated J_{sc} from the external quantum efficiency (EQE) agreed with that from *J*-*V* curves (Fig. 1D). Moreover, PNTB6-Cl:BTP-Si4:Y6 ternary devices [~15 weight % (wt %) of Y6] exhibited an enhanced PCE of 17.0 ± 0.11% (PCE_{max} = 17.1%). We attributed these higher PCEs to the optimal balance between the broader absorption and lower lowest unoccupied molecular orbital (LUMO) of Y6 versus BTP-Si4 (fig. S4), which enhanced J_{sc} but reduced V_{oc}.

To better understand device performance, charge transport and energy loss measurements were performed. The BTP-Si4 electron mobility (μ_e) was slightly lower than that of Y6 (3.6×10^{-4} versus 4.5×10^{-4} $cm^2V^{-1}s^{-1}$) (fig. S5 and table S3). For the blend films, hole mobility (μ_h) values of 2.7×10^{-4} and 3.1×10^{-4} $cm^2V^{-1}s^{-1}$, respectively, were also near μ_e values of 3.5×10^{-4} and 4.4×10^{-4} $cm^2V^{-1}s^{-1}$, respectively, so that μ_e/μ_h were balanced at 1.3 and 1.4, respectively, and contributed to the overall high device FFs and PCEs.

Furthermore, the total energy loss (E_{loss}) and three E_{loss} components (ΔE_1, ΔE_2, and ΔE_3) of the corresponding devices (figs. S6 and S7

[1]Wuhan National Laboratory for Optoelectronics, Huazhong University of Science and Technology, Wuhan, China. [2]School of Materials Science and Engineering, Georgia Institute of Technology, Atlanta, GA, USA. [3]Woodruff School of Mechanical Engineering, Georgia Institute of Technology, Atlanta, GA, USA. [4]Department of Chemistry and Key Laboratory for Preparation and Application of Ordered Structural Materials of Guangdong, Shantou University, Shantou, Guangdong, China. [5]Department of Chemistry, Materials Research Center, Northwestern University, Evanston, IL, USA. [6]The Trienens Center for Sustainability and Energy, Northwestern University, Evanston, IL, USA.
***Corresponding author. Email: wuqh@stu.edu.cn (Q.W.); ssj3@gatech.edu (S.S.J.); afacchetti6@gatech.edu (A.F.); mingshao@hust.edu.cn (M.S.)**
†These authors contributed equally to this work.

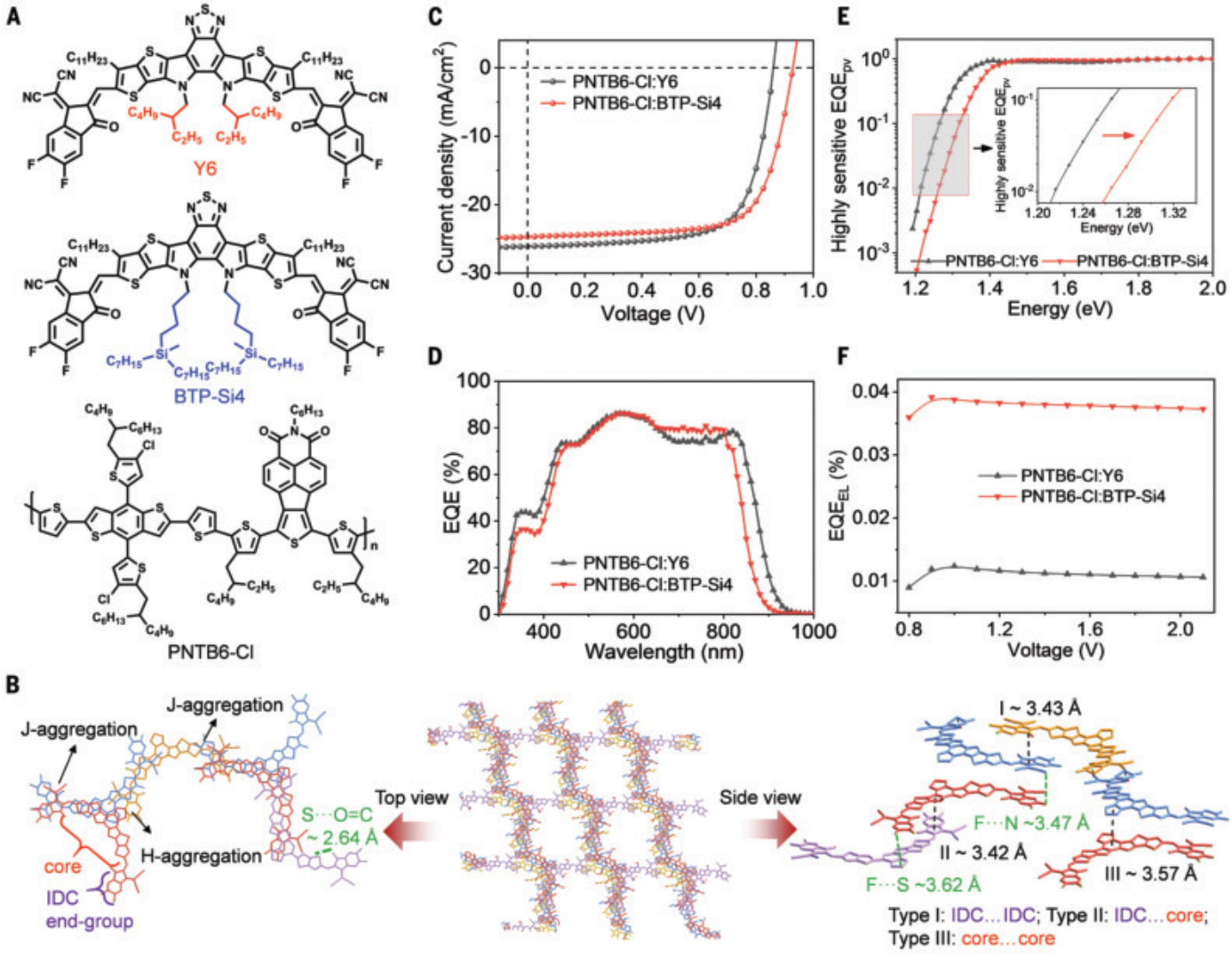

Fig. 1. Molecular structures and photovoltaic response of the photoactive materials. (**A**) Molecular structures of donor polymer PNTB6-Cl and acceptors Y6 and BTP-Si4. (**B**) The single crystal and π-π stacking in one unit cell and the 3D network packing of BTP-Si4 along the *a* axis. (**C**) *J-V* curves and (**D**) EQE response plots of OSCs. (**E**) The photovoltaic external quantum efficiency (EQE_{pv}) plots of the indicated OSCs. (**F**) EL quantum efficiencies (EQE_{EL}) of the indicated OSCs at various voltages. Note that the donor:acceptor weight ratios of PNTB6-Cl:Y6 and PNTB6-Cl:BTP-Si4 were 1:1.25 and 1:1.40, respectively, and, unless indicated, all data were obtained by using PNTB6-Cl batch-1.

and table S4) indicated that PNTB6-Cl:BTP-Si4 blend films had a steep low energy tail (Fig. 1E) and a higher charge transfer (CT) energy level with respect to the Y6 blend films (E_{CT} = 1.36 versus 1.32 eV; fig. S7), suggesting a smaller ΔE_2. Additionally, BTP-Si4 devices exhibited an enhanced electroluminescence quantum yield EQE_{EL} versus those of the Y6 devices (Fig. 1F), suggesting reduced nonradiative recombination (ΔE_3 = 0.20 versus 0.23 eV) (*42*). Thus, BTP-Si4 with an inherent high electroluminescence efficiency and high CT state suppressed nonradiative charge recombination, consistent with the light intensity (P_{light})–dependent J_{sc} and V_{oc} and exciton dissociation probabilities (P_{diss}) measurements (fig. S8), thereby enhancing V_{oc} and PCE.

Mechanical properties of the photoactive materials and blends

The pristine material and blend mechanical properties were assessed with the "film-on-water tensile test" (FOW) method (*43*). The pristine PNTB6-Cl films showed a ε_u of 66.3 ± 1.4% ($\varepsilon_{u,max}$ = 67.7%) and is a promising ductile donor for *s*-OSCs (fig. S9A).

It was difficult to obtain stress-strain measurement of SMA films because of their brittle nature (fig. S9C). In Fig. 2A, PNTB6-Cl:Y6 films showed a ε_u of 9.7 ± 0.4%. Notably, the blends based on BTP-Si4 were far more ductile with the PNTB6-Cl:BTP-Si4 films, exhibiting an ε_u of 93.9 ± 1.7% ($\varepsilon_{u,max}$ = 95.5%) (movie S1). Additionally, the ternary PNTB6-Cl:BTP-Si4:Y6 blends, which, as rigid OSCs, yielded a PCE > 17%, also exhibited a high ε_u of 74.0 ± 0.5% (fig. S11).

Optical microscopy imaging further supports enhanced stretchability of the BTP-Si4 blend films (Fig. 2B). Even at a 100% strain, only a few small cracks were detected in PNTB6-Cl:BTP-Si4, implying that it is a ductile film (*44*). In addition, the dichroic ratio (DR) of Y6-blend films plateaued after a 25% strain because of crack formation (figs. S9D and S10), whereas the DR of PNTB6-Cl:BTP-Si4 blend films showed a steady increase up to a 100% strain, indicative of impressive strain tolerance.

Figure 2C compares the present ε_u with reported data along with PCEs of the corresponding rigid OSCs (table S5). Most blends exhibited a trade-off between PCE and stretchability

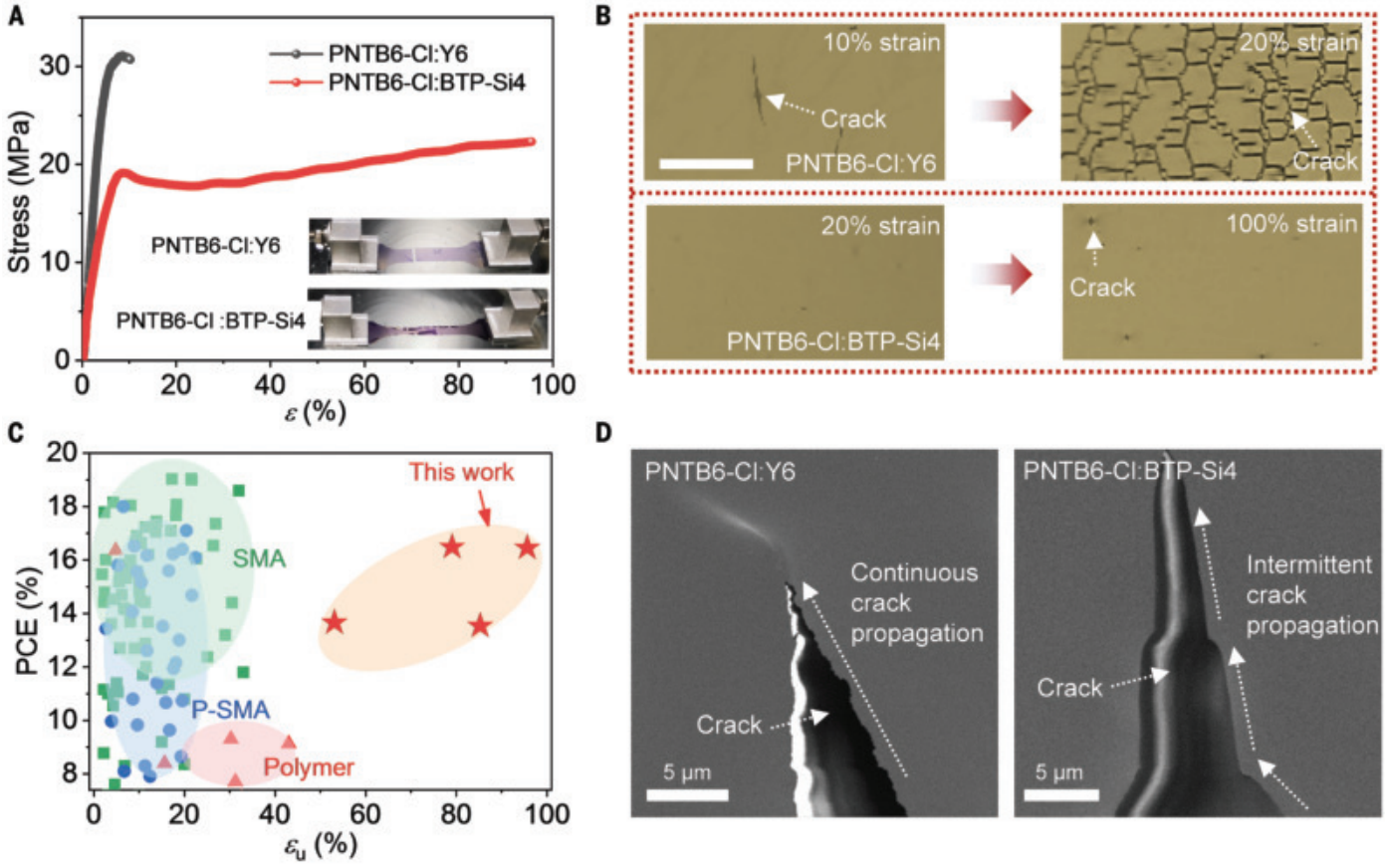

Fig. 2. Mechanical and morphological properties of blend films. (**A**) Stress–strain (ε) curves of the indicated free-standing blend films. The inset shows the images of blend films after the tensile test. (**B**) Optical images of selected blend films coated on PDMS elastomer under different strains. Scale bar, 50 μm. (**C**) PCE versus ultimate strain (ε_u) of high-performance blend films based on different acceptor classes [polymer and SMA (small-molecule acceptor), P-SMA (polymerized SMA)] reported in the literature and in this study. (**D**) SEM images collected during in situ deformation for the PNTB6-Cl:Y6 and PNTB6-Cl:BTP-Si4 blends. Note that the donor:acceptor weight ratios of PNTB6-Cl:Y6 and PNTB6-Cl:BTP-Si4 were 1:1.25 and 1:1.40, respectively.

(*27*, *36*, *45*), but the PNTB6-Cl:BTP-Si4 binary films were simultaneously efficient (PCE > 16%) and stretchable (ε_u > 95%). Consistent with the ε_u values, the elastic modulus (E) and the tensile strength (σ) of BTP-Si4–blend films were lower than those of the Y6 blend (E = 0.34 ± 0.01 GPa and σ = 23.3 ± 0.8 MPa for PNTB6-Cl:BTP-Si4 versus E = 0.69 ± 0.05 GPa and σ = 30.9 ± 0.5 MPa for PNTB6-Cl:Y6), whereas the toughness (G) of the BTP-Si4 blends (18.8 ± 0.8 MJ m^{-3}) was approximately nine times greater than that of the Y6 counterpart (2.2 ± 0.2 MJ m^{-3}), corroborating mechanical robustness (fig. S9, E and F, and table S6).

Film morphology and microstructure analysis

Grazing-incidence wide-angle x-ray scattering (GIWAXS) measurements were used to define the microstructure of pristine and blend films (fig. S12, A and B). Both pristine BTP-Si4 and Y6 films exhibited an out-of-plane (010) reflection at 1.77 $Å^{-1}$, indicating preferential π-face-on molecular orientation at similar π-π distances (d_π) of ~3.6 Å (table S7). However, the crystal coherence length of BTP-Si4 (15.0 Å) was smaller than that of Y6 (18.7 Å).

Additionally, in the in-plane direction, a (100) reflection at 0.26 and 0.31 $Å^{-1}$ for BTP-Si4 and Y6, respectively, corresponds to lamellar distances (d_l) of 24.2 and 20.3 Å, respectively. These results implied that BTP-Si4 N-substitution retained short d_π, substantially increased the d_l, and suppressed crystallinity. Similarly, both PNTB6-Cl:BTP-Si4 and PNTB6-Cl:Y6 blends exhibited an identical out-of-plane (010) reflection (d_π = 3.6 Å) as well as an in-plane (100) reflection at a d_l = 23.3 and 21.7 Å, respectively. Again, the former blend was less textured along the π-stacking direction. The relative degree of crystallinity of the PNTB6-Cl:BTP-Si4 and PNTB6-Cl:Y6 blends was 0.87 and 1.0, respectively, confirming the overall reduced texturing of the former blend (fig. S12, C and D).

1D grazing-incidence small-angle x-ray scattering (GISAXS) indicated that the acceptor domain size ($2R_g$ = 26.3 nm) and fractal dimension (D = 2.4) of PNTB6-Cl:BTP-Si4 were smaller than those of PNTB6-Cl:Y6 ($2R_g$ = 44.6 nm, D = 2.6), corroborating suppressed BTP-Si4 aggregation in the former blend (fig. S12E and table S8). Both atomic force microscopy and transmission electron microscopy imaging indicated a well-dispersed bicontinuous fibrillar film morphology for the Y6 blend, whereas far smaller fibril bundles were observed in the BTP-Si4 blends (fig. S13).

We used in situ scanning electron microscopy (SEM) and in situ optical microscopy (Fig. 2D and figs. S14 and S15) to probe the crack propagation in the various blends. Cracks in PNTB6-Cl:Y6 grew steadily, and the crack tip always remained sharp as the strain increased, implying a low plastic deformation zone around the tip and brittle nature (*44*). By contrast, crack formation and propagation in PNTB6-Cl:BTP-Si4 was intermittent and exhibited "crack-arrest behavior" as well as tip blunting upon increasing the strain because of the large plastic deformation zone for energy dissipation. Further strain increase caused collapse of the plastic deformation zone, and

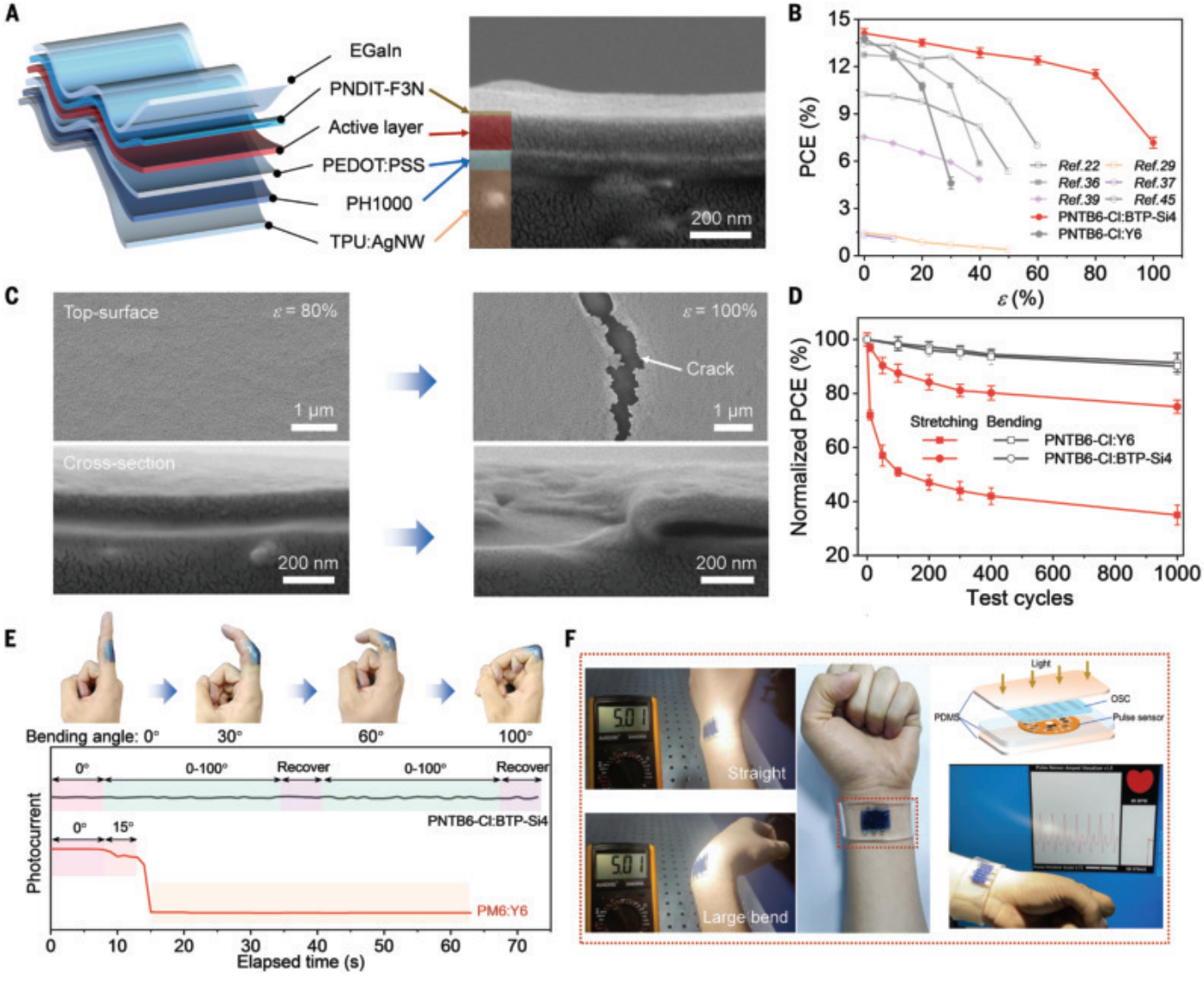

Fig. 3. Stretchable OSC characterization. (**A**) Device structure of our *s*-OSC. (**B**) PCE versus strain (ε) plots of *s*-OSCs reported in the indicated literature and in this study. (**C**) Top-surface and cross-section SEM images of our *s*-OSC under strains. (**D**) PCE as a function of bending (2-mm bending radius) and stretching (15% strain for PNTB6-Cl:Y6 and 30% strain for PNTB6-Cl:BTP-Si4) test cycles. Note that the donor:acceptor weight ratios of PNTB6-Cl:Y6 and PNTB6-Cl:BTP-Si4 were 1:1.25 and 1:1.40, respectively. (**E** and **F**) Photographs of PNTB6-Cl:BTP-Si4 *s*-OSCs adhered on the knuckle to monitor the photocurrent under different bending angles (E), attached on the wrist, and integrated with a pulse sensor (F) to monitor human heart rate demonstrating the flexibility, bendability, and stretchability.

the crack tip propagated slowly. Additionally, the fractured PNTB6-Cl:BTP-Si4 film was rougher (root-mean-square roughness, R_q = 86.5 nm) than PNTB6-Cl:Y6 (R_q = 8.2 nm), which was further proof of ductile nature.

Stretchable OSCs

Taking advantage of the ductility of PNTB6-Cl:BTP-Si4, *s*-OSCs were fabricated (Fig. 3A and fig. S16), with devices on the basis of PNTB6-Cl:BTP-Si4 exhibiting an average PCE of 14.1 ± 0.30% (PCE_{max} = 14.6%) with a V_{oc} = 0.90 ± 0.004 V, FF = 70.1 ± 0.94%, and J_{sc} = 22.5 ± 0.36 mA/cm^2 (fig. S17A and table S9). Figure 3B summarizes the PCEs of all published *s*-OSCs and demonstrates the substantial performance advances reported in this work (*37*, *45*). The PNTB6-Cl:BTP-Si4 *s*-OSCs exhibited negligible PCE deterioration (~4%) at a 20% strain and retained ~82% of the initial PCE at the large strain of ~80% (table S10). Improved PCE retention under this strain reflected the large PNTB6-Cl:BTP-Si4 mechanical ductility and the absence of film delamination in the device stack (Fig. 3C). However, increasing the strain to ~100% led to crack formation and functional layer delamination, decreasing PCE.

Durability evaluations under various deformations were also performed, and the results are shown in Fig. 3D and fig. S17, B to D. The PNTB6-Cl:BTP-Si4–based *s*-OSCs are ultraflexible, retaining >90% of the initial PCE after 1000 bending cycles at radius *r* = 2 mm. Moreover, PNTB6-Cl:BTP-Si4 *s*-OSCs exhibited superior ductility and experienced only mild PCE decrease (~25%) even after 1000 cycles of 30% strain. The device retained intimate multilayer adhesion after this cycling test, establishing good mechanical robustness (fig. S17D).

Lastly, *s*-OSCs were integrated with highly deformable human knuckle and wrist (Fig. 3E), exhibiting stable photocurrent output up to ~45% tensile strain. Also, a stretchable solar module consisting of six series-connected *s*-OSCs retains an output voltage of 5 V when bending the wrist (~30% strain), satisfying the requirement for most wearable electronics (Fig. 3F). We realized a self-powered health

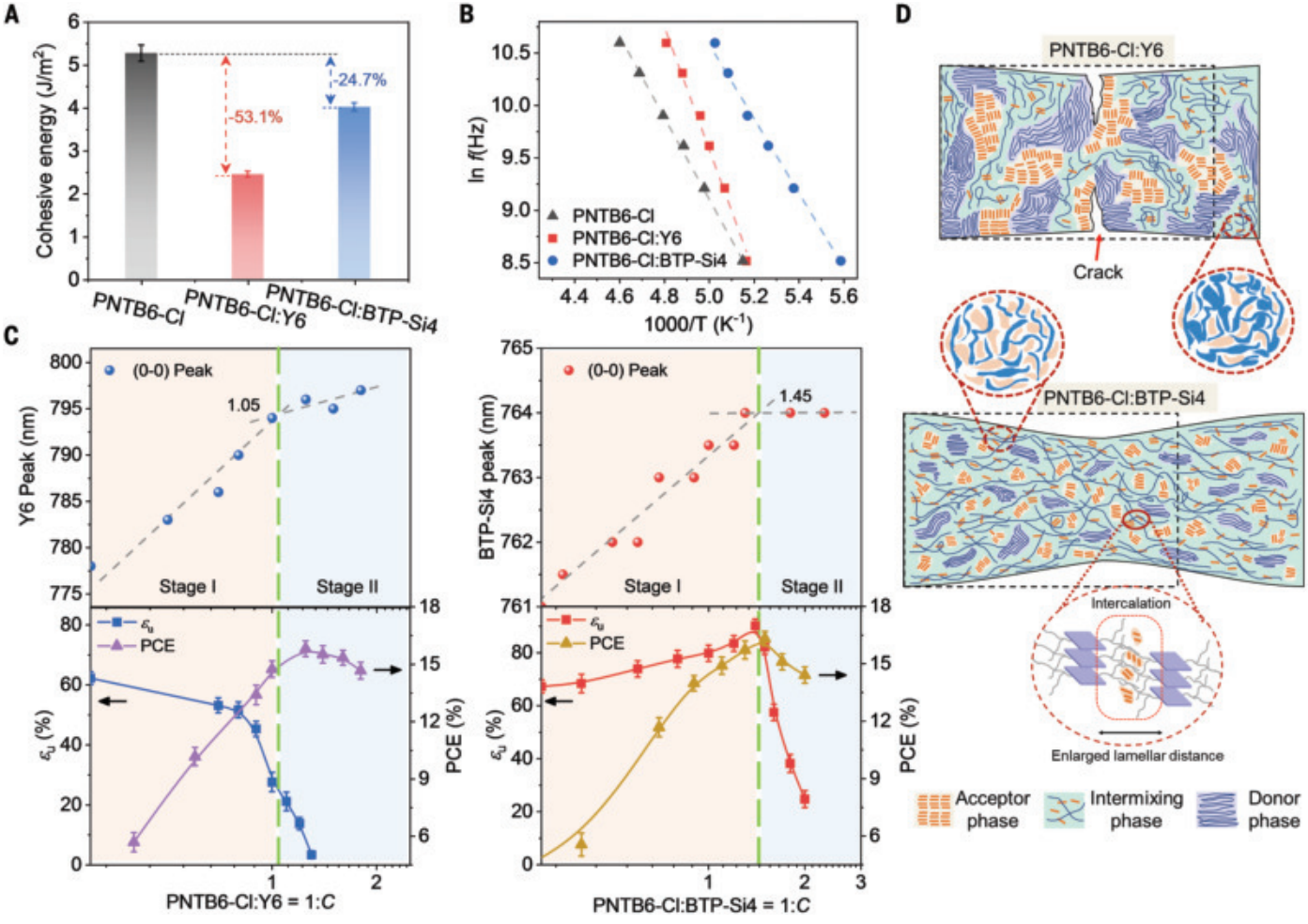

Fig. 4. Ultimate strain enhancement mechanism of blend films. (**A**) Cohesive energy of the indicated neat and blend films. (**B**) The applied frequencies (ln*f*) as a function of 1000/*T* of PNTB6-Cl for pristine PNTB6-Cl, PNTB6-Cl:Y6 (weight ratio = 1:1), and PNTB6-Cl:BTP-Si4 (weight ratio = 1:1) at temperature of β relaxation (T_β). The dashed lines represent the fitting to the Arrhenius law. (**C**) Acceptor main peak (0-0) location (up) as well as the ε_u and PCE values (down) as a function the ratio of Y6 and BTP-Si4 to PNTB6-Cl. Note that this data was obtained by using PNTB6-Cl batch-2. See table S15 for details. (**D**) Schematic illustration of the morphology of blend films. In PNTB6-Cl:BTP-Si4 blend, the long-range ordering (large acceptor domains) is suppressed while retaining sufficient short-range order to ensure efficient electron transport, resulting in excellent photovoltaic performance and considerable stretchability. Instead, Y6 texture and domain size in the blend are excessive, which deteriorate blend morphology and stiffen blend films.

monitoring system by integrating a pulse oximeter with the *s*-OSC (movie S2), demonstrating potential for early disease diagnosis and treatment.

Molecular structure and blend morphology versus mechanical properties

A combination of additional experiments and computations were performed to understand the ductility of the PNTB6-Cl:BTP-Si4–blend film, which we attribute to the twisted and wavy conjugated PNTB6-Cl backbone, the BTP-Si4 *N* functionalization, and the pronounced PNTB6-Cl and BTP-Si4 miscibility. Thus, we first investigated how the molecular weight of both donors affects ductility and found that it is not a major factor for the high stretchability of PNTB6-Cl (fig. S18). Furthermore, we used density functional theory and molecular dynamics (MD) simulations to model the PNTB6-Cl molecular conformation versus a planar or stiffer donor polymer, such as PM6 (ε_u = 25.0 ± 0.9%; see structure in fig. S19A) (*46*). Compared with PM6, large steric hindrance in PNTB6-Cl twisted the backbone and created a wavy conformation, preventing strong chain aggregation and depressing film crystallinity and enhanced ductility (ε_u = 66.3 ± 1.4%).

Additionally, the fast-decaying bond vector correlation of PNTB6-Cl indicated shorter persistence length and greater polymer chain flexibility (fig. S19B). Control mechanical tests on PM6:Y6 and PM6:BTP-Si4 blends revealed brittle blends (ε_u = 2.6 ± 0.6% and 17.4 ± 1.0%, respectively), although blends based on BTP-Si4 remained more ductile (table S11), further confirming ductility imparted by BTP-Si4. Thus, the PNTB6-Cl conformation greatly contributed to dissipating stress energy upon strain and improving film stretchability. BTP-Si4 also played a critical role in increasing ε_u from 10.2% for PNTB6-Cl:Y6 to 95.5% for PNTB6-Cl:BTP-Si4. Thus, sidechain branching and extension through the BTP-Si4 tetrahedral Si atom versus Y6 was essential for balancing miscibility with the donor polymer, mechanical stretchability, and PCE.

We performed semiquantitative miscibility and composition measurements on the intermixed phase. The miscibility of different blend components was quantified by contact-angle measurements (fig. S20 and table S12). The lower disparity in the surface tension between donor and BTP-Si4 corroborated greater intermixing compared with Y6. Additionally, the Flory-Huggins interaction parameter (χ) was calculated from the melting point depression of Y6 and BTP-Si4 in blends (fig. S21). The lower χ of PNTB6-Cl:BTP-Si4 (~1.13) compared with that of PNTB6-Cl:Y6 (~1.56) indicated greater miscibility and a more intimately mixed

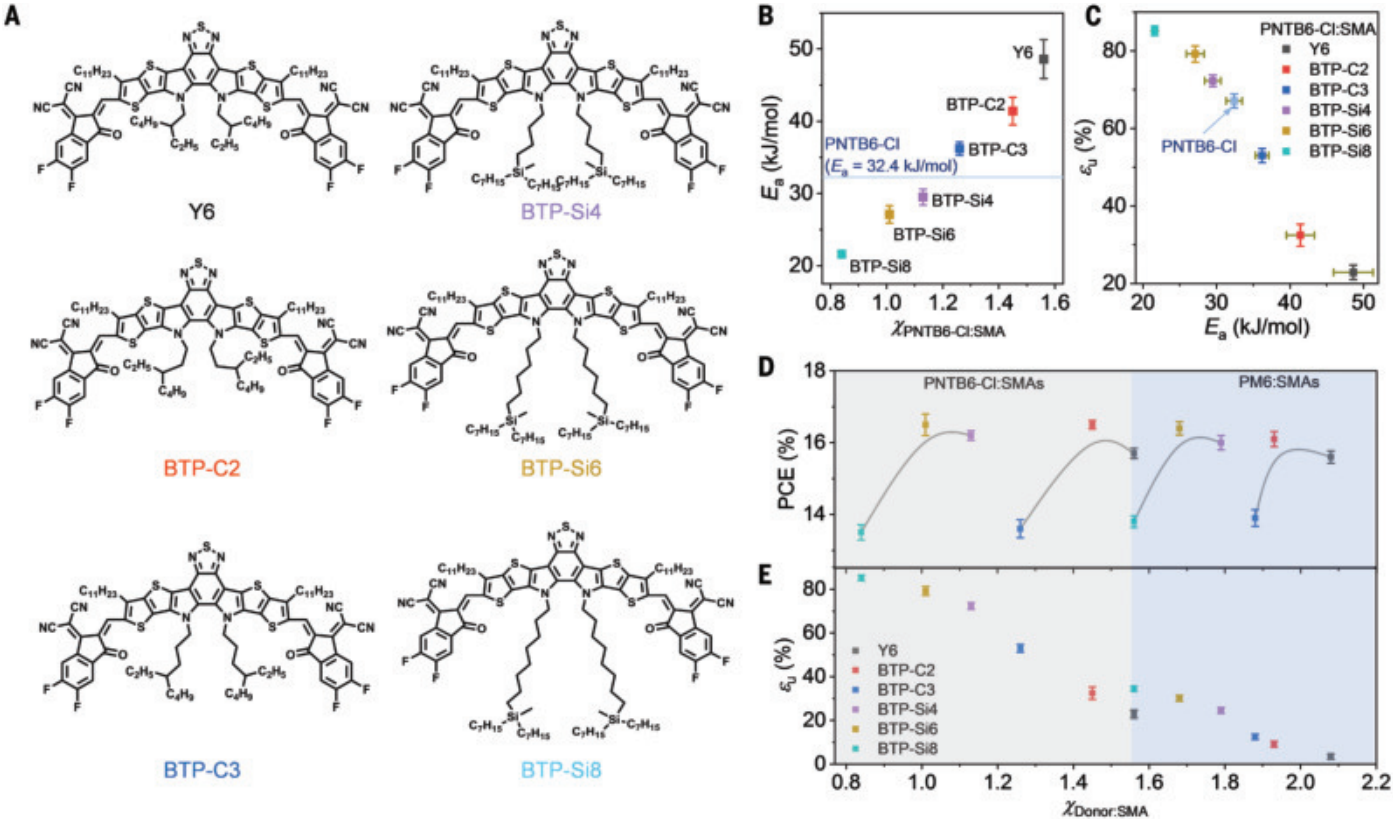

Fig. 5. The relationships between molecular structure, miscibility, apparent activation energy and ultimate strain. (**A**) Molecular structures of the SMAs used in this study. (**B**) Plot of apparent activation energy (E_a) of T_β transition versus miscibility (χ) of PNTB6-Cl with the indicated SMAs. (**C**) The ultimate strain (ε_u) versus E_a for the indicated blends. (**D** and **E**) The relationship between PCE, ε_u, and χ for the indicated blends. Note that lines are guides for the eyes, and, for all blends, the donor:acceptor weight ratio is 1:1.

morphology. The enhanced miscibility of BTP-Si4 is further reflected by the computed lower structural factor (fig. S22) and was consistent with the experimental GISAXS data.

The greater miscibility of BTP-Si4 into PNTB6-Cl should be reflected by a drop of blend cohesive energy (G_c) (Fig. 4A). Indeed, blending Y6 with PNTB6-Cl (1:1 wt%) decreased G_c from 5.3 to 2.3 J/m^2, whereas that of the BTP-Si4-based blend remained much higher (4.0 J/m^2), implying that more BTP-Si4 intercalates into PNTB6-Cl domains enhanced molecular affinity (*47*, *48*). Moreover, SMA intercalation can alter the thermomechanical relaxations of the donor polymer and film toughness. We used dielectric relaxation spectroscopy (DRS) to investigate the secondary thermal relaxations (sub-T_g) of PNTB6-Cl in these blends (Fig. 4B and fig. S23) (*49*, *50*). The DRS data indicated that the apparent activation energy (E_a) of β relaxation (T_β) transitions of PNTB6-Cl in the blend with BTP-Si4 (29.5 kJ/mol) was lower than those of both pristine PNTB6-Cl (32.4 kJ/mol) and the PNTB6-Cl:Y6 blend (48.6 kJ/mol), demonstrating a lower energy barrier for polymer chain motion and an increased free volume in PNTB6-Cl:BTP-Si4. The enlarged free volume in the latter blend was also supported by MD simulations (PNTB6-Cl:Y6 ~1405.1 ± 5.8 Å^3 versus PNTB6-Cl:BTP-Si4 ~1608.9 ± 22.4 Å^3; table S13).

We quantitatively investigated SMA aggregation in the intermixed phase by monitoring the blend film absorption spectra as a function of SMA concentration (Fig. 4C and fig. S24) (*51*). Note that the transition SMA concentration (C_{AP} ~ 1.45) of PNTB6-Cl:BTP-Si4 was greater than that of PNTB6-Cl:Y6 (C_{AP} ~ 1.05), reflecting the higher miscibility of the former blend. SMA aggregation played a crucial role and correlated with both ε_u and PCE of the corresponding blends and OSCs, respectively.

The ε_u of PNTB6-Cl:Y6 film first fell slightly from 66 to ~52% upon increasing the Y6 concentration C from 0 to 0.8 and then rapidly dropped to ~3% when C exceeded 1.05, which we attributed to Y6 brittleness. In stark contrast, the ε_u of PNTB6-Cl:BTP-Si4 exhibited the opposite trend and dramatically increased from 66 to ~90% when the BTP-Si4 concentration approached the C_{AP} ~1.40, and then decreased to ~25% for C = 2.

These results were consistent with peak force quantitative nanomechanical mapping measurements (fig. S25). The modulus of PNTB6-Cl:BTP-Si4 gradually fell when increasing the BTP-Si4 concentration, a typical mechanical behavior of a ductile polymer-plasticizer system. Conversely, the modulus of PNTB6-Cl:Y6 rapidly increased and gradually saturated with increasing Y6 concentration, thus exhibiting antiplasticization (fig. S26).

Notably, the device PCE gradually increased with the SMA concentration reaching a similar value of ~16%. However, for the PNTB6-Cl:Y6 blend, the Y6 composition that maximized the PCE exceeded C_{AP}, thus resulting in a low ε_u for the blend affording the best device. Thus, our results revealed that an appropriate C_{AP} composition of the intermixed phase, dominated by the miscibility, is crucial for maximizing both mechanical and photovoltaic performance of a blend film, as shown schematically in Fig. 4D. Additionally, the PNTB6-Cl:Y6 and PNTB6-Cl:BTP-Si4 device shelf-lifetime (room temperature) and thermal (at 55°C) stabilities were tested and found to be comparable (fig. S27), suggesting an optimal and stable morphology (fig. S28). The above blend and device results are in line with dynamic mechanical analysis and ultrasensitive fast scanning calorimetry (FSC) (fig. S29), where BTP-Si4 addition to the donor polymer resulted in distinctive thermal relaxation behavior.

SMA molecular design for high PCE and ductility

Comparison of molecular, blend, and OSC properties of BTP-Si4 with reference to Y6 raised the question of whether a more general relationship exists between molecular structure, miscibility, and ductility or whether BTP-Si4 behavior is unusual. To address this question, we synthesized two SMA series. In the first (Y6-like), we shifted the branching points of the alkyl chains of Y6 to the second and third positions, yielding BTP-C2 and BTP-C3, respectively. In the second (BTP-Si4–like), we introduced a silicon atom as the branching element and extended the length preceding the branching point, producing BTP-Si4, BTP-Si6, and BTP-Si8 (Fig. 5A).

The ε_u, E_a, and χ of all PNTB6-Cl:SMA blends (1:1 wt %) were accessed (figs. S30 and S31; see the supplementary materials for details). Note that all the blends afforded functional OSCs with PCEs of ~14 to 17% (see supplementary materials and table S14), reaching the maximum for intermediate chain extension. However, these materials had greatly different ductility. As depicted in Fig. 5B, increasing the alkyl chain length preceding the branch point consistently reduced both χ and E_a for both SMA series. This result confirmed that enhanced miscibility promotes SMA intercalation in the donor polymer phase, thereby lowering E_a and increasing the blend free volume.

Moreover, Fig. 5C revealed that ε_u was inversely proportional to the E_a of the donor T_β transitions. Notably, the blend ε_u of the Y6 series [22.9% (Y6), 32.5% (BTP-C2), and 53.0% (BTP-C3)] with E_a values of 48.6, 41.4, and 36.2 kJ/mol, respectively, were all much lower than that of the pristine PNTB6-Cl film (67.1%). Thus, the Y6 series always embrittled the resulting blend compared to the pristine donor, and further chain extension dramatically decreased PCE (Fig. 5D). By contrast, the ε_u/E_a of the PNTB6-Cl:BTP blends [72.3%/29.5 kJ/mol (BTP-Si4), 79.2%/27.1 kJ/mol (BTP-Si6), and 85.2%/21.6 kJ/mol (BTP-Si8)] were much larger or smaller than those of both the PNTB6-Cl and Y6 blend series while retaining large PCEs.

These findings underscore strong correlations between SMA branching position or extension (molecular design) and E_a and χ (heteromolecular interactions), translating to linear χ (miscibility)–ε_u (ductility) plots (coefficient of determination R^2 ~99% within each SMA family, ~95% for both SMA families) and demonstrating that ε_u always increased when χ decreased (Fig. 5E and fig. S33). Additionally, the miscibility χ is a known parameter for modifying the phase separation morphology and OSC PCE (*52*). As seen from the nonmonotonic χ-PCE relationship (Fig. 5D), the highest PCE could be achieved by optimizing χ. To simultaneously increase PCE and enhance ε_u versus the pristine donor matrix, χ must be reduced (<1.2 for PNTB6-Cl) and optimized, but this approach was effective only for the BTP-Si4-like SMAs because further chain extension in the Y6-like series would result in poor device performance.

Thus, the branching design of BTP-Si4–like SMAs suppressed excessive core aggregation and promoted blending with the donor polymer, enhancing PCE until excessive greasy components (BTP-Si8) depress photovoltaic response. Consequently, optimal miscibility, as in the case of BTP-Si4 (and BTP-Si6), increased the free volume in blend film and facilitated the conformational changes of the polymer chain under deformation, resulting in large PCE and ε_u. Notably, this result is not specific to PNTB6-Cl because PM6:SMA blends behaved similarly; the BTP-Si4–like series always outperformed the Y6 one in terms of ductility, established linear χ-ε_u plots (R^2 > 98% within each SMA family, and >96% for both SMA families) and the need to reduce χ (<1.8 for PM6) to plasticize the donor and achieve the greatest PCE (Fig. 5, D and E, and figs. S32 and S33), supporting further generality and applicability of the present SMAs to other blend families.

Discussion

We have demonstrated the use of the stretchable PNTB6-Cl donor and BTP-Si4 acceptor for highly deformable OSCs. BTP-Si4 design, characterized by a Si branching point in the SMA, suppresses excessive crystallization in the blend and promotes miscibility with the donor phase. Thus, BTP-Si4 and the PNTB6-Cl:BTP-Si4 blend behaved very differently than reported precedents, enabling a stretchability of 95.5%. Equally as notable, *s*-OSCs showed a PCE of 14.6% as well as mechanical robustness, with these cells retaining 82% of the initial PCE at a large tensional strain of 80%. These results demonstrate that rational acceptor molecular design, optimized over several SMAs, and optimal donor-acceptor miscibility are paramount for realizing highly efficient and mechanically robust OSCs.

REFERENCES AND NOTES

1. S. Wang *et al.*, *Nature* **555**, 83–88 (2018).
2. S. Hou *et al.*, *Adv. Funct. Mater.* **33**, 2301268 (2023).
3. T. Sekitani *et al.*, *Science* **321**, 1468–1472 (2008).
4. J. Liang, L. Li, X. Niu, Z. Yu, Q. Pei, *Nat. Photonics* **7**, 817–824 (2013).
5. T. Sekitani *et al.*, *Nat. Mater.* **8**, 494–499 (2009).
6. Z. Zhang *et al.*, *Nature* **603**, 624–630 (2022).
7. N. Matsuhisa *et al.*, *Nature* **600**, 246–252 (2021).
8. K. R. Jinkins *et al.*, *Sci. Adv.* **8**, eabo0537 (2022).
9. K. Nan *et al.*, *Sci. Adv.* **4**, eaau5849 (2018).
10. J. Li *et al.*, *Sci. Adv.* **9**, eadg1837 (2023).
11. B. Zhang *et al.*, *Nature* **628**, 84–92 (2024).
12. Y. Sun *et al.*, *Nat. Electron.* **2**, 513–520 (2019).
13. Y. Wei *et al.*, *Adv. Mater.* **36**, e2304225 (2024).
14. Y. Wu *et al.*, *Adv. Energy Mater.* **12**, 2103957 (2022).
15. S. Xiong *et al.*, *Nat. Commun.* **15**, 681 (2024).
16. C. Chen *et al.*, *Nat. Commun.* **15**, 6865 (2024).
17. S. Guan *et al.*, *Adv. Mater.* **36**, e2400342 (2024).
18. Y. Jiang *et al.*, *Nat. Energy* **9**, 975–986 (2024).
19. J. Fu *et al.*, *Nat. Commun.* **15**, 1830 (2024).
20. S. Park *et al.*, *Nature* **561**, 516–521 (2018).
21. L. Li *et al.*, *ACS Appl. Mater. Interfaces* **9**, 40523–40532 (2017).
22. S. Lee *et al.*, *Adv. Energy Mater.* **13**, 2300533 (2023).
23. C. Yan, J. Qin, Y. Wang, G. Li, P. Cheng, *Adv. Energy Mater.* **12**, 2201087 (2022).
24. J. Wang *et al.*, *Adv. Mater.* **34**, e2205009 (2022).
25. D. J. Lipomi, B. C.-K. Tee, M. Vosgueritchian, Z. Bao, *Adv. Mater.* **23**, 1771–1775 (2011).
26. J. Han *et al.*, *Adv. Funct. Mater.* **30**, 2003654 (2020).
27. S. Chen *et al.*, *Angew. Chem. Int. Ed.* **57**, 13277–13282 (2018).
28. Z. Peng *et al.*, *Adv. Mater.* **33**, e2106732 (2021).
29. Q. Zhu *et al.*, *Small* **17**, e2007011 (2021).
30. W. Song *et al.*, *Matter* **5**, 1877–1889 (2022).
31. H. Hu *et al.*, *Adv. Mater.* **31**, e1808279 (2019).
32. W. Huang *et al.*, *Joule* **4**, 128–141 (2020).
33. Y. Ding *et al.*, *Angew. Chem. Int. Ed.* **63**, e202403139 (2024).
34. J.-W. Lee *et al.*, *Nano Energy* **125**, 109541 (2024).
35. C. Lin *et al.*, *Angew. Chem. Int. Ed.* **63**, e202407040 (2024).
36. J.-W. Lee *et al.*, *Adv. Mater.* **34**, e2207544 (2022).
37. E. J. Sawyer *et al.*, *Extreme Mech. Lett.* **8**, 78–87 (2016).
38. J. Huang *et al.*, *Energy Environ. Sci.* **16**, 1251–1263 (2023).
39. Z. Wang *et al.*, *Adv. Funct. Mater.* **31**, 2103534 (2021).
40. H. Chen *et al.*, *Angew. Chem. Int. Ed.* **60**, 3238–3246 (2021).
41. X. Gu *et al.*, *Adv. Mater.* **36**, e2401370 (2024).
42. X.-K. Chen *et al.*, *Nat. Energy* **6**, 799–806 (2021).
43. J.-H. Kim *et al.*, *Nat. Commun.* **4**, 2520 (2013).
44. M. A. Alkhadra *et al.*, *Chem. Mater.* **29**, 10139–10149 (2017).
45. Q. Wan *et al.*, *J. Am. Chem. Soc.* **145**, 11914–11920 (2023).
46. T. Yang *et al.*, *Adv. Funct. Mater.* **32**, 2208950 (2022).
47. C. Bruner, N. Cates, M. D. McGehee, R. H. Dauskardt, *Adv. Funct. Mater.* **23**, 2863–2871 (2013).
48. N. Cates *et al.*, *Adv. Energy Mater.* **2**, 1208–1217 (2012).
49. N. Balar *et al.*, *Chem. Mater.* **32**, 6540–6549 (2020).
50. A. S. Maxwell, L. Monnerie, I. M. Ward, *Polymer* **39**, 6851–6859 (1998).
51. J. Fang *et al.*, *Cell Rep. Phys. Sci.* **3**, 100983 (2022).
52. L. Zhang *et al.*, *Adv. Mater.* **34**, e2106316 (2022).

ACKNOWLEDGMENTS

We thank the Analytical and Testing Center of Huazhong University of Science and Technology and Shanghai Synchrotron Radiation Facility (SSRF) for the characterization. We also thank X. Gao for the discussions. **Funding:** This work was supported by the National Key Research and Development Project of China (2022YFA1404001) and the Funds of the National Natural Science Foundation of China (grant no. 62174062). T.J.M. and A.F. acknowledge support by U.S. Office of Naval Research Contract N00014-24-1-2109 (Northwestern University), N00014-24-1-2110 (Georgia Institute of Technology), the Northwestern University Materials Research Science and Engineering Center, National Science Foundation award DMR-230869, and the Binational Science Foundation contract 2020384. Y.S. and J.K. acknowledge support by U.S. National Science Foundation grant DMR-2043264. **Author contributions:** Z.W., D.Z., and L.Y. contributed equally to this work. Z.W. performed solar cell fabrication. M.X. and Y.G. fabricated the devices, and L.Y. performed GIWAXS, GISAXS, DRS, and DSC. D.Z., R.L., S.M., and Q.W. synthesized the photoactive layer materials. J.H. assisted with the processing of materials. Z.W., J.L., J.H., X.J., Z.L., and L.Y. assisted with the fabrication, testing, and demonstration of devices. O.A. conducted the simulations with the guidance of S.S. M.W. carried out FSC with the guidance of N.S. Y.S. conducted the in situ SEM measurements with the guidance of J.K., Y.Y., and X.Z., and T.J.M. participated in the discussion. A.F. and M.S. conceived the project and designed the experiments, integrated data interpretation, and codrafted the paper. All authors discussed the results and commented on the paper. **Competing interests:** The authors declare that they have no competing interests. **Data and materials availability:** All data are available in the main text or the supplementary materials.

SUPPLEMENTARY MATERIALS

science.org/doi/10.1126/science.adp9709
Materials and Methods
Figs. S1 to S48
Tables S1 to S15
References (*53*–*120*)
Movies S1 and S2

Submitted 24 April 2024; resubmitted 9 October 2024
Accepted 12 December 2024
10.1126/science.adp9709

ZEOLITES

Atomic locations and adsorbate interactions of Al single and pair sites in H-ZSM-5 zeolite

Guangchao Li[1,2]†, Christopher Foo[1,3]†, Raymond Fan[3], Mingji Zheng[4,5], Qiang Wang[4,5], Yueying Chu[4], Jiasi Li[1], Sarah Day[3], Paul Steadman[3], Chiu Tang[3], Tsz Woon Benedict Lo[2]*, Feng Deng[4]*, Shik Chi Edman Tsang[1,2]*

The distribution of substitutional aluminum (Al) atoms in zeolites affects molecular adsorbate geometry, catalytic activity, and shape and size selectivity. Accurately determining Al positions has been challenging. We used synchrotron resonant soft x-ray diffraction (RSXRD) at multiple energies near the Al K-edge combined with molecular adsorption techniques to precisely locate "single Al" and "Al pairs" in a commercial H-ZSM-5 zeolite. This analysis depicts three distinct Al tetrahedral (T) sites: T8, T6, and T4. A combined suite of characterizations, including ammonia temperature-dependent desorption, neutron powder diffraction, solid-state nuclear magnetic resonance spectroscopy, and density functional theory calculations, reveal isolated ammonia adsorption on T8 as "single Al" in the straight channel and bridged ammonia adsorption on T6 and T4 as an "Al pair" (Al_{T6}-O-Si_{T5}-O-Al_{T4}) in the straight-sinusoidal intersection.

Zeolites are highly ordered microporous crystalline materials with a three-dimensional (3D) porous network of corner-sharing SiO_4 tetrahedral (T) sites. The substitution of silicon (Si) atoms in the zeolite framework with aluminum (Al) atoms imparts catalytic activity and functionality to the otherwise inert silicate matrix. These catalytic sites, which include protons, single metal ions, or metal-oxo complexes, are anchored to the Al sites. As a result, the local aluminum distribution in confined geometry governs the locations of adsorption and catalytic sites, thereby influencing their physicochemical properties and the mechanisms of the reactions that they catalyze.

Recently, particular attention has been paid to the presence of isolated Al in silicate matrix ("single Al") and Al-O-(Si-O)$_n$-Al ($n \leq 2$) with spatial proximity ("Al pairs") in zeolite frameworks (*1*). The Al pairs, consisting of two Al atoms in close geometric proximity, can optimally balance the adsorption of divalent counterion species through electrostatic interactions. Moreover, the coadsorption of molecules to two proximal Al atoms may enhance bimolecular reactions within zeolites or create synergistic interactions with adsorbates (*2*). Therefore, the site-selective distribution of Al atoms within the zeolite framework is anticipated to have a critical impact on molecular adsorption geometries (*3*), influencing reaction mechanisms for both mono- and bimolecular reactions (*4*) and affecting the orientation specificity of reactions (*5*).

The distribution of Al atoms within the zeolite framework is not statistical, and the preferred distribution is affected by synthesis conditions (*6*–*8*). Existing methodologies mainly based on indirect probe-spectroscopic methods [as discussed in the supplementary materials (SM)] have offered limited insights into Al sitting and have proven inadequate for accurately pinpointing the position of Al within the zeolite framework (*9*). For example, solid-state nuclear magnetic resonance spectroscopy (SSNMR) has been a common tool for probing the distribution of Al in zeolites by examining the local chemical environment of Al species (*10*). However, the interpretation of spectra often relies on models with assumptions that may not be fully substantiated. Additionally, the complex spectral shift contributions from neighboring sites and the lack of precise atomic coordinates in zeolite unit cells limit its impacts (their characterizations in benchmarking to our combined method are shown in the SM).

X-ray absorption spectroscopy has also been applied to investigate Al sitting in zeolites by analyzing the x-ray absorption near-edge structure at the Al K-edge (*11*). X-ray standing waves have also been used to ascertain atom positions within the lattice on the basis of the generated standing wave pattern (*12*). Furthermore, atom probe tomography has offered 3D atomic-scale insights into the structure and composition of zeolites, but its sensitivity and resolution limitations hinder complete structural elucidation (*13*).

More recently, integrated differential phase contrast scanning transmission electron microscopy (iDPC-STEM) has been used to indirectly infer the location of Brønsted acid sites (BAS) in H-ZSM-5 by using guest probes in the straight channel; however, visualization in the sinusoidal channel has not been facilitated (*14*, *15*). High-resolution synchrotron x-ray powder diffraction (SXRD) and neutron powder diffraction (NPD) have been used to locate probe molecules adsorbed on BAS in zeolites (*16*, *17*). Combined with Rietveld refinement, these techniques allow visualization of the overall crystalline atomic structure, including the bulk-averaged bonding interaction between BAS and basic adsorbate (*18*–*20*). However, the use of SXRD under the far-from-edge regime, in which scattering is solely dictated by nondispersive atomic scattering factors, f_0 (fig. S1A) (*21*, *22*), cannot provide sufficient contrast for Al sitting because of the similar scattering factor values for Al^{3+} and Si^{4+}. Thus, standard elastic diffraction techniques have not been sensitive enough to the Al^{3+}-Si^{4+} pair and have been ineffectual in the definitive determination of Al sitting in zeolite frameworks.

Resonant soft x-ray scattering

According to the quantum mechanical theory of x-ray scattering proposed in 1925 by Kramers and Heisenberg (*23*), in the resonant regime, the scattering factor, f, must be corrected by two anomalous scattering factors (ASF), f' and f'', which account for deviations in amplitude and phase, respectively (Eq. 1). The ASF are energy dependent but not angle dependent (fig. S1B), leading to dispersion effects. Alterations in the scattering factors affect the resulting structure factors and the corresponding Fourier transform, which in turn affects electron scattering density (Eqs. 2 and 3). As a result, the resonant soft x-ray diffraction (RSXRD) technique can in principle offer a direct way to elucidate the Al positions in zeolites as well as the crystallographic sitting of extra-framework atoms. This technique has been successfully used to resolve the positions of extra-framework Zn^{2+}/Na^+ in zeolite Y (*24*) and Sr^{2+}/Rb^+ in zeolite X (*25*). More recently, van Bokhoven and colleagues (*26*) have applied RSXRD to analyze the Al T-site distribution in a highly symmetrical FER-type zeolite (consisting of only four T-sites). However, no evidence for interactions between Al sites is presented.

$$f = f_0(2\theta) + f'(\lambda) + if''(\lambda) \quad (1)$$

$$F_{(h,k,l)} = \sum_{j=1}^{\text{atoms}} f_j e^{[i2\pi(hx_j+ky_j+lz_j)]} \quad (2)$$

$$\rho_{(xyz)} = \frac{1}{V}\sum_{hkl}^{+\infty}_{-\infty} |F(hkl)| \cdot e^{-2\pi i[hx+ky+lz-\phi(hkl)]} \quad (3)$$

[1]Wolfson Catalysis Centre, Department of Chemistry, University of Oxford, Oxford, UK. [2]State Key Laboratory of Chemical Biology and Drug Discovery, Department of Applied Biology and Chemical Technology, The Hong Kong Polytechnic University, Hong Kong. [3]Diamond Light Source, Rutherford Appleton Laboratory, Didcot, UK. [4]National Centre for Magnetic Resonance in Wuhan, State Key Laboratory of Magnetic Resonance Spectroscopy and Imaging, Wuhan Institute of Physics and Mathematics, Innovation Academy for Precision Measurement Science and Technology, Chinese Academy of Sciences, Wuhan, China. [5]University of Chinese Academy of Sciences, Beijing, China.
*Corresponding author. Email: benedict.tw.lo@polyu.edu.hk (T.W.B.L.); dengf@wipm.ac.cn (F.D.); edman.tsang@chem.ox.ac.uk (S.C.E.T.)
†These authors contributed equally to this work.

Herein, by using combined RSXRD and a suite of molecular adsorption characterization (i.e., the isotopic ammonia adsorptions with both $^{15}NH_3$ and ND_3) techniques, we provide a detailed elucidation of the atomic locations of single and paired Al within the framework of a commercial H-ZSM-5 (Si/Al = ~17) with respect to the ammonia adsorbates and zeolite unit cell, in which the Al atoms occupy various T-sites in straight, sinusoidal, and cross-channel positions.

Zeolite structural studies

As illustrated in Fig. 1, A and B, and fig. S23, the Pawley-refined reflection intensities exhibited nonsystematic variations with the incident beam energy. This observation suggested that the resonant energies were influencing the diffraction intensities in a manner that could be indicative of the Al locations within the H-ZSM-5 structure. Further details on the intensity variations and their implications for Al sitting are discussed in the SM. On the basis of the refinement results across the five energies, the T8, T6, and T4 sites were consistently identified as the preferred sites with the greatest site occupancy factors (SOF) (figs. S24 to S27). This finding aligned with the work of Sklenak *et al.*, who suggested through computational studies that Al occupies only three to five sites (*27*). From the RSXRD data and subsequent refinements for the given five energies, we determined that the overall Al occupancies were distributed among three T-sites: T8 [0.320(1)], T6 [0.116(2)], and T4 [0.244(2)] within the stated experimental error. All other sites were refined to zero occupancy, with insignificant associated errors (Fig. 1, C and D). This Al distribution within this H-ZSM-5 zeolite framework is displayed in Fig. 1, E and F.

Large-molecule adsorbate probe studies

As stated, probe molecules are commonly used in conjunction with various techniques such as SSNMR, SXRD, Fourier transform infrared spectroscopy, and temperature-programmed desorption to characterize the BAS in zeolites. In general, basic molecules containing lone pair electrons either in oxygen or nitrogen could form stable adsorbate adducts with the BAS protons. However, the exact accessibility and the interactions with BAS in 3D stereospecific locations for these common probe molecules are not fully understood. Figure 2 and figs. S28 to S30 show the Rietveld refined structures of typical probes, including trimethylphosphine oxide (TMPO), acetone, and pyridine within the H-ZSM-5 (adsorption geometries and interactions with framework atoms are depicted in the SM) and in relation to the Al sites established by RSXRD. Notably, when an excess of probe molecules was used, only two adsorbed probe molecules were identified per zeolite unit cell by simulated annealing difference, despite the presence of three BAS as shown by RSXRD. The short distances between oxygen and nitrogen in the probe molecules with the BAS oxygen clearly indicated the ready adsorption of the molecules with the T8 and T6, which are both confirmed as Al sites by RSXRD (Fig. 1). However, the Al-occupied T4 site appeared to be devoid of intersections with the probe molecules in this zeolite. The atomic structure of H-ZSM-5 revealed that the T8 site was located in the straight channel and physically distant from the other two Al sites. T6 was situated at the intersection void, whereas T4 was in the "inner" sinusoidal channel. These latter two sites were in close proximity, forming an Al pair as Al_{T6}-O-Si_{T5}-O-Al_{T4} (Fig. 1, E and F). Thus, this proximity may have prevented typical probe molecules from accessing the T4 site, raising questions about the dependence of adsorption geometry and reaction mechanisms on the distribution of Al sites within H-ZSM-5.

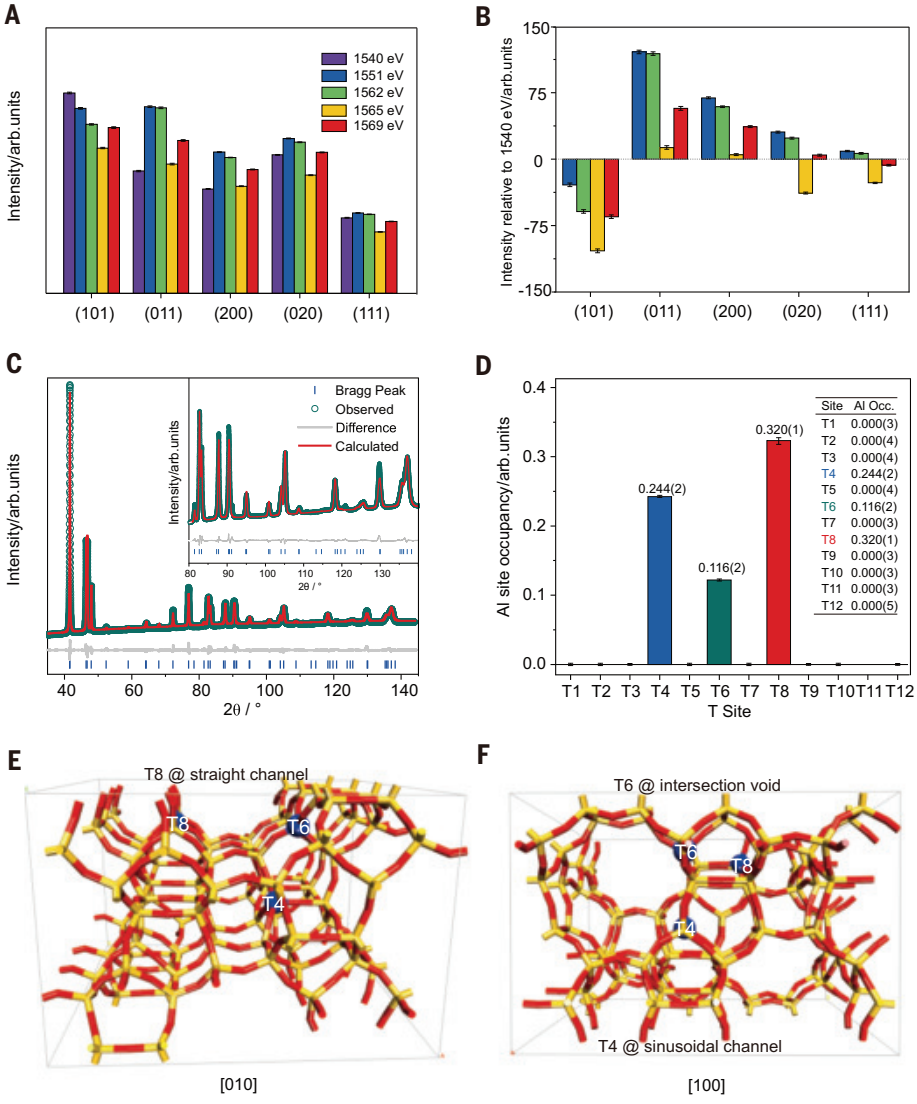

Fig. 1. Determination of framework precise structure and locations of Al in the H-ZSM-5 zeolite. Integrated reflection intensities of experimentally observed H-ZSM-5 (**A**) absolute intensity and (**B**) change in intensity relative to lowest incident energy 1540 eV. arb., arbitrary. (**C**) Rietveld refinement against experimental diffraction data at 1569 eV. (**D**) The overall refined Al occupancy from the five energies with the constraint on total occupancy. Inset shows the refined occupancy of Al in each T-site based on the constraint of the Al content determined by inductively coupled plasma mass spectrometry (ICP-MS). (**E** and **F**) The refined framework Al locations at T4 (sinusoidal channel), T6 (intersection void), and T8 (straight channel) are viewed along the [010] and [100] projections. Experimental details of RSXRD and SXRD, validities, errors, and sensitivities can be found in the SM (figs. S1 to S24 and tables S1 to S6).

Small-molecule adsorbate-ammonia probe studies

Figure 3A illustrates the final high-quality fit (goodness of fit, *GoF* = 1.15) achieved by the

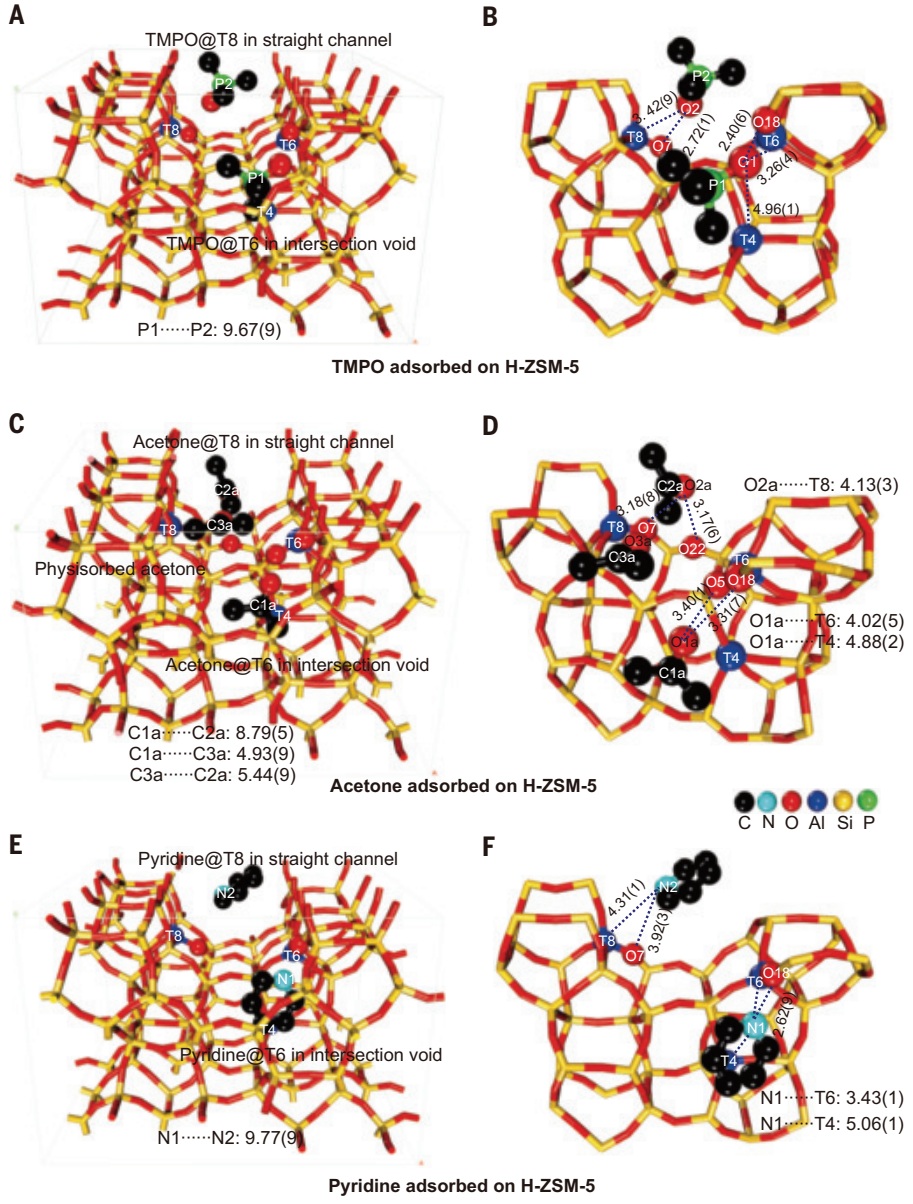

Fig. 2. Identification of acid sites by normal probe molecules with SXRD. The Rietveld refined adsorption structures of (**A** and **B**) trimethylphosphine oxide, (**C** and **D**) acetone, and (**E** and **F**) pyridine on H-ZSM-5 by SXRD are shown. The closest contacts between the adsorbates and framework are labeled (in angstroms). Symmetry in adsorption sites is disregarded for clarity. The original synchrotron x-ray diffraction patterns and Rietveld refinement profiles are shown in figs. S28 to S30. The corresponding atomic and crystallographic parameters are summarized in tables S7 to S10. Their adsorption geometries and interactions with framework atoms are also depicted in the SM.

refinement of ND_3 positions in H-ZSM-5 against NPD data, affirming the accuracy of the determined atomic positions of ND_3 with respect to the specific Al positions from the RSXRD. From the derived structure (Fig. 3B), the distances between the three N species are confirmed at 7.16(5) Å for N1···N2, 6.56(8) Å for N1···N3, and 4.86(2) Å for N3···N2, indicating that N3 is positioned between N1 and N2. Figure 3, C to E, illustrates the detailed local structures within the H-ZSM-5 zeolite, highlighting the positions of the adsorbed ND_3 molecules. There are three distinct ND_3 sites in the channels of H-ZSM-5: (i) bridged N1 adsorbed on two BAS (T6 and T4) as an ammonium ion in the intersection void; (ii) isolated N2 adsorbed on BAS of T8 as an ammonium ion in the straight channel; and (iii) N3 as a neutral ammonia molecule physisorbed in the intersection void. These three sites are correlated with the three distinct temperature-programmed desorption peaks observed for ammonia-loaded H-ZSM-5 (fig. S31) (*28*), which ranged from weak ammonia physisorption (N–H···O), to NH_4^+ ($O^{-}\cdots{}^{+}HN$) on a single Al site to the strongly resonated bridged NH_4^+ on synergistic Al pair sites (additional information on ammonia probe techniques is provided in the SM).

Upon adsorption of $^{15}NH_3$, the ^{1}H magic-angle spinning (MAS) SSNMR spectrum (Fig. 4A) displayed peaks at 2.0 and 4.2 parts per million (ppm), which we assigned to the Si-OH and residual BAS, respectively (*29*). Additional multiple peaks in the two ranges from 2.7 to 3.3 ppm and from 4.7 to 6.5 ppm were also observed. Previous studies have shown that peaks in the former range can be attributed to the H of molecular $^{15}NH_3$, and peaks in the latter range are attributed to single $^{15}NH_4^+$ and $^{15}NH_3$-$^{15}NH_4^+$ complexes owing to the intersection between $^{15}NH_3$ and H of BAS (*30*, *31*). In the ^{15}N MAS SSNMR spectrum (Fig. 4B), four distinct peaks at −376.1, −372.7, −365.0, and −358.8 ppm were identified. These peaks fell outside the chemical shift range for physisorbed $^{15}NH_3$ in zeolites (*32*, *33*), indicating that they correspond to $^{15}NH_3$ adsorbed on different sites, such as BAS and Si-OH. To elucidate the assignments of these peaks, the 2D ^{15}N-^{1}H heteronuclear correlation (HETCOR) MAS SSNMR experiment was performed (Fig. 4C). All four ^{15}N MAS SSNMR peaks were correlated to the ^{1}H MAS SSNMR peaks in the range from 1 to 4 ppm, which we assigned to the self-correlation of $^{15}NH_3$. Moreover, we attributed the peak at −376.1 ppm to the $^{15}NH_3$ over defects sites because of the single correlation peak at (−376.1, 1.8 to 2.7) ppm. The other three peaks at −372.7, −365.0, and −358.8 ppm are all correlated to the ^{1}H peaks in the chemical shift range from 4.7 to 6.5 ppm, suggesting that those three peaks can be attributed to $^{15}NH_3$ adsorbed over BAS with different states. The strong correlation peak at (−365.0, 6.5) ppm was attributed to the typical $^{15}NH_4^+$ species resulting from the adsorption of $^{15}NH_3$ over BAS (*34*). The correlation peak at (−372.7, 4.7 to 5.9) ppm was assigned to $^{15}NH_4^+$ species hydrogen bonded with adjacent $^{15}NH_3$ molecules, as hydrogen bonding to the proton of NH_4^+ would produce the upfield shift of ^{15}N MAS SSNMR (*35*). In contrast, the downfield shift of ^{15}N MAS SSNMR peak at −358.8 ppm implied a strong interaction between $^{15}NH_3$ and the corresponding BAS. On the basis of RSXRD results for Al distribution and NPD refinement of ND_3, this can be attributed to the resonant structure of $^{15}NH_3$ adsorption formed over BAS of T4 and T6 simultaneously as an Al pair.

Furthermore, we conducted symmetry-based resonance-echo saturation-pulse double-resonance (S-RESPDOR) experiments (*36*) to estimate the ^{15}N-^{27}Al heteronuclear dipolar interactions and derive their interatomic distances (fig. S32). Quantitative internuclear distances can

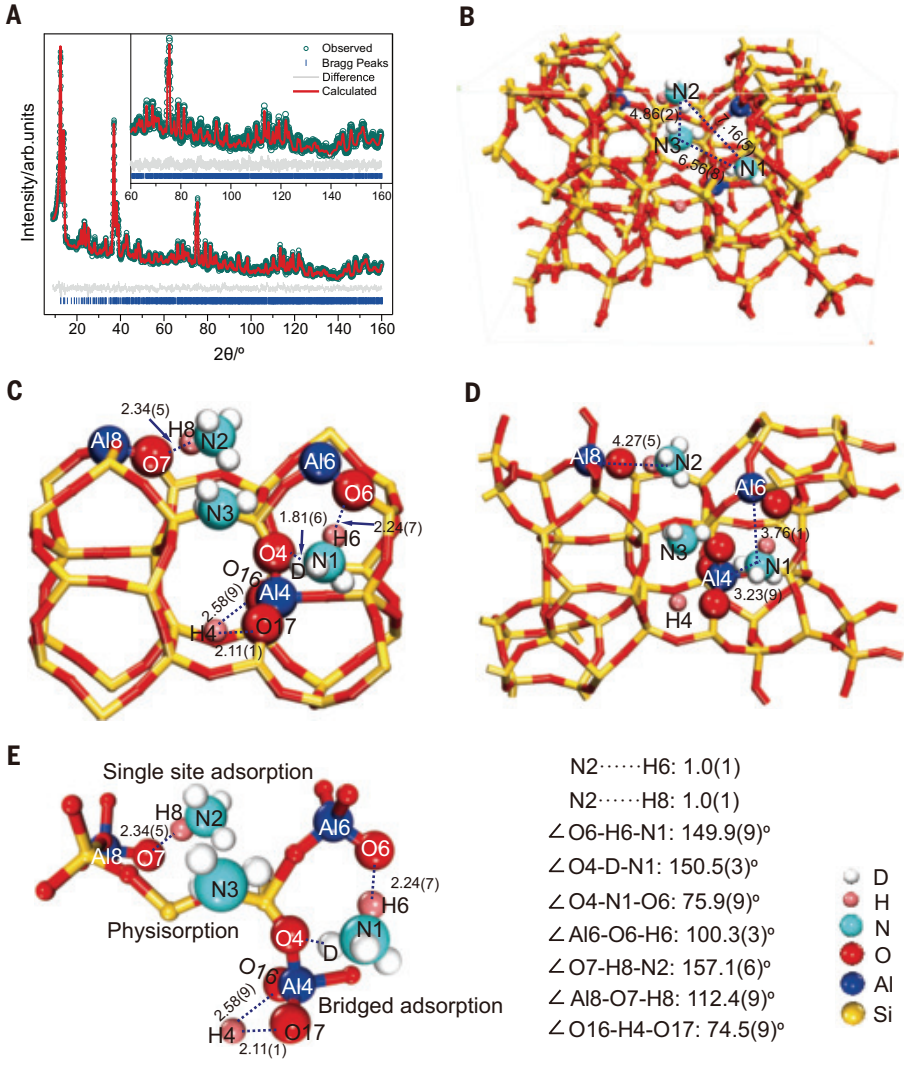

Fig. 3. Characterization of ND_3 adsorption behaviors on H-ZSM-5 by NPD. (**A**) Rietveld refinement profiles of NPD data [wavelength, λ = 2.43953(2) Å; weighted profile residual, R_{wp} = 1.77%; expected profile residual, R_{exp} = 1.54%; *GoF* = 1.15]. Zeolite structures with the determined ND_3 sites (N1, N2, and N3) with the bond length information (in angstroms) retrieved by means of NPD-Rietveld refinement. (**B**) The refined periodic structure and (**C** and **D**) enlarged detailed views. The atomic and crystallographic parameters are summarized in tables S11 and S12. (**E**) ND_3 adsorption geometries with bond lengths and angles. Symmetry in adsorption sites is disregarded for clarity. The detailed characterization of adsorption geometries and behaviors for ND_3 on acid sites by NPD is given in the SM.

be obtained by evaluating the dephasing curve, that is, by plotting $\Delta S/S_0$ versus recoupling time (Fig. 4, D to F). This confirms that the bridged $^{15}NH_3$ molecule is in proximity to two framework Al atoms simultaneously, corroborating the ND_3 adsorption observations by NPD (Fig. 3).

Discussion

The crystallographic sitting of Al in zeolite is vital in understanding its spatial relationship to the pore network. Such spatial information, often lacking in specificity, is critical for comprehending the zeolite's chemical activity beyond just the local Al concentration. For example, in ZSM-5 zeolite catalysis, it is generally acknowledged that the primary reaction sites are located at the intersection of the channels (*a* and *b* axes), whereas the straight channels aligned with the *b* axis are noted for molecule diffusion (*37*) and side-product formation (*38*). This difference has been exploited in some recent attempts to manipulate reaction productivity and selectivity using *b* axis–oriented nanosheet ZSM-5 zeolites (*39*, *40*).

However, a substantial advancement in the strategic design of zeolite catalysts for improved specificity in catalytic transformations would require a more detailed molecular understanding of active sites and adsorption structures and spatial characteristics (*41*, *42*). The advent of advanced iDPC-STEM technique has enabled the visualization of adsorbed probe molecules within zeolite channels, offering the indirect localization of acid sites within the framework (*14*, *15*). On the other hand, this methodology predominantly yields observations in the linear channels along the *b* axis, whereas the spatial resolution of acid sites in the intersection void or within sinusoidal pores remains a formidable challenge, obscured by the zeolite's atomic framework through a stacking occlusion effect.

Additionally, the inherent symmetry of the ZSM-5 zeolite structure may introduce structural ambiguity in the direction perpendicular to the straight channels, complicating the accurate pinpointing of acid site positions (*43*). Using the RSXRD technique, we have demonstrated that the precise Al atomic locations can be obtained, namely T8, T6, and T4 sites, in a given commercial H-ZSM-5. According to our crystallographic mapping, T8 is located at the straight channel (along the *b* axis), T6 in cross-channel voids, and T4 in the sinusoidal channel (along the *a* and *c* axes; see fig. S2), giving further structural information to tailor zeolitic sites for improved catalysis in the future. It is apparent that T8 and T6 are readily accessible to probe molecules, and their presence can also be inferred by indirect probe-assisted techniques (Fig. 2; see SM). Conversely, the T4 site situated in the inner sinusoidal channel is less accessible to typical basic probe molecules such as TMPO, acetone, and pyridine, making its presence and impact less well understood.

Our findings also identify the T4 and T6 sites as framework positions for Al atoms in proximity to each other, marking the first direct crystallographic identification of an Al pair in this zeolite. Their presence may correlate with the long-observed channel-specific diffusion, mono- and bimolecular reactions, and shape and size selectivity of small adsorbate species. The Al pairs in zeolites have also been indirectly inferred through ^{1}H, ^{29}Si, and ^{27}Al MAS SSNMR, which suggests complex interactions between neighboring sites (*13*, *44*, *45*), as well as from our 2D ^{1}H-^{1}H double-quantum (DQ) MAS SSNMR (fig. S33) but with no spatial information. Furthermore, the combined RSXRD molecular adsorption results (Figs. 1D and 3) indicate that the quantity of T4 [occ. 0.244(2)] is greater than that of T6 [occ. 0.116(2)], which means that not all ammonia adsorption at the T4 and T6 positions is in the coadsorption state. Some extra ammonia still adsorbs separately at the T4 or T6 sites. This difference explains the observation of peaks at −365 ppm in the ^{15}N MAS SSNMR (Fig. 4), representing an average result

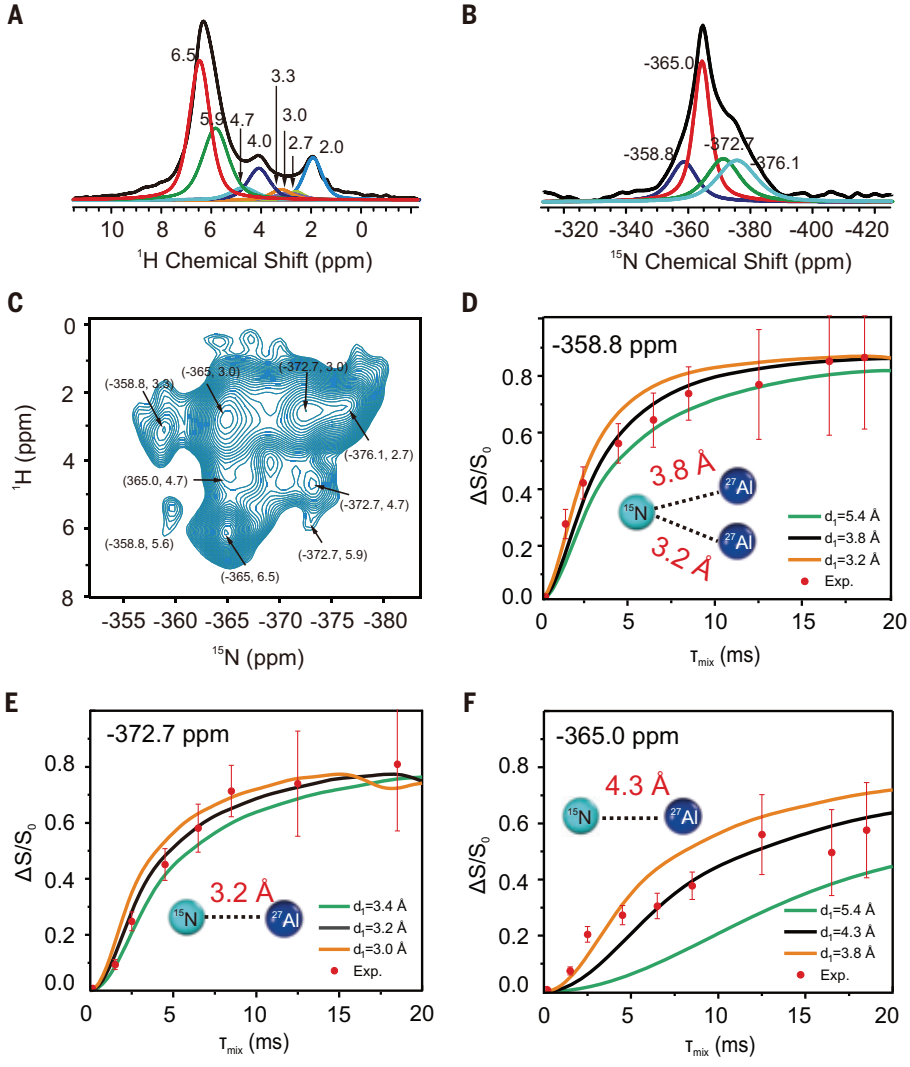

Fig. 4. Characterization of $^{15}NH_3$ adsorption behaviors on H-ZSM-5 by SSNMR. (**A**) ^{1}H, (**B**) ^{15}N, and (**C**) two-dimensional ^{15}N-^{1}H HETCOR MAS SSNMR spectra of $^{15}NH_3$ adsorbed on H-ZSM-5. ^{15}N-^{27}Al S-RESPDOR built-up data and simulated curves by plotting the signal fraction $\Delta S/S_0 = (S_0 - S')/S_0$ (S_0 and S' represent the signal intensity with and without dipolar dephasing, respectively) as a function of the recoupling time τ, for ^{15}N chemical shift at (**D**) −358.8 ppm, (**E**) −372.7 ppm, and (**F**) −365.0 ppm. d_1 represents the internuclear distance of the ^{15}N-^{27}Al spin pair.

from all the isolated adsorption of $^{15}NH_3$ on BAS (see SM).

The theoretical calculations also support this observation, as isolated adsorption modes for NH_3 at the T4, T6, and T8 sites yield similar ^{15}N chemical shifts at −368, −366, and −365 ppm, respectively (fig. S34). Notably, the results of the theoretical calculations for the ^{15}N chemical shifts based on our NPD refined structures match well with our experimental data. As shown in fig. S35, the calculated chemical shifts for the isolated and bridged adsorption modes of NH_3 based on our refined models after structural optimization are −362 and −353 ppm, respectively. Therefore, by using ammonia as a probe molecule, we have revealed the bridged adsorption of ammonia at the T4 and T6 sites, which reflects the distinctive adsorptive and catalytic properties of Al pairs differing from single Al sites for adsorption and bimolecular catalysis for small species in this H-ZSM-5.

As a result, this work demonstrates the combined strength of RSXRD at multiple energies near the Al K-edge and molecular adsorption studies as a powerful correlative and multimodal characterization tool, capable of determining the location and distribution of single Al sites, paired Al sites, and their molecular adsorbates, which can provide unprecedented direct structural elucidation of zeolite frameworks.

REFERENCES AND NOTES

1. J. Dědeček, Z. Sobalík, B. Wichterlová, *Catal. Rev., Sci. Eng.* **54**, 135–223 (2012).
2. K. Gołąbek *et al.*, *Commun. Chem.* **3**, 25 (2020).
3. M. Bernauer *et al.*, *J. Catal.* **344**, 157–172 (2016).
4. M. Xing *et al.*, *Fuel* **333**, 126541 (2023).
5. T. Y. Liang *et al.*, *ACS Catal.* **6**, 7311–7325 (2016).
6. V. Gábová, J. Dědecek, J. Cejka, *Chem. Commun.* **2003**, 1196–1197 (2003).
7. J. Dedecek, V. Balgová, V. Pashkova, P. Klein, B. Wichterlová, *Chem. Mater.* **24**, 3231–3239 (2012).
8. K. Muraoka, W. Chaikittisilp, Y. Yanaba, T. Yoshikawa, T. Okubo, *Angew. Chem. Int. Ed.* **57**, 3742–3746 (2018).
9. A. Bhan, E. Iglesia, *Acc. Chem. Res.* **41**, 559–567 (2008).
10. O. H. Han, C. S. Kim, S. B. Hong, *Angew. Chem. Int. Ed.* **41**, 469–472 (2002).
11. A. Vjunov *et al.*, *J. Am. Chem. Soc.* **136**, 8296–8306 (2014).
12. J. A. van Bokhoven *et al.*, *Nat. Mater.* **7**, 551–555 (2008).
13. D. E. Perea *et al.*, *Nat. Commun.* **6**, 7589 (2015).
14. B. Shen *et al.*, *Nature* **607**, 703–707 (2022).
15. B. Shen *et al.*, *Nature* **592**, 541–544 (2021).
16. B. T. W. Lo, L. Ye, S. C. E. Tsang, *Chem* **4**, 1778–1808 (2018).
17. B. T. Lo *et al.*, *Angew. Chem. Int. Ed.* **55**, 5981–5984 (2016).
18. G. Li *et al.*, *J. Am. Chem. Soc.* **143**, 8761–8771 (2021).
19. G. Li *et al.*, *Angew. Chem. Int. Ed.* **61**, e202204500 (2022).
20. K. C. Leung *et al.*, *J. Am. Chem. Soc.* **145**, 14548–14561 (2023).
21. H. Viervoll, O. Ögrim, *Acta Crystallogr.* **2**, 277–279 (1949).
22. F. Moore, *Acta Crystallogr.* **16**, 1169–1175 (1963).
23. H. A. Kramers, W. Heisenberg, *Z. Phys.* **31**, 681–708 (1925).
24. A. P. Wilkinson, A. K. Cheetham, S. C. Tang, W. J. Reppart, *J. Chem. Soc. Chem. Commun.* **1992**, 1485–1487 (1992).
25. H. Palancher *et al.*, *Angew. Chem. Int. Ed.* **44**, 1725–1729 (2005).
26. A. B. Pinar *et al.*, *J. Am. Chem. Soc.* **143**, 17926–17930 (2021).
27. S. Sklenak *et al.*, *Angew. Chem. Int. Ed.* **46**, 7286–7289 (2007).
28. L. Ye *et al.*, *Chem. Commun.* **52**, 3422–3425 (2016).
29. G. Paul *et al.*, *Chem. Soc. Rev.* **47**, 5684–5739 (2018).
30. W. P. J. H. Jacobs, J. W. de Haan, L. J. M. van de Ven, R. A. van Santen, *J. Phys. Chem.* **97**, 10394–10402 (2002).
31. F. Yin, A. L. Blumenfeld, V. Gruver, J. J. Fripiat, *J. Phys. Chem. B* **101**, 1824–1830 (1997).
32. V. M. Mastikhin, S. V. Filimonova, *J. Chem. Soc., Faraday Trans.* **88**, 1473–1476 (1992).
33. G. P. Holland, B. R. Cherry, T. M. Alam, *J. Phys. Chem. B* **108**, 16420–16426 (2004).
34. W. L. Earl, P. O. Fritz, A. A. V. Gibson, J. H. Lunsford, *J. Phys. Chem.* **91**, 2091–2095 (1987).
35. W. M. Litchman, M. Alei Jr., A. E. Florin, *J. Chem. Phys.* **50**, 1031–1032 (1969).
36. L. Chen *et al.*, *J. Magn. Reson.* **206**, 269–273 (2010).
37. D. Fu *et al.*, *Angew. Chem. Int. Ed.* **61**, e202114388 (2022).
38. B. Ali *et al.*, *J. Ind. Eng. Chem.* **88**, 127–136 (2020).
39. M. Choi *et al.*, *Nature* **461**, 246–249 (2009).
40. X. Zhang *et al.*, *Science* **336**, 1684–1687 (2012).
41. X. Wang, Y. Ma, Q. Wu, Y. Wen, F. S. Xiao, *Chem. Soc. Rev.* **51**, 2431–2443 (2022).
42. P. Kumar *et al.*, *Nat. Mater.* **19**, 443–449 (2020).
43. L. Liu *et al.*, *Angew. Chem. Int. Ed.* **59**, 819–825 (2020).
44. Z. Yu *et al.*, *Angew. Chem. Int. Ed.* **49**, 8657–8661 (2010).
45. M. B. Schmithorst, S. Prasad, A. Moini, B. F. Chmelka, *J. Am. Chem. Soc.* **145**, 18215–18220 (2023).

ACKNOWLEDGMENTS

We are indebted to SRIPT-SINOPEC for their supply of commercial H-ZSM-5 and P.-L. Ho from the Tsang group at Oxford University, who provided the STEM images of the sample. **Funding:** The support for this project from the Engineering and Physical Sciences Research Council (EPSRC) in the United Kingdom as a joint DPhil Studentship with Diamond Light Source (1947428), the Hong Kong Research Grants Council (15305722, 15301521, and 15300819), the Strategic Priority Research Program of the Chinese Academy of Sciences (XDB0540000), and the National Natural Science Foundation of China (grant 22161132028) is gratefully acknowledged. The RSXRD experiments were performed at Diamond Light Source (NR24677). Some preliminary SXRD experiments were conducted at SPring-8 (2022B054) and the National Synchrotron Radiation Research Center (2024-1-276-1). The NPD experiments were performed at the Australian Centre for Neutron Scattering with the approval of Australia's Nuclear Science and Technology Organisation (ANSTO) (ID 9577). A portion of SSNMR data was collected at the University Research Facility in

Chemical and Environmental Analysis at the Hong Kong Polytechnic University with financial support from the Department of Applied Biology and Chemical Technology (PolyU P0049034). **Author contributions:** G.L., C.F., and J.L. carried out SXRD and NPD analysis. G.L., M.Z., and Q.W. carried out SSNMR analysis. C.F., R.F., P.S., S.D., C.T., and T.W.B.L. collected RSXRD data at I10, Diamond Light Source (DLS), UK. M.Z., Q.W., and F.D. carried out SSNMR data collection at the National Centre for Magnetic Resonance in Wuhan, China. Y.C. carried out the chemical shift calculations. G.L., C.F., and S.C.E.T. wrote the paper. S.C.E.T. supervised the whole project. All authors approved the final version of the manuscript. **Competing interests:** The authors declare that they have no competing interests. **Data and materials availability:** The authors declare that the data supporting the findings of this study are available within the paper and its supplementary materials. **License information:** Copyright © 2025 the authors, some rights reserved; exclusive licensee American Association for the Advancement of Science. No claim to original US government works. https://www.science.org/about/science-licenses-journal-article-reuse

SUPPLEMENTARY MATERIALS

science.org/doi/10.1126/science.adq6644
Materials and Methods
Supplementary Text
Figs. S1 to S51
Tables S1 to S18
References (*46*–*81*)

Submitted 24 May 2024; accepted 11 December 2024
10.1126/science.adq6644

REPRODUCTION

Systematic identification of Y-chromosome gene functions in mouse spermatogenesis

Jeremie Subrini[1], Wazeer Varsally[1], Irina Balaguer Balsells[1,2], Maike Bensberg[1,3], Georgios Sioutas[1], Obah Ojarikre[1], Valdone Maciulyte[1], Björn Gylemo[1,3], Katharine Crawley[4], Katherine Courtis[4], Dirk G. de Rooij[5,6], James M. A. Turner[1]*

The mammalian Y chromosome is essential for male fertility, but which Y genes regulate spermatogenesis is unresolved. We addressed this by generating 13 Y-deletant mouse models. In *Eif2s3y*, *Uty*, and *Zfy2* deletants, spermatogenesis was impaired. We found that *Uty* regulates spermatogonial proliferation, revealed a role for *Zfy2* in promoting meiotic sex chromosome pairing, and uncovered unexpected effects of Y genes on the somatic testis transcriptome. In the remaining single Y-gene deletants, spermatogenesis appeared unperturbed, but testis transcription was still altered. Multigene deletions, including a human-infertility AZFa model, exhibited phenotypes absent in single Y deletants. Thus, Y genes may regulate spermatogenesis even if they show no phenotypes when deleted individually. This study advances our knowledge of Y evolution and infertility and provides a resource to dissect Y-gene functions in other tissues.

The mammalian sex chromosomes evolved from a pair of autosomes, with the Y chromosome degenerating and ultimately losing over 90% of its ancestral gene content (*1*–*3*). The remaining nonrecombining region of the mouse Y chromosome contains 16 gene families, which encode proteins with predicted regulatory roles including transcription activation, ubiquitylation, chromatin modification, RNA stability, and translation (*1*, *2*, *4*, *5*) (Fig. 1A). Four (*Rbmy*, *Sly*, *Srsy,* and *Ssty1/2*) are ampliconic, having been amplified into multiple copies, occupying the Y long arm and centromeric end of the Y short arm, and are implicated in spermiogenesis and sex ratio control (*6*–*11*). Of the remaining 12, *Uba1y*, *Kdm5d*, *Eif2s3y*, *Uty*, *Ddx3y*, *Usp9y*, *Sry*, *Zfy1*, *Zfy2*, and *Prssly* were present on the ancestral XY pair, whereas *Teyorf1* and the duplicated *H2al2y* (*H2al2b* and *H2al2c*) were more recently acquired in the mouse lineage (*4*, *12*).

[1]Sex Chromosome Biology Laboratory, The Francis Crick Institute, London, UK. [2]Developmental Epigenomics Group, MRC London Institute of Medical Sciences, Du Cane Road, London, UK. [3]Crown Princess Victoria Children´s Hospital, and Department of Biomedical and Clinical Sciences (BKV), Linköping University, Linköping, Sweden. [4]Genetic Modification Service (GeMS), The Francis Crick Institute, London, UK. [5]Reproductive Biology Group, Division of Developmental Biology, Department of Biology, Faculty of Science, Utrecht University, Utrecht, Netherlands. [6]Centre for Reproductive Medicine, Academic Medical Centre, University of Amsterdam, Amsterdam, Netherlands.
***Corresponding author: Email: james.turner@crick.ac.uk**

The majority (12 out of 16) of mouse Y-gene families exhibit testis-biased expression. This, together with the fact that large genomic deletions on the Y chromosome are associated with fertility defects in mice and men, highlights the importance of the Y chromosome in spermatogenesis (*5*). However, our understanding of the specific Y genes necessary for spermatogenesis and their precise roles remains incomplete. The functions of only a few genes have been identified. *Sry* is necessary and sufficient for testis determination (*13*). *Eif2s3y* is necessary for spermatogonial proliferation, but its mechanism of action remains unknown (*14*, *15*). *Zfy* genes have been shown to be important in meiosis and sperm morphogenesis, but their exact functions are not fully understood (*16*–*22*). Other Y genes have been targeted with no overt fertility phenotypes (*12*, *23*–*27*), but confirmation that the allele was a null was not always established, or deeper reproductive phenotyping was not performed (*16*, *23*–*26*). For some genes, knockouts (KOs) have never been made. In this study, we established a pipeline to systematically generate null Y-gene deletions and performed extensive fertility phenotyping, thereby determining which genes are involved in spermatogenesis and how they function.

Generating mouse models with Y-gene deletions

We targeted Y genes in XY mouse embryonic stem cells (mESCs), which were then used to produce Y-KO animals. For each Y gene, the entire coding region was excised using CRISPR-Cas9 with two flanking single guide RNAs (sgRNAs), thereby generating null alleles (Fig. 1B and fig. S1, A to C). The exception was the duplicated *H2al2y*, for which we used one sgRNA to generate indels (insertions and deletions) in both copies. We used this approach for *H2al2y* because the two identical copies *H2al2b* and *H2al2c* flank *Sry*, meaning that a whole-gene deletion strategy could inadvertently remove *Sry* and cause sex reversal (Fig. 1A and fig. S1D). For *Zfy1* and *Zfy2*, we created individual deletions and a combined *Zfy1&2*-double knockout (DKO) deletion, allowing us to examine functional overlap between these paralogs. We also generated an animal model of the *az*oospermia factor a (AZFa) deletion, encompassing *Uty*, *Ddx3y*, and *Usp9y*, which in men causes the most severe form of infertility characterized by a complete absence of germ cells (*28*). We used this model to understand the etiology of AZFa-related infertility and to examine functional divergence of the Y chromosome in mice and men. The multigene KOs also allowed us to interrogate combinatorial effects of Y-gene loss on spermatogenesis.

Once fully validated by low-pass whole-genome sequencing (fig. S1, E and F) and MiSeq analysis of on- and off-target mutations (fig. S1, G and H), deletant mESC lines were used to make animals. This is usually achieved by blastocyst mESC injection and breeding of resulting chimeras to attain germline transmission. Such an approach was not suitable for mutations that could compromise fertility. We therefore used tetraploid aggregation to generate founders that were fully derived from the mESCs, which means they were fully mutant. We improved the typically low birth and offspring survival rates associated with this technology (*29*–*32*) (see materials and methods for details) and generated founders from all our Y-KO mESC lines. We conclude that *Eif2s3y*, *Zfy1*, *Zfy2*, *Uty*, *Uba1y*, *Usp9y*, *Ddx3y*, *Kdm5d*, *H2al2y*, *Teyorf1*, and *Prssly* are all dispensable for embryonic survival.

Spermatogenic defects in a subset of Y-gene KOs

To determine which Y genes are necessary for reproduction, Y-KO males were mated with wild-type females. Consistent with previous studies, *Eif2s3y*-KO and *Zfy1&2*-DKO founders

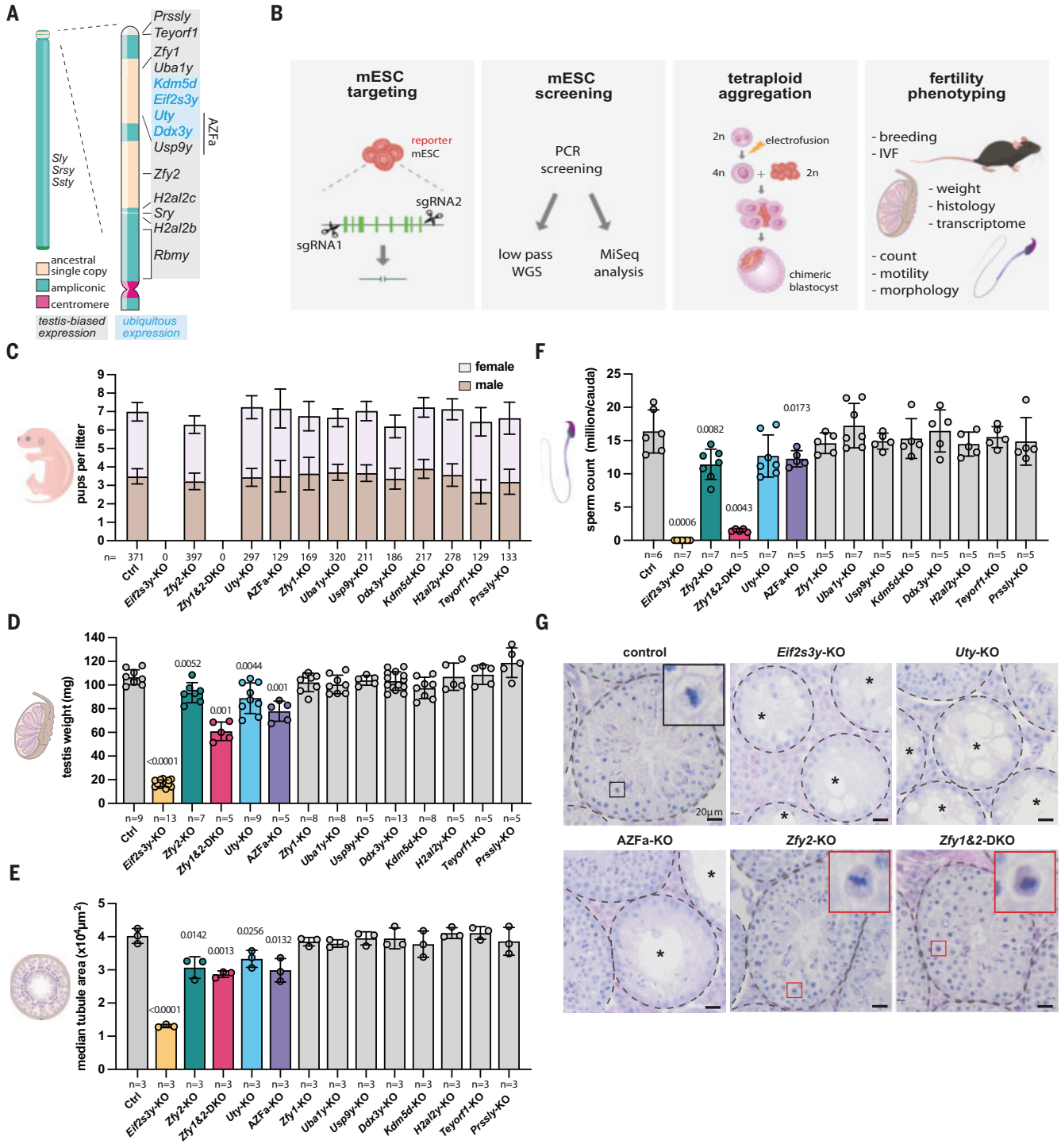

Fig. 1. Generation and screening of 13 Y-deletant mouse models for abnormal gamete production. (**A**) Structure and gene content of the mouse Y chromosome. (**B**) Experimental strategy to generate and study Y-gene deletant mouse models. IVF, in vitro fertilization; PCR, polymerase chain reaction; WGS, whole genome sequencing. (**C**) Mean numbers of male and female pups born per litter from control and Y-deletant matings. *n* = total number of pups born. Error bars represent 95% confidence interval. (**D**) Mean testis weight in controls and Y-deletants. *n* = number of males. Error bars represent standard deviation. (**E**) Median seminiferous tubule area in control and Y-deletants. *n* = number of biological replicate males. At least 40 tubules were counted per replicate. Error bars represent standard deviation. (**F**) Mean sperm count in controls and Y-deletants. Sperm was collected from the cauda epididymis. *n* = number of males. Error bars represent standard deviation. (**G**) Periodic acid–Schiff (PAS)–stained testis sections of control, *Eif2s3y*-KO, *Uty*-KO, AZFa-KO, *Zfy2*-KO, and *Zfy1&2*-DKO. Tubules are circled by dotted lines. Asterisks indicate tubules with severe germ cell depletion. Black inset: control metaphase; red insets: dark cytoplasmic signal is visible, indicative of apoptosis. Scale bars, 20 µm. Statistical analysis by two-sided chi-square test for (C), Mann Whitney test for (D) and (F), and two tailed *t* test for (E). Significant *P* values (<0.05) are shown.

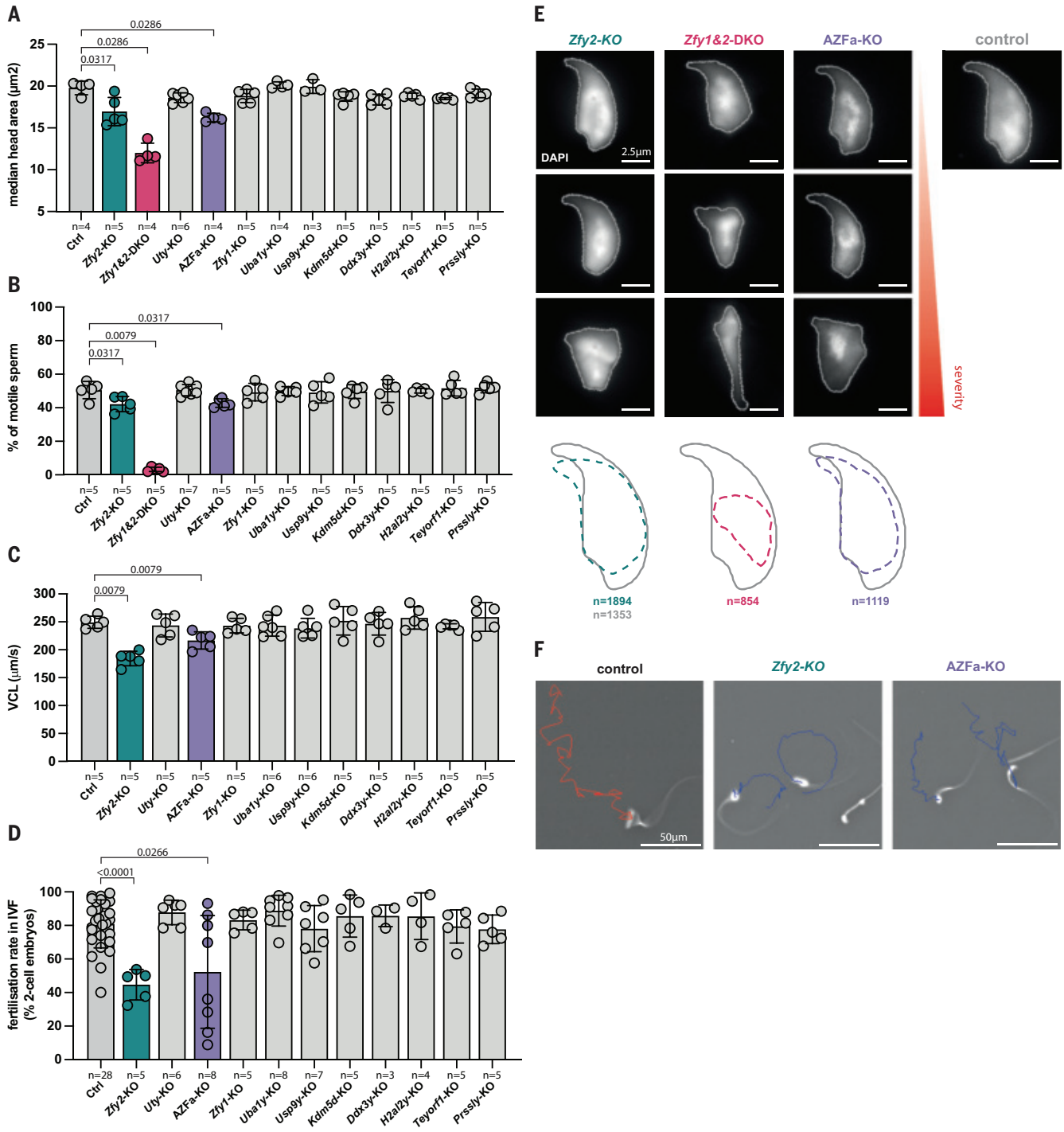

Fig. 2. Screening for reduced gamete quality in 13 Y-deletant mouse models. (**A**) Median sperm head area for control and Y-deletants. *n* = number of males. Error bars represent standard deviation. On average, 260 sperm were analyzed per male. (**B**) Mean percentage of motile sperm in the cauda epididymis of controls and Y-deletants. *n* = number of males. Error bars represent standard error of the mean. (**C**) Mean sperm curvilinear velocity (VCL) in controls and Y-deletant. *n* = number of males. Error bars represent standard error of the mean. (**D**) Mean fertilization rate of sperm from control and Y-deletant males in IVF assays. *n* = number of males. Error bars represent standard deviation. Statistical analysis by Mann Whitney test, with significant *P* values (<0.05) shown. (**E**) DAPI-stained sperm heads from *Zfy2*-KO, *Zfy1&2*-DKO, and AZFa-KO showing a range of abnormalities, from least (top) to most severe (bottom), compared to a control sperm head with stereotypical shape. Scale bars, 2.5 µm. The average sperm profile of the three deletants is compared to that of the control. *n* = number of sperm heads used to build the average outline. (**F**) Sperm from control, *Zfy2*-KO, and AZFa-KO tracked over 1 s using computer-assisted sperm analysis (CASA). Red trajectory represents a rapid progressive sperm and blue trajectories slow, nonprogressive sperm. Scale bars, 50 µm.

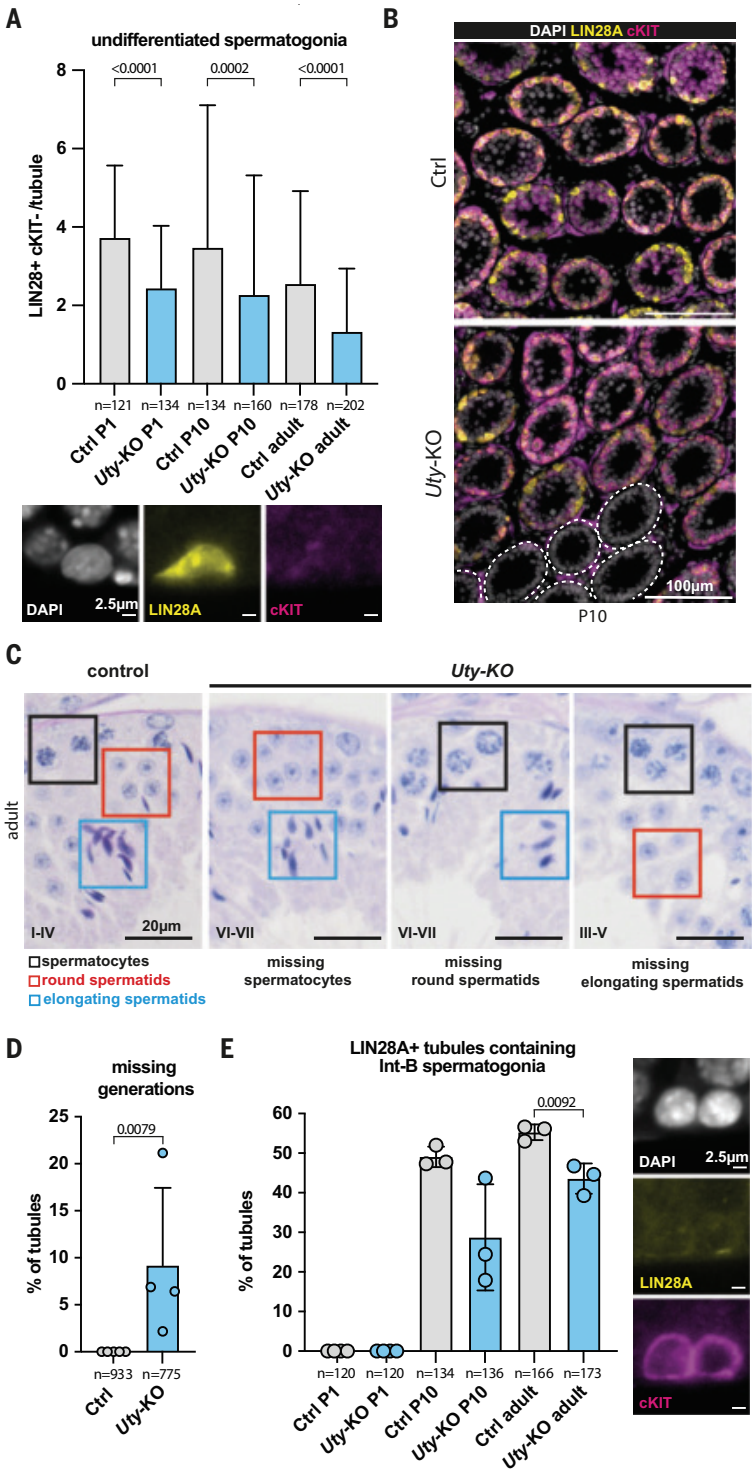

Fig. 3. Defects in the establishment and differentiation of the spermatogonial pool in *Uty*-deleted mice.
(**A**) Number of undifferentiated spermatogonia per tubule in control and *Uty*-KO P1, P10, and adults, quantified in testis immunostaining for LIN28A and cKIT. *n* = number of tubules counted across three biological replicates. *P* values calculated by Mann Whitney test. Scale bars, 2.5 µm. (**B**) P10 testis sections immunostained for LIN28A. Dashed lines encircle tubules with no germ cells. Scale bars, 100 µm. (**C**) Adult PAS-stained testis sections, with *Uty*-KO exhibiting different missing generations compared to control. Epithelial stages are shown in roman numerals. Spermatocytes, and round and elongated spermatids, are expected at all these stages. Scale bars, 20 µm. (**D**) Percentage of tubules exhibiting stage-specific missing generations. *n* = number of tubules counted across four biological replicates. (**E**) Quantification of percentage of tubules with differentiating In-B spermatogonia using P1, P10, and adult testis sections immunostained with LIN28A and cKIT. Scale bars, 2.5 µm. Tubules lacking progenitor cells (with no LIN28A+ cells) were excluded. *n* = number of tubules counted across three biological replicates. All error bars represent standard deviation. Statistical analysis by Mann Whitney test for (A) and (D) and two-tailed *t* test for (E). Significant *P* values (<0.05) are shown.

were infertile, with severe spermatogenic defects (*17*, *33*) (Fig. 1, C to G). The remaining 11 Y-deletant lines all produced offspring (Fig. 1C). Thus, 3 of the 11 deleted Y-gene families are necessary but not sufficient for mice to father offspring (*13*–*15*, *19*): *Sry* (necessary for testis determination), *Eif2s3y* (necessary for spermatogonial proliferation), and *Zfy* (at least one copy needed to produce functional sperm).

Ability to reproduce does not necessarily mean that spermatogenesis is normal. We therefore developed a phenotyping pipeline to exhaustively characterize the reproductive fitness of individual Y deletants. We assayed litter sizes, offspring sex ratios, testis weights and histology, sperm counts, sperm head morphology, sperm motility, and in vitro fertilization (IVF) success rates. Notably, all these parameters remained unaffected for deletion of *Zfy1*, *Uba1y*, *Usp9y*, *Ddx3y*, *Kdm5d*, *H2al2y*, *Teyorf1*, and *Prssly*, showing that these genes are dispensable for mouse spermatogenesis when deleted individually (Figs. 1, C to F, Fig. 2, A to D, and fig. S2, A to I). Litter sizes remained stable as the Y deletants were progressively backcrossed to C57BL/6J, suggesting that strain background did not overtly influence fertility (fig. S3, A to I).

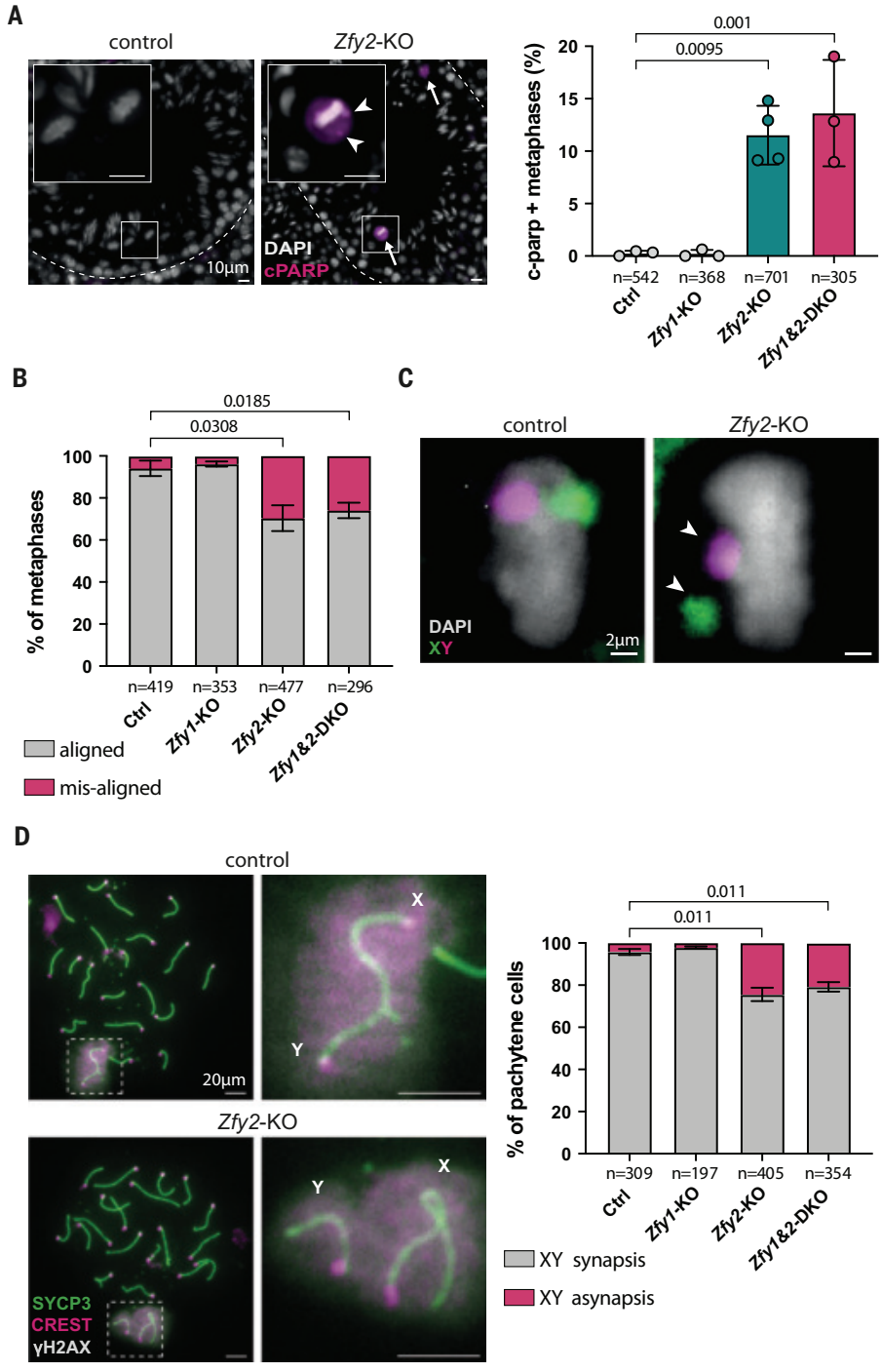

Fig. 4. Defects in meiotic sex chromosome pairing in the absence of *Zfy2*. (**A**) cPARP immunostaining in testis sections to quantify metaphase apoptosis in control and *Zfy* deletants. Arrows indicate apoptotic metaphase cells. Arrowheads point to misaligned chromosomes. Insets show example metaphase cells. Scale bars, 10 μm. *n* = number of metaphases counted across three to four biological replicates. Error bars represent standard deviation. DAPI, 4′,6-diamidino-2-phenylindole; cPARP, cleaved poly(ADP-ribose) polymerase. (**B**) Percentage of metaphase cells with aligned and misaligned chromosomes in control and *Zfy* deletants. *n* = number of metaphases counted across three biological replicates. Error bars represent standard error of the mean. (**C**) Representative aligned and misaligned metaphase plates in testis sections painted with X (green) and Y (magenta) whole-chromosome paints. Arrowheads point to misaligned chromosomes. Scale bars, 2 μm. (**D**) Pachytene spermatocytes immunostained for SYCP3 (green), CREST (magenta), and γH2AX (gray) to quantify X-Y asynapsis in control and *Zfy* deletants. Insets show sex chromosomes, with synapsed and asynapsed X-Y in control and *Zfy2*-KO, respectively. Scale bars, fs20 μm. *n* = number of pachytene cells counted across three biological replicates. Error bars represent standard error of the mean. Statistical analysis by unpaired two-tailed *t* test, with significant *P* values (<0.05) shown.

By contrast, *Eif2s3y*-KO, *Uty*-KO, AZFa-KO, *Zfy2*-KO, and *Zfy1&2*-DKO males all exhibited defective germ cell production, manifested as reduced testis weight, seminiferous tubule area, and sperm counts (Fig. 1, D to F). We found Y genes to be involved in all the major steps of spermatogenesis: mitosis, meiosis, and spermiogenesis. *Eif2s3y*-KO males showed severe germ cell depletion, consistent with the role of this gene in spermatogonial proliferation (*14*) (Fig. 1G). *Uty*-KO and AZFa-KO males also exhibited germ cell–depleted tubules, revealing a role for *Uty* in spermatogonia (Figs. 1G and 3, A to E, and fig. S4A; see also "*Uty* regulates spermatogonial pool establishment and differentiation").

Zfy2-KO and *Zfy1&2*-DKO males exhibited phenotypes at two stages of spermatogenesis. The first occurred during meiosis, with some metaphase cells undergoing apoptosis (Fig. 1G; see also "*Zfy2* regulates X-Y chromosome pairing at meiosis"). The second occurred during spermiogenesis, with abnormal sperm morphology and motility affecting fertilization (Fig. 2, A to F, and figs. S2, B to I, and S4, B to D). These defects were more severe in the *Zfy1&2*-DKO males, illustrating partially redundant roles of *Zfy1* and *Zfy2* in developing sperm (Figs. 1C and 2 and fig. S4, B to D).

Notably, AZFa KO males also exhibited abnormal sperm morphology and motility, ultimately causing decreased IVF success (Fig. 2, A to F). Sperm defects were not observed in *Uty*, *Usp9y,* or *Ddx3y* single mutants (fig. S2, A to I), indicating that multi–Y gene deletions can create phenotypes that are not observed in single-gene deletants and unmask potential synergistic roles of Y genes. We conclude that genes exhibiting no observable effects when deleted individually may still affect spermatogenesis. Furthermore, the observation that, unlike men, AZFa-KO mice can produce sperm provides experimental evidence that the mouse and human Y chromosomes are divergent in their spermatogenic functions.

Uty regulates spermatogonial pool establishment and differentiation

Adult *Uty*-KO males exhibited some tubules with few or no germ cells, suggesting a defect at the spermatogonial stage (Fig. 1G). This phenotype could arise through failure to establish, differentiate, or renew the spermatogonial stem cell (SSC) pool. There was no difference in testis weights, seminiferous tubule area, or sperm counts between adult (13 to 15 weeks) and aged (43 weeks) *Uty*-KO males, suggesting that SSC self-renewal was unaffected (fig. S5, A to C). We therefore focused on SSC establishment and spermatogonial differentiation. To examine SSC establishment, testis sections were costained for LIN28A (a marker of undifferentiated and A1-A4 spermatogonia) and cKIT (a marker of differentiating A1 to B spermatogonia)

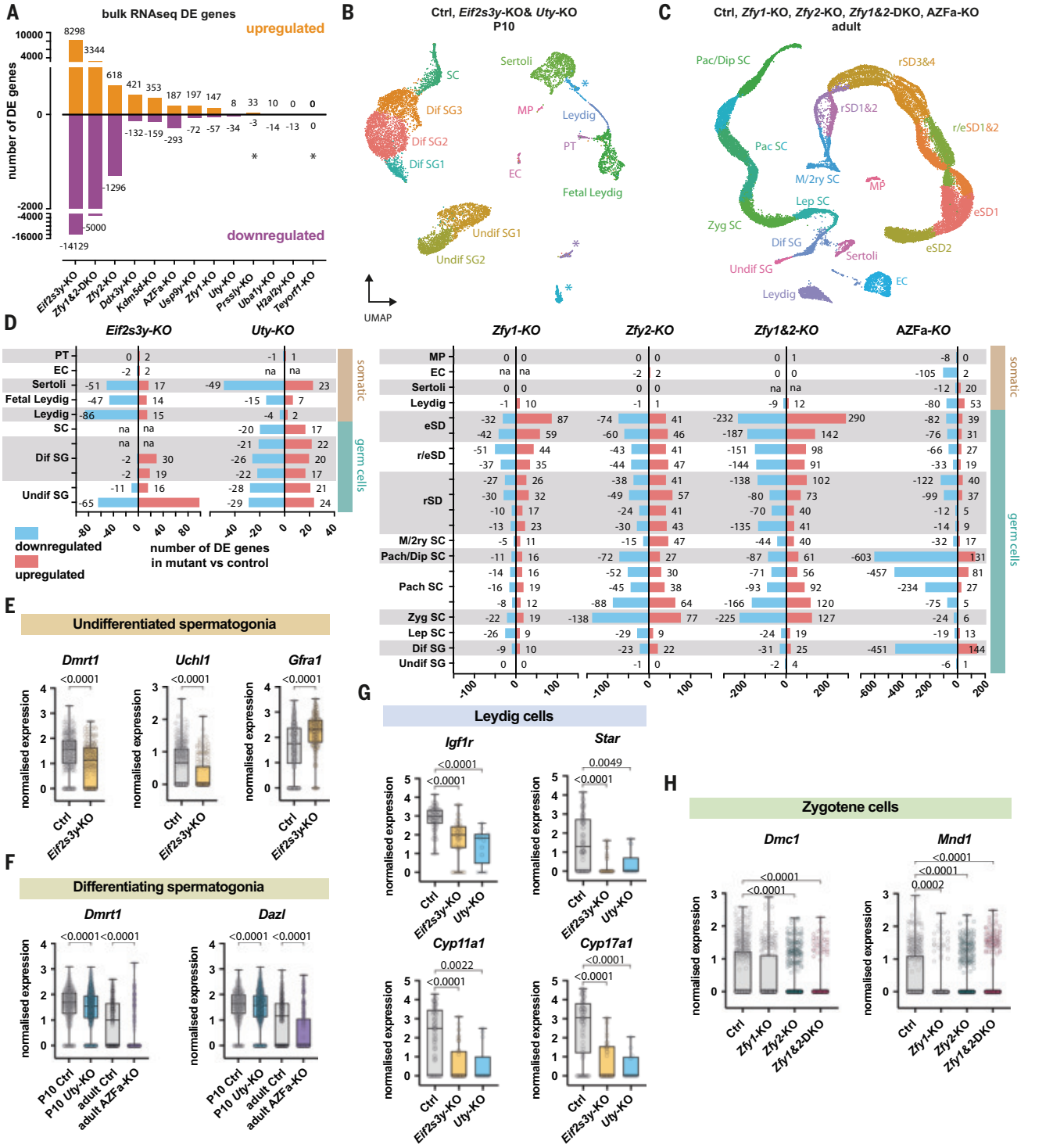

Fig. 5. Transcriptional deregulation in Y-deletant testes. (**A**) Quantification of differentially expressed (DE) genes in bulk RNAseq of Y-KO testes compared to controls. A threshold of log2 fold change ≥0.5 was used. Asterisks indicate Y genes not annotated in the mouse genome assembly, which thus will not appear as down-regulated. (**B** and **C**) Uniform manifold approximation and projection (UMAP) visualization of testis single-nuclei RNA sequencing (snRNA-seq) datasets. (B) Integrated P10 UMAP from control, *Eif2s3y*, and *Uty* KO samples (see fig. S8E for individual UMAPs). (C) Integrated adult samples from control, *Zfy1*, *Zfy2*, Zfy1&2, and AZFa KOs (see fig. S8F for individual UMAPs). Undifferentiated and differentiating (Undif and Dif) spermatogonia (SG); leptotene (Lep); zygotene (Zyg); pachytene (Pach); diplotene (Dip); metaphase (MM) and secondary (2ry) spermatocytes (SC); round and elongating spermatids (rSD and eSD); fetal Leydig; adult Leydig; Sertoli; peritubular (PT); endothelial (EC); and macrophage (MP) cells are shown. Asterisks show unknown clusters with no clear signatures. (**D**) Quantification of DE genes for each cell type in P10 *Eif2s3y* and *Uty* KOs and adult *Zfy1*, *Zfy2*, *Zfy1&2*, and AZFa KOs. Cell types with fewer than 10 nuclei in the mutants are marked as na. (**E**) Expression of the differentiation markers *Dmrt1*, *Uchl1*, and the progenitor marker *Gfra1* in *Eif2s3y*-KO and control Undif SG1. (**F**) Expression of the

differentiation markers *Dmrt1* and *Dazl* in *Uty*-KO, AZFa-KO, and control Dif SG. (**G**) Expression of members of the steroid synthesis pathway in *Eif2s3y*-KO, *Uty*-KO, and control Leydig cells. (**H**) Expression of the recombinases *Dmc1* and *Mnd1* in *Zfy1*, *Zfy2*, *Zfy1&2* KOs, and control zygotene cells. Statistical analysis by Kolmogorov Smirnov test, with significant *P* values (<0.05) shown. For box plots, center line is the median; box limits, 25th and 75th percentile; whiskers, minimum to maximum; points, outliers.

at postnatal day 1 (P1), P10, and adult (13 to 15 weeks old) (*34*, *35*) (fig. S5D). The number of undifferentiated spermatogonia (LIN28A+; cKIT−) was reduced in *Uty*-KO males at all ages (Fig. 3A). Accordingly, the number of differentiating A1-A4 and In-B spermatogonia (cKIT+; LIN28A−) was also lower (fig. S5, E and F). In some tubules, this phenotype was particularly severe and manifested as a complete absence of spermatogonial cells (Fig. 3B and fig. S5G). The finding that spermatogonia numbers were reduced as early as P1 demonstrates that *Uty* is required for the proper establishment of the spermatogonial pool.

To examine whether differentiation was also compromised, we examined testis histology and the proportion of undifferentiated versus differentiated spermatogonia in *Uty*-KO males. Of note, some tubules lacked entire generations of germ cells during stages of the seminiferous epithelium cycle where their presence would typically be expected. Because this defect was not cell-type specific and affected spermatocytes, round, and elongating spermatids at different stages of the seminiferous cycle, it was most likely caused by an early differentiation failure in spermatogonia (Fig. 3, C and D). Supporting this hypothesis, we observed a reduction in the proportion of tubules containing late-stage differentiating spermatogonia (cKIT+; LIN28A−) and in the ratios of In-B to A1-A4 spermatogonia (Fig. 3E and fig. S5H). We conclude that *Uty* has two functions in early spermatogenesis, first regulating spermatogonial stem cell establishment, and later spermatogonial differentiation.

Zfy2 regulates X-Y chromosome pairing at meiosis

In *Zfy2*-KO and *Zfy1&2*-DKO males, we observed apoptosis in meiotic metaphases (Fig. 1G), which we quantified by cPARP immunostaining (Fig. 4A). Metaphase apoptosis is commonly caused by misaligned chromosomes, which trigger the spindle assembly checkpoint (SAC) (*36*). Indeed, misaligned chromosomes were clearly apparent in DAPI-stained *Zfy2*-KO and *Zfy1&2*-DKO metaphase cells (Fig. 4, A to C). Because sex chromosomes are more prone to misalignment than autosomes (*36*), we used X- and Y-chromosome painting to determine whether they were misaligned. In 99.51% of cases, the misaligned chromosome was the X or the Y, confirming a sex chromosome–specific effect (Fig. 4C). Despite this X-Y misalignment, there was no increase in sex chromosome aneuploid spermatids in *Zfy2*-deficient males (fig. S6A). This finding indicated that, contrary to a previous report using transgenesis in a mouse model lacking a Y chromosome (*20*), the SAC functions efficiently without *Zfy2*.

We suspected that the misalignment phenotype at metaphase resulted from a failure to establish synapsis and recombination between the X and Y chromosomes earlier, at pachynema. To test this hypothesis, we quantified synapsis using antibodies to the axial elements (SYCP3), centromeres (CREST), and the X-Y pair (γH2AX) (Fig. 4D). *Zfy2*-KO and *Zfy1&2*-DKO males exhibited a higher frequency of X-Y asynapsis than controls, whereas autosomal synapsis was unaffected (Fig. 4D and fig. S6B). The incidence of X-Y asynapsis was similar between *Zfy2*-KO and *Zfy1&2*-DKO males, and *Zfy1*-KOs were unaffected, indicating a specific role for *Zfy2* and not *Zfy1* in promoting X-Y pairing. Asynapsed X-Y pairs failed to form crossovers, as demonstrated by MLH3 staining (fig. S6C). ZFY2 thus promotes X-Y synapsis and reciprocal recombination.

The impact of Y genes on the testis transcriptome

To interrogate how Y genes affect the testis transcriptome, we performed bulk RNA sequencing (RNAseq) on adult testes from our 13 mutants. Consistent with their more pronounced spermatogenic defects, *Eif2s3y*-KO, *Zfy1&2*-DKO, and *Zfy2*-KOs showed the greatest separation from other samples on a principal component analysis (PCA; fig. S7, A and B) and exhibited the highest number of differentially expressed (DE) genes compared with controls (Fig. 5A). Gene set enrichment analysis (GSEA) revealed that gene ontology terms related to spermatogenesis were deregulated in these mutants (fig. S7 C and, D, and tables S1 and S2). In mutants with no phenotypes, we observed an unexpectedly wide range of effects on gene expression. Although some mutants exhibited few or no DE genes (such as *Teyorf1*-KO), others exhibited hundreds of DE genes (such as *Ddx3y*-KO and *Kdm5d*-KO) (Fig. 5A and tables S1 and S2). In the case of *Ddx3y*-KO, other genes associated with RNA helicase activity were also down-regulated (fig. S7E). We conclude that Y genes for which deletion creates no apparent spermatogenic phenotype can still regulate multiple downstream targets in the testis. Because most Y genes have X-linked homologs, and *Zfy* and *Ddx3y* also have autosomal homologs, we assessed their expression in mutants lacking a phenotype. We found that these homologs were not up-regulated, suggesting they do not compensate for Y-gene loss at the transcriptional level (fig. S7, F to J).

To gain deeper molecular insights into each spermatogenic defect, we performed single-nuclei RNA sequencing on *Eif2s3y*-KO, *Uty*-KO, AZFa-KO, *Zfy1*-KO, *Zfy2*-KO, and *Zfy1&2*-DKO males. P10 testes from *Eif2s3y* and *Uty*-KOs were used to enrich for spermatogonia, because this was where the phenotypes manifested, and adult testes were used for *Zfy1*, *Zfy2*, *Zfy1&2*, and AZFa-KOs to capture all cell types (Fig. 5, B and C). Using published marker genes (*37*, *38*), we identified all the expected somatic testis and germ cell populations (Fig. 5, B and C, and fig. S8, A to F).

By quantifying DE genes across clusters, we identified transcriptomic deregulation in unexpected cell types (Fig. 5D and tables S3 to S8). In *Eif2s3y*-KO, the earliest undifferentiated spermatogonial cluster had the most DE genes (Fig. 5D). The transcriptional deregulation therefore begins much earlier than the known proliferation defect, which manifests in differentiating spermatogonia (*14*, *33*, *39*). Moreover, *Eif2s3y*-KOs, *Uty*-KOs, and AZFa-KOs had extensive deregulation in Leydig and Sertoli cells, revealing an unexpected impact on the somatic testis transcriptome (Fig. 5D). Notably, despite *Zfy2* being predominantly expressed in spermatids (*18*), the highest number of DE genes in the *Zfy2*-KO was found at zygonema (Fig. 5D). In AZFa-KOs, the number of DE genes increased throughout pachynema, even though no visible defects were observed at this stage (Fig. 5D). In AZFa-KO, we also observed changes in the expression levels of the corresponding X-linked and autosomal homologs in some cell types, which could compensate for the loss of the three Y-chromosome genes (fig. S9, A to J).

Using GSEA, we identified multiple pathways affected by Y-gene loss that may contribute to the spermatogonial defects in *Eif2s3y*, *Uty*, and AZFa deletants; the meiotic defects in *Zfy2* and *Zfy1&2* mutants; and the spermatid defects in *Zfy2*, *Zfy1&2*, and AZFa mutants (tables S9 to S14). To find candidate genes contributing to each phenotype, we also examined DE genes along with the expression of known spermatogenic regulators. In *Eif2s3y*-KOs, genes involved in spermatogonial differentiation, including *Dmrt1*, *Uchl1*, and *Stra8*, were down-regulated, whereas markers of the undifferentiated state, including *Gfra1* and *Etv5*, were up-regulated (Fig. 5E

and fig. S10, A and B). *Eif2s3y* could therefore act to suppress the program that maintains an undifferentiated state (*40*), or it could promote activation of the differentiation program. In *Uty*-KOs, known regulators of spermatogonial development were down-regulated, including *Dmrt1* and *Dazl* (Fig. 5F). Notably, the steroidogenesis pathway, including genes such as *Igf1r*, *Star*, *Cyp11a1*, and *Cyp17a1*, was down-regulated in Leydig cells of *Eif2s3y*, *Uty*, and AZFa deletants (Fig. 5G and fig. S10, C to E). Because production of steroid hormones such as testosterone is crucial for germ cell homeostasis (*41*), it is possible that the observed germ cell defects are, at least partially, caused by dysfunctional somatic cells, which could be investigated in future endocrine studies (*41*).

We also found that multiple factors regulating meiotic synapsis and recombination, including *Dmc1*, *Mnd1*, and *Rad51ap2*, were down-regulated in *Zfy2*-deficient testes, implicating these factors in the X-Y pairing phenotype (Fig. 5H and fig. S10F). Comparing DE genes in all our *Zfy* deletants allowed us to identify putative stage-specific shared and specific targets of ZFY1 and ZFY2 transcription factors (fig. S10, G and H, and table S15). *Zfy1&2*-DKOs shared a higher number of DE genes with *Zfy2* than with *Zfy1* mutants, further indicating that *Zfy2* is the main contributor to the *Zfy1&2*-DKO phenotypes. Unexpectedly, however, most DE genes in the *Zfy1&2*-DKOs were not shared with either *Zfy1* or *Zfy2* mutants. This indicated that the effects of deleting both *Zfy* genes are not merely additive, but also combinatorial.

Discussion

Here, we generated a deletion series of the nonampliconic Y genes and used an exhaustive reproductive phenotyping pipeline to provide a comprehensive overview of Y-gene functions in spermatogenesis. We also generated a transcriptomic atlas of Y-mutant testes, revealing how Y genes regulate testis gene expression and providing a resource to the research community. We demonstrated that more Y genes are required for normal murine spermatogenesis than previously known, and they function in more spermatogenic processes than previously thought.

As shown by others (*1*, *2*, *42*), our comparative analyses across species and within the human population revealed that all the broadly conserved Y-chromosome genes that we studied are subject to purifying selection, regardless of whether their deletion causes spermatogenic defects (fig. S11, A and B). Whereas some Y genes are paramount for normal spermatogenesis, others have more subtle effects, which are revealed when deleted in combinations. This provides insights into human infertility. Most known cases of human Y chromosome–related infertility are caused by either AZFa, AZFb, or AZFc deletions (*28*). Because these deletions remove multiple Y genes, identifying which is causative remains a challenge in clinical genetics (*43*). Our work raises the possibility that the etiology of some infertility cases may result from the cumulative loss of several Y genes, each of which has only a minimal impact on spermatogenesis. Moreover, Y mutations may sensitize individuals to environmental insults and autosomal mutations. Subtle Y-gene functions may be shared with their X or autosomal homologs, and the presence of these homologs may be sufficient to prevent severe defects in some Y deletants. Variation in the extent to which homologs can compensate for Y mutations could explain the difference in phenotypes between mice and humans, as seen when AZFa is deleted.

Some Y genes are also expressed outside of the testis (Fig. 1A), and potential roles in nonreproductive organs may contribute to their evolutionary survival. A rapidly increasing volume of research supports this notion, linking Y chromosome loss to aging and a wide range of conditions including cancer and heart disease (*44*–*49*). Our Y-deletant mouse models present a valuable resource with which to unravel these phenotypes at the single-gene level.

REFERENCES AND NOTES

1. D. W. Bellott *et al*., *Nature* **508**, 494–499 (2014).
2. D. Cortez *et al*., *Nature* **508**, 488–493 (2014).
3. J. A. M. Graves, *Cell* **124**, 901–914 (2006).
4. Y. Q. S. Soh *et al*., *Cell* **159**, 800–813 (2014).
5. J. Subrini, J. Turner, *eLife* **10**, 1–20 (2021).
6. J. M. Riel *et al*., *J. Cell Sci.* **126**, 803–813 (2013).
7. J. Cocquet *et al*., *PLOS Biol.* **7**, e1000244 (2009).
8. C. C. Rathje *et al*., *Curr. Biol.* **29**, 3692–3698.e4 (2019).
9. A. Comptour *et al*., *FEBS J.* **281**, 1571–1584 (2014).
10. M. Szot *et al*., *Cytogenet. Genome Res.* **103**, 330–336 (2003).
11. J. Cocquet *et al*., *PLOS Genet.* **8**, e1002900 (2012).
12. J. F. Hughes *et al*., *BMC Biol.* **20**, 133 (2022).
13. P. Koopman, J. Gubbay, N. Vivian, P. Goodfellow, R. Lovell-Badge, *Nature* **351**, 117–121 (1991).
14. S. Mazeyrat *et al*., *Nat. Genet.* **29**, 49–53 (2001).
15. Y. Yamauchi, J. M. Riel, Z. Stoytcheva, M. A. Ward, *Science* **343**, 69–72 (2014).
16. T. Nakasuji *et al*., *PLOS Genet.* **13**, e1006578 (2017).
17. Y. Yamauchi *et al*., *Biol. Reprod.* **106**, 1312–1326 (2022).
18. N. Vernet *et al*., *PLOS ONE* **11**, e0145398 (2016).
19. Y. Yamauchi, J. M. Riel, V. Ruthig, M. A. Ward, *PLOS Genet.* **11**, e1005476 (2015).
20. N. Vernet *et al*., *Curr. Biol.* **21**, 787–793 (2011).
21. N. Vernet *et al*., *PLOS Genet.* **10**, e1004444 (2014).
22. N. Vernet, S. K. Mahadevaiah, D. G. de Rooij, P. S. Burgoyne, P. J. I. Ellis, *Hum. Mol. Genet.* **25**, 5300–5310 (2016).
23. T. Matsumura, T. Endo, A. Isotani, M. Ogawa, M. Ikawa, *J. Reprod. Dev.* **65**, 121–128 (2019).
24. K. B. Shpargel, T. Sengoku, S. Yokoyama, T. Magnuson, *PLOS Genet.* **8**, e1002964 (2012).
25. M. Kosugi *et al*., *Biochem. Biophys. Res. Commun.* **525**, 100–106 (2020).
26. E. Zuo *et al*., *Cell Res.* **27**, 933–945 (2017).
27. H. Holmlund, Y. Yamauchi, G. Durango, W. Fujii, M. A. Ward, *Biol. Reprod.* **107**, 752–764 (2022).
28. S. Colaco, D. Modi, *Reprod. Biol. Endocrinol.* **16**, 14 (2018).
29. S. M. Kirchain, A. M. Hayward, J. M. Mkandawire, P. Qi, A. A. Burds, *Comp. Med.* **58**, 145–150 (2008).
30. K. Eggan *et al*., *Proc. Natl. Acad. Sci. U.S.A.* **98**, 6209–6214 (2001).
31. H. Ohta, Y. Sakaide, K. Yamagata, T. Wakayama, *Biol. Reprod.* **79**, 486–492 (2008).
32. G. S. Eakin, A. K. Hadjantonakis, *Nat. Protoc.* **1**, 1145–1153 (2006).
33. Y. Matsubara *et al*., *Stem Cells Dev.* **24**, 1164–1170 (2015).
34. P. Chakraborty *et al*., *Stem Cells* **32**, 860–873 (2014).
35. B. A. Niedenberger, J. T. Busada, C. B. Geyer, *Reproduction* **149**, 329–338 (2015).
36. S. Lane, L. Kauppi, *Cell. Mol. Life Sci.* **76**, 1135–1150 (2019).
37. F. Murat *et al*., *Nature* **613**, 308–316 (2023).
38. C. Ernst, N. Eling, C. P. Martinez-Jimenez, J. C. Marioni, D. T. Odom, *Nat. Commun.* **10**, 1251 (2019).
39. M. J. Sutcliffe, P. S. Burgoyne, *Development* **107**, 373–380 (1989).
40. N. Li *et al*., *Oncotarget* **7**, 11321–11331 (2016).
41. K. de Mattos, K. J. Pierre, J. J. Tremblay, *Endocrines* **4**, 573–594 (2023).
42. P. Hallast *et al*., *Nature* **621**, 355–364 (2023).
43. A. K. Dicke *et al*., *Commun. Biol.* **6**, 350 (2023).
44. S. Sano *et al*., *Science* **377**, 292–297 (2022).
45. D. J. Thompson *et al*., *Nature* **575**, 652–657 (2019).
46. A. K. Godfrey *et al*., *Genome Res.* **30**, 860–873 (2020).
47. K. Horitani *et al*., *Nat. Cardiovasc. Res.* **3**, 343–355 (2024).
48. A. K. San Roman *et al*., *Cell Genom.* **4**, 100462 (2024).
49. Q. Zhang *et al*., *JCI Insight* **7**, e153768 (2022).

ACKNOWLEDGMENTS

The authors thank the Francis Crick Institute Genetic Modification Service (GeMS), Biological Research, Experimental Histopathology, Advanced Light Microscopy, and Advanced Sequencing facilities for their contributions and expertise. We thank the members of the J.M.A.T. lab for comments and discussion on the manuscript. We thank P. Cohen for the gift of the MLH3 antibody. We thank F. Zhang and A. Ventura for the gift of the px459v2 and px333 vectors, respectively. This article is dedicated to the memory of Paul Burgoyne, who spent his career researching the mouse Y chromosome.
Funding: This work was supported by the Francis Crick Institute, which receives its core funding from Cancer Research UK (CC2052), the UK Medical Research Council (CC2052), and the Wellcome Trust (CC2052). **Author contributions:** J.M.A.T. and J.S. conceived the project. J.S., I.B.B. and M.B. generated the Y-deletant mESCs. J.S. performed testis weight, sperm count, sperm head, and sperm motility analyses. J.S. extracted bulk RNA and single nuclei for RNA sequencing. J.S. and D.G.d.R. analyzed testis histology. J.S., I.B.B., and G.S. performed and analyzed immunostaining. I.B.B. performed XY chromosome painting. O.O. maintained the mouse colonies. W.V. performed analysis of bulk and snRNAseq datasets. V.M. derived the initial mESC line and advised on immunostaining and nuclei extraction. B.G. advised on snRNAseq analysis. K.Cr. and K.Co. oversaw the tetraploid aggregations. J.S. and J.M.A.T. wrote the manuscript.
Competing interests: The authors declare that they have no competing interests. **Data and materials availability:** Bulk RNAseq and single nuclei RNAseq data have been deposited at GEO (accession no. GSE274100 and GSE274095, respectively).

SUPPLEMENTARY MATERIALS

science.org/doi/10.1126/science.ads6495
Materials and Methods
Figs. S1 to S11
Tables S1 to S19
References (*50*–*61*)
MDAR Reproducibility Checklist

Submitted 22 August 2024; accepted 21 November 2024
10.1126/science.ads6495

METALLURGY

Ductilization of 2.6-GPa alloys via short-range ordered interfaces and supranano precipitates

Yong-Qiang Yan[1]†, Wen-Hao Cha[2,3]†, Sida Liu[2]*, Yan Ma[4], Jun-Hua Luan[5], Ziyuan Rao[6,7], Chang Liu[1]*, Zhi-Wei Shan[1], Jian Lu[8]*, Ge Wu[1]*

Higher strength and higher ductility are desirable for structural materials. However, ultrastrong alloys inevitably show decreased strain-hardening capacity, limiting their uniform elongation. We present a supranano (<10 nanometers) and short-range ordering design for grain interiors and grain boundary regions, respectively, in fine-grained alloys based on vanadium, cobalt, and nickel, with additions of tungsten, copper, aluminum, and boron. The pronounced grain boundary–related strengthening and ductilization mechanism is realized through segregation of the short-range ordering near the grain boundary. Furthermore, the supranano ordering with a larger size has an enhanced pinning effect for dislocations and stacking faults, multiplied and accumulated in grain interiors during plastic deformation. These mechanisms promote continuously increased flow stress until fracture of the alloy at 10% strain with 2.6-gigapascal tensile stress.

Grain refinement is a practical approach to simultaneously enhance strength and ductility for coarse- and fine-grained alloys (*1*) that has been widely applied in industry. The yield strength of fine-grained alloys is usually <1 GPa (*2*, *3*). Although the extreme refinement of grains to nanoscale can substantially enhance the strength, ductility decreases as a result. A gradient structure, with nano-sized grains on the surface to coarse grain in the sample interior (*4*), and heterostructures (with different grain sizes) (*5*) are successful alloy design strategies to simultaneously increase strength and ductility. The strength is enhanced because of grain boundary (GB) strengthening from the nanograin region. During plastic deformation, dislocation multiplication in the coarse grains and the generation of geometrically necessary dislocations near transition zones between the nanograin and coarse-grain regions (*5*) facilitate high strain-hardening rates, and thus, the ductility is enhanced. Nanostructuring for the grain interior is another important approach. Successful strategies include introductions of coherent nanoprecipitates (*6*–*9*), short-range ordering (SRO) (*10*–*12*), chemical heterogeneities (*13*, *14*), and nanotwins (*15*), among others. The atomic interactions among these nanostructures and dislocations promote multiplication of dislocations in the grain interior, also enhancing strain-hardening rates. The tensile strength of these alloys can be improved to 1 to ~2 GPa. To further strengthen alloys to an ultrahigh strength level (e.g., >2.5-GPa tensile strength), various strengthening mechanisms should be introduced. However, the resultant decreased strain-hardening rate usually induces unstable necking or formation of Lüders bands, for example. The localized deformation substantially shortens uniform elongation (e.g., <5% strain for 2.5-GPa alloys) (*16*–*18*). Different from the above alloy design strategies, which focus on distribution of variant grain sizes or nanostructuring of grain interiors, here we use SRO decorating GB regions (short-range ordered interfaces) of the face-centered cubic (FCC) phase in a fine-grained FCC-BCC (body-centered cubic) dual-phase alloy, facilitated by positive interfacial interaction energy between the SRO and the FCC matrix. The short-range ordered interface can be categorized as a GB complexion (*19*), substantially increasing the stress barrier against dislocation motion—i.e., a higher yield strength. Therefore, more dislocations pile up near GB regions than in grain interiors during plastic deformation. The activities of dislocations (gliding and pile-up) disrupt the ordered structure of the SRO, transformed into disordered solid solution—i.e., the order-to-disorder transition. This behavior weakens stress concentrations on GB regions and thus impedes cracking from GBs of the FCC phase. Furthermore, we introduce orderings (precipitates) of <10 nm (supranano) in the grain interior of the FCC phase. The supranano (*20*) is a metric unit of length that is <10 nm, which is much larger than the size of SROs (<1 nm). Therefore, the supranano orderings have a stronger pinning effect for dislocations and stacking faults (SFs). Such orderings make the motion of dislocations and SFs slow, which increases the possibility of their interaction and entanglement with other moveable dislocations. This behavior promotes multiplication and accumulation of these defects upon loading. The supranano orderings are uniformly distributed in the grain interior, and thus, the distribution of the generated defects is also uniform, which alleviates stress localization. These two kinds of orderings have mutually complementary strengthening and ductilization mechanisms near GB regions and in grain interiors of the FCC phase, respectively, facilitating a high strain-hardening rate and large elongation. The received ultrahigh flow stress transforms a portion of the BCC phase (7.7% fraction) to a FCC structure during deformation.

Results and discussion

Microstructure and composition

To realize ultrahigh yield strength, we refined the grain size and introduced a secondary harder phase by thermal treatments and rolling processes. The reduced grain size shortens the mean-free path of dislocations in the grain interior and enhances interactions of the dislocations with the short-range ordered GB regions in the FCC phase. We then performed thermal aging to trigger formation of the precipitate ordering, facilitating large uniform elongation. The received VCoNi-W-Cu-Al-B alloy has a dual phase structure (Fig. 1, A and B), composed of FCC and $L2_1$ (an ordered BCC phase) structures, with an average grain size of 1 μm for both phases (fig. S1). The FCC phase has an area fraction of 78.7%, dominating the main structure of the material. Further reduction in the fraction of the FCC phase might induce embrittlement of the alloy (*21*). The structure evolution of the alloy during thermal and mechanical treatments is shown in fig. S2. The compositions of the FCC and $L2_1$ phases are $Ni_{37}Co_{34}V_{27}Al_2$ atomic % (at %) and $Co_{31}V_{25}Ni_{25}Al_{18}Cu_{0.5}W_{0.5}$ at % (Fig. 1, C and D), respectively. Some tiny boride nanoparticles with an average diameter of 240 nm discontinuously embed between adjacent FCC-BCC phase boundaries (fig. S3). The $L2_1$ phase and boride nanoparticles may also contribute to the strengthening effect. The $L2_1$ phase reveals a typical superlattice feature in a selected-area electron diffraction (SAED) pattern (Fig. $1B_1$). The SAED pattern of the FCC phase depicts very weak diffraction spots of $L1_2$ structure among the matrix lattice (Fig. $1B_2$), which is different from that of other $L1_2$ nanoprecipitated alloys (*6*–*9*). We performed atom-resolved investigations from the <1 1 2> zone axis (Fig. 1F) using aberration-corrected scanning transmission electron microscopy (STEM). The

[1]Center for Advancing Materials Performance from the Nanoscale (CAMP-Nano), Hysitron Applied Research Center in China (HARCC) and Center for Alloy Innovation and Design (CAID), State Key Laboratory for Mechanical Behavior of Materials, Xi'an Jiaotong University, Xi'an, China. [2]Laboratory for Multiscale Mechanics and Medical Science, SV LAB, School of Aerospace, Xi'an Jiaotong University, Xi'an, China. [3]Faculty of Georesources and Materials Engineering, RWTH Aachen University, Aachen, Germany. [4]Department of Materials Science and Engineering, Delft University of Technology, Delft, Netherlands. [5]Inter-University 3D Atom Probe Tomography Unit, Department of Mechanical Engineering, City University of Hong Kong, Hong Kong, China. [6]Max Planck Institute for Sustainable Materials, Düsseldorf, Germany. [7]National Engineering Research Center of Light Alloy Net Forming, Shanghai Jiao Tong University, Shanghai, China. [8]Centre for Advanced Structural Materials, Department of Materials Science and Engineering, City University of Hong Kong, Hong Kong, China.
*Corresponding author. Email: gewuxjtu@xjtu.edu.cn (G.W.); chang.liu@xjtu.edu.cn (C.L.); sidaliu@xjtu.edu.cn (S.L.); jianlu@city.edu.hk (J.L.)
†These authors contributed equally to this work.

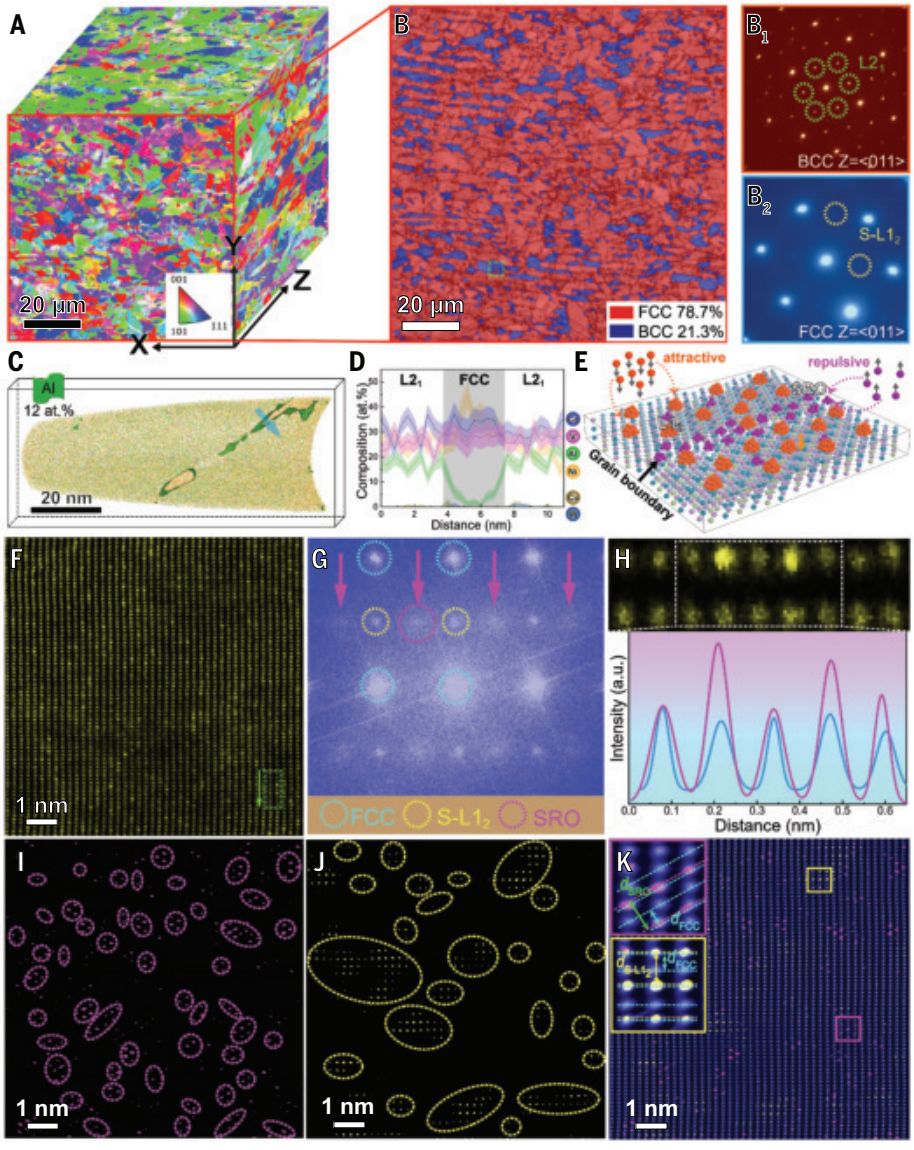

Fig. 1. Structure of the SS-alloy (containing both SRO and S-L1$_2$ particle in the FCC phase). (**A**) Reconstructed three-dimensional EBSD inverse pole figure probed from normal direction (*y*), rolling direction (*z*), and transverse direction (*x*). (**B**) Phase image of the square region in (A), showing the FCC-BCC dual-phase structure. Area fractions of FCC and BCC phases are 78.7 and 21.3%, respectively. (**B$_1$** and **B$_2$**) SAED patterns of the two phases, probed from BCC <0 1 1> and FCC <0 1 1> zone axes, respectively. (**C**) One-nanometer-thick side slice of the three-dimensional reconstruction of a typical atom probe tomography (APT) dataset, showing Al-enriched and Al-depleted regions highlighted by an isoconcentration surface in terms of an Al threshold value of 12 at %. The APT tip may be sampled from the area similar to the cyan dashed square region in (B), with FCC phase embedded in BCC phase. (**D**) One-dimensional compositional profile across the region indicated with the arrow in (C), showing the compositions of the FCC and BCC ($L2_1$) phases. The light shadows indicate statistical errors in terms of the standard deviations. (**E**) Schematic illustration from MD calculation, depicting the segregation and precipitation behaviors of SRO and $L1_2$ particle near GB region and in grain interior, respectively. (**F**) Aberration-corrected high-angle annular dark-field (HAADF) STEM image of the FCC phase, probed from <1 1 2> zone axis. (**G**) Fast Fourier transformation (FFT) image of (F), showing the main diffraction spots of the FCC matrix (cyan dashed circles), weak diffraction spots of the S-$L1_2$ particles (yellow dashed circles), and blurry diffraction disks of the SRO (pink arrows and dashed circles). (**H**) Enlarged HAADF-STEM image (upper panel) of the dashed green rectangle region in (F), showing the atoms of an ordered particle and the disordered matrix arranged with and without periodic Z-intensity, respectively (lower panel). a.u., arbitrary units. (**I** and **J**) IFT images of (F) generated by using the masks of SRO and S-$L1_2$ diffraction spots and disks in (G), respectively, highlighting the SRO and S-$L1_2$ regions in real space. (**K**) Combined IFT image, generated by using the masks of FCC, SRO, and S-$L1_2$ diffraction (*d*) spots and disks in (G), respectively, showing the configurations of the SRO and S-$L1_2$ particle in the FCC matrix. The insets are enlarged images of the solid square regions and reveal lattice structures of the SRO and S-$L1_2$ particle, coherent with the FCC matrix.

result shows a major disordered solid solution structure but with occasionally brighter atoms (Fig. 1, F and H) within the matrix lattice. A careful inverse Fourier transformation (IFT) analysis (Fig. 1, I and J) shows that the brighter atoms are not randomly distributed. Rather, they aggregate into two kinds of local orderings, SRO and supranano $L1_2$ (S-$L1_2$) particle. Because of their different crystalline structures, the S-$L1_2$ particles are mainly formed by nucleation in the FCC matrix instead of growth from the SRO during aging. In this study, the fractions of the S-$L1_2$ particle and SRO are 30 and 22%, respectively, in the FCC phase (fig. S4). The size of S-$L1_2$ particles and SRO are 0.5 to ~4 nm and <1 nm, respectively (Fig. 1, I and J). Therefore, the corresponding diffraction spots of the S-$L1_2$ particles are substantially weaker than those of previously reported $L1_2$ nanoprecipitated alloys (*6*–*9*), which usually have a much larger precipitation size of 10 to tens of nanometers. Furthermore, the diffraction feature of the S-$L1_2$ particles reveals weak spots (Fig. 1G, dashed yellow circles) compared with blurry disks for SRO (Fig. 1G, dashed pink circles) because of a much larger size of the S-$L1_2$ particles. The SROs with heterogeneous structures and compositions are generally believed to multiply dislocations during plastic deformation, improving ductility of the materials (*10*–*12*). In fine-grained alloys, the volume fraction of GB is large, so that the GB structure has a big influence on mechanical behavior. We performed careful composition investigation on GB regions of the FCC phase using electron probe microanalysis (EPMA), showing the absence of B (fig. S3). Therefore, the change of atomic packing structure near GB regions by segregation of B (*22*, *23*) can be ruled out. We then performed molecular dynamics (MD) simulation to study GB segregation tendency of the SRO and S-$L1_2$ particles in the FCC phase. The result shows that the interfacial interaction energy between the SRO and the FCC matrix lattice is positive, which indicates a repulsive interaction (Fig. 1E and fig. S5). This behavior facilitates segregation of the SRO toward GB regions of the FCC phase. By contrast, the interfacial interaction energy is negative for the case of S-$L1_2$ particles, promoting their precipitation in grain interiors (Fig. 1E and fig. S5).

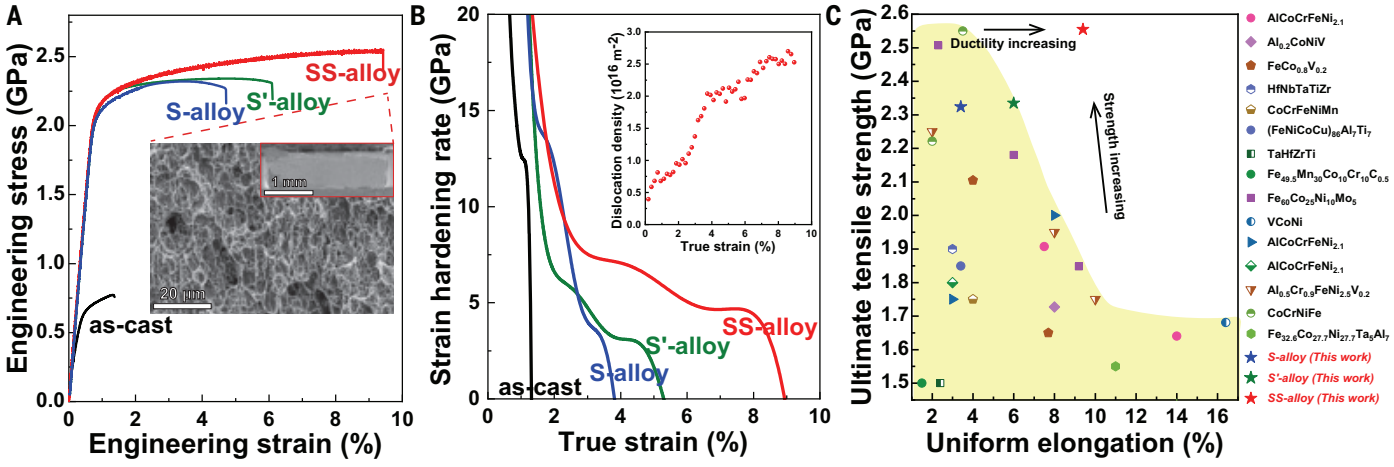

Fig. 2. Room-temperature tensile property of the SS-alloy. (**A**) Engineering tensile stress-strain curves of the SS-alloy, S'-alloy, S-alloy, and as-cast alloy. The insets are fracture surface of the SS-alloy sample after tensile testing, revealing dimple-type pattern. (**B**) Strain-hardening rate evolutions of the alloys during tensile straining. (Inset) Dislocation density evolution of the FCC phase in the SS-alloy during tensile straining. (**C**) UTS versus uniform elongation relation of the alloys in the current study, compared with that of other ultrastrong CCAs (*8*, *16*, *18*, *39*–*50*).

The experimental observations (Fig. 3G_1 and fig. S6) confirm this theoretical result.

Mechanical properties

We performed identical tensile tests on as-cast alloy, S-alloy (containing SRO in the FCC phase), S'-alloy, and SS-alloy (containing both SRO and S-$L1_2$ particle in the FCC phase) (Fig. 2A). The as-cast alloy has a yield strength of 0.7 GPa and total elongation of 1.3% strain. The yield strength and total elongation increase to 2.1 GPa and 4.7% strain, respectively, after additional rolling and thermal treatments for the S-alloy. The enhancement of mechanical property is mainly due to the refined dual-phase structure and embedded SRO in the FCC phase (fig. S7). The ultimate tensile strength (UTS) is 2.3 GPa at 2.6% strain, and strain softening occurs subsequently. After an additional 5 hours of aging at 500°C, the yield strength and total elongation increase to 2.2 GPa and 6.0% strain, respectively, for the S'-alloy. The UTS is still 2.3 GPa but with a much larger uniform elongation of 4.9% strain. With further aging time (20 hours' aging at 500°C), the received SS-alloy has a further increased uniform elongation of 9.5% strain and a yield strength of 2.2 GPa. We also conducted identical tensile tests on a much thicker SS-alloy, and its mechanical properties do not substantially change (fig. S8). The morphology of the fracture surface reveals a dimple-type pattern (Fig. 2A, inset), a ductile signature of the alloy. After yielding, strain hardening lasts until fracture of the alloy, inducing an ultrahigh UTS of 2.6 GPa (Fig. 2, A and B). The structure difference of the SS-alloy is the addition of S-$L1_2$ particles after thermal aging compared with the reference S-alloy, facilitating an increased yield strength and much higher strain-hardening rate (Fig. 2B). We calculated dislocation density of the FCC phase in the SS-alloy on the basis of in situ synchrotron x-ray diffraction during tensile tests. The result shows that dislocation density increases during deformation. The dislocation density of the FCC phase continuously increases to >1 × 10^{16} m^{-2} after 2.6% strain (Fig. 2B, inset), where that is the reference S-alloy's UTS point. Such a high density of dislocations is comparable to that of severely plastic deformed alloys (*24*), promoting a high strain-hardening rate and preventing strain softening as in the reference S-alloy. Dislocation motion can also be activated in the ordered BCC phase during plastic deformation, although this phase is generally known to be brittle (*25*, *26*). We show that the ultrahigh flow stress induces BCC-to-FCC phase transformation, and the confinement deformation activates dislocation motions in the BCC phase. We compared the mechanical properties of the SS-alloy with those of other ultrahigh-strength (UTS > 1.5 GPa) compositional complex alloys (CCAs) at room temperature (Fig. 2C and fig. S9). For a fair comparison, we do not include the data of dilute alloys or the alloys revealing nonuniform deformations (e.g., with post-yielding, largely serrated plastic flow). To highlight strain-hardening capacity at ultrahigh flow stress, UTS versus uniform elongation (Fig. 2C) and yield strength versus hardened strength relations (fig. S9) are plotted. The SS-alloy shows a good combination of UTS, uniform elongation, and strain-hardening capacity. The existing alloys with UTS exceeding 2.5 GPa usually have very limited uniform elongation (<5% strain). Furthermore, previous ultrastrong alloys show limited strain-hardening capacity if their yield strength is >2.0 GPa, restricting further hardening to UTS of 2.6 GPa. The mechanical instability of these ultrastrong alloys is usually attributed to early necking by strain localization (*1*). Compared with the reference S-alloy, the additional supranano ordering in the SS-alloy can solve this problem.

Deformation mechanisms

The atomic interactions from the supranano particles in the FCC phase facilitate the "extra" strain hardening compared with that of the reference S-alloy. Furthermore, we performed TEM and aberration-corrected STEM investigations on the deformed FCC phase to reveal deformation mechanisms (Fig. 3). The initial FCC phase already contains a large number of dislocations (Fig. 3A), consistent with the synchrotron x-ray diffraction result (dislocation density of 4.0 × 10^{15} m^{-2}; Fig. 2B, inset). A high density of dislocations is introduced by a cold-rolling process, inducing the high yield strength of the SS-alloy. We performed careful TEM investigations (fig. S10) on hot-rolled recrystallized alloys with or without thermal aging [the alloys have a much larger grain size of 2 μm (fig. S2) and reduced density of dislocations], respectively, showing that the formation of SRO and S-$L1_2$ particles is similar to that of the S-alloy and SS-alloy. This indicates that grain size and dislocation density do not have substantial influence on the formation of SRO and S-$L1_2$ particles in the FCC phase. The dislocation density should have dynamic increasing during plastic deformation to maintain strain-hardening capacity (*24*, *27*–*29*); otherwise, subsequent necking-induced instability prevails, which decreases the ductility of the alloy (S-alloy; Fig. 2A). In the current SS-alloy, dislocation density has substantial improvements during the whole deformation process, shown by both TEM (Fig. 3, A to D) and synchrotron x-ray diffraction (Fig. 2B, inset) results. The plasticity carriers are mainly dislocations at the beginning of plastic deformation

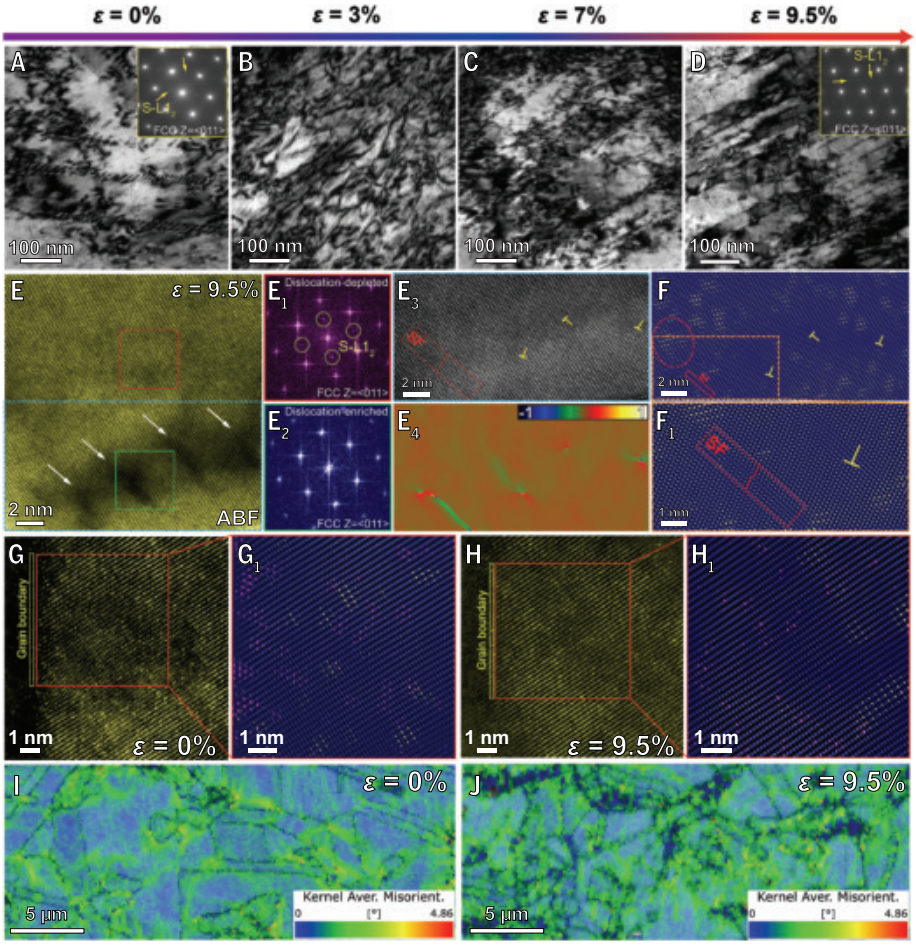

Fig. 3. Structure evolution of the FCC phase in the SS-alloy upon tension. (**A** to **D**) Bright-field TEM images of the FCC phase under different tensile strains, showing evolutions of dislocations and SFs. The TEM images are in two-beam condition probed from <0 1 1> direction with a g = {1 1 −1} vector. The insets in (A) and (D) are corresponding SAED patterns probed from <0 1 1> zone axis, showing weakening of S-L1$_2$ diffraction spots after tension. (**E**) Aberration-corrected annular bright-field (ABF) STEM image of the FCC phase after 9.5% tensile straining. The upper and lower regions contain few and substantial (denoted by white arrows) dislocations, respectively. (**E$_1$** and **E$_2$**) FFT patterns derived from the red and green square regions in (E), respectively, showing disappearing of S-L1$_2$ diffraction spots in dislocation-enriched regions. (**E$_3$**) Enlarged aberration-corrected HAADF-STEM image of the dislocation-enriched region in (E), showing a SF on the left and three dislocations on the right. (**E$_4$**) Corresponding strain mapping of (E_3) based on geometrical phase analysis, revealing strain localizations by SF and dislocations. (**F**) Combined IFT image generated from (E_3), showing interactions among dislocations or SFs and S-L1$_2$ particles. (**F$_1$**) Enlarged image of the dashed rectangle region in (F). (**G**) Aberration-corrected HAADF-STEM image of a FCC region near GB before tension, probed from <1 1 2> zone axis. (**G$_1$**) Enlarged combined IFT image generated from the red square region in (G), showing enrichment of SROs near GB. (**H**) Aberration-corrected HAADF-STEM image of a FCC region near GB after 9.5% tensile straining, probed from <1 1 2> zone axis. (**H$_1$**) Enlarged combined IFT image generated from the red square region in (H). The distribution of SROs is uniform across GB, indicating disruption of the ordering by motion of dislocations. (**I**) Kernel average misorientation (KAM) mapping of the SS-alloy before tension. Strains are concentrated in most GB regions, which may be due to the enrichment of SROs near GB. (**J**) KAM mapping of the SS-alloy after 9.5% tensile straining. Strain concentrations are uniformly distributed across GB and grain interior.

(3% strain; Fig. 3B), and then SFs initiate subsequently (Fig. 3, C and D). The diffraction spots of the S-L1$_2$ phase become less pronounced after deformation (Fig. 3, A and D, insets), indicating an order-to-disorder transition. This behavior is further demonstrated by an in situ TEM tension experiment (fig. S11). Aberration-corrected high-resolution STEM observations reveal that dislocation-enriched regions contain much fewer S-L1$_2$ particles (Fig. 3, E_3 and F). This indicates that the motion of dislocations disrupts the ordered particles, transformed into disordered solid solution. Although the order-to-disorder transition of the S-L1$_2$ particles may lower the degree of precipitation strengthening in the FCC phase, the dislocations can be effectively multiplied to counteract this softening and further provide strain hardening. This effect is mainly due to the hindering of dislocation motion by the S-L1$_2$ particles ahead. Moreover, there are almost no S-L1$_2$ particles on SFs, indicating another order-to-disorder transition effect by SF motion (Fig. 3F$_1$). Larger-sized S-L1$_2$ particles still exist on two ends of the SF (Fig. 3F$_1$), which impedes the SF's propagation. One particle (~3-nm size) is highlighted by a red dashed circle in Fig. 3F, which shows how it is much larger than the average particle size (1.4 nm; fig. S4). Therefore, more SFs are generated from other planes, refining the microstructure (Fig. 3D). The dynamically shortened mean-free path of dislocations elevates the stress barrier against dislocation motion, further enhancing the strain-hardening capacity. The SROs are much smaller than S-L1$_2$ particles, and thus, the pinning effect for dislocations and SFs is less pronounced. This explains the shorter uniform elongation of the reference S-alloy compared with that of the SS-alloy (Fig. 2A). One may argue that it is better to replace SROs with S-L1$_2$ particles to enhance the ductility. That argument will be correct if the SROs only precipitated in the grain interior.

The current SRO provides an "extra" ductilization mechanism, which cannot be realized by the S-L1$_2$ particles. The S-L1$_2$ particles precipitate in grain interiors, but the SRO has the opposite tendency, segregating near GB regions of the FCC phase (Fig. 3, G and G$_1$). This segregation scenario induces strain concentrations on GBs (Fig. 3I). This effect elevates the stress barrier against nucleation of dislocations from GBs, enhancing the yield strength. However, it is reported that a large number of dislocations may pile up on the strain-concentrated GBs during plastic deformation (*4*, *30*, *31*), favoring generation of microcracks. This effect is severe in conventional ultrafine-grained alloys, owing to the short mean-free path of dislocations. In the current SS-alloy after tensile deformation, however, the SROs are uniformly distributed across the GB region and grain interior of the FCC phase (Fig. 3H$_1$)—the SRO near the GB region is substantially weakened. This indicates a higher probability of order-to-disorder transition events of SRO near the GB region compared with the grain interior because of the more intense dislocation activities. The complex SF energy and antiphase boundary energy of the CCAs decay after dislocation glide (*32*), and the dislocation activities inevitably distort the local atomic packing structure of the SRO (*33*), promoting the transition toward random solid solution. Because SROs have a weaker pinning effect for dislocations than S-L1$_2$ particles have, the dislocation pile-up

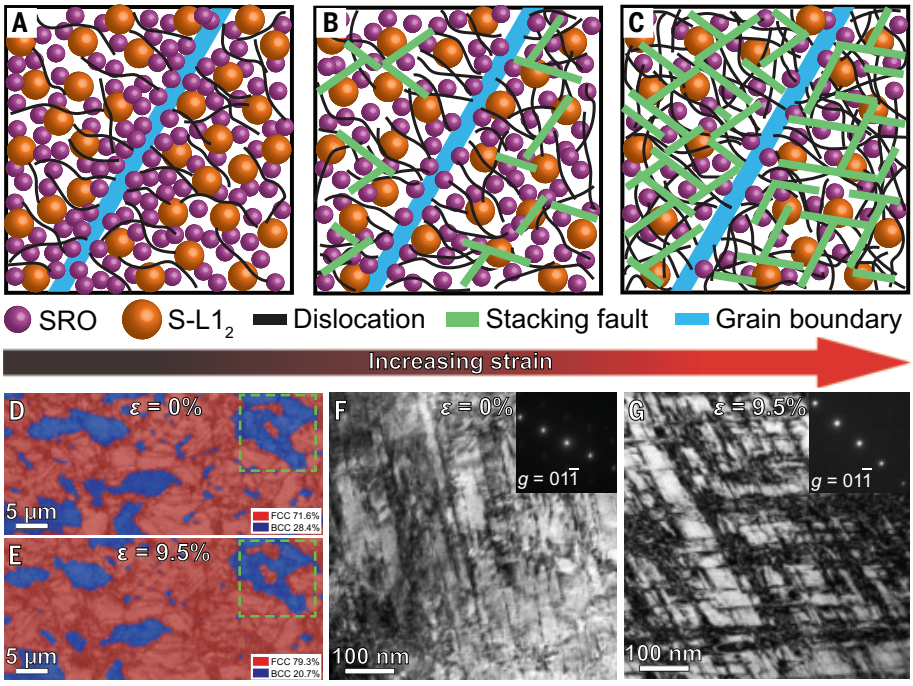

Fig. 4. Deformation mechanism of the SS-alloy. (**A** to **C**) Schematic illustration showing the structure evolution of the FCC phase upon tension. SRO and S-L1$_2$ particles are enriched near GB and in grain interior, respectively, before tension (A). During tension, dislocation activities near GB induce order-to-disorder transition of the SROs near GB, releasing strain concentrations (B). Large numbers of dislocations and SFs are multiplied and accumulated in grain interiors because of the enhanced pinning effect from S-L1$_2$ particles compared with that from SROs (C). (**D** and **E**) EBSD phase mapping images of the same region in the SS-alloy before and after tension, showing BCC-to-FCC phase transformation from the phase boundary. (**F** and **G**) TEM images of the ordered BCC phase before and after tension, probed from <0 1 1> direction with a g = {0 1 –1} vector. The insets are corresponding SAED patterns.

configuration is also weaker. The disordering of the SROs with a weaker dislocation pile-up feature substantially relieves strain concentrations on the GB regions, impeding microcrack generation. Meanwhile, the uniformly distributed SRO and S-L1$_2$ particles in the grain interior favor the uniform accumulation feature of dislocations. As a result, strain concentration scenarios are similar in the GB region and grain interior of the FCC phase (Fig. 3J). This strain delocalization mechanism postpones crack generation and prolongs the elongation. The uniformly multiplied dislocations in the grain interiors and GB regions of the FCC phase promote strain hardening.

The ordered BCC phase is usually harder than the FCC phase, contributing to a higher yield strength but reduced ductility (*21*). We performed electron backscattered diffraction (EBSD) investigations on the same region of an SS-alloy sample before and after tension (Fig. 4, D and E), which showed that the fraction of the FCC phase increases from 71.6 to 79.3% upon deformation, indicating a strain-induced BCC to FCC phase transformation phenomenon. This corresponds well with the in situ synchrotron x-ray diffraction results during tensile test (fig. S12). The BCC-to-FCC phase transformation usually occurs at the crack tip, where it is under an ultrahigh stress level (*34*, *35*). It is suggested that shearing of the lattice on a $\{0\,1\,1\}_{BCC}$ habit plane in the $<1\,-1\,1>_{BCC}$ direction induces this phase transformation, known as the Nishiyama-Wassermann model (*36*). In the current SS-alloy, ~2.6-GPa flow stress is an ultrahigh level among the reported CCAs (Fig. 2C). The boundary of a FCC region migrates into the adjacent BCC region (Fig. 4, D and E, green dashed square), but the SS-alloy seldom reveals nucleation of the FCC phase inside a BCC grain upon deformation. This indicates that the BCC-to-FCC phase transformation mainly occurs from the FCC-BCC phase boundary. The FCC phase, BCC phase, and boride nanoparticles at the FCC-BCC phase boundary have different intrinsic mechanical properties (namely, differences in shear modulus and Burgers vector), and thus, stress localization preferably occurs at the phase boundary. Therefore, the stress level should be much higher than the average flow stress of the alloy, promoting the BCC-to-FCC phase transformation. The displacive movements of lattice planes can relieve stress concentrations. For comparison, we also performed identical mechanical tests on reference alloys without W and Cu and without B, W, and Cu (fig. S13). The reference alloys have reduced yield strength and elongation, which in turn demonstrates the strengthening and ductilization effect from the boride nanoparticles in the SS-alloy. Dislocation motion can be activated in the BCC phase (Fig. 4, F and G) and boride nanoparticles (fig. S3, C and D), although the L2$_1$ BCC phase (*25*, *26*) and the boride are generally known to be brittle. Because the FCC phase has the highest fraction, has a larger grain size, and causes the ductile deformation mechanism in the SS-alloy, the dislocation motions in the brittle phases are mainly due to confinement deformation with the FCC phase (*37*, *38*). Geometrically necessary dislocations generated in the softer FCC phase pile up near the phase boundaries, rendering back stress in the softer FCC phase and forward stress in the harder phases (the hetero-deformation–induced stresses) (*5*). This hetero-deformation mode near the phase boundaries can also induce strain hardening of the different phases (*5*). The harder phases should have globular-like morphology and be distributed uniformly among the alloy, delocalizing stress concentrations on the phase boundaries. These behaviors further ductilize the SS-alloy. If the plastic flow stress of an alloy could not be maintained at such a high level (e.g., traditional dual-phase alloys with low flow stress), the BCC-to-FCC transformation will not occur. Therefore, the strengthening and ductilization mechanisms from the SRO and S-L1$_2$ particles (Fig. 4, A to C) in the FCC phase are the key preconditions for this behavior.

Conclusions

In summary, we present a ductilization strategy for 2.6-GPa alloys through short-range ordered interfaces and supranano precipitates. The supranano precipitates are L1$_2$ particles with a diameter of 0.5 to ~4 nm, coherent with the FCC solid-solution matrix. They have a stronger pinning effect for dislocations and SFs during plastic deformation compared with SROs, triggering multiplication and accumulation of dislocations in grain interiors of the FCC phase and thus a higher strain-hardening rate. The SROs have positive interfacial interaction energy with the FCC matrix, promoting their segregation near GB regions of the FCC phase. This configuration is helpful for the enhancement of yield strength. The less pronounced pinning effect for dislocations favors dislocation motion near GB regions of the FCC phase, inducing the order-to-disorder transition of the SROs. This behavior, together with the weaker dislocation–pile-up configuration, relieves strain concentrations at GBs of the FCC phase during plastic deformation. Consequently, strain variation is uniformly distributed across GB regions and grain interiors of the FCC phase. Furthermore, the BCC-to-FCC phase transformation occurs at FCC-BCC

phase boundaries because of an ultrahigh stress level during plastic deformation. The hetero-deformation mode near the phase boundaries can also induce strain hardening, and the displacive phase transformation relieves stress concentrations at the phase boundaries, further ductilizing the alloy. The combined precipitation structuring by supranano ordering and interfacial decoration by SRO offer a strategy to ductilize ultrastrong alloys, achieving large uniform elongation with continuous strain hardening until fracture, especially for alloys exceeding 2.5-GPa tensile strength.

REFERENCES AND NOTES

1. F. C. Campbell, Ed., *Elements of Metallurgy and Engineering Alloys* (ASM International, 2008).
2. K. Rahman, V. Vorontsov, D. Dye, *Acta Mater.* **89**, 247–257 (2015).
3. F. Khodabakhshi, M. Haghshenas, H. Eskandari, B. Koohbor, *Mater. Sci. Eng. A* **636**, 331–339 (2015).
4. K. Lu, *Science* **345**, 1455–1456 (2014).
5. Y. Zhu, X. Wu, *Prog. Mater. Sci.* **131**, 101019 (2023).
6. T. Yang *et al*., *Science* **362**, 933–937 (2018).
7. J. He *et al*., *Acta Mater.* **102**, 187–196 (2016).
8. L. Han *et al*., *Nature* **608**, 310–316 (2022).
9. Y. Yang *et al*., *Nature* **595**, 245–249 (2021).
10. E. Ma, C. Liu, *Prog. Mater. Sci.* **143**, 101252 (2024).
11. X. Chen *et al*., *Nature* **592**, 712–716 (2021).
12. L. Wang *et al*., *Nat. Mater.* **22**, 950–957 (2023).
13. Z. Lei *et al*., *Nature* **563**, 546–550 (2018).
14. Q. Ding *et al*., *Nature* **574**, 223–227 (2019).
15. K. Lu, L. Lu, S. Suresh, *Science* **324**, 349–352 (2009).
16. H. Kwon *et al*., *Acta Mater.* **248**, 118810 (2023).
17. M. Niu *et al*., *Acta Mater.* **179**, 296–307 (2019).
18. J. Man *et al*., *J. Mater. Sci. Technol.* **177**, 79–84 (2024).
19. P. R. Cantwell *et al*., *Acta Mater.* **62**, 1–48 (2014).
20. G. Wu, K.-C. Chan, L. Zhu, L. Sun, J. Lu, *Nature* **545**, 80–83 (2017).
21. J. He *et al*., *Acta Mater.* **62**, 105–113 (2014).
22. T. Yang *et al*., *Science* **369**, 427–432 (2020).
23. R. Wu, A. J. Freeman, G. B. Olson, *Science* **265**, 376–380 (1994).
24. B. B. He *et al*., *Science* **357**, 1029–1032 (2017).
25. Y. Mu *et al*., *Acta Mater.* **232**, 117975 (2022).
26. X. Chen *et al*., *J. Mater. Res. Technol.* **25**, 3273–3284 (2023).
27. Y. Li *et al*., *Science* **379**, 168–173 (2023).
28. H. Li *et al*., *Nature* **604**, 273–279 (2022).
29. B. Xu *et al*., *Nat. Mater.* **23**, 755–761 (2024).
30. Y. Wang, M. Chen, F. Zhou, E. Ma, *Nature* **419**, 912–915 (2002).
31. R. O. Ritchie, *Nat. Mater.* **10**, 817–822 (2011).
32. Q.-J. Li, H. Sheng, E. Ma, *Nat. Commun.* **10**, 3563 (2019).
33. Y. Yang *et al*., *Nat. Commun.* **15**, 1402 (2024).
34. S. J. Wang *et al*., *Nat. Commun.* **5**, 3433 (2014).
35. J. Zhang *et al*., *Nat. Commun.* **12**, 2218 (2021).
36. Z. Nishiyama, *Sci. Rep. Tohoku Univ.* **23**, 637 (1934).
37. P. Shi *et al*., *Science* **373**, 912–918 (2021).
38. Q. Wu *et al*., *Nat. Commun.* **13**, 4697 (2022).
39. J. Ren *et al*., *Nature* **608**, 62–68 (2022).
40. T. J. Jang *et al*., *Nat. Commun.* **12**, 4703 (2021).
41. H. Chung *et al*., *Nat. Commun.* **14**, 145 (2023).
42. B. Schuh *et al*., *Acta Mater.* **142**, 201–212 (2018).
43. H. Shahmir, J. He, Z. Lu, M. Kawasaki, T. G. Langdon, *Mater. Sci. Eng. A* **676**, 294–303 (2016).
44. R. Zheng, J. Chen, W. Xiao, C. Ma, *Intermetallics* **74**, 38–45 (2016).
45. H. Huang *et al*., *Adv. Mater.* **29**, 1701678 (2017).
46. J. Su, D. Raabe, Z. Li, *Acta Mater.* **163**, 40–54 (2019).
47. J. M. Park *et al*., *Mater. Res. Lett.* **9**, 315–321 (2021).
48. S. R. Reddy *et al*., *Sci. Rep.* **9**, 11505 (2019).
49. I. Wani *et al*., *Mater. Sci. Eng. A* **675**, 99–109 (2016).
50. L. Wang *et al*., *Acta Mater.* **216**, 117121 (2021).

ACKNOWLEDGMENTS

We thank Y.-B. Qin, P.-C. Zhang, C.-S. Ma, Z.-J. Ren, Y.-N. Chen, P. Zhang, Q.-Q. Fu, and D.-L. Zhang at Xi'an Jiaotong University for technical support. **Funding:** We acknowledge supports from National Natural Science Foundation of China (52361165617, 52371162, 52271114, and 52401216) and National Natural Science Foundation of China/Hong Kong Research Grants Council Joint Research Scheme (project no. N_CityU151/23). G.W. and C.L. acknowledge supports from National Natural Science Fund for Excellent Young Scientists Fund Program (Overseas). We acknowledge supports from CityU (grant 9360161) for APT research at the Inter-University 3D APT Unit of City University of Hong Kong (CityU). We acknowledge DESY (Hamburg, Germany), a member of the Helmholtz Association HGF, for the provision of experimental facilities. Parts of this research were carried out at PETRA III beamline P02.1. Beamtime was allocated for proposal I-20230050. **Author contributions:** G.W., C.L., Z.-W.S., and J.L. guided the project; Y.-Q.Y. and G.W. designed the alloys; Y.-Q.Y. and G.W. conducted FIB and TEM experiments; Y.-Q.Y. conducted mechanical testing, (S)TEM characterization, and EBSD and EPMA experiments; Y.M. conducted synchrotron XRD experiments; J.-H.L. and Z.R. conducted APT characterization and data analysis; W.-H.C. and S.L. did MD simulations; G.W., C.L., J.L., and Z.-W.S. contributed to the interpretations of the observations; Y.-Q.Y. and G.W. wrote the paper; all authors contributed to the discussion of the results. **Competing interests:** The authors declare no competing interests. **Data and materials availability:** All data are available in the manuscript or the supplementary materials.

SUPPLEMENTARY MATERIALS

science.org/doi/10.1126/science.adr4917
Materials and Methods
Figs. S1 to S13
References (*51*–*68*)

Submitted 3 July 2024; accepted 20 December 2024
10.1126/science.adr4917

MATING SYSTEMS

A single gene orchestrates androgen variation underlying male mating morphs in ruffs

Jasmine L. Loveland[1,2]*†, Alex Zemella[1,3]*†, Vladimir M. Jovanović[3,4], Gabriele Möller[5], Christoph P. Sager[6], Bárbara Bastos[3,7], Kenneth A. Dyar[5], Leonida Fusani[2,8], Manfred Gahr[1], Lina M. Giraldo-Deck[1], Wolfgang Goymann[1,9], David B. Lank[10], Janina Tokarz[5], Katja Nowick[3], Clemens Küpper[1]*

Androgens are pleiotropic and play pivotal roles in the formation and variation of sexual phenotypes. We show that differences in circulating androgens between the three male mating morphs in ruff sandpipers are linked to 17-beta hydroxysteroid dehydrogenase 2 (HSD17B2), encoded by a gene within the supergene that determines the morphs. Low-testosterone males had higher *HSD17B2* expression in blood than high-testosterone males, as well as in brain areas related to social behaviors and testosterone production. Derived HSD17B2 isozymes, which are absent in high-testosterone males but preferentially expressed in low-testosterone males, converted testosterone to androstenedione faster than the ancestral isozyme. Thus, a combination of evolutionary changes in regulation, sequence, and structure of a single gene introduces endocrine variation underlying reproductive phenotypes.

Testosterone is instrumental for the development of the male reproductive tract, sperm production, secondary sex characteristics, skeletal muscle mass, and expression of social behaviors, including those that are sexual, aggressive, and courtship-related (*1*–*5*). Although both sexes produce testosterone, males generally have higher circulating testosterone concentrations than females (*4*, *6*–*8*). In males, testosterone is synthesized primarily in the testes, with its production controlled through a feedback-control loop in the hypothalamic-pituitary-gonadal (HPG) axis. Male testosterone levels typically peak during the breeding season (*9*, *10*) but vary considerably between individuals depending on life history, reproductive trade-offs, and alternative mating tactics (*2*, *11*, *12*). Usually, dominant territorial males have high levels of circulating testosterone while subdominant males or males that use alternative mating tactics, such as sneaking, have low testosterone levels (*11*).

Testosterone levels fluctuate diurnally and seasonally, but a proportion of the variation between individuals may have a genetic basis and quantitative genetic studies have suggested substantial heritability for testosterone in tetrapods (*13*). In humans, 65% of variation in serum testosterone concentrations between male twins was explained by genetics (*14*). Genome-wide association studies provided a number of candidate genes for testosterone variation including the sex-hormone binding globulin locus and multiple loci on the X chromosome (*8*, *15*, *16*). In addition, genes expressed along the HPG and hypothalamic-pituitary-adrenal (HPA) axes have been studied for their contributing roles to the rate of testosterone

[1]Max Planck Institute for Biological Intelligence, Seewiesen, Germany. [2]Department of Cognitive and Behavioral Biology, University of Vienna, Vienna, Austria. [3]Institut für Biologie, Freie Universität Berlin, Berlin, Germany. [4]Bioinformatics Solution Center, Freie Universität Berlin, Berlin, Germany. [5]Metabolic Physiology, Institute for Diabetes and Cancer, Helmholtz Munich, German Research Center for Environmental Health, Neuherberg, Germany. [6]Lindenstrasse 9, Allschwil, Switzerland. [7]Research Centre in Biodiversity and Genetic Resources, University of Porto, Vairão, Portugal. [8]Konrad Lorenz Institute of Ethology, University of Veterinary Medicine, Vienna, Austria. [9]Department Biologie II, Ludwig Maximilians University Munich, Martinsried-Planegg, Germany. [10]Department of Biological Sciences, Simon Fraser University, Burnaby, Canada.
***Corresponding author. Email: jasmine.loveland@univie.ac.at (J.L.L.); alex.zemella@bi.mpg.de (A.Z.); clemens.kuepper@bi.mpg.de (C.K.)**
†These authors contributed equally to this work.

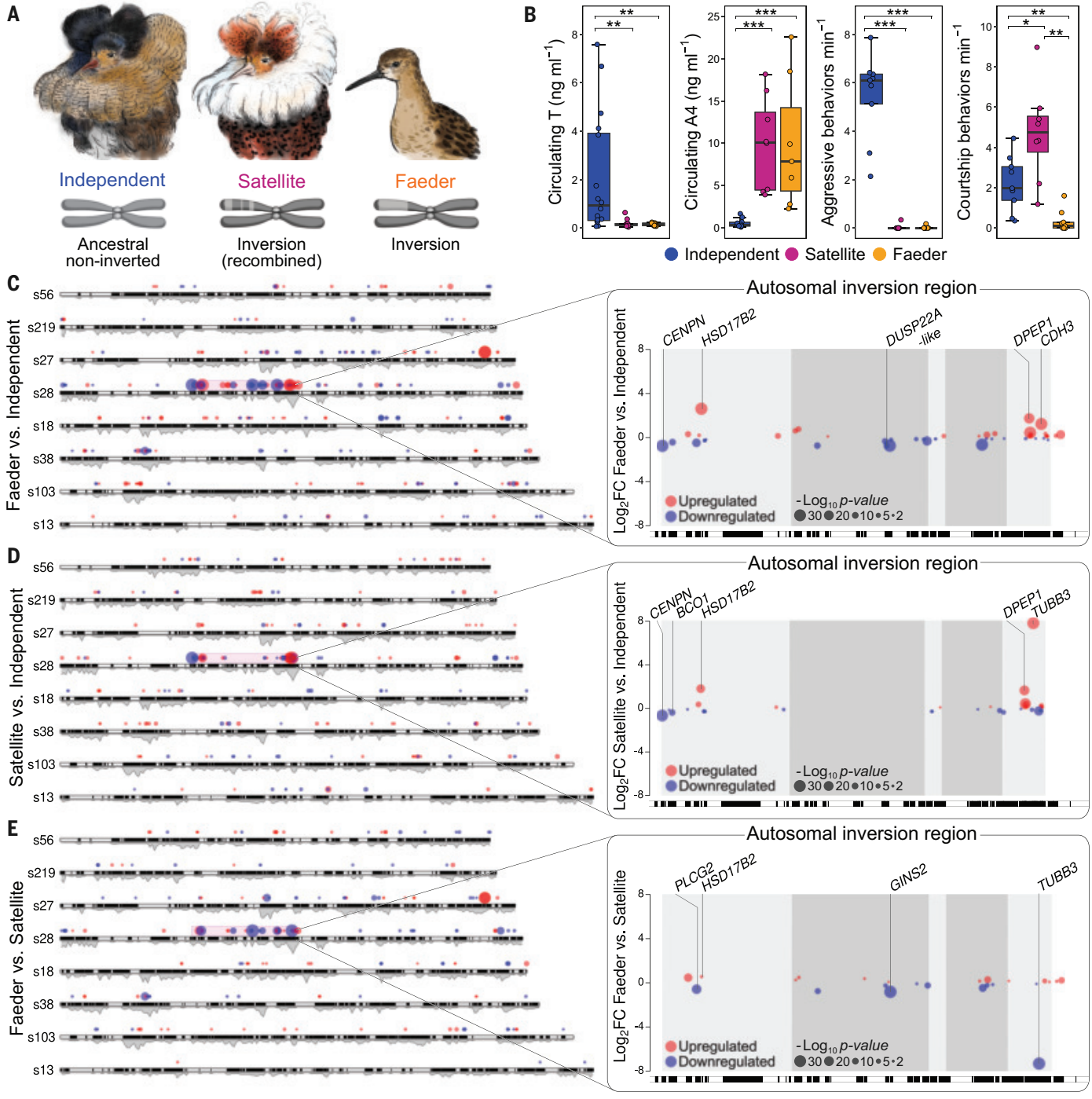

Fig. 1. Gene expression between male morphs is concentrated in the supergene region. (**A**) Male ruff morphs differ in ornamental plumage and supergene haplotypes. (**B**) Morph-specific concentrations of circulating testosterone (n = 36), androstenedione (n = 25), aggression and courtship (n = 26). The morph model differentially expressed genes in pairwise comparisons. (**C**) Faeder versus independent (n = 26). (**D**) Satellite versus independent (n = 27) and (**E**) Faeder versus satellite (n = 19), aligned to karyoplots for a subset of representative scaffolds. The supergene region is magnified on right panels with recently recombined areas shaded in dark gray. Each circle is a differentially expressed gene; red and blue circles denote higher and lower expression levels in the first versus second morph, respectively. The top differentially expressed genes with the largest absolute $\log_2$ fold change are labeled. Karyoplot shading denotes gene presence (black) and absence (white). Gene density plot calculated in 10^5 base pair (bp) windows. Kruskal-Wallis tests followed by Wilcoxon rank tests with Bonferroni adjusted P-values were used in (B), asterisks indicate $^*P < 0.05$, $^{**}P < 0.01$, $^{***}P < 0.001$. (B) modified from (*38*).

production and metabolism (*17*, *18*), including the use of prohormones such as dehydroepiandrosterone to avoid costs of high circulating testosterone (*19*). However, a detailed characterization of genetic variants linked to testosterone concentrations, including a confirmation of functional effects on testosterone production or metabolism, has so far remained elusive.

Species with multiple reproductive morphs often exhibit systemic androgen variation between male types. Ruffs (*Calidris pugnax*) feature three mating morphs that are fixed for

life: independents, satellites, and faeders. The morphs show nearly discrete differences in size, plumage ornamentation, aggressive behavior, and courtship behavior (*20*) (Fig. 1, A and B). During the mating season, males of the most common independent morph compete aggressively with each other to establish a dominance hierarchy on leks. The most competitive independents display on small lek courts to entice visiting females. Satellites, with their conspicuous pale plumage ornaments, co-display submissively with selected independents and mate opportunistically when their independent partners are momentarily distracted (*21*, *22*). Faeders, the rarest and smallest males, have no ornamental feathers but mimic females in appearance and behavior to sneak copulations (*23*). Breeding males exhibit clear morph variation in circulating androgens (*20*, *24*, *25*). Independents have high circulating testosterone levels but low levels of androstenedione, a less potent androgen and testosterone precursor and metabolite. The nonaggressive satellite and faeder males show the reverse pattern (Fig. 1B). The morphs are differentiated by an autosomal supergene that arose through a chromosomal inversion about 3.8 million years ago (Mya) and harbors about 100 genes, including several involved in steroid metabolism (*20*, *26*). Faeders carry the oldest inversion haplotype whereas the satellite haplotype arose through a rare recombination only 0.07 Mya (*27*). Since one inversion breakpoint is homozygous-lethal, faeders and satellites always carry an ancestral independent haplotype and a derived morph–specific haplotype (*20*, *26*). Here, we capitalize on the existing natural endocrine and genetic contrasts between reproductive morphs to identify and characterize the major genes related to the pronounced androgen differences between males.

Supergene-linked loci show differential expression and allelic imbalance

We sampled adult males from all three morphs during the breeding season, when the differences in androgen levels and social behaviors are most distinct (*20*, *25*). To examine transcriptomic differences, we performed RNA-Seq on tissues highly relevant to behavior or the production/metabolism of sex steroid hormones: brain (seven areas), pituitary glands, adrenal glands, liver and testes. Sampled brain areas comprised nine brain nuclei that include parts of the social behavior network, mesolimbic reward pathway (*28*, *29*), and serotonergic system. These nuclei are either expected to have high expression of sex steroid receptors (preoptic area, lateral septum, nucleus taeniae, hypothalamus), contain major populations of dopamine neurons (ventral tegmental area and substantia nigra), serotonin neurons (raphe), or are involved in executive functions in birds (caudal nidopallium, a putative partial homolog to the mammalian prefrontal cortex) (*30*) (fig. S1). Hypothalamus samples included anterior, ventromedial, lateral, and posterior hypothalamic nuclei (see supplementary materials for details).

Genome-wide, we found a large number of differentially expressed genes in pairwise comparisons of morphs considering all tissues (faeders versus independents: 1762; satellites versus independents: 1438; faeders versus satellites: 1395.) The supergene region had a notable enrichment of differentially expressed genes [faeders versus independents (odds ratio = 8.15, *P*-adjusted = 2.15e-15); satellites versus independents (odds ratio = 5.56, *P*-adjusted = 8.66e-12); faeders versus satellites (odds ratio = 3.05, *P*-adjusted = 6.13e-05)] (Fig. 1, C to E, and table S1). Consistent with the evolutionary histories of their different haplotypes, faeders and independents—which carry the most divergent haplotypes (*20*, *26*, *27*)—had the highest number of differentially expressed genes with a relatively even distribution across the inversion region (Fig. 1C). By contrast, there was a notable absence of differentially expressed genes in recently recombined regions of the satellite haplotype in the satellite versus independent comparison (Fig. 1D), although these regions harbored many differentially expressed genes in the faeder versus satellite comparison (Fig. 1E). The spatial pattern of differentially expressed genes suggests an important role for cis regulatory elements in controlling expression of nearby loci in the inversion region.

Next, we examined variation in gene expression by tissue. Principal component analysis revealed clear clustering and separation by organ and then brain area, with one cluster representing samples from lateral septum and preoptic area, which are adjacent brain areas (fig. S2). Hypothalamus, pituitary, and adrenal glands, three tissues prominently involved in the regulation of systemic androgen levels, stood out with large numbers of differentially expressed genes (fig. S3). In most tissues, comparisons involving independents had more differentially expressed genes than those of the faeder versus satellite comparison (fig. S3).

Recombination between non-inverted and inverted haplotypes is exceptionally rare (*31*), and as a result the derived faeder and satellite haplotypes have accumulated mutations leading to the presence of distinct inversion alleles. This allowed us to quantify allele-specific expression from RNA-Seq data across different tissues (fig. S4). Faeders showed allelic imbalance in 87 of 97 measurable protein-coding genes, spread throughout the entire inversion region. In satellites, we detected imbalance in 68 of 79 measurable protein-coding genes; however, regions that recently recombined with the independent haplotype showed fewer genes with allelic imbalance than the non-recombined regions.

HSD17B2 expression and isozyme variation differentiates ancestral from derived morphs

To identify candidate genes for the distinct variation in circulating androgens between morphs (Fig. 1B), we investigated individual differentially expressed genes associated with the supergene that showed pronounced expression differences between independents and the other two morphs, particularly in tissues related to androgen regulation and metabolism. Differences in circulating androgen concentrations among male morphs may arise from changes in the expression of genes encoding steroidogenic enzymes (*18*, *32*), gonadotropins and their receptors (*33*), or receptors for sex steroids (*34*). However, neither gonadotropin, androgen nor estrogen receptors were differentially expressed among ruff morphs [fig. S5, see also (*24*)]. Instead, the top candidate for morph differentiation was the 17-beta hydroxysteroid dehydrogenase 2 gene (*HSD17B2*), whose enzymatic product converts testosterone to androstenedione, estradiol to estrone, and 20-alpha dihydroprogesterone to progesterone (*35*). HSD17B2 belongs to a large family of more than a dozen highly multifunctional HSD17B enzymes that catalyze conversions between 17-keto steroids and 17-beta hydroxy steroids (*36*, *37*). Although the full HSD17B family has not been extensively studied in birds, ruff HSD17B2 is likely functionally homologous to the human enzyme as all conserved functional domains are present (*38*) and the gene synteny is high.

The ruff *HSD17B2* gene is located within a nonrecombined area of the supergene and stood out among inversion genes because it was a top differentially expressed gene with strong allele-specific expression of the inversion allele in faeders and satellites (Fig. 2A). In multiple tissues—including the hypothalamus, a brain area essential to androgen regulation in vertebrates—*HSD17B2* had lower expression in independents than in satellites or faeders (Fig. 2, B and C). It also showed a strong bias toward the inversion allele in most tissues (Fig. 2D and fig. S4), including all brain areas investigated (range of inversion allele-specific expression proportion in satellites: 80 to 100%; faeders: 91 to 100%) (fig. S4).

The expression bias toward the inversion allele is puzzling because simulation models predicted that inversion haplotypes accumulate deleterious mutations (*39*). The coding sequences for *HSD17B2* show several nonsynonymous mutations, including four amino acid substitutions shared between faeders and satellites (Fig. 3A). Notably, a selection test using a branch model and annotated HSD17B2 sequences from six related Charadriiform species revealed strong selection signatures on the satellite and faeder haplotypes with three of their four shared residues (A235S, L279F,

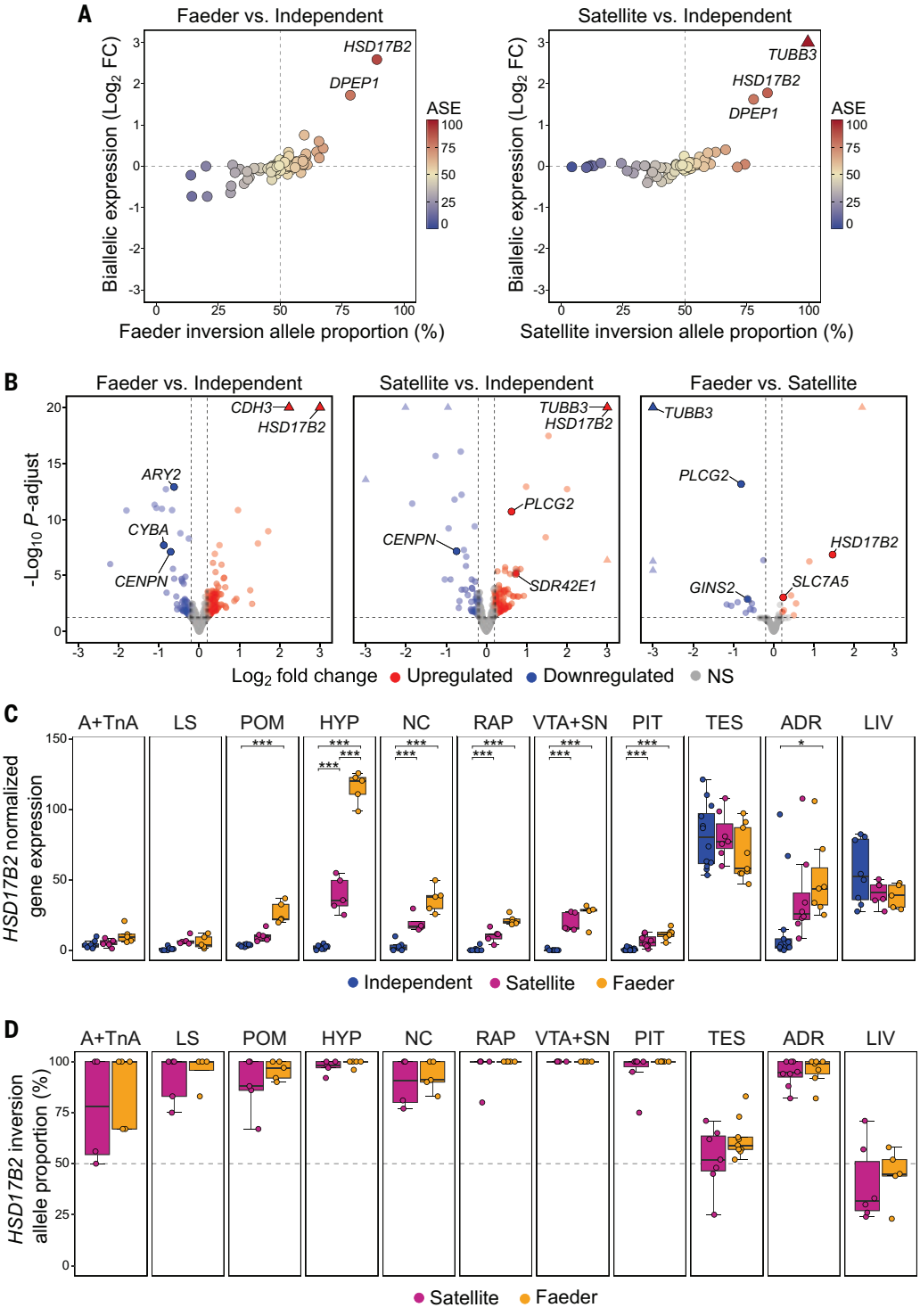

Fig. 2. Differential expression and allelic imbalance in *HSD17B2* across tissues and morphs. (**A**) Gene expression in faeders (n [birds, samples] = 9, 63) and satellites (n = 10, 63) for loci in inverted regions shown as biallelic expression ($\log_2$ fold change, y-axis) relative to independents (n = 17, 103) and proportion expressed from respective inversion alleles (x-axis). Genes (circles) colored according to inversion allele-specific expression (ASE) bias. Dashed lines represent no difference in gene expression (horizontal) and no allelic bias (vertical). (**B**) Hypothalamic differentially expressed genes ($-\log_{10}$ P-adjust value >1.25) comparing first and second-listed morph (n per plot = 13, 13, 10 birds). Genes with $\log_2$ fold change <−0.2 are shown in blue and $\log_2$ fold change >0.2 are shown in red. NS, nonsignificant. Genes with values beyond axes' ranges are shown as triangles. Labels highlight five inversion genes with the largest absolute $\log_2$ fold change. Tissue-specific *HSD17B2* expression as (**C**) biallelic and (**D**) inversion-allele proportion; n [birds, samples] = 36, 229. Asterisks denote differential expression, P-values are Benjamini-Hochberg corrected (*P < 0.05, ***P < 0.001). A+TnA, arcopallium and nucleus taeniae; LS, lateral septum; POM, preoptic area; HYP, hypothalamus; NC, caudal nidopallium; RAP, raphe; VTA+SN, ventral tegmental area and substantia nigra; PIT, pituitary; TES, testes; ADR, adrenals; LIV, liver. Brain area details in fig. S1.

I329T) being positively selected (fig. S6). In addition, the variation in circulating androgens between independents and the two inversion-carrying morphs suggests that the enzymatic activity of HSD17B2 has not deteriorated; on the contrary, it appears to have increased (Fig. 1B).

To evaluate whether and how these mutational changes altered enzymatic function, we investigated the molecular interactions in ruff HSD17B2 variants with testosterone and its co-factor nicotinamide adenine dinucleotide (NAD^+) in silico, and determined their enzymatic kinetics for testosterone conversion through in vitro assays. Since HSD17B2 is anchored in the membrane of the endoplasmic reticulum (*40*), we used a truncated protein structure without amino acids in the transmembrane topology as in (*41*) for the in silico computer simulation. We restricted the comparison to ruff homodimers as they should be the predominant dimers found in faeder and satellite cells, given the widespread allele-specific expression favoring derived *HSD17B2* alleles. The homology models revealed lower $\Delta G_{binding}$ values in satellite and faeder than independent HSD17B2 isozymes, suggesting higher binding affinities for both testosterone and NAD^+ in the

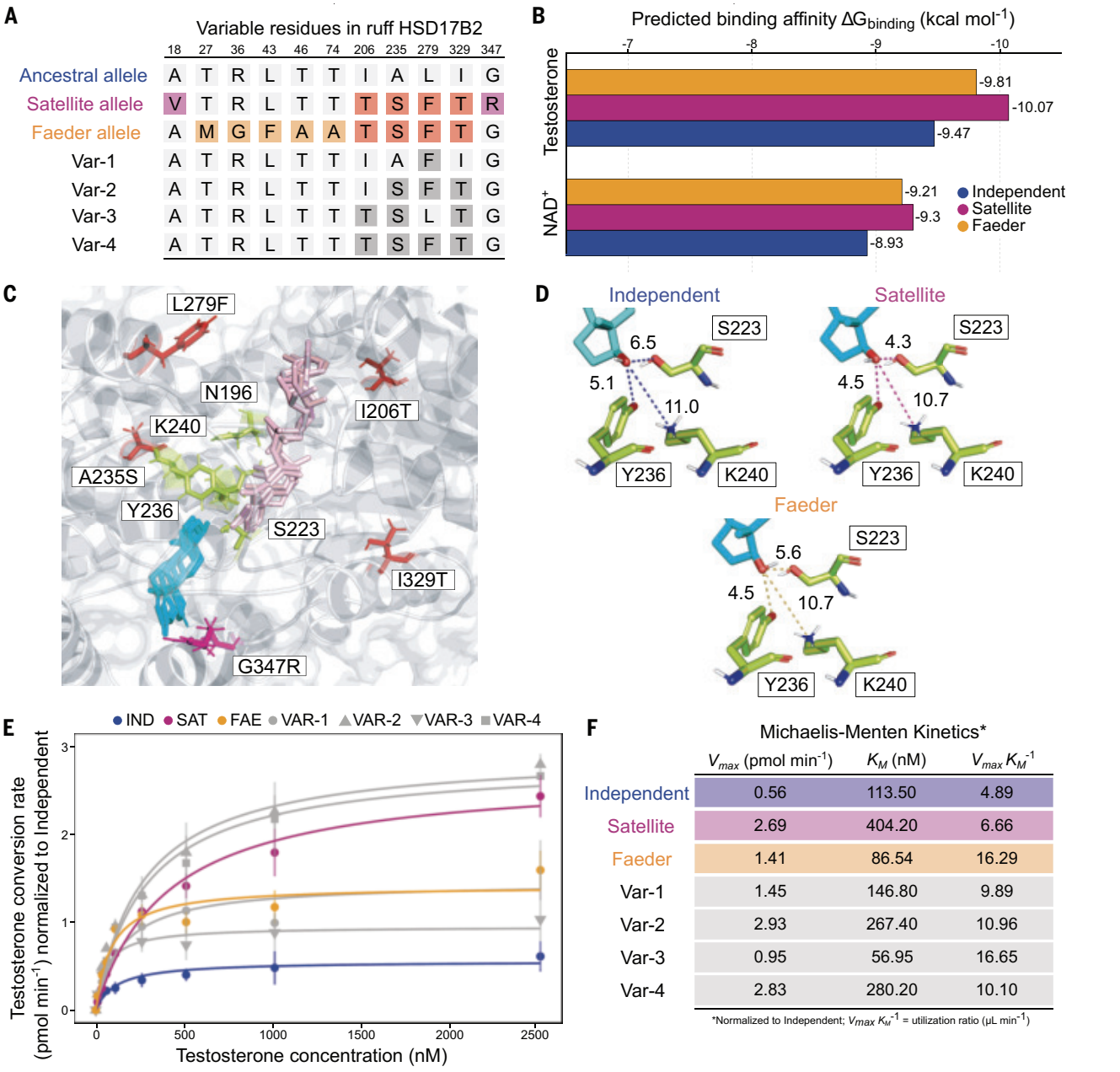

Fig. 3. Derived HSD17B2 isozymes show faster testosterone conversion than the ancestral isozyme. (**A**) Variable residues among ruff HSD17B2 isozymes and engineered mutant variants (Var-1 to Var-4) tested for enzymatic activity. Relative to the ancestral (independent) allele, mutated residues shared by satellite and faeder alleles are in orange; position numbers from XP_014797711.1. (**B**) In silico model predicts better binding affinity (lower values) for testosterone and NAD^+ in faeders and satellites than independents. (**C**) Predicted three-dimensional monomeric structure of independent HSD17B2 (gray) zoomed in to the binding pocket with testosterone (cyan) and NAD^+ (pink). Residues (N196, S223, Y236, K240) from the canonical "NSYK" catalytic tetrad of short chain dehydrogenase/reductase enzymes (light green). Residues that are mutated in satellite and faeder isozymes (red) feature in close vicinity to the binding pocket. (**D**) In silico models reveal shorter atomic distances (in Ångstroms) between testosterone and functional catalytic "SYK" (S223, Y236, K240) sites in satellite and faeder variants, indicating potential for faster catalytic turnover than with the independent variant. (**E**) In vitro rates of testosterone conversion for different isozymes across a range of substrate concentrations. IND, independent; SAT, satellite; FAE, faeder; VAR, variant. Error bars are ±SD from three replicates. (**F**) Michaelis-Menten kinetics calculated from (E).

two derived isozymes compared to the ancestral isozyme (Fig. 3B). Moreover, in satellite and faeder isozymes, testosterone was closer to the residues that initiate and perform the catalytic reaction, suggesting enhanced substrate binding, catalysis, and product release in derived variants (Fig. 3, C and D).

We then performed enzymatic assays in vitro, comparing ruff homodimers (Fig. 3A). All isozymes retained function but varied in their enzymatic characteristics (Fig. 3, E and F). Satellite and faeder homodimers showed higher maximum velocity (v_{max}) for testosterone conversion than the independent homodimer. The isozymes also showed significant variation in their Michaelis constants (K_M), indicating that the faeder and satellite homodimers require a lower and higher substrate concentration, respectively, than that of the independent to achieve half v_{max}. The resulting utilization rates (v_{max}/K_M) were more than three times

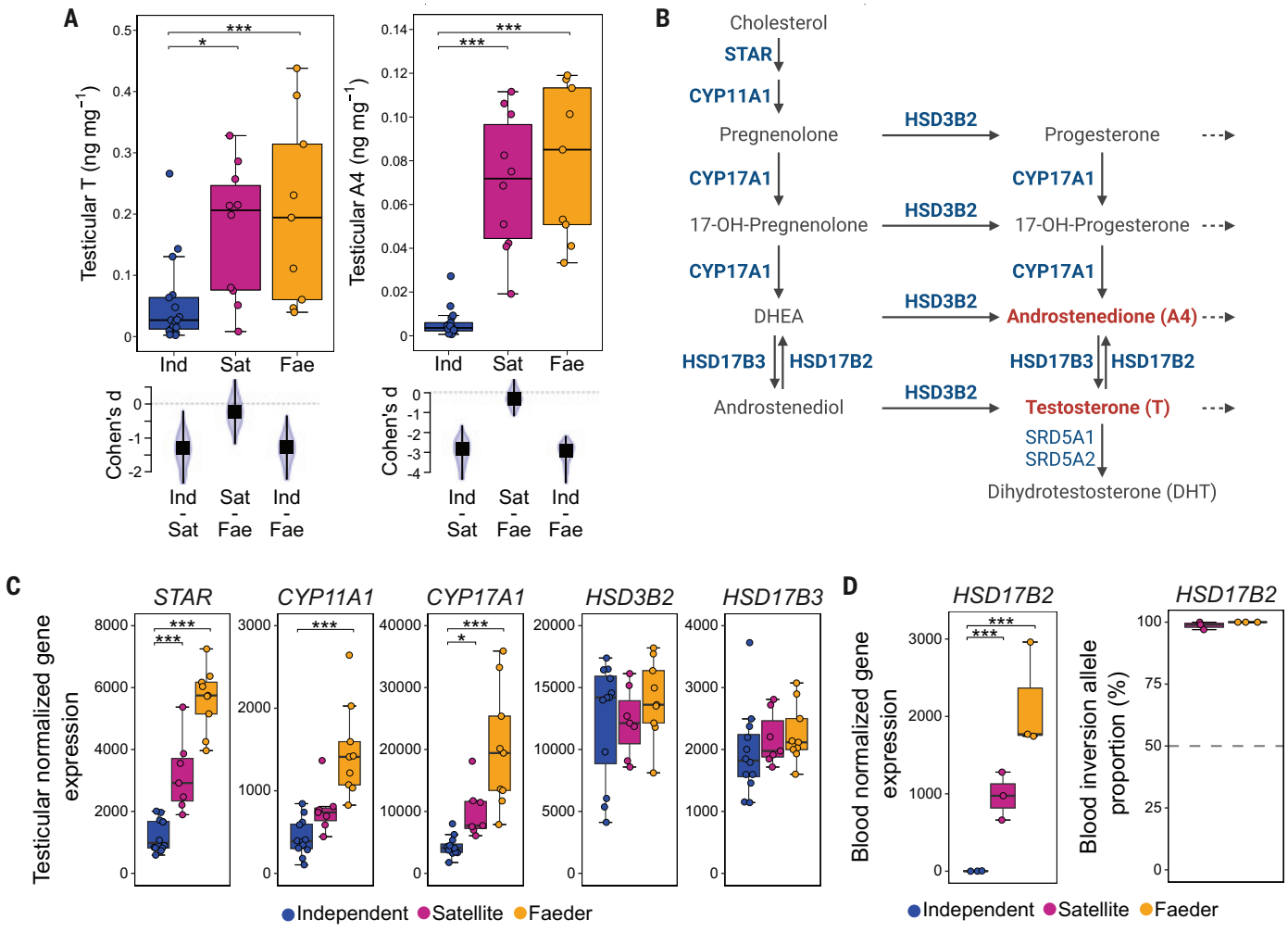

Fig. 4. Sources of androgen variation between male morphs in testes and blood. (**A**) Morph-specific testicular testosterone and androstenedione levels including effect sizes (Cohen's d) for pairwise comparisons (n = 36). (**B**) Simplified androgen biosynthesis pathway showing key enzymes responsible for steps from cholesterol to testosterone. (**C**) Testicular expression of genes shown in bold in (B) (n = 28). (**D**) Blood *HSD17B2* expression and allele-specific expression (n = 9). Asterisks denote statistically clear differences, P-values are Benjamini-Hochberg corrected (*P < 0.05, **P < 0.01, ***P < 0.001). Ind, independent; Sat, satellite; Fae, faeder.

higher for the faeder than for the independent homodimer, with the satellite homodimer showing intermediate rates (Fig. 3F). To understand how individual mutations in the faeder and satellite isozymes affect kinetics of the derived variants, we next examined engineered variants (Var-1 to Var-4) with different combinations of the four shared residues for in vitro tests. As previously predicted (*38*), a single amino acid change (L279F, represented by Var-1) led already to a two times greater utilization rate in comparison to the independent isozyme (Fig. 3F).

Androgen and gene expression variation in male testes and blood

The male testes are the primary organs for testosterone synthesis but *HSD17B2* was not differentially expressed in this tissue (Fig. 2C). To examine androgen production in testes, we quantified testosterone and androstenedione concentrations through a radioimmunoassay. Based on the known circulating androgen levels and differences in HSD17B2 activity, we predicted that satellites and faeders would have high levels of androstenedione and low levels of testosterone in testes, and the reverse pattern in independents. Contrary to our expectations, we found that testes of satellites and faeders had, on average, seven to eight times higher testosterone and 20 times higher androstenedione concentrations than independents (Fig. 4A).

To illuminate regulatory variation that may underlie the unexpected testicular androgen profiles of satellites and faeders, we conducted a detailed analysis on gene expression variation between morphs in this tissue. This revealed, first, an overrepresentation of differentially expressed genes with the gene ontology terms "steroid hormone biosynthetic process" and "hormone metabolic processes" in both faeders and satellites, compared with independents (fig. S7). Examining expression differences between the major genes involved in androgen synthesis, we detected high variation during the early catalytic steps in this pathway with higher expression of *STAR*, *CYP11A1*, and *CYP17A1* in satellites and faeders than in independents (Fig. 4, B and C). Other genes such as *HSD3B2* and even *HSD17B3*—responsible for the reverse conversion of androstenedione to testosterone (Fig. 4B)—were highly but similarly expressed in all three morphs, and we found no evidence of altered expression of genes involved in steroid transport (table S2). This suggests that differentially expressed genes early in the androgen synthesis pathways instigate morph variation in androgens in the testes. Notably, *HSD17B2* was not differentially expressed in testes and its overall expression was about 25 times lower than expression of *HSD17B3* (Figs. 2C and 4C). Our results were fully consistent with an earlier study on morph

differences in a few selected genes of the androgen synthesis pathway (*24*) and point to functional requirements such as the need of testosterone for sperm production constraining *HSD17B2* expression variation in testes.

To inspect morph variation in androgens, we compared androstenedione and testosterone concentrations in blood plasma and testes (fig. S8). In independents, we found strong positive relationships between concentrations of both androgens (table S3). In satellites and faeders, this was also the case between androstenedione and testosterone concentrations measured in the testes, but not for correlations involving plasma testosterone, which circulates in very low concentrations in these morphs. One explanation is that *HSD17B2* is differentially expressed in the blood of morphs. However, *HSD17B2* expression and activity in blood is typically either absent or rarely detected (*42*, *43*). To explore this conundrum, we conducted further RNA-Seq in nine males to compare *HSD17B2* expression in blood between morphs. This revealed extreme morph variation in blood *HSD17B2* expression, much higher than in all other tissues examined. Consistent with low activity reported in human blood (*42*, *43*) and their own high circulating testosterone concentrations, *HSD17B2* expression was nearly absent in independents. Conversely, *HSD17B2* was highly expressed in faeders and satellites, with a strong bias toward the derived allele (Fig. 4D). It remains unclear which blood cells overexpress *HSD17B2* in faeder and satellites because, unlike mammals, red blood cells in birds are nucleated. This localized hyperactivity of HSD17B2 in the blood of the two low testosterone morphs may represent an evolutionary innovation that effectively limits the pleiotropic actions of testosterone outside of the testes. High HSD17B2 activity in the blood and hypothalamus of faeders and satellites then results in fast metabolism of testosterone and alters the HPG feedback loop that controls testicular androgen synthesis.

Taken together, our findings imply that a combination of changes in regulation and coding sequence of the *HSD17B2* gene resulted in increased testosterone conversion of derived variants. The supergene-induced suppression of recombination likely accelerated the evolution of the derived variants. The changes of this single gene are expected to have widespread consequences through genetic and hormonal pleiotropy. First, HSD17B2 itself is multifunctional and metabolizes other sex steroids in addition to testosterone (*44*). One of these, estradiol, is also required to mediate effects on territorial mating behaviors in many bird species (*45*–*47*). Future studies should examine how the changes to HSD17B2 affect the conversion rates of its other substrates. Second, the substrates of HSD17B2 are highly pleiotropic signaling molecules that coordinate physiological and developmental processes and can foster the evolution of correlated traits (*48*–*51*). Vertebrate genomes contain hundreds to thousands of response elements for sex steroid receptors that may alter gene expression (*52*, *53*). For example, the swift metabolization of testosterone in the blood of low testosterone morphs will starve androgen receptors in target tissues of one of their most significant ligands and severely affect systemic responses that have evolved over millions of years. In the case of ruffs, the changes in circulating androgens may underlie the profound differences in male aggression that exist between morphs and may be at the heart of the pronounced sexual antagonism that has been introduced by the inversion alleles (*54*). Identifying how androgen levels are altered genetically opens new avenues for understanding the evolution of diverse reproductive phenotypes, antagonistic pleiotropy, and the regulation of social behaviors.

REFERENCES AND NOTES

1. R. F. Oliveira, *Adv. Stud. Behav.* **34**, 165–239 (2004).
2. M. Hau, *BioEssays* **29**, 133–144 (2007).
3. L. Fusani, *Horm. Behav.* **54**, 227–233 (2008).
4. W. Goymann, J. C. Wingfield, *Behav. Ecol.* **25**, 685–699 (2014).
5. D. J. Handelsman, A. L. Hirschberg, S. Bermon, *Endocr. Rev.* **39**, 803–829 (2018).
6. N. L. Staub, M. De Beer, *Gen. Comp. Endocrinol.* **108**, 1–24 (1997).
7. E. D. Ketterson, V. Nolan Jr., M. Sandell, *Am. Nat.* **166**, S85–S98 (2005).
8. N. Sinnott-Armstrong, S. Naqvi, M. Rivas, J. K. Pritchard, *eLife* **10**, e58615 (2021).
9. W. Goymann, *Gen. Comp. Endocrinol.* **163**, 149–157 (2009).
10. M. Mokkonen, E. Koskela, T. Mappes, S. C. Mills, *J. Anim. Ecol.* **81**, 277–283 (2012).
11. R. F. Oliveira, M. Taborsky, H. J. Brockmann, Eds., *Alternative Reproductive Tactics: An Integrative Approach* (Cambridge Univ. Press, 2008).
12. J. E. Mank, *Nat. Rev. Genet.* **24**, 44–52 (2023).
13. A. T. Pavitt, C. A. Walling, J. M. Pemberton, L. E. B. Kruuk, *Biol. Lett.* **10**, 20140685 (2014).
14. V. Bogaert *et al.*, *Clin. Endocrinol. (Oxf.)* **69**, 129–135 (2008).
15. C. Ohlsson *et al.*, *PLOS Genet.* **7**, e1002313 (2011).
16. K. S. Ruth *et al.*, *Nat. Med.* **26**, 252–258 (2020).
17. E. D. Ketterson, J. W. Atwell, J. W. McGlothlin, *Integr. Comp. Biol.* **49**, 365–379 (2009).
18. K. A. Rosvall, C. M. Bergeon Burns, S. P. Jayaratna, E. K. Dossey, E. D. Ketterson, *Integr. Comp. Biol.* **56**, 225–234 (2016).
19. K. K. Soma, N. M. Rendon, R. Boonstra, H. E. Albers, G. E. Demas, *J. Steroid Biochem. Mol. Biol.* **145**, 261–272 (2015).
20. C. Küpper *et al.*, *Nat. Genet.* **48**, 79–83 (2016).
21. A. J. Hogan-Warburg, *Ardea* **54**, 109–229 (1966).
22. J. D. M. Tolliver, K. Kupán, D. B. Lank, S. Schindler, C. Küpper, *Anim. Behav.* **197**, 131–154 (2023).
23. J. Jukema, T. Piersma, *Biol. Lett.* **2**, 161–164 (2006).
24. J. L. Loveland, D. B. Lank, C. Küpper, *Front. Genet.* **12**, 641620 (2021).
25. J. L. Loveland *et al.*, *Horm. Behav.* **127**, 104877 (2021).
26. S. Lamichhaney *et al.*, *Nat. Genet.* **48**, 84–88 (2016).
27. J. Hill *et al.*, *Mol. Biol. Evol.* **40**, msad224 (2023).
28. J. L. Goodson, *Horm. Behav.* **48**, 11–22 (2005).
29. L. A. O'Connell, H. A. Hofmann, *Science* **336**, 1154–1157 (2012).
30. K. von Eugen, S. Tabrik, O. Güntürkün, F. Ströckens, *J. Comp. Neurol.* **528**, 2929–2955 (2020).
31. M. Kapun, T. Flatt, *Mol. Ecol.* **28**, 1263–1282 (2019).
32. K. A. Rosvall, C. M. Bergeon Burns, S. P. Jayaratna, E. D. Ketterson, *Horm. Behav.* **84**, 1–8 (2016).
33. I. T. Huhtaniemi, I. T. Huhtaniemi; Themmen APN, *Endocr. Rev.* **21**, 551–583 (2000).
34. J. R. Merritt *et al.*, *Proc. Natl. Acad. Sci. U.S.A.* **117**, 21673–21680 (2020).
35. L. Wu *et al.*, *J. Biol. Chem.* **268**, 12964–12969 (1993).
36. R. Mindnich, G. Möller, J. Adamski, *Mol. Cell. Endocrinol.* **218**, 7–20 (2004).
37. C. Prehn, G. Möller, J. Adamski, *J. Steroid Biochem. Mol. Biol.* **114**, 72–77 (2009).
38. J. L. Loveland, L. M. Giraldo-Deck, A. M. Kelly, *Front. Physiol.* **13**, 1011629 (2022).
39. E. L. Berdan, A. Blanckaert, R. K. Butlin, C. Bank, *PLOS Genet.* **17**, e1009411 (2021).
40. M. Tsachaki, J. Birk, A. Egert, A. Odermatt, *Biochim. Biophys. Acta* **1853**, 1672–1682 (2015).
41. C. P. Sager *et al.*, *J. Steroid Biochem. Mol. Biol.* **206**, 105790 (2021).
42. L. Schiffer *et al.*, *Eur. J. Endocrinol.* **184**, 353–363 (2021).
43. Z. Zhou, C. H. L. Shackleton, S. Pahwa, P. C. White, P. W. Speiser, *Mol. Cell. Endocrinol.* **138**, 61–69 (1998).
44. S. Andersson, N. Moghrabi, *Steroids* **62**, 143–147 (1997).
45. G. F. Ball, J. Balthazart, *Physiol. Behav.* **83**, 329–346 (2004).
46. L. Fusani, M. Gahr, J. B. Hutchison, *Gen. Comp. Endocrinol.* **122**, 23–30 (2001).
47. J. T. Watson, E. Adkins-Regan, *Horm. Behav.* **23**, 432–447 (1989).
48. T. Flatt, M.-P. Tu, M. Tatar, *BioEssays* **27**, 999–1010 (2005).
49. J. W. McGlothlin, E. D. Ketterson, in *Snowbird: Integrative Biology and Evolutionary Diversity in the Junco*, E. D. Ketterson, J. W. Atwell, Eds. (Univ. of Chicago Press, 2016), pp. 100–119.
50. T. N. Wittman, C. D. Robinson, J. W. McGlothlin, R. M. Cox, *Evol. Lett.* **5**, 397–407 (2021).
51. B. Dantzer, E. M. Swanson, *Integr. Comp. Biol.* **57**, 372–384 (2017).
52. R. M. Cox, *Mol. Cell. Endocrinol.* **502**, 110668 (2020).
53. B. Gegenhuber, M. V. Wu, R. Bronstein, J. Tollkuhn, *Nature* **606**, 153–159 (2022).
54. L. M. Giraldo-Deck *et al.*, *Nat. Commun.* **13**, 1384 (2022).
55. A. Zemella, azemella/Ruff_adults_RNASeq_gene_expression_2024: Update MD analysis and results, v6.0.0, Zenodo (2024); https://zenodo.org/records/14056330.

ACKNOWLEDGMENTS

We thank M. Trappschuh for technical assistance in steroid quantifications, S. Roilo for assistance in sample collection, and C.D. Corrales Parada for help with behavioral coding. M. Hau und H. Brumm kindly provided comments on an earlier draft. Y. Pei provided the artwork in Fig. 1A. **Funding:** This work was supported by a sequencing grant from the German Research Foundation (DFG) (KU 3051/2-1) (to C.K., K.N.); a grant by the Austrian Science Fund (FWF) (M3302-B) (to J.L.L.); Helmholtz Munich, German Research Center for Environmental Health; the National Science and Engineering Research Council of Canada (NSERC) (to D.B.L.); and the Max Planck Society. The sequencing was done in the scope of the DFG-funded NGS-Competence Network by the Dresden-concept Genome Center, c/o Center for Molecular and Cellular Bioengineering (CMCB), Technology Platform of the TUD Dresden University of Technology, 01062 Dresden, Germany and MPI-CBG, Pfotenhauerstr. 108, 01307 Dresden, Germany. **Author contributions:** J.L.L., A.Z., V.M.J., G.M., B.B., J.T., and W.G. generated and analyzed the data. J.L.L. and L.M.G.-D. collected tissues. D.B.L. raised and maintained the captive birds. M.G., L.F., and K.A.D. provided reagents and dedicated infrastructure. C.K., K.N., J.L.L., and D.B.L. obtained funds. C.K., K.N., and J.L.L. supervised the work. C.K. conceived the study. C.K., J.L.L., and A.Z. wrote the initial manuscript. All authors edited and approved the final manuscript. **Competing interests:** Authors declare that they have no competing interests. **Data and materials availability:** The RNA sequencing data have been uploaded to NCBI under the BioProject PRJNA1099138. Plasmid accession codes and identifiers of publicly available genomic data are listed in materials and methods and table S8. All code and materials used in the analysis are available at Zenodo (*55*).

SUPPLEMENTARY MATERIALS

science.org/doi/10.1126/science.adp5936
Materials and Methods
Figs. S1 to S11
Tables S1 to S8
References (*56*–*97*)
MDAR Reproducibility Checklist

Submitted 23 April 2024; accepted 26 November 2024
10.1126/science.adp5936

IMMUNOLOGY

Affinity maturation of antibody responses is mediated by differential plasma cell proliferation

Andrew J. MacLean[1]*, Lachlan P. Deimel[1], Pengcheng Zhou[1], Mohamed A. ElTanbouly[1], Julia Merkenschlager[1]†, Victor Ramos[1], Gabriela S. Santos[1], Thomas Hägglöf[1], Christian T. Mayer[2], Brianna Hernandez[1], Anna Gazumyan[1], Michel C. Nussenzweig[1,3]*

Increased antibody affinity over time after vaccination, known as affinity maturation, is a prototypical feature of immune responses. Recent studies have shown that a diverse collection of B cells, producing antibodies with a wide spectrum of different affinities, is selected into the plasma cell (PC) pathway. How affinity-permissive selection enables PC affinity maturation remains unknown. We found that PC precursors (prePCs) expressing high-affinity antibodies received higher levels of T follicular helper cell (T_{FH} cell)–derived help and divided at higher rates compared with their lower-affinity counterparts once they left the germinal center. Our findings indicate that differential cell division by selected prePCs accounts for how diverse precursors develop into a PC compartment that mediates serological affinity maturation.

Increasing antibody affinity over time after vaccination is a prototypical feature of humoral immune responses. Experiments in transgenic mice suggest that in the early germinal center (GC)–independent stages of the immune response, B cells expressing high-affinity B cell receptors are preferentially selected into the plasma cell (PC) compartment (*1*–*3*).

Selection within the GC reaction itself is governed by T follicular helper cells (T_{FH} cells) that recruit B cells and control the degree of B cell clonal expansion (*4*). B cells expressing receptors that bind to and can capture antigen displayed on the surface of follicular dendritic cells in the light zone (LZ) process and present antigens to a limited number of T_{FH} cells in exchange for help signals. Selected LZ B cells initiate a transcriptional program that enables them to move into the dark zone (DZ), where they undergo division and somatic mutation before returning to the LZ to test their newly mutated receptors in subsequent rounds of selection. The number of division cycles and the speed of cell division in the DZ is directly related to the strength of T_{FH} cell signals and is governed by the level of *Myc* expression (*5*–*7*). Iterative cycles of DZ division and LZ selection produce GC B cells with increasing affinity for the immunogen over the course of an immune response. However, loss of affinity owing to persistent somatic mutation and evolution of the T_{FH} cell compartment eventually leads to GC diversification and increasing inclusion of lower-affinity B cells (*8*–*12*).

[1]Laboratory of Molecular Immunology, The Rockefeller University, New York, NY, USA. [2]Experimental Immunology Branch, Center for Cancer Research, National Cancer Institute, National Institutes of Health, Bethesda, MD, USA. [3]Howard Hughes Medical Institute (HHMI), The Rockefeller University, New York, NY, USA.
*Corresponding author. Email: nussen@rockefeller.edu (M.C.N.); amaclean@rockefeller.edu (A.J.M.)
†Present address: Department of Immunology, Harvard Medical School, Boston, MA, USA.

High-affinity cells of GC origin become enriched in the antibody-secreting PC compartment over time after immunization (*13*–*16*). This observation, in conjunction with the known selection mechanisms within the GC, originally supported a model whereby high-affinity cells preferentially undergo PC differentiation. In contrast to these findings, three recent independent studies have shown that in genetically intact animals, diverse collections of GC B cells develop into PC progenitors (*8*, *17*, *18*). Additionally, these studies found little or no enrichment for high-affinity antibody–expressing cells among the precursor population, PC precursors (prePCs) (*19*, *20*), in the GC (*8*, *17*, *18*). How this population of GC precursors that expresses antibodies with a broad range of affinities gives rise to a PC compartment dominated by cells producing high-affinity antibodies is not understood.

High-affinity cells are overrepresented in the PC compartment

To examine the relationship between GC B cells and PCs, we tracked the two cell types using fate mapping of S1pr2-CreERT2 $R26^{lsl\text{-}ZSGreen}$ mice in which tamoxifen administration permanently labels GC cells and their subsequent products (*21*). Administration of tamoxifen to immunized mice confirmed that this reporter strain labels GC B cells and activated B cells but not mature PCs (fig. S1, A to C). Tamoxifen was administered 5 days after immunization with the model hapten antigen 4-hydroxy-3-nitrophenyl (NP) conjugated to the carrier protein ovalbumin (OVA) (NP-OVA), and single-cell sequencing was performed on labeled GC B cells and PCs isolated from the draining lymph node on day 14 (Fig. 1, A and B). Uniform manifold approximation and projection (UMAP) integrating cellular indexing of transcriptomes and epitopes by sequencing (CITE-seq) data revealed distinct clusters of GC B cells and PCs characterized by Fas and CD86 or by CD138 surface protein expression, respectively (fig. S2).

Immunoglobulin (Ig) sequence analysis showed expanded clones of cells that were further subdivided into nodes containing one or more cells expressing identical antibodies. The combined clonal trees consisted of 535 individual nodes with 1 to >100 members (Fig. 1C). On the basis of surface staining and gene expression profiles, nodes were divided into those consisting of only GC B cells, both GC B cells and PCs ("mixed nodes"), or only PCs. Nodes consisting of only PCs were the least abundant, representing <8% of the nodes (38 of 535 nodes; Fig. 1D). Most PCs were found within mixed nodes that were also larger than either GC- or PC-only nodes (Fig. 1, E to G). IGHV1-72 antibody expression is associated with relatively high-affinity NP binding (*22*). Notably, compared with GC nodes, nodes containing PCs were enriched for affinity-enhancing mutations in IGHV1-72 [W33L (i.e., Trp^{33}→Leu), K59R (Lys^{59}→Arg), or Y99G (Tyr^{99}→Gly)] (*22*, *23*) (Fig. 1H). Furthermore, irrespective of node identity, PCs were enriched for affinity-enhancing mutations compared with contemporaneously labeled GC B cells (63 ± 23% PC versus 42 ± 11% GC; $P = 0.02$; Fig. 1I). Thus, although prePC antibody affinity is indistinguishable from contemporaneous GC B cells (*8*, *17*, *18*), PCs are enriched for high-affinity antibodies. Moreover, the presence of identical antibody sequences in large, expanded nodes containing GC B cells and PCs suggests that the mechanisms that govern clonal expansion of the two cell types overlap.

Differential expansion of high-affinity PCs

Two nonexclusive cellular processes could contribute to the observed enrichment of high-affinity PCs over GC B cells: differential cell death and/or division. To determine whether cell death contributed to PC affinity maturation, we purified live and dying PCs from draining lymph nodes of NP-OVA–immunized mice using the $Rosa26^{INDIA/INDIA}$ apoptosis reporter mice (*24*). Ig sequence analysis revealed similar abundance of high-affinity IGHV1-72–expressing cells in live and dying PC fractions (fig. S3, A to D). In addition, most Ig sequences found among apoptotic PC clones were also present in the live fraction (fig. S3C). Thus, differential cell death did not appear to drive the accumulation of high-affinity PCs over time.

To determine whether high-affinity PCs have a proliferative advantage, we tracked cell division using Vav^{tTa} Col1A1-tetO-histone $H2B^{mCherry}$ reporter mice (H2B-mCherry) (*25*). Under steady-state conditions, tTA is expressed in hematopoietic cells and induces high levels of the histone H2B-mCherry fusion protein expression. Administration of doxycycline represses histone H2B-mCherry synthesis, and therefore mCherry fluorescence dilutes in

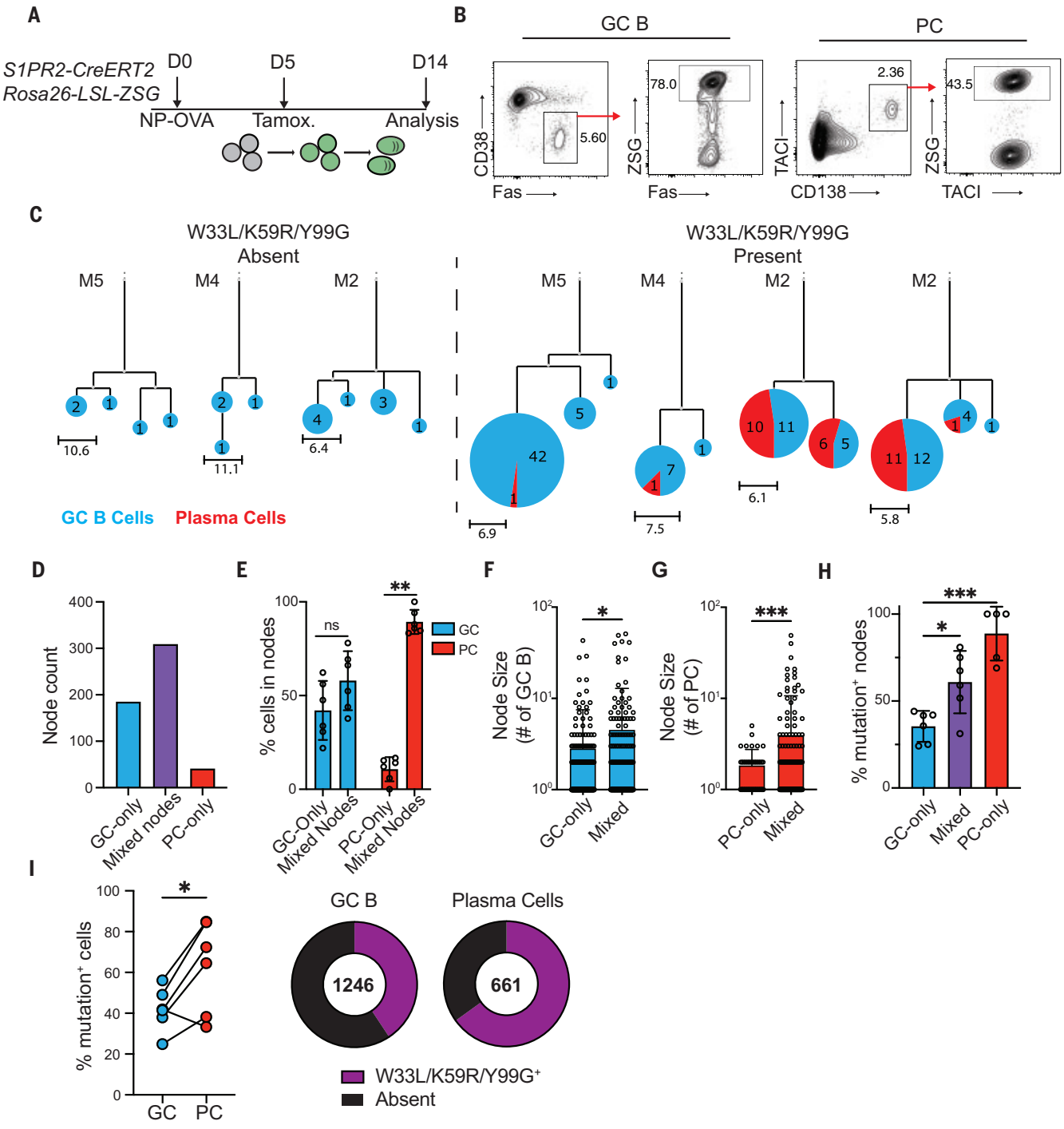

Fig. 1. High-affinity antibody–producing PCs are overrepresented relative to contemporaneous GC B cells. (**A**) Experimental layout for (B) to (H). D0, day 0; Tamox., tamoxifen. (**B**) Representative flow cytometry plots showing strategy for isolating popliteal lymph node (pLN) GC B cells (pregated on live, $TACI^-$ $CD138^-$ $B220^+$; $CD38^-Fas^+ZSG^+$) and PCs (pregated on live; $CD138^+TACI^+ZSG^+$). Full gating strategy is displayed in fig. S2A. (**C**) Representative IgH+IgL sequence-based phylogenetic trees highlighting GC B cell (blue) and PC (red) distribution. Expanded clones containing (right) or not containing (left) affinity-enhancing mutations. Each circle represents one node of cells with identical sequences. Scale represents mutational distance observed between related sequences. (**D**) Total numbers of GC-only, PC-only, or mixed nodes analyzed. (**E**) Frequency of GC B cells (blue bars) or PCs (red bars) found within mixed or single-cell–type nodes. Each point represents one animal. (**F** and **G**) Node size: Number of individual GC B cells (F) or PCs (G) in either uniform or mixed nodes. (**H**) Frequency of nodes with affinity-enhancing mutations. Each point represents one mouse, summarizing 51 to 176 nodes per mouse. (**I**) Frequency of affinity-enhancing mutations within total GC B cells and PCs. (Left) Summary. Each pair of connected points represents GC B cells and PCs isolated from one animal. (Right) Quantitation of total cells. Numbers in center represent total number of sequences analyzed. *P < 0.05; **P < 0.005; ***P < 0.0005; ns, not significant. Statistics by analysis of variance (ANOVA) [(F) and (G)], mixed effects analysis (H), or paired two-tailed Student's t test (I). Data are pooled from two independent experiments, n = 6 mice per group.

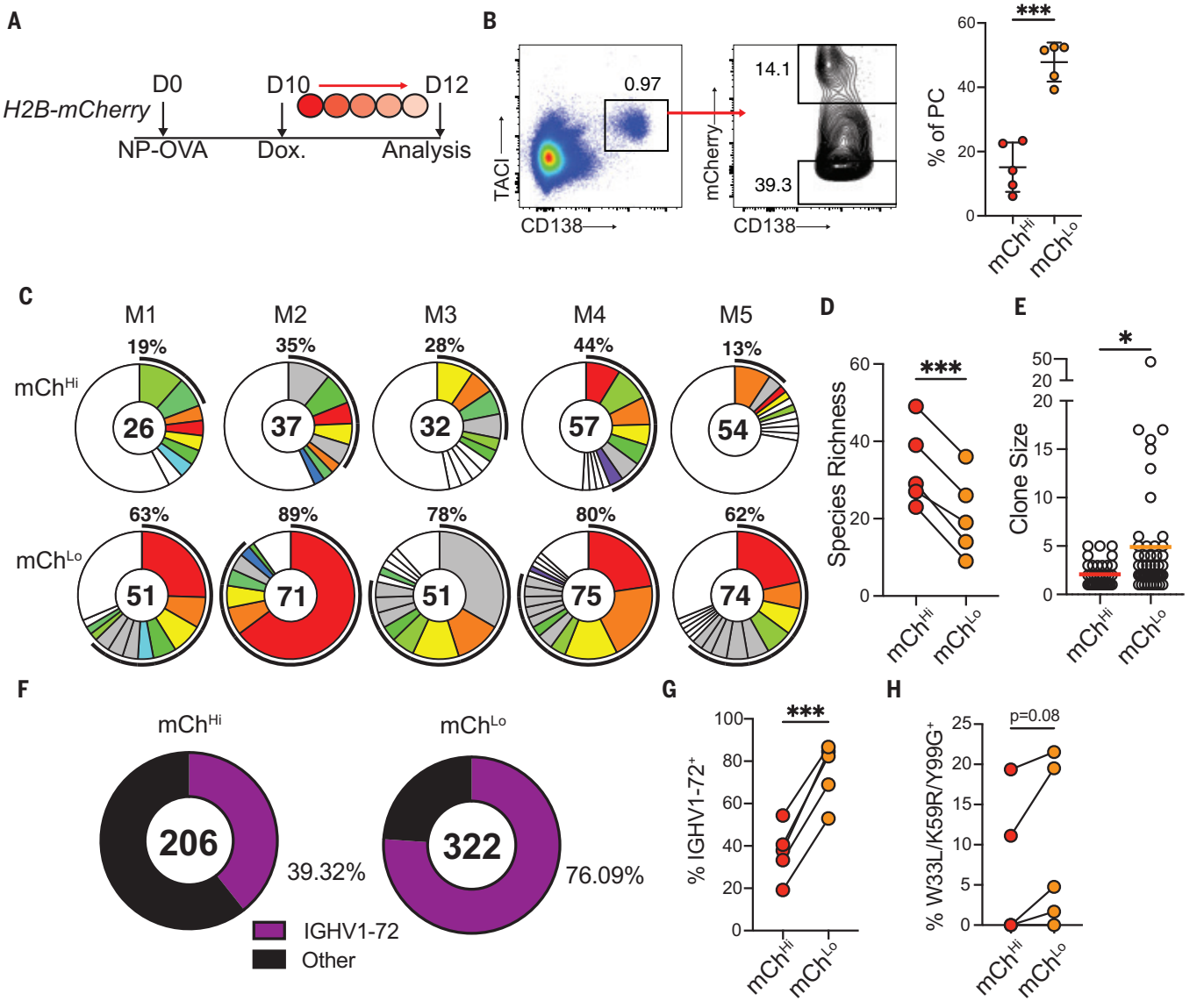

Fig. 2. High-affinity antibody–producing PCs are more proliferative. (**A**) Experimental layout for (B) to (F). Dox., doxycycline. (**B**) (Left) Flow cytometry profile showing TACI^{+}CD138^{+} PCs and gating for mCherry^{hi} (mCh^{hi}) and mCherry^{lo} (mCh^{lo}) cells from pLNs. (Right) mCh^{lo} and mCh^{hi} PC frequency. Each point represents one mouse. Graphs display means ± SDs. (**C**) Clonal distribution of paired Ig sequences (IgH+IgK/IgL) among mCh^{hi} and mCh^{lo} PCs isolated from each mouse. Colored segments represent expanded clones, and singlets are represented by white segments. The number in the center represents the number of sequences analyzed per population. The outer segment annotation denotes the percentage of cells that are members of expanded clones. (**D**) Chao1 species richness quantification. Each pair of points represents one mouse. (**E**) Clone size. Each point represents one clone. (**F**) Frequency of mCh^{hi} or mCh^{lo} PCs bearing high-affinity IGHV1-72 B cell receptors. Number in center represents total number of sequences. (**G**) Summary of (F). Each pair of points represents one mouse. (**H**) Frequency of high-affinity mutation–containing sequences among IGHV1-72^{+}–expressing mCh^{hi} or mCh^{lo} PCs. *P < 0.05; ***P < 0.0005. Statistics by paired two-tailed Student's t test [(B), (D), (G), and (H)] or unpaired Student's t test (E). Data are pooled from two independent experiments, n = 5 mice per group.

proportion to cell division (*25*). H2B-mCherry mice were immunized with NP-OVA and were administered doxycycline 10 days after immunization. PCs were isolated from draining lymph nodes 2 days later on the basis of their high or low levels of division (mCherry^{lo} and mCherry^{hi} PCs, respectively; Fig. 2, A and B). mCherry^{lo} PCs that had undergone greater levels of division showed reduced species richness and larger clonal families when compared with their non-dividing counterparts, indicating rapid clonal expansion in this population (Fig. 2, C to E). Notably, there was an enrichment of PCs expressing high-affinity IGHV1-72 among the more divided PCs (75.1 ± 14% mCherry^{lo} versus 37.1 ± 12% mCherry^{hi}; P = 0.0001; Fig. 2, F and G). At this early time point, the W33L, K59R, and/or Y99G affinity-enhancing mutations were largely absent from both IgHV1-72^{+} PC populations, but there was a trend toward enrichment in the more divided mCherry^{lo} group (Fig. 2H; P = 0.08). These findings were confirmed using Blimp1-CreERT2 R26$^{lsl\text{-}ZSGreen}$ mice, a reporter strain that selectively labels differentiated PCs (fig. S4, A and B). Blimp1-CreERT2 R26$^{lsl\text{-}ZSGreen}$ mice were combined with H2B-mCherry mice to enable tamoxifen-mediated ZsGreen (ZSG) labeling of a synchronized cohort of PCs, which can be division tracked by mCherry dilution. Isolation of mCherry^{hi} and mCherry^{lo} ZSG^{+} PCs revealed that among mature PCs, the more proliferative cells were enriched for NP bait binding and expression

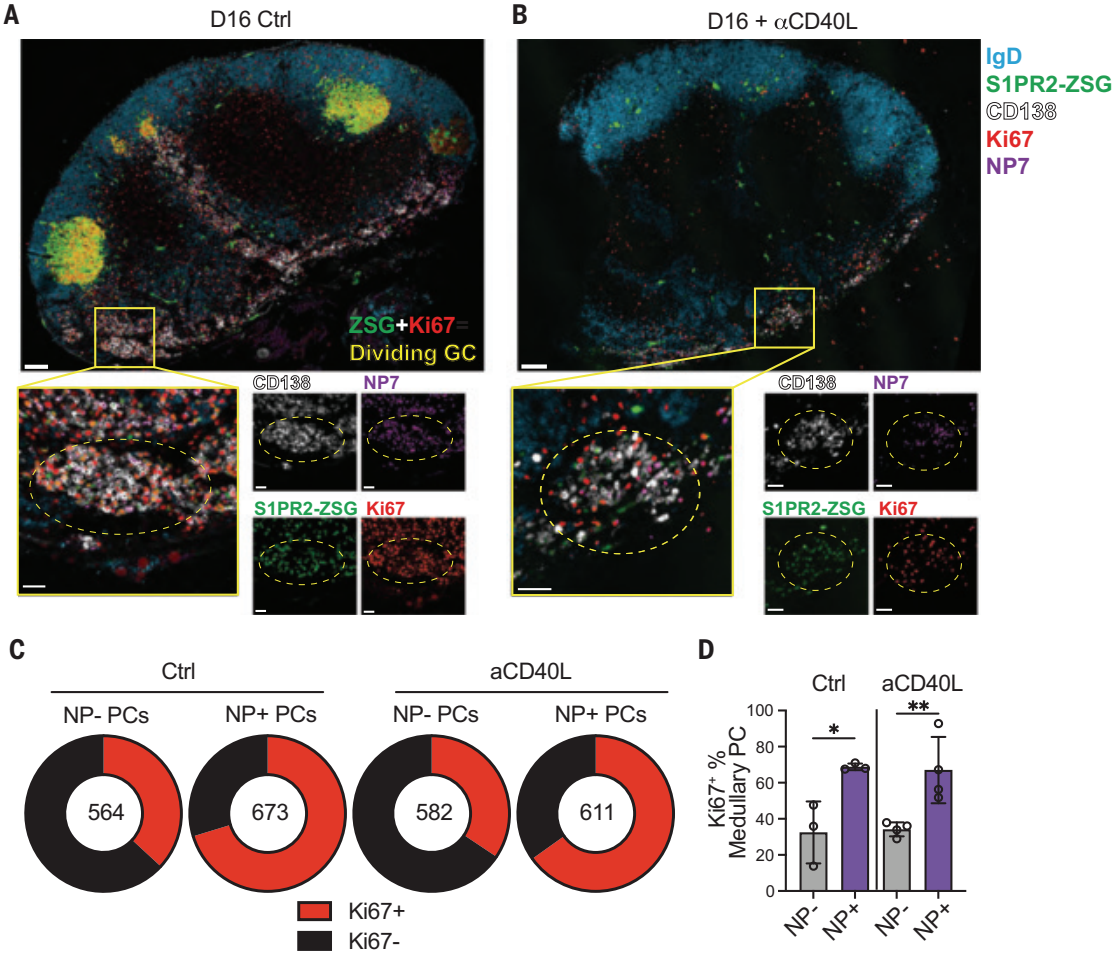

Fig. 3. Post-GC expansion of PCs. (**A** and **B**) Confocal microscopy images of pLNs isolated from S1pr2-CreERT2 R26$^{lsl\text{-}ZSGreen}$ mice immunized with NP-OVA, treated with tamoxifen on D8 and anti-CD40L or isotype control on D10 and D12. Large tiles show overview of pLN architecture. Inset boxes show individual clusters of dividing Ki67^{+} NP^{+} PCs that are highlighted by dashed circles. Individual channels are shown beside merged images. Scale bars, 100 μm (large tiles) and 30 μm (inset boxes). Ctrl, control. (**C**) Quantitation of fraction of medullary PCs that are Ki67^{+} among NP^{+} and NP^{-} populations, as quantified from confocal images, as in (A). The number in the center represents the number of cells analyzed per population. (**D**) Summary of (C). Each point represents one mouse. Graph displays means ± SDs. *P < 0.05; **P < 0.005; ordinary one-way ANOVA. Data are representative of three experiments, n = 3 to 4 mice per group.

of high-affinity Ig gene rearrangements (fig. S4, C to H). These data indicated that higher-affinity B cell receptor expression was associated with differential division at the mature PC stage.

To validate these findings using vaccine antigens, we immunized H2B-mCherry mice with either severe acute respiratory syndrome coronavirus 2 (SARS-CoV-2) receptor binding domain (RBD) or combined tetanus and diphtheria toxoid antigens (Tenivac) and administered doxycycline on day 10 after vaccination. Antigen binding was used as a surrogate for higher-affinity antigen binding cells (fig. S5, A and B). Flow cytometric analysis revealed that RBD or tetanus and diphtheria toxoid binding cells were enriched and showed higher mean fluorescence among the divided mCherry^{lo} compared with mCherry^{hi} cells, even when normalized for surface Ig expression levels (fig. S5, C to H). The combined dataset indicated that high-affinity PCs underwent greater levels of clonal expansion than lower-affinity PCs irrespective of the composition of the administered immunogen or adjuvant formulation.

PC selection outside of the GC

To examine the site of affinity-driven PC clonal expansion, S1pr2-CreERT2 R26$^{lsl\text{-}ZSGreen}$ mice were immunized with NP-OVA, treated with tamoxifen on day 8, and then given anti-CD40L or isotype control antibodies on days 10 and 12 after immunization. In this setting, tamoxifen will label GC products and anti-CD40L will terminate the GC reaction 2 days later, allowing a cohort of PCs generated between days 8 and 10 to be tracked. Draining lymph nodes were examined by confocal microscopy on day 16 after immunization (Fig. 3, A and B, and fig. S6A).

Large GCs, in which many of the cells were actively dividing (as determined by positive staining for Ki67), were observed in control mice that did not receive anti-CD40L. In addition, we found discrete clusters of dividing NP-binding PCs (marked by CD138^{+}ZSG^{+}Ki67^{+}NP^{+}) that were particularly abundant in the lymph node medulla. Anti-CD40L treatment aborted the GC reaction (Fig. 3, A and B, and fig. S6, A and B). By contrast, the clusters of proliferating NP-specific PCs persisted (Fig. 3, A and B). Quantitation of medullary PC division by Ki67 staining revealed a higher proportion of dividing NP-binding PCs than nonbinding PCs. Moreover, this feature was retained on anti-CD40L treatment and GC depletion (Fig. 3, C and D). Thus, dividing antigen-specific PCs were observed in medullary foci outside of the anatomical confines of the GC, and these foci were maintained in the absence of active GCs during the observation period.

To determine whether the observed enrichment of high-affinity PCs continued in a post-GC compartment, we isolated PCs from anti-CD40L–treated S1pr2-CreERT2 R26$^{lsl\text{-}ZSGreen}$ mice. The mice also received the drug FTY720 to inhibit S1PR1-driven egress signals and to prevent PCs from leaving the node (*26*). Treatment with anti-CD40L effectively depleted draining lymph nodes of GCs and activated B cells within 2 days (Fig. 3, A and B, and fig. S6, A to D). Ig sequence analysis on day 10 showed that 67% of labeled PCs were IGHV1-72^{+} and that by day 16, this increased to 83% under control conditions (P = 0.037; Fig. 4, A to E). Notably, the PC compartment was equally enriched for high-affinity clones on day 16 in

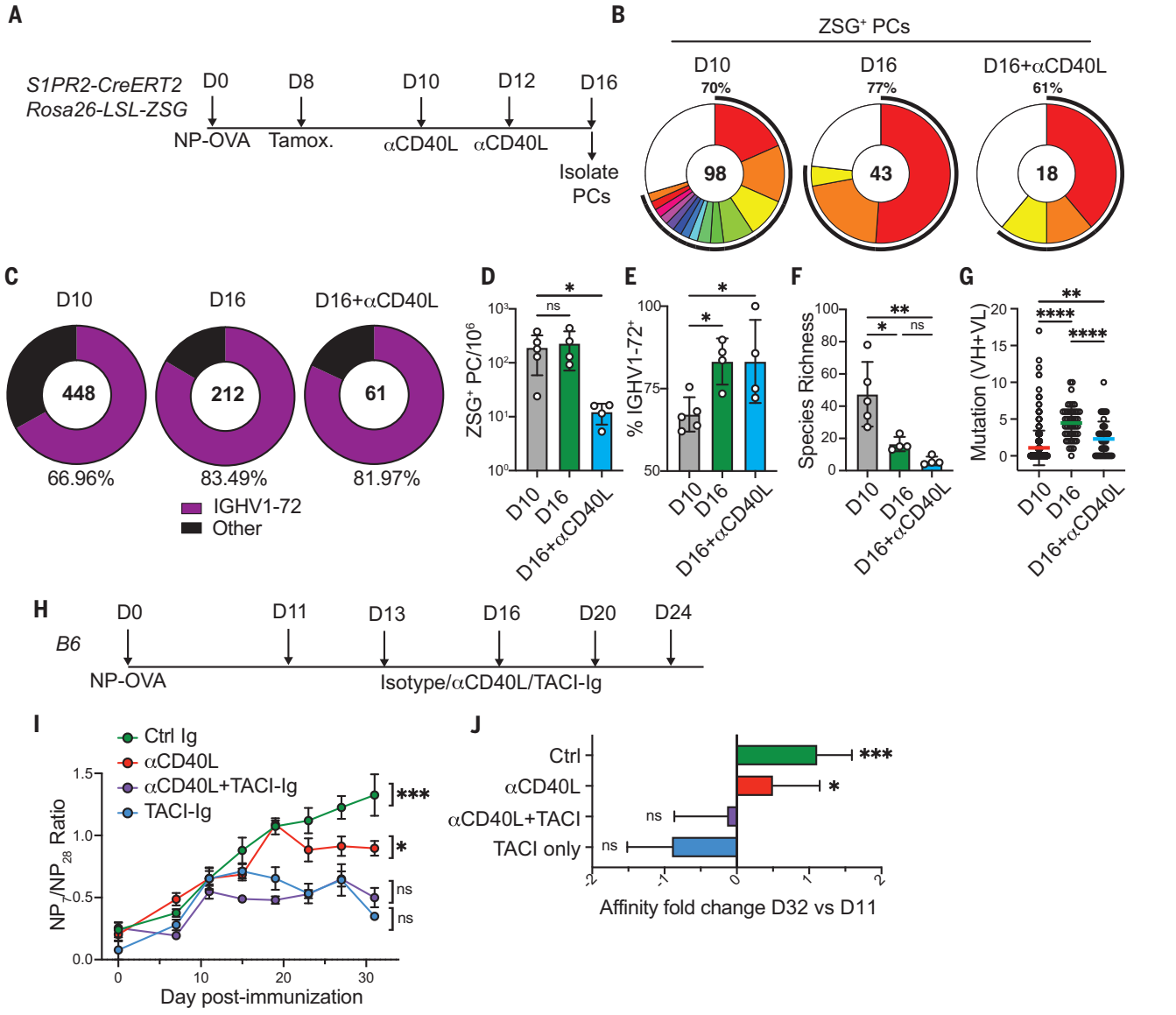

Fig. 4. Post-GC evolution of the PC repertoire and serological affinity maturation. (**A**) Experimental layout for (B) to (G). (**B**) Clonal distribution of paired Ig sequences from representative mice. Colored segments represent expanded clones, and singlets are represented by white segments. The number in the center represents the number of sequences analyzed per population. The outer segment annotation denotes the percentage of cells that are members of expanded clones. (**C**) Frequency of ZSG$^+$ PCs expressing IGHV1-72. The number in the center represents the number of sequences analyzed. (**D**) Number of ZSG$^+$ PCs in each experimental group. (**E**) Summary of IGHV1-72 frequency presented in (C). (**F**) Chao1 species richness. In (D) to (F), each point represents one mouse, n = 4 to 5 mice per condition. (**G**) Number of VH+VL mutations in paired Ig sequences. Each point represents one cell. (**H**) Experimental layout for (I) and (J). (**I**) Ratio of NP_7/NP_{28}-binding IgG in serum measured by enzyme-linked immunosorbent assay (ELISA). (**J**) Fold change in affinity (NP_7/NP_{28} ratio) at D32 versus D11. Data are presented as means ± SDs. Data are representative of two experiments, n = 5 to 10 mice per group. *P < 0.05; **P < 0.005; ****P < 0.0001. Statistics by ordinary one-way ANOVA [(D) to (F)], Kruskal-Wallis test (G), or mixed effects analysis [(I) and (J)]. For full statistical comparisons, see fig. S4E.

mice treated with anti-CD40L under conditions that depleted GCs (Fig. 4, C to E). In addition, the PC compartment in CD40L-treated mice displayed the same characteristic reduction in species richness that was indicative of clonal expansion seen in control mice (Fig. 4, B and F). Finally, labeled PCs obtained from anti-CD40L–treated mice displayed a reduced mutational load, which suggests that they were derived from GC precursors that exited the GC at a time when mutations were less abundant (Fig. 4G).

Serological affinity maturation is typified by a rapid increase in the affinity of circulating antibodies (*27*). We hypothesized that the continued preferential expansion of high-affinity PCs after GC depletion (Fig. 4, A to G) would lead to measurable improvements of serum anti-NP affinity. To determine whether PCs in anti-CD40L–treated mice continue to support affinity maturation after depletion of GC and activated B cells, we measured the serum antibody binding to bovine serum albumin derivatized with either 7 or 28 molecules of NP (Fig. 4H and fig. S6, A to E). Control mice displayed a marked increase in NP_7/NP_{28} immunoglobulin G (IgG) binding ratio between days 12 and 32,

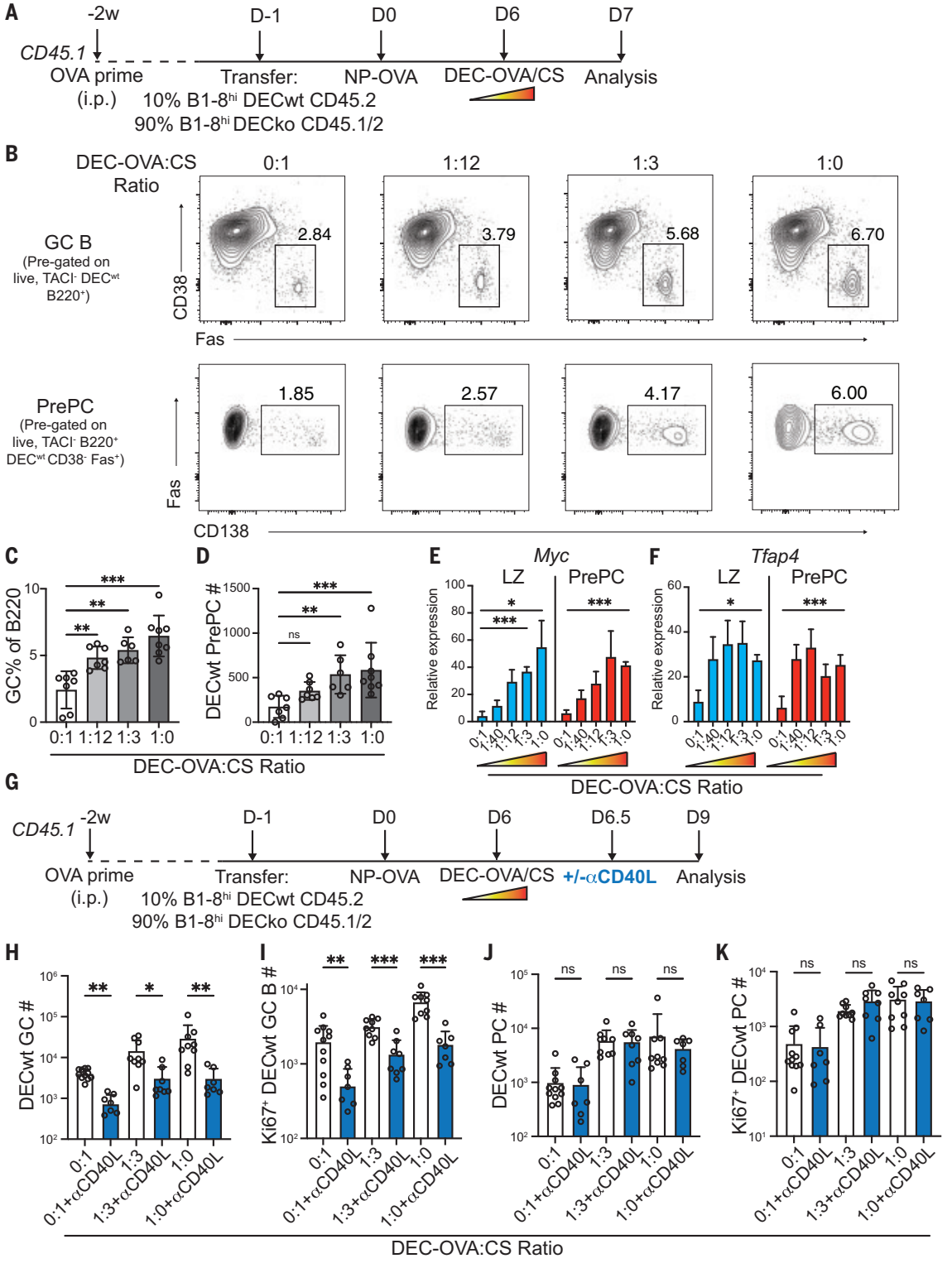

Fig. 5. PC proliferation is proportional to signal strength. (**A**) Experimental outline for (B) to (F). i.p., intraperitoneal; ko, knockout. (**B**) Representative flow cytometry plots showing GC B cells ($B220^+CD38^-Fas^+$; top) and prePCs ($B220^+CD38^-Fas^+CD138^+$; bottom) after treatment with different ratios of anti–DEC-205–OVA:CS. (**C** and **D**) Quantitation of DEC^{WT} (WT, wild-type) GC B cells (C) and prePCs (D) 24 hours after anti–DEC-205 treatment. (**E** and **F**) Quantitative polymerase chain reaction (qPCR) of sorted DEC^{WT} GC LZ ($CD86^+CXCR4^-$ GC B cells) and prePCs (as above), showing glyceraldehyde-3-phosphate dehydrogenase (GAPDH)–normalized relative expression for *Myc* (E) and *Tfap4* (F). Data in (A) to (D) and (E) and (F) are representative of three independent experiments, $n = 6$ to 8 mice per group. (**G**) Experimental outline for (H) to (K). (**H** and **I**) Quantitation of DEC^{WT} GC B cells (H) and $Ki67^+$ DEC^{WT} GC B cells (I). (**J** and **K**) Quantitation of DEC^{WT} PCs (J) and $Ki67^+$ DEC^{WT} PCs (K). Data are presented as means ± SDs. Each point in (C), (D), and (H) to (K) represents one mouse. Data in (H) to (K) are representative of four independent experiments. $^*P < 0.05$; $^{**}P < 0.005$; $^{***}P < 0.0005$. Statistics by ANOVA (C) or Kruskal-Wallis test [(D) and (H) to (K)].

indicating a rapid increase in anti-NP affinity that was aborted by depleting PCs with TACI-Ig (Fig. 4I). Notably, and consistent with the above sequencing data, the serum antibody response continued to undergo affinity maturation for several weeks after anti-CD40L treatment (Fig. 4, I and J).

We concluded that serological affinity maturation can proceed in the absence of continued output from the GC reaction, and it was suppressed by PC depletion. These findings suggest that after export from the GC, newly generated PCs undergo affinity-based expansion in a manner that contributes to increasing serum antibody affinity.

PC division is proportional to the strength of T cell help

GC B cells in the LZ of the GC structure compete for limited help signals from T_{FH} cells, a process known as positive selection. The amount of help received by a B cell is directly proportional to the amount of antigen captured and

presented by the B cell (*25*, *28*). Positively selected GC B cells up-regulate expression of the transcription factor *Myc* in proportion to the strength of T cell signals and migrate to the DZ, where they undergo cycles of T_{FH} cell–independent inertial cell division in proportion to the amount of *Myc* expression (*5*, *25*, *29*).

To determine whether a similar process regulates the relative amount of PC expansion, we delivered graded doses of the antigen OVA to ongoing GCs using chimeric anti–DEC-205–OVA antibodies (*28*) (Fig. 5A). Protein antigens loaded onto anti–DEC-205 are delivered to DEC-205$^+$ GC B cells, supplying a B cell receptor–independent supply of antigen that can be processed and presented to T_{FH} cells (*28*). As expected, GC B cells expanded in direct proportion to the amount of antigen delivered (Fig. 5, B and C). Antigen delivery by anti–DEC-205–OVA also produced a rapid increase in the frequency and numbers of prePCs (B220^{hi} CD38$^-$ Fas$^+$ CD138$^+$; Fig. 5, B and D). To determine whether prePCs in the LZ of the GC also expressed *Myc* in proportion to antigen delivery by DEC-205, we purified these cells 24 hours after graded doses of anti–DEC-205–OVA injection. Consistent with their commitment to the PC fate, these cells displayed elevated levels of *Irf4*, a transcription factor that promotes PC differentiation, and lower expression levels of the antigen receptor signaling-induced factor *Nr4a1* compared with other LZ GC B cells (fig. S7, A and B). Notably, they showed increases in *Myc* that were directly proportional to the amount of antigen delivered (Fig. 5E). *Tfap4*, a transcription factor downstream of c-Myc, also showed a similar induction pattern, although the expression of this factor plateaued at lower antigen concentrations (Fig. 5F). In addition, prePC proliferation, as measured by Ki67 expression, was proportional to the amount of antigen supplied (fig. S7, C and D).

To test whether T_{FH} cell help in the LZ could support continued PC expansion, anti-CD40L was administered 12 hours after anti–DEC-205–OVA. In this setting, GC B cells acquired high levels of cognate antigen and interacted with T_{FH} cells for ~12 hours, after which subsequent T cell help was inhibited by CD40L blockade as evidenced by GC collapse (Fig. 5G; Fig. 3, A and B; and fig. S6, A and B). Treatment with anti-CD40L 12 hours after anti–DEC-205–OVA injection prevented further GC B cell expansion and blocked additional Ki67 expression in GC B cells, including prePCs (Fig. 5, H and I, and fig. S7, E and F). By contrast, mature PCs continued to expand and divide in the days after anti-CD40L treatment in direct proportion to the amount of antigen captured (Fig. 5, J and K). The data indicated that after a short pulse of T cell help, developing prePCs up-regulated *Myc* and underwent cycles of cell division in the absence of continued T cell signals.

Other signals are known to enhance the magnitude of the PC response (*14*). For example, PCs are highly sensitive to the levels of the cytokine interleukin-21 (IL-21) (*30*, *31*), and IL-21–producing T cells have been reported to localize in foci outside of the B cell follicle (*32*). To test whether IL-21 could support the expansion of committed PCs, we fate mapped PCs on day 8 using Blimp1-CreERT2 reporter mice and subsequently treated with anti-CD40L or anti–IL-21R from days 10 to 12. PC division was assessed by Ki67 staining. As expected, analysis of ZSG-labeled PCs revealed that continued CD40L signals were not required to sustain PC proliferation (fig. S8, A to C). By contrast, partial blockade of IL-21R led to reduced proliferation of mature ZSG$^+$ PCs, which indicates that IL-21 supports the post-GC expansion of PCs (fig. S8, B and C).

Discussion

Current models of PC differentiation suggest that B cell receptor affinity is deterministic of cell fate (*14*, *15*, *27*). Our experiments indicated that although a heterogeneous collection of prePCs—including those expressing low-affinity receptors—developed into PCs, they subsequently underwent differential affinity-dependent division. As a result, PCs expressing higher-affinity antibodies contributed disproportionately to serum antibodies, promoting affinity maturation.

Antibody responses develop in two stages: a GC-independent early phase during which B cells rapidly develop into dividing plasmablasts that produce relatively lower-affinity antibodies and a second GC-dependent phase that produces higher-affinity antibodies responsible for serologic affinity maturation. In transgenic mice that carry high-affinity antibodies, the early GC-independent rapid burst of PC development and expansion is affinity dependent (*1*, *2*). By contrast, under physiologic circumstances, this early PC response produces primarily germline-encoded antibodies with relatively lower affinity compared with those produced in GCs (*15*, *33*, *34*). In animals with a polyclonal B cell repertoire, GCs enable B cell clonal expansion and antibody hypermutation, both of which are essential for antibody affinity maturation (*27*, *35*, *36*). Our experiments elucidated the mechanisms by which GC-dependent PC selection enables affinity maturation in polyclonal immune responses.

The GC LZ also contains prePCs that express IRF4, CD138, and variable levels of Myc and share many of the transcriptional features of LZ B cells selected for DZ reentry (*8*, *14*). Similar to DZ B cells, PC descendants of prePCs undergo rapid cell division in GC-adjacent sites, but they do not undergo additional somatic mutation and so retain antibody specificity (*37*). Our experiments show that the amount of clonal expansion by newly exported PCs was directly proportional to affinity and the strength of historic selection signals that these cells received in the LZ, providing a mechanistic explanation for how PC selection is regulated in relation to affinity. Notably, our data are entirely consistent with the observation that the PC pool tends to be more clonal than the contemporary GC B cells or prePCs from which they develop (*8*, *17*). In addition to PCs in the lymph nodes, long-lived PCs in the bone marrow are also enriched for high-affinity antibody–producing cells (*38*, *39*). Our data suggest that this phenomenon is likely a result of overrepresentation of high-affinity PCs among dividing plasmablasts that subsequently seed the bone marrow.

Post-GC PC clonal expansion in proportion to historical T_{FH} cell signals and *Myc* expression parallels Myc-regulated GC B cell clonal expansion, thereby enabling rapid affinity maturation. The proposed model does not preclude permissive selection of GC cells with diverse affinities into the PC compartment (*8*, *17*, *18*). Instead, our findings help resolve the apparent contradiction between affinity-permissive selection into the PC compartment and rapid affinity maturation.

REFERENCES AND NOTES

1. D. Paus *et al.*, *J. Exp. Med.* **203**, 1081–1091 (2006).
2. T. D. Chan *et al.*, *J. Immunol.* **183**, 3139–3149 (2009).
3. T. G. Phan *et al.*, *J. Exp. Med.* **203**, 2419–2424 (2006).
4. S. Crotty, *Immunity* **50**, 1132–1148 (2019).
5. S. Finkin, H. Hartweger, T. Y. Oliveira, E. E. Kara, M. C. Nussenzweig, *Immunity* **51**, 324–336.e5 (2019).
6. D. Dominguez-Sola *et al.*, *Nat. Immunol.* **13**, 1083–1091 (2012).
7. D. P. Calado *et al.*, *Nat. Immunol.* **13**, 1092–1100 (2012).
8. M. A. ElTanbouly *et al.*, *J. Exp. Med.* **221**, e20231838 (2024).
9. T. Hägglöf *et al.*, *Cell* **186**, 147–161.e15 (2023).
10. R. V. H. de Carvalho *et al.*, *Cell* **186**, 131–146.e13 (2023).
11. J. Merkenschlager *et al.*, *Nature* **591**, 458–463 (2021).
12. J. Merkenschlager *et al.*, *Nat. Commun.* **14**, 6944 (2023).
13. T.-A. Yang Shih, E. Meffre, M. Roederer, M. C. Nussenzweig, *Nat. Immunol.* **3**, 570–575 (2002).
14. W. Ise, T. Kurosaki, *Immunol. Rev.* **288**, 64–74 (2019).
15. S. L. Nutt, P. D. Hodgkin, D. M. Tarlinton, L. M. Corcoran, *Nat. Rev. Immunol.* **15**, 160–171 (2015).
16. A. Radbruch *et al.*, *Nat. Rev. Immunol.* **6**, 741–750 (2006).
17. A. Sprumont, A. Rodrigues, S. J. McGowan, C. Bannard, O. Bannard, *Cell* **186**, 5486–5499.e13 (2023).
18. H. J. Sutton *et al.*, *Immunity* **57**, 245–255.e5 (2024).
19. W. Ise *et al.*, *Immunity* **48**, 702–715.e4 (2018).
20. N. J. Kräutler *et al.*, *J. Exp. Med.* **214**, 1259–1267 (2017).
21. R. Shinnakasu *et al.*, *Nat. Immunol.* **17**, 861–869 (2016).
22. D. Allen, T. Simon, F. Sablitzky, K. Rajewsky, A. Cumano, *EMBO J.* **7**, 1995–2001 (1988).
23. K. Furukawa, A. Akasako-Furukawa, H. Shirai, H. Nakamura, T. Azuma, *Immunity* **11**, 329–338 (1999).
24. C. T. Mayer *et al.*, *Science* **358**, eaao2602 (2017).
25. A. D. Gitlin, Z. Shulman, M. C. Nussenzweig, *Nature* **509**, 637–640 (2014).
26. K. Kabashima *et al.*, *J. Exp. Med.* **203**, 2683–2690 (2006).
27. G. D. Victora, M. C. Nussenzweig, *Annu. Rev. Immunol.* **40**, 413–442 (2022).
28. G. D. Victora *et al.*, *Cell* **143**, 592–605 (2010).
29. J. Pae *et al.*, *J. Exp. Med.* **218**, e20201699 (2021).
30. Z. Chen *et al.*, *Sci. Immunol.* **8**, eadd1728 (2023).
31. K. Ozaki *et al.*, *J. Immunol.* **173**, 5361–5371 (2004).
32. J. M. Odegard *et al.*, *J. Exp. Med.* **205**, 2873–2886 (2008).
33. I. C. MacLennan *et al.*, *Immunol. Rev.* **194**, 8–18 (2003).
34. J. G. Cyster, C. D. C. Allen, *Cell* **177**, 524–540 (2019).
35. N. S. De Silva, U. Klein, *Nat. Rev. Immunol.* **15**, 137–148 (2015).
36. J. Jacob, G. Kelsoe, K. Rajewsky, U. Weiss, *Nature* **354**, 389–392 (1991).

37. Y. Zhang *et al*., *J. Exp. Med.* **215**, 1227–1243 (2018).
38. M. J. Robinson *et al*., *Sci. Immunol.* **7**, eabm8389 (2022).
39. Y. Takahashi, P. R. Dutta, D. M. Cerasoli, G. Kelsoe, *J. Exp. Med.* **187**, 885–895 (1998).

ACKNOWLEDGMENTS

We thank T. Kurosaki for providing S1pr2-CreERT2 mice, T. Eisenreich for mouse colony management, K. Gordon for cell sorting, A. M. Newen for INDIA mice immunizations, and all members of the Nussenzweig laboratory for helpful discussions. **Funding:** This work was supported in part by National Institutes of Health (NIH) grant 5R37 AI037526, NIH Center for HIV/AIDS Vaccine Immunology and Immunogen Discovery (CHAVID) 1UM1AI144462-01 to M.C.N., and the Stavros Niarchos Foundation Institute for Global Infectious Disease Research. J.M. is a Branco Weiss fellow. M.C.N. is a Howard Hughes Medical Institute (HHMI) investigator. **Author contributions:** A.J.M. and M.C.N. conceived the study, designed experiments, interpreted data, and wrote the manuscript. A.J.M., L.P.D., P.Z., and J.M. designed and performed experiments. V.R. and G.S.S. performed bioinformatic data analysis. M.A.E. designed and generated the Blimp1-CreERT2 mouse strain. A.G., T.H., M.A.E., C.T.M., and B.H. designed and produced critical reagents. A.J.M., L.P.D., P.Z., J.M., V.R., G.S.S., T.H., M.A.E., C.T.M., B.H., A.G., and M.C.N. contributed to editing the manuscript. **Competing interests:** M.C.N. is on the scientific advisory board of Celldex Therapeutics. All other authors declare that they have no competing interests. **Data and materials availability:** All data needed to evaluate the conclusions in the paper are available in the main text and supplementary materials. Sequencing datasets have been deposited in National Center for Biotechnology Information (NCBI)'s Gene Expression Omnibus (GEO) and are available through GEO accession no. GSE282284. Reagents, including mouse strains, are available from A.J.M. and M.C.N. under a material transfer agreement with The Rockefeller University.

SUPPLEMENTARY MATERIALS

science.org/doi/10.1126/science.adr6896
Materials and Methods
Figs. S1 to S8
References (*40*–*50*)
MDAR Reproducibility Checklist

Submitted 12 July 2024; resubmitted 8 October 2024
Accepted 28 November 2024
Published online 19 December 2024
10.1126/science.adr6896

BIODIVERSITY

Variable impacts of land-based climate mitigation on habitat area for vertebrate diversity

Jeffrey R. Smith[1,2]*, Evelyn M. Beaury[1,2,3] Susan C. Cook-Patton[4], Jonathan M. Levine[1,2]

Pathways to achieving net zero carbon emissions commonly involve deploying reforestation, afforestation, and bioenergy crops across millions of hectares of land. It is often assumed that by helping to mitigate climate change, these strategies indirectly benefit biodiversity. Here, we modeled the climate and habitat requirements of 14,234 vertebrate species and show that the impact of these strategies on species' habitat area tends not to arise through climate mitigation, but rather through habitat conversion. Across locations, reforestation tends to provide species more habitat through both land-cover change and climate mitigation, whereas habitat loss from afforestation and bioenergy cropping typically outweighs the climate mitigation benefits. This work shows how and where land-based mitigation strategies can be deployed without inadvertently reducing the area of habitat for global biodiversity.

To address the ongoing climate crisis, society must not only reduce greenhouse gas emissions but also increase the amount of carbon removed from the atmosphere (*1*–*3*). Land-based mitigation strategies [LBMSs; sensu (*4*)] that harness carbon fixation by plants represent the only currently scalable methods of carbon removal. Some of the most prominent strategies include natural reforestation (regeneration of tree cover in historically forested biomes), afforestation (increase of tree cover in historically unforested biomes through shifts in management), and bioenergy cropping with carbon capture and storage (*5*–*9*). Despite concerns over the environmental and socioeconomic consequences of deploying these LBMSs (*10*–*16*), they remain central to many national plans to reach net zero CO_2 emissions (*9*, *17*, *18*) and have already been deployed at scale (*8*, *19*, *20*). However, how these strategies will affect the concurrent biodiversity crisis, a central motivation for addressing climate change, is uncertain and likely varies by strategy (*21*–*25*). As efforts to address climate change accelerate, it is urgent to ensure that by deploying LBMSs we do not inadvertently imperil biodiversity.

Determining the potential impacts of LBMSs on biodiversity is challenging because there are distinct, and potentially competing, pathways through which LBMSs may affect species, two of which we emphasize here. First, LBMSs can change local land cover, increasing or decreasing the habitat available to species depending on their habitat affinities: the "habitat conversion effect" (*26*–*29*). Second, when deployed at scale, LBMSs can mitigate the intensity of climate change, changing species' geographic range limits: the "climate mitigation effect" (*30*). The relative impacts of these habitat conversion and climate mitigation pathways on global biodiversity remain unknown. We might expect habitat conversion effects, which may be large for species with ranges that intersect a land-based mitigation project (*26*–*29*), to dominate the overall impacts of these projects for global biodiversity. Conversely, the climate mitigation effect, although small for individual species, affects the ranges of all species globally and could therefore have a large cumulative impact (*30*).

Resolving the biodiversity consequences of LBMS deployment has been challenging because the habitat conversion and climate mitigation effects tend not to be quantified in the same currency and at the same geographic scale, making them difficult to compare. For example, the positive habitat conversion effects of reforestation (*26*, *31*) and the negative impacts of afforestation (*10*, *29*) and bioenergy cropping (*27*, *32*) on local species diversity have been widely explored, but how these impacts compare with climate mitigation effects, which are often measured by changes in species' range size, is poorly resolved. Change in species' area of habitat (AOH) is one potential common currency for comparing these effects. Indeed, at the global scale, we know that addressing climate change can benefit biodiversity by reducing the contraction of climatically suitable habitat (*30*). However, most past work assesses potential benefits to biodiversity from transforming the world's energy system (*15*, *33*, *34*), not the more modest climate mitigation from the deployment of LBMSs [but see (*35*)]. Thus, to determine whether LBMSs themselves will benefit or harm the habitat available to global biodiversity, we must ask a more pointed question: What are the individual and combined impacts of habitat conversion and climate mitigation on species' AOH that are directly attributable to LBMSs?

Here, we calculated the change in AOH (*36*) of 14,234 vertebrate species in response to the habitat conversion and climate mitigation associated with three LBMSs proposed for large-scale deployment: reforestation, afforestation, and bioenergy cropping (with carbon capture and storage where geologically feasible) (*9*, *36*, *37*). This enabled us to answer three interrelated questions. First, in response to a global-scale deployment of LBMSs, do individual species gain or lose AOH primarily through the habitat conversion effects or the climate mitigation effects of these strategies? Second, how do the effects of LBMS deployment on the AOH for

[1]Department of Ecology and Evolutionary Biology, Princeton University, Princeton, NJ, USA. [2]High Meadows Environmental Institute, Princeton University, Princeton, NJ, USA. [3]Center for Conservation and Restoration Ecology, New York Botanical Garden, Bronx, NY, USA. [4]Global Natural Climate Solutions Science Team, The Nature Conservancy, Arlington, VA, USA.
*Corresponding author. Email: jeffreysmith@princeton.edu

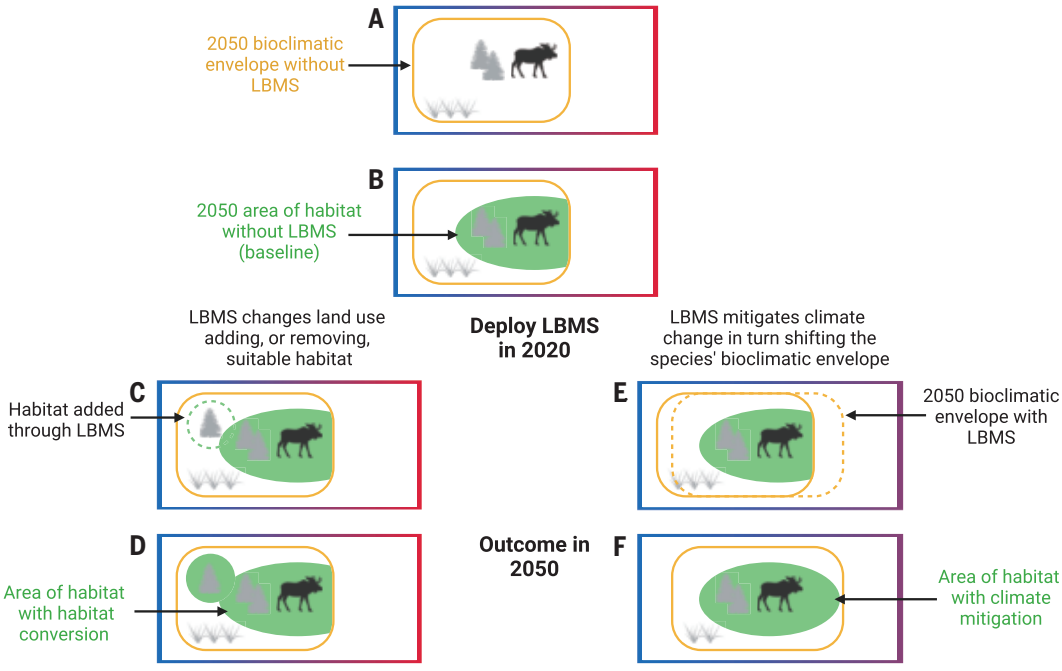

Fig. 1. Approach to quantifying the habitat conversion and climate mitigation effects of LBMSs on species' AOH. (**A**) We begin by generating a focal species' [the moose (*Alces alces*) in this figure] climate-determined geographic range limits, its bioclimatic envelope, in the year 2050 under SSP2-RCP4.5 (yellow outline). In this schematic, the focal species tends to occur in cooler regions (the blue end of the bounding box). (**B**) We next use a map of global habitat types and the focal species' known affinity for those habitat types to limit the AOH to locations with suitable climate and suitable habitat conditions under a baseline, or no-intervention, scenario (green shape). We compare this baseline AOH with the scenario in which we deploy a LBMS (forestation in this schematic) in the year 2020. (**C** and **D**) show how we quantify the habitat conversion effect. In this example, moose have a high affinity for forest, so the LBMS [forestation, dotted circle in (C)] increases the habitat available to the focal species [green shape in (D)]. For other species, including open-habitat specialists, this land cover change would have negative effects (fig. S1). (**E** and **F**) show how we quantify the climate mitigation effect. In this case, the LBMS partially mitigates climate change (noted by the cooler colors of the bounding box) and in turn shifts the species' bioclimatic envelope [dotted yellow outline in (E)]. This in turn grants the species access to habitats that would otherwise be climatically unsuitable [green shape in (F)]. For each species, we quantify the habitat conversion and climate mitigation effect as the change in AOH with LBMS deployment [green shapes in (D) and (F)] versus nondeployment [green shape in (B)]. We provide a walkthrough of this workflow for the moose across the continental United States and Canada with real data in the supplementary materials (figs. S49 to S64). [Figure created with BioRender.com]

vertebrate species vary depending on where they are geographically deployed? And third, for a given geographic location, which of the studied LBMSs maximizes the gains, or minimizes the losses, in AOH for vertebrate biodiversity?

Approach

We developed an analysis pipeline to quantify the habitat conversion and climate mitigation effects of LBMSs on the AOH for each vertebrate species in the year 2050. Our analyses use the middle-of-the-road SSP2-RCP4.5 land-use change and emissions pathway as a baseline scenario (*37*, *38*). We then compared the AOH for each vertebrate species under this baseline with a hypothetical future in which LBMSs were implemented in the year 2020. These interventions are assumed to (i) transform local land cover and thus the suitable habitat for species with ranges that intersect the LBMS deployment and (ii) remove CO_2 from the atmosphere for a period of 30 years, partially mitigating the magnitude of climate change and thereby affecting all species' distributions globally.

To disentangle the habitat conversion and climate mitigation effects of the implemented LBMSs, we began by modeling each species' AOH as a function of climate and land cover (Fig. 1 and figs. S1 and S2). We assumed that a species' geographic range is bounded by climate conditions and that within this climatically suitable range, local land cover determines the available habitat for each species following the International Union for Conservation of Nature (IUCN) habitat affinity scores (*39*) (table S1). To quantify the habitat conversion effect, we calculated the change in each species' AOH associated with implementing a LBMS (Fig. 1D) relative to the species' AOH under the no-intervention scenario (Fig. 1B). To determine the climate mitigation effect, we first estimated the carbon removal associated with deploying a given strategy using previously published maps of carbon removal potential (*40*–*43*) modified to incorporate changes in albedo due to reforestation and afforestation (*44*). We then used a radiative forcing function to estimate the effect of this carbon removal on global mean temperature (*44*) and CMIP6 global climate projections to relate global mean temperature to a suite of regional climate variables (*38*) (figs. S3 to S8 and table S2). Finally, we used these changes in regional climate variables to quantify the change in each species' 2050 AOH under the LBMS-mitigated climate (Fig. 1F) versus AOH in the unmitigated climate scenario (Fig. 1B).

We applied this approach to predict the global biodiversity impacts, measured as mean change in AOH (*36*), of deploying LBMSs at all locations (10 × 10 km pixels) that were biophysically capable of supporting either forest (*45*) or bioenergy crops with sufficient management (*41*) (figs. S9 to S12). To reduce potential conflicts with food security, which is an important determinant of where LBMSs are deployed, we did not consider the conversion of current arable lands or higher-intensity pastures (stocking density of at least 1 head per km^2) to LBMSs (*6*, *40*). Likewise, to maintain high carbon ecosystems, we did not allow for the conversion of forested lands to LBMSs (*6*). This leaves three broad land cover classes for possible conversion to forest or bioenergy cropping: grasslands, shrublands, and savannas (17 subclasses; table S1 and fig. S9). In historically forested biomes, these land classes represent areas for reforestation because their presence likely indicates past agricultural use, current low-intensity grazing, or other historical or present-day human use. By contrast, in historically open biomes where grassland, shrubland, and savanna habitat types are expected based on climatic and disturbance regimes, adding trees likely represents afforestation. In both cases, our analysis assumes natural regeneration [sensu (*40*)], which may involve changing management regimes (e.g., fire or browsing by herbivores).

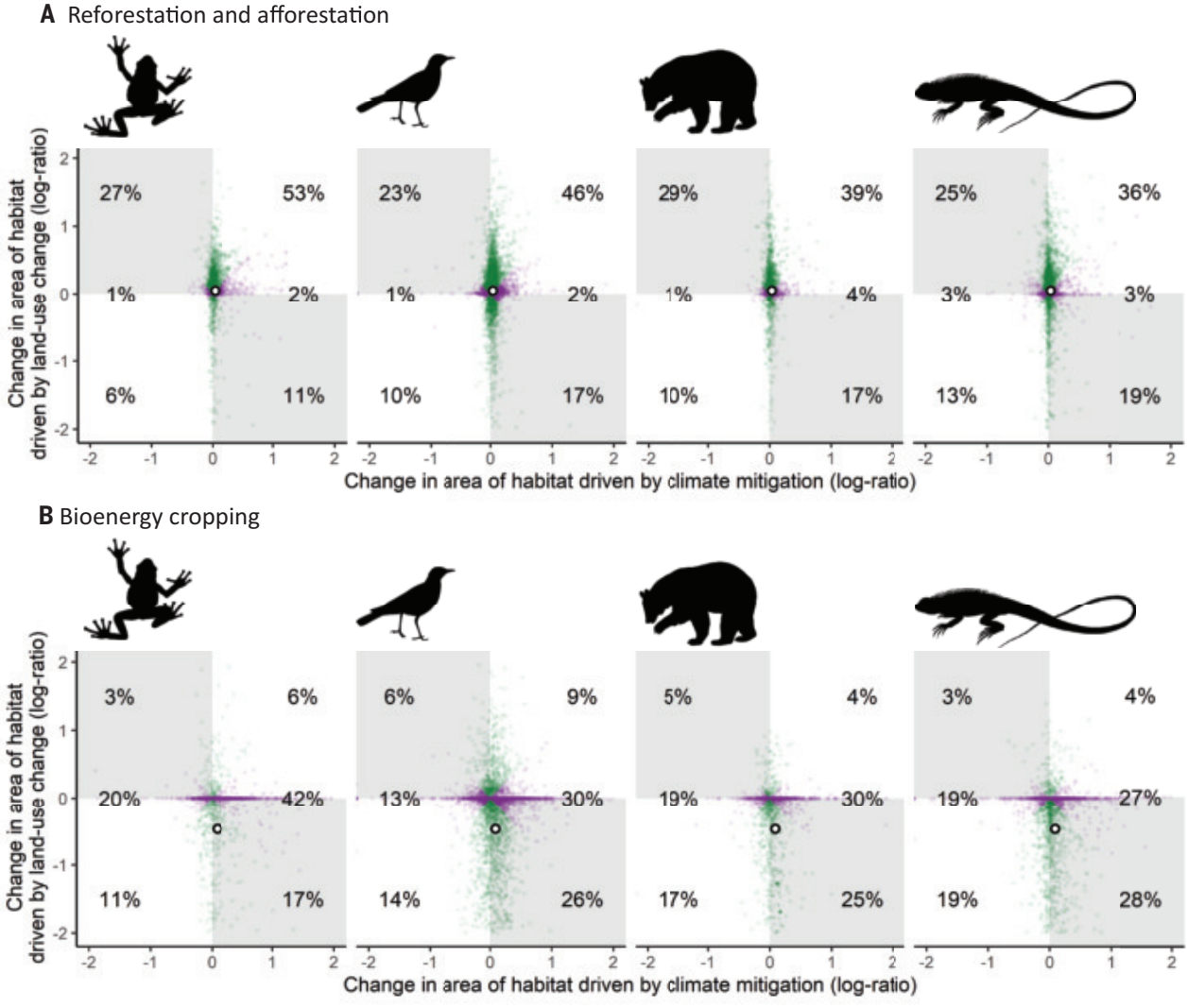

Fig. 2. The habitat conversion and climate mitigation effects of forestation (A) and bioenergy cropping (B) on four vertebrate classes. Points show the response of individual species' AOH to climate mitigation (along the *x* axis) and habit conversion (along the *y* axis) associated with LBMSs. Points to the right of the vertical zero line represent species that will experience range contractions under climate change, and therefore efforts to mitigate climate change will increase their range relative to the no-intervention baseline. Species lying to the left of zero have the opposite response. Points falling above the horizontal line show species that will gain habitat through the deployment of the LBMS, and points below the line indicate species that will lose habitat. The percentages of points in each quadrant are indicated in the corners of the graph. The fraction of points on the horizontal 0 line (no response to habitat conversion) is shown with separate percentages on the left (species with a negative climate mitigation effect) and right (species with a positive climate mitigation effect) of the axis. Points colored in green indicate species for which the habitat conversion effect is stronger than the climate mitigation effect, and purple points indicate species for which the reverse is true. To illustrate, a green point in the top-right quadrant is a species that gains AOH through both the habitat conversion effect and the climate mitigation effect but gains more habitat through habitat conversion. By contrast, a purple point in the bottom-left quadrant is a species that loses AOH through both the climate mitigation and habitat conversion effects but loses more through climate mitigation. Each white point with a black outline represents the mean value of all points for a given taxon's response to either forestation or bioenergy cropping.

To quantify the habitat conversion and climate mitigation responses of individual species to the deployment of LBMSs, we followed the methods diagrammed in Fig. 1 to explore hypothetical scenarios in which all eligible grasslands, shrublands, and savannas are converted either to forest or to bioenergy crops. We do not model these scenarios for their realism, but rather to assess the relative magnitude and sign of the habitat conversion and climate mitigation effects on species globally. To address where and through which mechanism the deployment of LBMSs will affect the AOH for global biodiversity, we averaged all species' AOH responses to the habitat conversion or climate mitigation effects of a given location's conversion to a land-based mitigation strategy. Finally, to determine which LBMS maximizes the biodiversity benefit, or minimizes the harm, we combined the habitat conversion and climate mitigation impacts for each LBMS deployed at each location and compared their overall effects on AOH with one another and with a scenario in which the current habitat is left intact.

Species-level responses to LBMSs

Across all 14,234 vertebrates, adding forest cover to the landscape through reforestation or afforestation (collectively called forestation) most commonly increased the AOH for species through both habitat conversion (69.1% of species, points above 0 in Fig. 2A) and climate

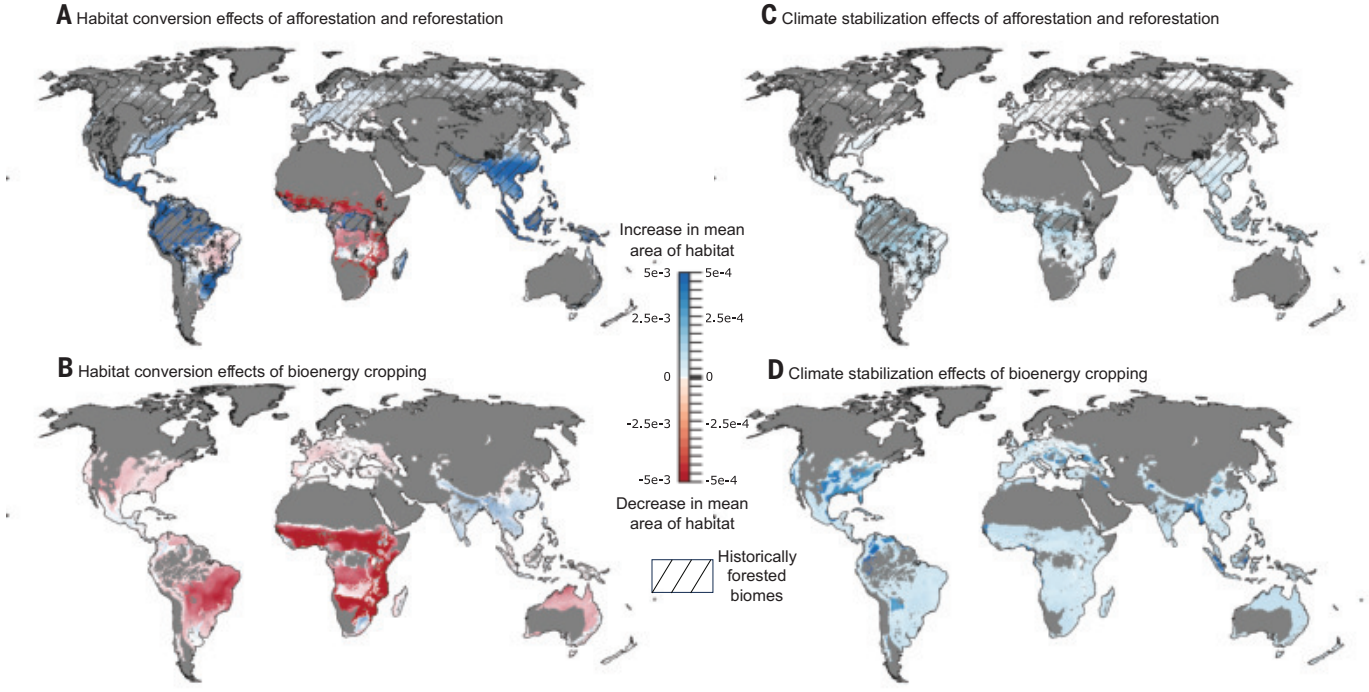

Fig. 3. Global vertebrate biodiversity impact of habitat conversion and climate mitigation associated with forestation [(A) and (C)] and bioenergy cropping [(B) and (D)]. Shown is the global biodiversity impact of deploying a given LBMS in a given pixel, which is calculated as the change in species' AOH averaged over all vertebrate species globally. Note the order of magnitude greater scale on the color bar for habitat conversion effects (left) than climate mitigation effects (right). The darker blue areas in (D) overlay areas where a belowground storage reservoir exists, allowing for bioenergy with carbon capture and storage. Areas in gray represent pixels with <1% of their area eligible for conversion to LBMSs. Hatched areas in (A) and (C) indicate historically forested biomes. The maps were reprojected to a Robinson projection for visualization. Qualitatively similar results for individual vertebrate groups (amphibians, breeding birds, mammals, and reptiles) can be found in figs. S25 to S30.

mitigation (62.2% of species, points to the right of 0 in Fig. 2A). These results follow from the documented habitat affinities of vertebrate species globally, with more species inhabiting forests than open habitats (table S3 and figs. S13 to S15) and there being larger range sizes under mitigated climate conditions (table S4). Given that our analysis treats all forest as habitat for forest-dwelling species, it overlooks the possibility that afforested sites are of lesser quality than reforested sites, the effect of which we explore in supplementary analyses (figs. S16 to S18). We further found that 43.2% of species benefited from both habitat conversion and climate mitigation effects, and only 10.3% of species would lose AOH from both effects. Habitat conversion had a greater impact than climate mitigation for 69.4% of species (green points in Fig. 2A).

In our model, individual species respond positively or negatively to climate mitigation regardless of strategy. Therefore, the same fraction of species are predicted to benefit from climate mitigation associated with bioenergy cropping as with forestation (62.2%), although the magnitude of the effect was greater for bioenergy deployment than forestation (Fig. 2B). In further contrast to species' response to forestation, almost half of species (47.4%) did not respond to the conversion of grassland, savanna, or shrubland to bioenergy crops (points lying exactly on the x axis of Fig. 2B). Of these species, 90.6% are forest specialists that cannot use any of these habitats, and the remainder are broad generalists (table S3). Therefore, 66.1% of species were more sensitive to the climate mitigation effects of bioenergy cropping than its habitat conversion effects. However, if we exclude forest specialist species, 64.8% of species were more strongly affected by habitat conversion than by the climate mitigation effects of bioenergy cropping (fig. S19), and the conversion effects of bioenergy were predominantly negative (78.2% of these species). These responses to forestation and bioenergy crop deployment across all vertebrates analyzed are similar to the responses that would be seen if we used a subset of either threatened and endangered species or species that responded most strongly to LBMS deployment (figs. S21 and S22).

Geographic variation in effects of LBMSs

Even though our analysis assumes that each species responds similarly to reforestation and afforestation (Fig. 2 and fig. S16), we found strong differences in their impacts on AOH in different geographic locations (*36*). Reforestation (pixels in the hatched regions of Fig. 3A) had overwhelmingly positive habitat conversion effects on the mean AOH for vertebrate species globally, whereas afforestation tended to reduce the mean AOH. These results do not stem from any methodological difference in how we treated reforestation and afforestation, but rather arise from the naturally occurring variation in regional species pools. In historically forested regions, the species pool is composed mainly of forest-adapted species that are more likely to make use of reforested habitats. Although some species in these regions would lose out with reforestation, their numbers are outweighed by those that benefit. By contrast, habitats suitable for afforestation contain fewer vertebrate species with an affinity for forest and more species with an affinity for open habitats. Thus, across species, afforestation tended to reduce AOH due to the local extirpation of many grassland, shrubland, and savanna specialist species (nonhatched regions in Fig. 3A) while increasing habitat for the far fewer species that can exploit forest.

We further found that the habitat conversion effects of bioenergy cropping, averaged across species globally, resulted in a negative AOH outcome nearly everywhere that this

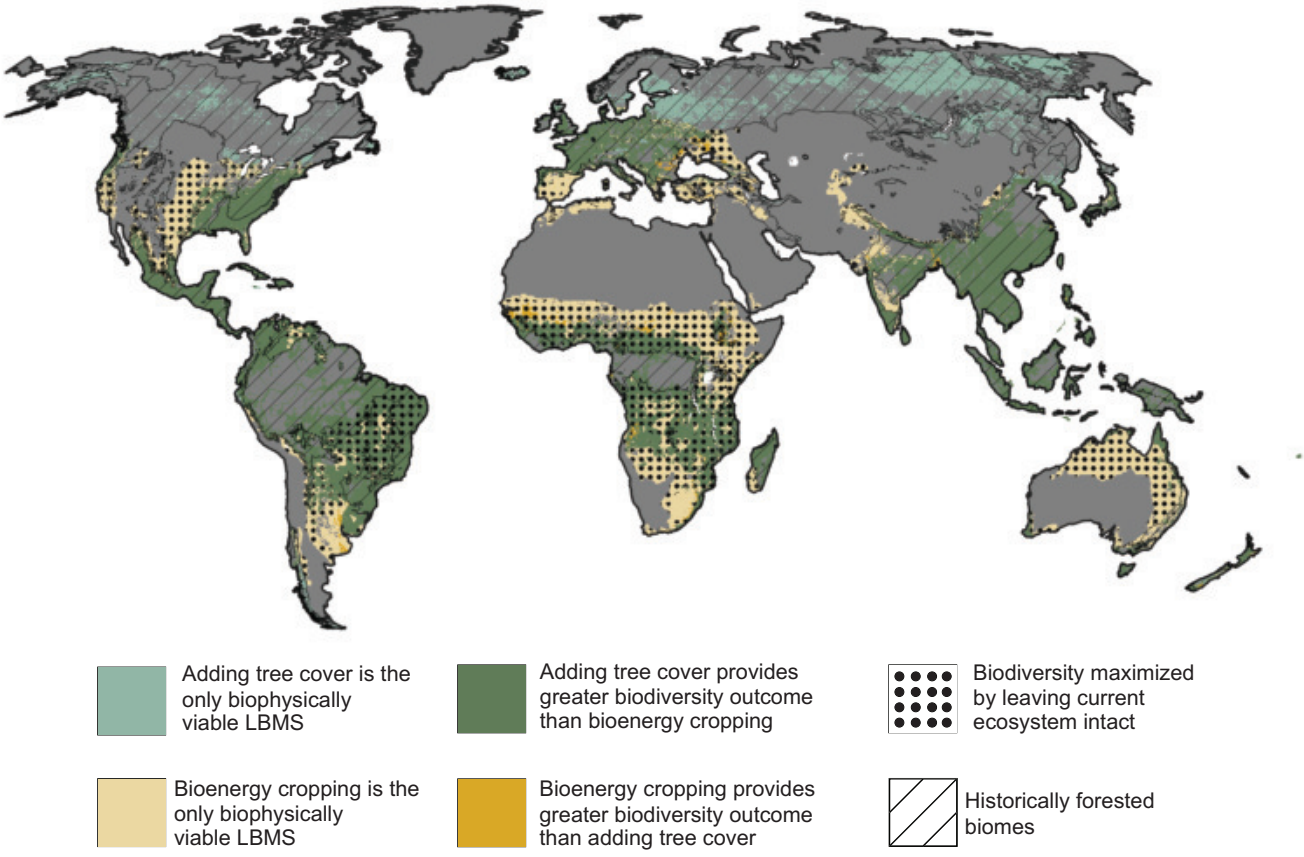

Fig. 4. Optimal LBMS strategy for maximizing the AOH for vertebrate species. The impact of LBMS deployment in an individual pixel reflects the combined effect of habitat conversion and climate mitigation on species' AOH averaged over all species globally. Note that areas colored dark green and dark yellow indicate where forestation or bioenergy cropping generates the higher mean global AOH, not an absolute biodiversity benefit. In fact, areas overlaid with black circles indicate regions where the highest mean global AOH is achieved by maintaining the current habitat (i.e., the possible LBMSs are harmful). Although this map is useful for examining geographic scale patterns, results for any point location are uncertain. This uncertainty stems from the fact that whereas at a global scale, we have good coverage of species, at any individual location key species of concern may not have been modeled. To allow readers to explore which species are driving patterns at individual locations, we have provided supplementary data files showing the species-level habitat conversion effects at point locations distributed uniformly around the globe (*60*). Areas in gray represent pixels with <1% of their area eligible for conversion to LBMSs. The map was reprojected to a Robinson projection for visualization.

strategy was deployed (Fig. 3B). There were some exceptions, such as Southeast Asia and Central America, but in nearly all of these locations, forestation more strongly increased mean AOH across vertebrate species (Fig. 3A).

In contrast to the habitat conversion effect, which drove positive or negative changes in mean AOH depending on the location of LBMS deployment, the climate mitigation associated with deploying LMBSs in any location increased mean AOH (Fig. 3, C and D). This is because, from a strictly climate mitigation perspective, species are agnostic to how and where terrestrial carbon storage is achieved. LBMSs are typically able to remove more carbon per unit area in warm and wet regions where plant growth is highest (*40*, *41*), thereby increasing the climate mitigation benefits when deployed in those areas. For bioenergy crops specifically, the climate mitigation benefit is approximately double in regions that overlap sedimentary basins suitable for CO_2 injection, which enable carbon capture and storage (Fig. 3D) (*36*).

Although the climate mitigation effects of LBMSs were consistently positive, they were generally small relative to the habitat conversion effects, matching the species-level results. For 94.2% of forestation pixels and 86.6% of bioenergy cropping pixels, the habitat conversion effect (a strong effect over a small area) outweighed the climate mitigation effect (a weak effect over the global extent; Fig. 3). These same general patterns, in both the direction and magnitude of the effect, hold across taxonomic groups and for the subset of species that are threatened and endangered (figs. S23 to S30).

The LBMS that maximizes biodiversity outcomes

We next investigated which LBMS, if any, would maximize mean global vertebrate AOH if deployed at each location. For each strategy, we calculated the combined impact of the habitat conversion and climate mitigation pathways for each pixel biophysically suitable for LBMSs (*36*). We found that of the locations suitable for either forest or bioenergy crops, 96.5% were projected to sustain higher global mean AOH for vertebrate species when converted to forest rather than bioenergy crops (Fig. 4).

We found that in most locations suitable for afforestation or bioenergy crops, maintaining the current habitat resulted in the highest mean global AOH for vertebrate species (dotted area in Fig. 4). In 78.4% of pixels where bioenergy cropping was biophysically feasible and in 21.5% of pixels where adding tree cover (through reforestation or afforestation) was feasible, leaving the grassland, shrubland, or savanna in its natural state would lead to the highest mean global AOH of the three interventions considered. Of the areas where forestation was

harmful, 72.2% represented afforestation, including large portions of Africa, the Brazilian Cerrado, and the Mediterranean. Collectively, these results suggest that the detrimental habitat conversion effects of afforestation and bioenergy cropping on biodiversity often outweigh the climate mitigation benefits to global biodiversity.

Ensuring LBMSs are a win-win for biodiversity and climate

As is true with all global modeling efforts, our approach involves a number of assumptions, the importance of which we examined with sensitivity analyses. We found that our central findings held across vertebrate taxa (figs. S24 to S30) and occurrence thresholds for species inclusion (figs. S31 and S32), as well as assumptions about the dispersal capacity of species (figs. S33 to S36), the efficacy of reforestation (fig. S37) and afforestation (figs. S16 to S18 and S37), the relative habitat value of bioenergy crops (fig. S38), the carbon benefits of bioenergy (figs. S39 to S44), and the equilibration of atmospheric CO_2 with the ocean and land sinks (figs. S45 to S48). By necessity, our analysis (figs. S49 to S64) overlooks potentially substantial climate feedbacks, such as those with fire regimes (*12*) and changing microclimates driven by the deployment of LBMSs (*46*). Further, by focusing only on the changing AOH for vertebrates, our analysis does not incorporate changes to species composition, nor the myriad other ways that climate change and habitat conversion can affect biodiversity [e.g., shifts in phenology (*47*), demographic shifts (*48*), sublethal physiological effects (*49*), loss of connectivity (*50*), fragmentation (*51*), and edge effects (*52*)]. Finally, although our work identifies the harmful effects of bioenergy cropping and afforestation on vertebrate biodiversity, there are many other detrimental effects associated with these LBMSs that further argue against their deployment. These include the loss of nonvertebrate biodiversity (*27*, *29*), changes to water availability (*53*, *54*) and fire frequency (*12*), and loss of access to grazing lands (*13*). Moreover, many socioeconomic factors must figure into decisions about the deployment of all three LBMSs to safeguard local communities and livelihoods (*14*, *16*, *22*, *55*).

In conclusion, we found that at a global scale, reforestation is likely to have dual benefits to vertebrate biodiversity, both directly by creating habitat for species and indirectly by helping to mitigate climate change. This mitigation in turn allows species to make use of habitats in regions that would otherwise be climatically unsuitable. By contrast, whereas afforestation and bioenergy cropping may similarly benefit biodiversity by helping to mitigate climate change, this benefit is generally small relative to the loss of habitat driven by these LBMSs. More generally, it is often assumed that by addressing climate change, LBMS will also help to stem the tide of biodiversity loss (*33*, *34*). However, as shown here, assuming a net positive effect on global biodiversity by curbing climate change overlooks the far greater local impact of LBMSs through habitat conversion. It is therefore critical that LBMS projects draw on local knowledge to accurately forecast potential biodiversity outcomes and ensure that in addressing climate change we do not inadvertently worsen the biodiversity crisis.

REFERENCES AND NOTES

1. I. Dafnomilis, M. den Elzen, D. P. van Vuuren, *Ann. N. Y. Acad. Sci.* **1522**, 98–108 (2023).
2. H. L. van Soest, M. G. J. den Elzen, D. P. van Vuuren, *Nat. Commun.* **12**, 2140 (2021).
3. R. S. Haszeldine, S. Flude, G. Johnson, V. Scott, *Philos. Trans. A Math. Phys. Eng. Sci.* **376**, 20160447 (2018).
4. M. H. Gvein *et al*., *Commun. Earth Environ.* **4**, 39 (2023).
5. National Academies of Sciences, Engineering, and Medicine, *Accelerating Decarbonization of the U.S. Energy System* (National Academies Press, 2021); https://www.nap.edu/catalog/25932.
6. B. W. Griscom *et al*., *Proc. Natl. Acad. Sci. U.S.A.* **114**, 11645–11650 (2017).
7. S. Roe *et al*., *Glob. Chang. Biol.* **27**, 6025–6058 (2021).
8. S. J. Mandley, V. Daioglou, H. M. Junginger, D. P. van Vuuren, B. Wicke, *Renew. Sustain. Energy Rev.* **127**, 109858 (2020).
9. K. Dooley *et al*., "The Land Gap Report" (Land Gap, 2022); http://www.landgap.org.
10. J. W. Veldman *et al*., *Bioscience* **65**, 1011–1018 (2015).
11. J. C. Doelman *et al*., *Glob. Chang. Biol.* **26**, 1576–1591 (2020).
12. V. Hermoso, A. Regos, A. Morán-Ordóñez, A. Duane, L. Brotons, *Glob. Chang. Biol.* **27**, 3001–3003 (2021).
13. V. Ramprasad, A. Joglekar, F. Fleischman, *Ecol. Soc.* **25**, art1 (2020).
14. W. J. Bond, N. Stevens, G. F. Midgley, C. E. R. Lehmann, *Trends Ecol. Evol.* **34**, 963–965 (2019).
15. C. Hof *et al*., *Proc. Natl. Acad. Sci. U.S.A.* **115**, 13294–13299 (2018).
16. K. Calvin *et al*., *Glob. Chang. Biol. Bioenergy* **13**, 1346–1371 (2021).
17. K. Dooley, K. L. Christiansen, J. F. Lund, W. Carton, A. Self, *Nat. Commun.* **15**, 9118 (2024).
18. C. L. Parr, M. Te Beest, N. Stevens, *Science* **383**, 698–701 (2024).
19. M. D. Turner *et al*., *Annu. Rev. Environ. Resour.* **48**, 263–287 (2023).
20. C. D. Philipson *et al*., *Science* **369**, 838–841 (2020).
21. N. Pettorelli *et al*., *J. Appl. Ecol.* **58**, 2384–2393 (2021).
22. N. Seddon, *Science* **376**, 1410–1416 (2022).
23. A. Santangeli *et al*., *Glob. Chang. Biol. Bioenergy* **8**, 941–951 (2016).
24. A. Chausson *et al*., *Glob. Chang. Biol.* **26**, 6134–6155 (2020).
25. I. B. Key *et al*., *Front. Environ. Sci.* **10**, 905767 (2022).
26. J. M. Rey Benayas, A. C. Newton, A. Diaz, J. M. Bullock, *Science* **325**, 1121–1124 (2009).
27. M. M. Núñez-Regueiro, S. F. Siddiqui, R. J. Fletcher Jr., *Conserv. Biol.* **35**, 77–87 (2021).
28. J. Atkinson *et al*., *Ecol. Lett.* **25**, 1725–1737 (2022).
29. S. Gómez-González, R. Ochoa-Hueso, J. G. Pausas, *Science* **368**, 1439 (2020).
30. R. Warren, J. Price, E. Graham, N. Forstenhaeusler, J. VanDerWal, *Science* **360**, 791–795 (2018).
31. A. E. Latawiec *et al*., *Biotropica* **48**, 844–855 (2016).
32. D. J. Immerzeel, P. A. Verweij, F. van der Hilst, A. P. C. Faaij, *Glob. Chang. Biol. Bioenergy* **6**, 183–209 (2014).
33. H. Ohashi *et al*., *Nat. Commun.* **10**, 5240 (2019).
34. A. Hirata *et al*., *Commun. Earth Environ.* **5**, 259 (2024).
35. S. V. Hanssen *et al*., *Glob. Chang. Biol. Bioenergy* **14**, 307–321 (2022).
36. Materials and methods can be found in the supplementary materials.
37. M. Chen *et al*., *Sci. Data* **7**, 320 (2020).
38. J. M. Gutiérrez *et al*., "IPCC WGI Interactive Atlas" in *Climate Change 2021: The Physical Science Basis. Contribution of Working Group I to the Sixth Assessment Report of the Intergovernmental Panel on Climate Change* (IPCC, 2021); https://interactive-atlas.ipcc.ch/.
39. M. Jung *et al*., *Sci. Data* **7**, 256 (2020).
40. S. C. Cook-Patton *et al*., *Nature* **585**, 545–550 (2020).
41. W. Li *et al*., *Earth Syst. Sci. Data* **12**, 789–804 (2020).
42. US Geological Survey, "2000 World Assessment Data (DDS60)" (USGS, 2000); https://certmapper.cr.usgs.gov/data/apps/we-data/.
43. National Energy Technology Laboratory, "NATCARB Atlas Saline Basin 10km Grid - EDX" (NETL, 2015); https://edx.netl.doe.gov/dataset/natcarb-atlas-saline-basin-10km-grid.
44. N. Hasler *et al*., *Nat. Commun.* **15**, 2275 (2024).
45. J.-F. Bastin *et al*., *Science* **365**, 76–79 (2019).
46. S. Alibakhshi *et al*., *Commun. Earth Environ.* **5**, 577 (2024).
47. D. W. Inouye, *Wiley Interdiscip. Rev. Clim. Change* **13**, e764 (2022).
48. K. E. Selwood, M. A. McGeoch, R. Mac Nally, *Biol. Rev. Camb. Philos. Soc.* **90**, 837–853 (2015).
49. M. C. Urban *et al*., *Science* **353**, aad8466 (2016).
50. M. R. Felipe-Lucia *et al*., *Proc. Natl. Acad. Sci. U.S.A.* **117**, 28140–28149 (2020).
51. L. Fahrig, *Annu. Rev. Ecol. Evol. Syst.* **34**, 487–515 (2003).
52. J. N. G. Willmer, T. Püttker, J. A. Prevedello, *Biol. Conserv.* **272**, 109654 (2022).
53. R. B. Jackson *et al*., *Science* **310**, 1944–1947 (2005).
54. K. Schwärzel, L. Zhang, L. Montanarella, Y. Wang, G. Sun, *Glob. Chang. Biol.* **26**, 944–959 (2020).
55. F. Fleischman *et al*., *Bioscience* **70**, 947–950 (2020).
56. The Global Biodiversity Information Facility, "Derived dataset GBIF.org (3 June 2024), Filtered export of GBIF occurrence data" (GBIF, 2024); https://doi.org/10.15468/DD.HBJJEX.
57. International Union for Conservation of Nature, "The IUCN Red List of Threatened Species" (IUCN, 2019); https://www.iucnredlist.org/en.
58. S. A. Spawn, C. C. Sullivan, T. J. Lark, H. K. Gibbs, *Sci. Data* **7**, 112 (2020).
59. Food and Agriculture Organization of the United Nations, "Global Soil Organic Carbon Map (GSOCmap) Version 1.5: Technical Report" (FAO, 2020); https://www.fao.org/documents/card/en?details=ca7597en/.
60. J. R. Smith, Code and data for: Variable impacts of land-based climate mitigation on habitat area for vertebrate diversity, Zenodo (2024); https://doi.org/10.5281/zenodo.11127407.

ACKNOWLEDGMENTS

We thank S. Pacala, E. Shevliakova, S. Malyshev, and members of the Levine lab for helpful comments on the manuscript. **Funding:** This work was funded by the Princeton University Carbon Mitigation Initiative funded by bp. The Bezos Earth Fund supported S.C.C.-P.'s time on this work. Computational resources were provided by the Princeton Institute for Computation Science and Engineering. **Author contributions:** J.R.S., E.M.B., and J.M.L. designed the study. J.R.S. conducted the analysis and wrote the manuscript with input from E.M.B., S.C.C.-P., and J.M.L. **Competing interests:** The authors declare no competing interests. **Data and materials availability:** The data used in this analysis are publicly available from the following sources: GBIF point occurrences (*56*), IUCN range maps (*57*), current and future climate conditions (*38*), global habitat types (*39*), projected change in land cover under SSP2 (*37*), current above- and belowground biomass (*58*), soil carbon levels (*59*), tree canopy potential (*45*), carbon accumulation potential with natural forest regeneration (*40*), albedo effects of natural forest regeneration (*44*), bioenergy crop productivity (*41*), and sedimentary basins (*42*, *43*). The code used to conduct the analysis and the data and code to create the figures can be found on Zenodo (*60*).

SUPPLEMENTARY MATERIALS

science.org/doi/10.1126/science.adm9485
Materials and Methods
Figs. S1 to S64
Tables S1 to S5
References (*61*–*89*)
MDAR Reproducibility Checklist

Submitted 10 January 2024; accepted 9 December 2024
10.1126/science.adm9485

MOLECULAR BIOLOGY

Molecular basis of FIGNL1 in dissociating RAD51 from DNA and chromatin

Alexander Carver[1,2]†, Tai-Yuan Yu[3]†, Luke A. Yates[1,2], Travis White[3], Raymond Wang[3], Katie Lister[1,2], Maria Jasin[3]*, Xiaodong Zhang[1,2]*

Maintaining genome integrity is an essential and challenging process. RAD51 recombinase, the central component of several crucial processes in repairing DNA and protecting genome integrity, forms filaments on DNA, which are tightly regulated. One of these RAD51 regulators is FIGNL1 (fidgetin-like 1), which prevents RAD51 genotoxic chromatin association in normal cells and persistent RAD51 foci upon DNA damage. The cryogenic electron microscopy–imaged structure of FIGNL1 in complex with RAD51 reveals that FIGNL1 forms a nonplanar hexamer and encloses RAD51 N terminus in the FIGNL1 hexamer pore. Mutations in pore loop or catalytic residues of FIGNL1 render it defective in filament disassembly and are lethal in mouse embryonic stem cells. Our study reveals a distinct mechanism for removing RAD51 from bound substrates and provides the molecular basis for FIGNL1 in maintaining genome stability.

RAD51 recombinase is a key protein involved in homologous recombination, the most faithful repair process for a double-stranded DNA (dsDNA) break (*1*–*3*). RAD51 together with its meiosis specific homolog DMC1 also perform analogous functions in meiotic recombination when parental homologous chromosomes pair and recombine (*4*). The RAD51–single stranded DNA (ssDNA) filament catalyzes the essential processes of homology search, strand invasion, and heteroduplex formation (*1*, *3*, *5*). RAD51 needs to be removed from heteroduplex DNA before homology-directed DNA synthesis, repair, and recombination can proceed. Aberrant loading of RAD51 on ssDNA can lead to multiple strand invasions across chromosomes, which in turn can lead to the formation of ultrafine bridges and chromosome instability, a hallmark of cancer (*6*, *7*). Furthermore, RAD51 is shown to be essential for DNA replication, especially in dealing with replication stress, and to maintain a stable replication fork (*8*, *9*). Overexpression and accumulation of RAD51 on chromosomes has been associated with increased drug resistance in tumor cells and increased genome instability and apoptosis in normal cells (*10*). Consequently, RAD51 activity is tightly regulated. For example, the tumor suppressors BRCA2 and RAD51 paralog complex BCDX2 promote RAD51-ssDNA filament formation and stability, and several DNA helicases and translocases such as RAD54, the RecQ family, HELQ, RTEL1, and FBH1 can disassemble RAD51-ssDNA or -dsDNA filaments (*5*, *11*–*16*). *FIGNL1* (fidgetin-like 1), an essential gene in mice belonging to the large AAA+ adenosine triphosphatase (ATPase) family, has recently been shown to prevent persistent RAD51 foci

[1]DNA Processing Machines Laboratory, Francis Crick Institute, London, UK. [2]Section of Structural and Synthetic Biology, Department of Infectious Disease, Imperial College London, London, UK. [3]Developmental Biology Program, Memorial Sloan Kettering Cancer Center, New York, USA.
***Corresponding author. Email: xiaodong.zhang@imperial.ac.uk (X.Z.); jasinm@mskcc.org (M.J.)**
†These authors contributed equally to this work.

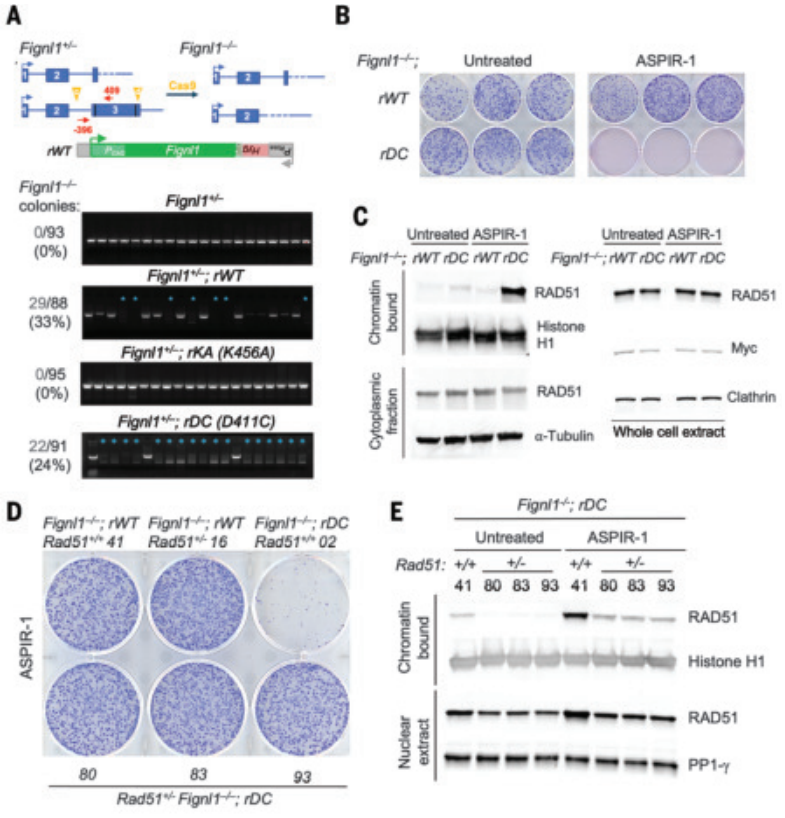

Fig. 1. FIGNL1 ATPase activity is required for its functionality in cells. (**A**) FIGNL1 is required for the viability of mESCs. *Fignl1*$^{+/-}$ cells were targeted at the *Rosa26* locus with expression cassettes for wild-type *Fignl1* (*rWT*) or mutants K456A in the ATPase Walker A motif (*rKA*) or D411C for chemical inhibition (*rDC*) and then selected for *Hyg* gene expression from the *Rosa26* promoter. After confirmation of correct targeting, the second *Fignl1* allele was subjected to CRISPR-Cas9 editing by using single guide RNAs (sgRNAs) ("c" and "d") to delete the entire *Fignl1* coding region. Genomic DNA was screened by means of polymerase chain reaction (PCR) by using primers −396 and 409 for the undeleted allele. Successful deletion is indicated with a blue asterisk. The number of *Fignl1*$^{-/-}$ colonies is indicated, along with the total number of colonies that were screened. (Single-letter abbreviations for the amino acid residues are as follows: A, Ala; C, Cys; D, Asp; E, Glu; F, Phe; K, Lys; Q, Gln; R, Arg; and W, Trp. In the mutants, other amino acids were substituted at certain locations; for example, K456A indicates that lysine at position 456 was replaced by alanine.) (**B**) Chemical inhibition of the FIGNL1 ATPase is lethal. Covalent modification of FIGNL1 at D411C in the ATPase domain by ASPIR-1 impairs colony formation. (**C**) Chemical inhibition of FIGNL1 (left) leads to RAD51 accumulation on chromatin but (right) does not affect overall RAD51 levels. *Fignl1*$^{-/-}$*;rDC* or *Fignl1*$^{-/-}$*;rWT* cells were treated with 0.25 μg/ml ASPIR-1 or dimethyl sulfoxide (DMSO) for 24 hours. Chromatin and cytoplasmic fractions or whole-cell extracts as indicated were subjected to Western blot analysis with antibodies to the indicated proteins. (**D**) *Rad51* heterozygosity rescues survival of the *Fignl1* mutant for colony formation in the presence of ASPIR-1 (0.25 μg/ml) for 7 days. Three independent clones were tested (80, 83, and 93). (**E**) *Rad51* heterozygosity reduces RAD51 chromatin association in the presence of ASPIR-1 to the level found in untreated *Rad51* wild-type cells. Three independent clones were treated with 0.25 μg/ml ASPIR-1 or DMSO for 24 hours and then subjected to chromatin and nuclear fractionation, followed by Western blot analysis with antibodies to the indicated proteins.

formation, prevent replication fork instability, and suppress ultrafine chromosome bridges (*17*–*20*). Conditional deletion of *FIGNL1* in mouse spermatocytes results in massive overloading of RAD51 and DMC1 in these cells (*17*, *19*). Recently, FIRRM/FLIP has been shown to form a stable complex with FIGNL1, and together they function in several DNA repair pathways—including homologous recombination (HR) and interstrand DNA cross-link repair, as well as replication fork protection—and FIGNL1–FIRRM/FLIP can disassemble RAD51 filaments (*19*, *21*–*25*). FIGNL1 has thus been firmly established as an important player in genome maintenance. However, the molecular mechanism of RAD51 modulation by FIGNL1 is currently unknown.

Results

FIGNL1 ATPase is essential for RAD51 filament disassembly

Silencing or deleting *FIGNL1* has been shown to be embryonic lethal in mice (*17*). *Fignl1*$^{-/-}$ mice die during embryogenesis (fig. S1A), and *Fignl1*$^{-/-}$ mouse embryonic stem cells (mESCs) are inviable (Fig. 1A and fig. S1, B to D). The role of the enzymatic activity of FIGNL1 has been contradictory. Earlier work indicated that adenosine 5′-triphosphate (ATP) binding and hydrolysis was important for HR (*18*), but a later study suggested that ATPase activity was not necessary for RAD51 filament disassembly (*26*). To understand whether and how enzymatic activity of FIGNL1 affects its functionalities, we developed a system to express various FIGNL1 mutants from the *Rosa26* locus in *Fignl1*$^{+/-}$ mESCs to ask whether the second endogenous allele could be disrupted (fig. S1). Although *Fignl1*$^{-/-}$ cells were viable if they expressed wild-type FIGNL1 from the locus, they were not viable if they expressed the mutant, K456A (K447 in human FIGNL1), in the nucleotide-binding Walker A motif (KA) (Fig. 1A and fig. S1E), indicating that nucleotide binding of FIGNL1 is essential.

To probe the effects of ATPase activity in cells in a controlled fashion, we used a chemical genetic approach to inhibit the ATPase activity of FIGNL1 by expressing an ATP-analog sensitive mutant with a cysteine in the active site (fig. S2A) (*27*). This modified version of FIGNL1 (D411C; equivalent to D402 in human FIGNL1) retains ATPase activity, but when exposed to the compound ASPIR-1, a covalent bond is formed at the active site to abrogate ATPase activity (*27*). We found that although *Fignl1*$^{-/-}$ cells ectopically expressing D411C at *Rosa26* were viable, treatment of these cells with ASPIR-1 was toxic (Fig. 1, A and B, and fig. S2B). Further, ASPIR-1 treatment of D411C-expressing cells resulted in markedly increased association of RAD51 with chromatin (Fig. 1C and fig. S2, C to F), which is known to increase chromosome aberrations and aneuploidy (*28*).

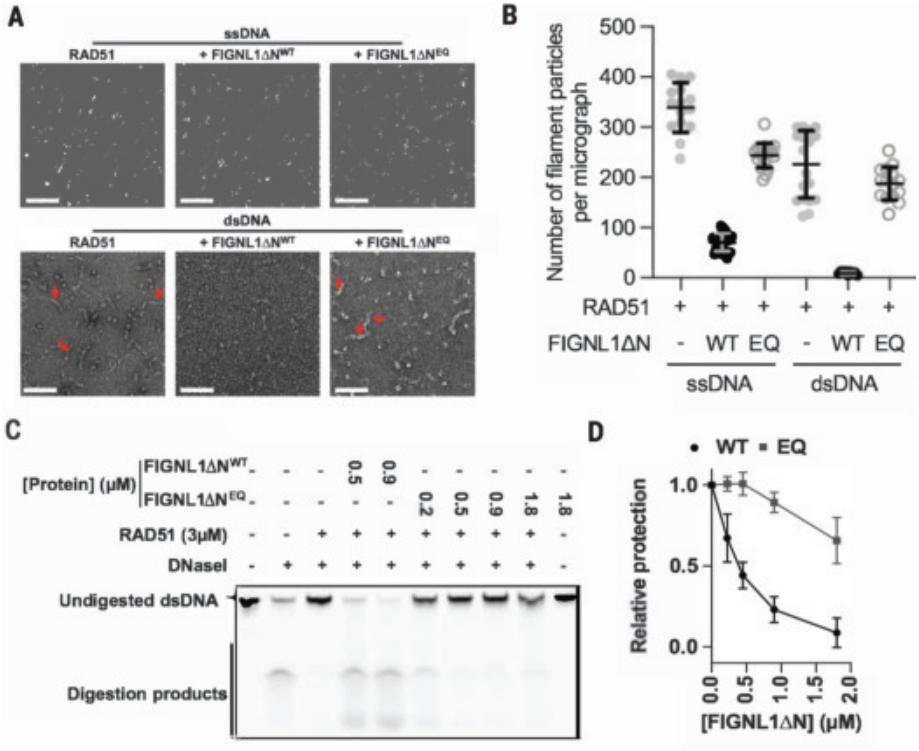

Fig. 2. Disassembly of RAD51 filaments is dependent on FIGNL1 ATPase activity. (**A**) Representative negative-stain electron micrographs of RAD51 filaments on both ssDNA and dsDNA in the absence or presence of FIGNL1ΔN or FIGNL1ΔN(E501Q), a mutant in the Walker B motif. Red arrows indicate some of the filaments. Scale bars, 100 nm. (**B**) Quantification of filaments observed in (A) indicates a decrease in the number of filaments per micrograph upon incubation with FIGNL1ΔN, whereas FIGNL1ΔN^{E501Q} has reduced effects. *n* = 18 to 20 micrographs per condition. (**C**) Image of gel, showing nuclease protection of dsDNA by RAD51 in the presence of increasing concentrations of FIGNL1ΔN or E501Q mutant. (**D**) Quantification of nuclease protection assays. *n* = 3 independent experiments, each data point indicates the mean ± SD. Wild-type (WT) FIGNL1ΔN data quantification is from independent repeats and 0.5 and 0.9 μM data points are shown in (C). Filament disruption assays shown in (A) to (D) were carried out by using 60-nucleotide ssDNA and 60–base pair dsDNA.

Consistent with a recent study (*23*), ATPase inhibition by ASPIR-1 did not significantly affect HR at a single DSB (fig. S2G). The lethality caused by *Fignl1* mutation was rescued by *Rad51* heterozygous deletion (Fig. 1D and fig. S1, F to H). Associated with the rescue, cells displayed reduced RAD51 chromatin accumulation (Fig. 1E), which is consistent with recent data showing that RAD51 inhibition could rescue cellular defects owing to *Fignl1* deletion (*20*). Together, these data support the notion that FIGNL1 ATPase activity is required for its functionality in the prevention of aberrant RAD51-chromatin association and genome instability.

To understand how FIGNL1's ATPase activity is linked to modulating RAD51's association with chromatin, we investigated the molecular mechanisms of FIGNL1-mediated RAD51 dissociation from DNA and filament disassembly in vitro. Previous studies have identified three functional domains in FIGNL1: a N-terminal domain containing a largely unstructured region responsible for localization to DNA damage sites and for interactions with other proteins, followed by the RAD51-binding FRBD (FIGNL1 RAD51-binding domain) and AAA+ ATPase domains (fig. S3A) (*18*, *19*). The N-terminal domain interacts with FIRRM/FLIP (*21*), and the interactions are important in vivo for the mutual stability of FIGNL1 and FIRRM/FLIP (*19*, *23*–*25*). To ensure protein stability in the absence of interacting partners while maintaining its activities for RAD51 modulation, we purified a N-terminal truncated fragment of human FIGNL1 (residues 287 to 674), equivalent to those used in earlier studies (*18*, *26*), that exhibits ATPase activity and RAD51 binding, which we term FIGNL1ΔN (fig. S3). As expected and consistent with previous studies (*17*, *22*, *26*, *29*), FIGNL1ΔN can dismantle RAD51 from both ssDNA and dsDNA (Fig. 2 and figs. S3 and S4).

To visualize filament disassembly and to compare the effects of various FIGNL1ΔN mutants to probe the requirement of ATPase activities, we imaged and quantified RAD51 filaments using negative stain electron microscopy (NS-EM)

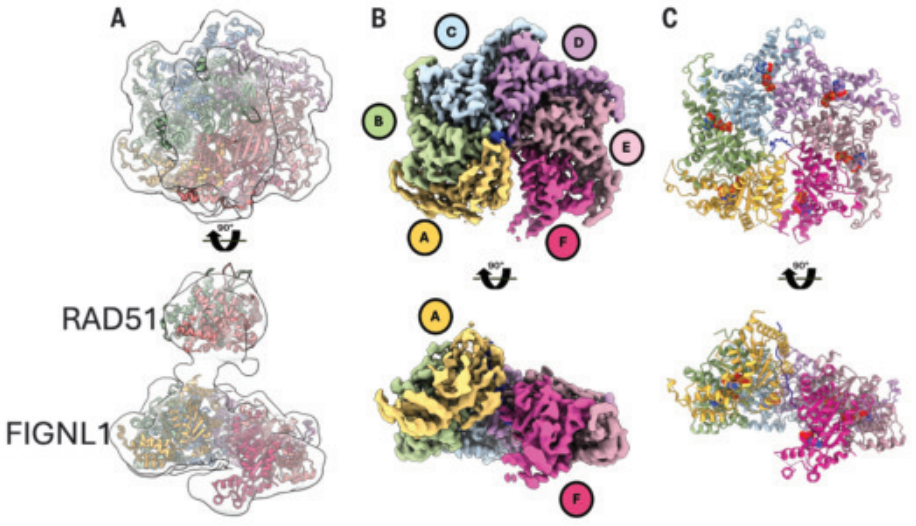

Fig. 3. Cryo-EM structures of the FIGNL1-RAD51 complex and FIGNL1 AAA+ hexamer. (**A**) Top and side views of the cryo-EM map and model of the FIGNL1ΔN^{E501Q}-RAD51 complex in the presence of ATP.Mg^{2+}. (**B**) Top and side views of the cryo-EM map (2.9 Å) of the FIGNL1 AAA+ hexamer in the presence of ATP.Mg^{2+}. (**C**) Top and side views of the atomic model of the FIGNL1 AAA+ hexamer modeled from the map shown in (B).

(Fig. 2, A and B, and fig. S4). To assess the activity in solution, we used a nuclease protection assay in which DNA coated by RAD51 is challenged to nuclease treatment (*30*). A decrease in protection indicates dissociation or remodeling of RAD51 from DNA. In the nuclease protection assays, adding FIGNL1ΔN resulted in a decrease in RAD51-mediated protection in a FIGNL1ΔN concentration–dependent fashion in both ssDNA and dsDNA (Fig. 2, C and D, and fig. S3C). Together with the NS-EM results (Fig. 2, A and B), these data confirm that FIGNL1ΔN disassembles RAD51-DNA filaments. To assess the role of FIGNL1 ATPase activity, we introduced a mutation in the catalytic Walker B motif (E501Q), which is defective in ATP hydrolysis (fig. S3, B and D). The E501Q mutant does not affect RAD51 binding (fig. S3E) but is severely defective in disassembling filaments, as judged by NS-EM and nuclease protection assays (Fig. 2 and figs. S3F and S4), suggesting that ATP hydrolysis is required for its activities. This mutant does not rescue lethality in mESCs (fig. S5). The Walker A mutant (K447A) is also defective in ATPase activity and filament disassembly (figs. S3, B and D to F, and S5).

Taken together, our cellular and in vitro data establish that both nucleotide binding and hydrolysis are required for FIGNL1 to dissociate RAD51 from DNA for filament disassembly and are essential for cell viability.

Architecture of the FIGNL1-RAD51 complex

Other known ATPases that disassemble RAD51 filaments (collectively termed antirecombinases) function as DNA translocases or helicases through their ATPase domains (*14*, *31*), whereas the AAA+ domain of FIGNL1ΔN does not readily bind DNA (fig. S3G), suggesting that FIGNL1 acts on RAD51 instead of on DNA. To gain insights into the molecular mechanism of FIGNL1-dependent regulation of RAD51, we used FIGNL1ΔN^{E501Q}, which forms a stable complex with RAD51 but is defective in filament disassembly, to obtain a structure of FIGNL1 in complex with RAD51, which likely represents an initial engaged state of FIGNL1. Using cryogenic electron microscopy (cryo-EM), we determined the structure of the FIGNL1ΔN^{E501Q}-RAD51 complex in the presence of ATP and Mg^{2+} (fig. S6). Single-particle analysis produced a three-dimensional (3D) reconstruction that revealed a hexameric ring shape, which we attributed to FIGNL1; a AAA+ protein that forms hexamers in the presence of nucleotide (ATPγs) (fig. S6E) (*24*); and additional density above the ring, tethered to the hexameric density, to be RAD51 (Fig. 3A). The resolution of this complex is limited, with a global resolution of ~8 Å, likely because of the innate flexibility of the FIGNL1-RAD51 complex (fig. S6). The identified RAD51-binding FRBD is predicted to be in a largely unstructured region (fig. S3A). The volume above the hexamer can accommodate two RAD51 monomers, and the stoichiometry is consistent with the mass photometry data (fig. S7, A and B). Using AlphaFold3 (*32*, *33*), we generated a model of the FIGNL1 FRBD in complex with a RAD51 dimer (fig. S7C). This model predicts that the AAA+ domain is tethered to the FRBD-RAD51 subcomplex through a flexible linker (fig. S7C), which is consistent with our cryo-EM reconstruction (fig. S7B). In this model, the FRBD can bind to two RAD51 molecules by using two sites, separated by ~40 amino acids (fig. S7C), which is consistent with a FIGNL1 hexamer engaging with two RAD51 monomers. The first site (FKTA), which has been previously identified (*18*), is predicted to bind to RAD51 analogous to that of the BRCA2 BRC4 motif (FxxA), which binds at the RAD51 protomer interface in the filament (*34*). A second site (FVPP), which is also present in BRCA2 and RAD51AP1 (*35*, *36*), binds the adjacent RAD51 protomer through a different location on RAD51 and does not overlap with the BRC4 binding site (fig. S7C). Mutating either of the two sites is only moderately defective in our nuclease protection assays, whereas mutating both sites severely reduced its ability in filament disassembly (fig. S7D). mESCs are viable even when both sites are mutated (fig. S7E), suggesting that there are other interaction sites between RAD51 and FIGNL1 in cells, either directly or through other interacting partners, to partially compensate for the lost interaction site. A recent study has shown that mutating site 1 (FxxA to ExxE) failed to suppress ultrafine bridge (UFB) formation in U2OS cells (*20*), suggesting a crucial role of this interaction site in UFB suppression.

To improve the resolution of the reconstruction, we focused on the FIGNL1ΔN hexamer for further processing, which was resolved to 2.9 Å (Fig. 3B and fig. S8). The six FIGNL1 AAA+ domains form a spiral hexamer (Fig. 3B), with chain F at the base of the spiral and chain A at the top. The quality of the electron density map is sufficient to allow a structural model of the AAA+ domain of FIGNL1 to be built (Fig. 3C, table S1, and fig. S8). We identified clear density for Mg^{2+}-ATP, bound in the nucleotide binding pocket of chains A, B, C, D, and E, in between adjacent protomers (Fig. 3C and fig. S8E). The electron density of chain F is of poorer quality, presumably owing to increased flexibility of this subunit (fig. S8, B and E). The structural model allowed us to map mutations found in cancer samples and variants of unknown significance in patients (fig. S9, A and B) (*37*, *38*). Mutations at residue E501 were identified in five tumors in the human cancer database COSMIC, and each, like E501Q, had a high pathogenicity score as gauged with AlphaMissense (0.994 for E501Q) (fig. S9C and table S2) (*39*, *40*), which is consistent with defects we observed in vitro and in cells. Several FIGNL1 mutations are located at the protomer-protomer interface, so that these mutations would be predicted to interfere with proper assembly of the functional hexamer (fig. S9, B and C). Further investigations are required to confirm their potential consequences.

FIGNL1 coordinates the RAD51 N-terminal peptide in its hexameric pore by using pore loops

We found additional density that is consistent with a polypeptide in the central pore of the FIGNL1 AAA+ hexamer (Fig. 4A). The polypeptide is tightly coordinated by two highly

conserved pore loops of FIGNL1 that form a helical staircase (Fig. 4, B to D). Many AAA+ proteins use pore loops to interact with their respective substrates, either protein polypeptides or nucleic acids (*41*–*44*). The N-terminal pore loop [residues 470 to 476; pore loop 1 (PL1)] contains a lysine-tryptophan dipeptide (KW) at its tip, which intercalates the side chains of the polypeptide (Fig. 4D). The C-terminal pore loop [residues 506 to 514; pore loop 2 (PL2)] is less tightly associated with the polypeptide but harbors H514, which tracks along the polypeptide backbone (Fig. 4, C and D). The extra density in the pore suggests that in addition to the two identified FRBD sites, an additional interaction site exists between RAD51 and FIGNL1. We could fit residues 2 to 13 of the RAD51 N terminus, which belong to an unstructured region not observed in previous crystal and cryo-EM structures (fig. S10A). The peptide is well resolved, with a local resolution of 2.7 Å (fig. S10, A and B). High *Q*-scores (*45*) not only indicate a good fit of these residues into the density, but the density has a high resolvability, providing further confidence in the residue assignment (fig. S10A). In this structural model, the highly conserved pore loops encircle the physiochemically conserved hydrophobic and polar amphipathic residue pattern found in the N terminus of RAD51 (Fig. 4, D and E, and fig. S10, B to E) through a close network of interactions, which may provide RAD51 sequence preference (Fig. 4, D and E, and fig. S10, D and E).

To probe the importance of the RAD51 N terminus, which has not previously been shown to have specific functions in filament regulation, we investigated whether FIGNL1 requires the RAD51 N terminus for filament disassembly. RAD51 that lacks the N-terminal 20 residues (RAD51ΔN) can form filaments and protect DNA from nuclease digestion (fig. S11, A to C). RAD51ΔN filaments could not be efficiently disrupted by FIGNL1ΔN in the nuclease protection assay (Fig. 4F and fig. S11D). This is not due to the lack of interactions between FIGNL1ΔN and RAD51ΔN because the binding, although reduced, is still sufficiently high to ensure interactions under the experimental conditions (fig. S11E). This is consistent with the FRBD being a major recruitment site between FIGNL1 and RAD51.

Given that ATPase activities of some AAA+ proteins are stimulated by their respective substrates (*42*, *46*), we tested whether RAD51 stimulates the ATPase activity of FIGNL1. The ATPase activity of FIGNL1ΔN is enhanced in the presence of RAD51 (Fig. 4G), but this enhancement is abolished when the N terminus of RAD51 is deleted (Fig. 4G). Adding FIGNL1ΔN defective in ATPase activity (K447R or E501Q) does not stimulate total ATP hydrolysis, whereas adding ATPase-defective RAD51 (K133R; RAD51-WA) still showed significant enhancement, suggesting that the majority of stimulation is due to increased ATPase activity of FIGNL1 in the presence of the N terminus of RAD51 (fig. S12, A and B). A synthetic peptide containing the complete unstructured 22–amino acid RAD51 N terminus, or the N-terminal 13 or 18 amino acids, can stimulate FIGNL1 ATPase equivalently (Fig. 4H and fig. S12C). This stimulation relies on the N-terminal amphipathic region of RAD51 observed in our cryo-EM structure because replacing the first five residues with alanine in this peptide diminishes the stimulation (Fig. 4H). Furthermore, FIGNL1 ATPase stimulation is specific to the RAD51 N terminus because high concentrations of a peptide of polyglutamate, tubulin C-terminal tails (*47*), ssDNA, and dsDNA all fail to enhance its ATPase activities (fig. S12, C and D). Together, these data reveal that FIGNL1ΔN uses the RAD51 N-terminal region to stimulate its ATPase activity, and that the RAD51 N terminus is essential for the ability of FIGNL1 to disassemble RAD51 filaments.

Pore loop integrity is required for filament disassembly and mESC viability

To corroborate the structural data and to further investigate the importance of the FIGNL1 pore loops, we substituted the KW of PL1 to a glutamic acid and alanine, respectively (K473E, W474A; herein referred to as the PL mutant) (fig. S13A). This mutant retained near wild-type ATPase activity and RAD51 binding (fig. S13, B and C). This mutant ATPase activity can be

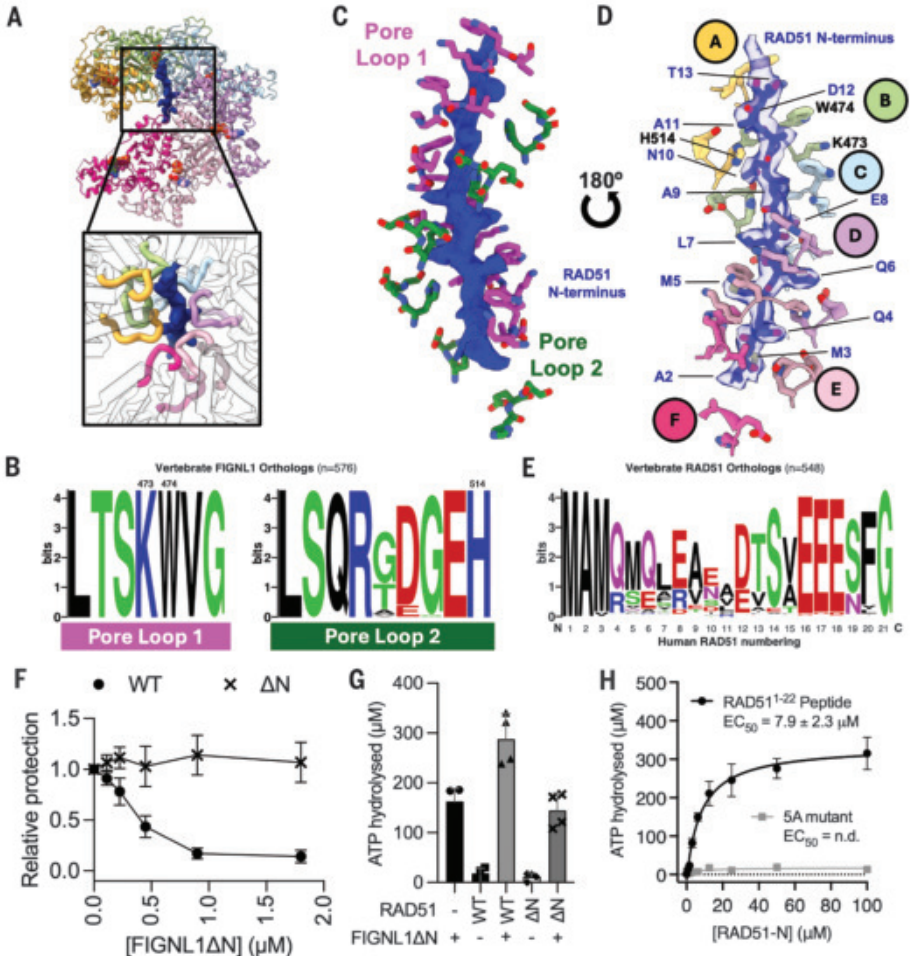

Fig. 4. FIGNL1 coordinates the N terminus of RAD51 through its central hexameric pore. (**A**) Extra density observed in the central pore of the FIGNL1 AAA+ hexamer. (**B**) Sequence conservation plots of the pore loops of FIGNL1 in vertebrates (n = 576 distinct genes). Residues 473, 474, and 514 are labeled. (**C**) The pore loops of FIGNL1 form two helical staircases enclosing the RAD51 N terminus. (**D**) The pore loop residues intercalate with the RAD51 N-terminal residues. (**E**) Conservation plot of the N-termini of RAD51 in 548 vertebrates. Numbering refers to the human RAD51 sequence. (**F**) Quantification of nuclease protection assays of dsDNA by RAD51 (WT) or RAD51 with N-terminal 20 amino acids deleted (ΔN), in the presence of increasing concentrations of FIGNL1ΔN. Each data point indicates the mean ± SD, n = 3 independent experiments. (**G**) Quantification of ATPase activity of FIGNL1 alone or incubated with RAD51 (WT) or RAD51ΔN (ΔN). (**H**) Dose-response ATPase activity of FIGNL1ΔN in the presence of increasing concentrations of the RAD51 N-terminal peptide or with the first five amino acids replaced by alanine (n = 4 independent experiments).

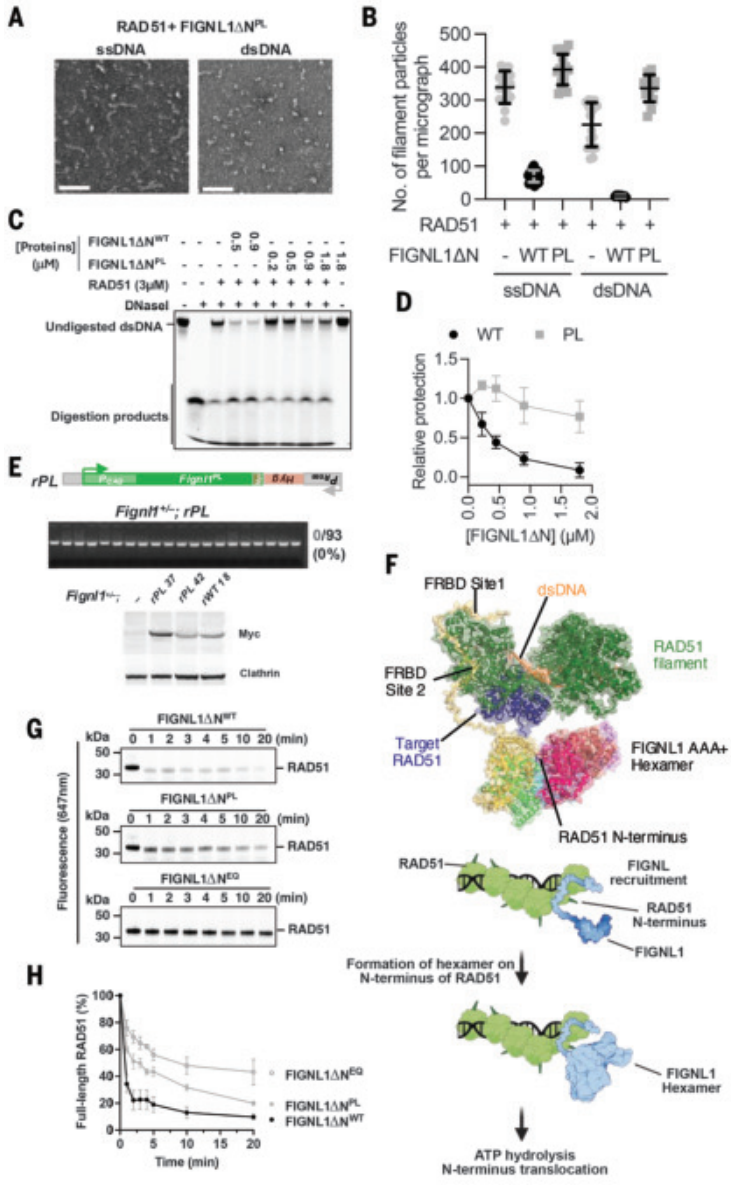

Fig. 5. Mutation of PL1 confers loss of RAD51 filament disassembly and cell lethality. (**A**) Representative micrographs of RAD51-DNA filaments treated by FIGNL1ΔN bearing mutations in PL1 K483E/W484A (PL mutant) with ssDNA or dsDNA. Scale bars, 100 nm. (**B**) Quantification of experiments shown in (A), highlighting the loss of filament disassembly by FIGNL1ΔN bearing PL mutation. *n* = 20 micrographs; data are shown as mean ± SD. WT FIGNL1ΔN data are for comparison and are as shown in Fig. 2. (**C**) Nuclease protection of dsDNA coated by RAD51 upon treatment with wild-type or PL mutant of FIGNL1ΔN. (**D**) Quantification of RAD51 + FIGNL1ΔN^{PL} experiments shown in (C). *n* = 3 independent experiments; data are shown as mean ± SD. WT FIGNL1ΔN data quantification are from independent repeats shown in Fig. 3 and 0.5 and 0.9 μM data points shown in (C). (**E**) FIGNL1 PL mutant is not compatible with cell survival. An expression cassette for the mutant (*rPL*^{Myc}) was targeted to *Rosa26* locus as in Fig. 1A. No *Fignl1*$^{-/-}$ colonies were obtained after CRISPR-Cas9 gene editing in *Fignl1*$^{+/-}$ cells with sgRNAs c and d as in Fig. 1A. Western blotting for the Myc tag confirms that the PL mutant is expressed. (**F**) (Top) An integrated structural model of FIGNL1 engaged on a RAD51-dsDNA filament by using our cryo-EM–imaged structure in conjunction with AlphaFold3 prediction of FRBD binding RAD51. FIGNL1 is colored by subunit as in Fig. 3. RAD51 protomers are colored green, except the target RAD51 engaged with FIGNL1 AAA+ pore, which is colored dark blue. For clarity, only a single FRDB is shown from one subunit of the FIGNL1 hexamer, and only a single N terminus is shown from RAD51. (Bottom) A proposed model of FIGNL1 recruitment and RAD51 filament disassembly. FIGNL1 is recruited to the RAD51 filament through its FRBD domain and forms a hexamer, enclosing the N terminus of RAD51, which stimulates the ATPase activity of FIGNL1 and promotes translocation of the N terminus in the hexamer pore, leading to the unfolding and removal of RAD51 from the filament, promoting disassembly. (**G**) SDS–polyacrylamide gel electrophoresis gels showing RAD51 degradation by proteases in the presence of FIGNL1ΔN and its mutants with ATP. (**H**) Quantification of RAD51 band intensity over time. Data points are mean ± SD; *n* = 3 independent experiments.

stimulated by the RAD51 N terminus but to a lesser extent as compared with wild type (fig. S13D). This mutant is severely defective in disassembling RAD51 filaments on both dsDNA and ssDNA as can be visualized by using NS-EM (Fig. 5, A and B) and nuclease protection assays (Fig. 5, C and D). The equivalent mutation in mESCs is incompatible with cell viability (Fig. 5E). Together, these data support a crucial role of the pore loops for FIGNL1 activity.

Recent studies have shown that FIGNL1 is important in meiotic DMC1-focus formation and resolution (*17*, *19*). We thus set out to test the ability of FIGNL1ΔN in disassembling DMC1 filaments in vitro. DMC1 does not efficiently protect dsDNA from nuclease (*48*); we therefore used ssDNA in our assays. FIGNL1ΔN could also reduce nuclease protection by DMC1 (fig. S14, A and B), indicating disruption of nucleoprotein complexes, and both DMC1 and DMC1 N-terminal peptide stimulate ATPase activity of FIGNL1ΔN (fig. S14, C and D). However, the DMC1 N-terminal peptide is 3 times less effective at stimulating FIGNL1 ATPase activity compared with that of RAD51 under the same experimental conditions (fig. S14D). DMC1 and RAD51 N-terminal regions share some degree of conservation (fig. S14E), suggesting that FIGNL1 substrate selection is somewhat plastic. The pore loop mutant is severely defective in disassembling DMC1 filaments (fig. S14, A and B). Together, these data suggest that FIGNL1 can also disrupt DMC1-DNA association by using a similar mechanism to that of RAD51, despite being less efficient in our assays. The precise mechanism and sequence specificity of FIGNL1 requires further investigation.

Our data presented here suggest a molecular mechanism by which FIGNL1 acts on RAD51 to promote dissociation from DNA and other substrates. Through its FRBD domain and other interacting partners such as FIRRM/FLIP, FIGNL1 is recruited to the side of the RAD51 filament. The FIGNL1 hexamer then assembles around and encloses the RAD51 N terminus (Fig. 5F). We propose that similarly to other AAA+ proteins that enclose substrate peptides in the central pores (fig. S15) (*41*, *42*, *49*–*53*), FIGNL1 acts as a peptide translocase that leads to RAD51 remodeling. RAD51 is sensitive to limited proteolysis in the presence of FIGNL1ΔN and ATP but markedly less so in the presence of PL or EQ mutants (Fig. 5, G and H, and fig. S16), supporting that RAD51 is unfolded and remodeled by FIGNL1 ATPase. Translocating or unfolding the RAD51 N-terminal peptide and the proceeding α-helical domain (N-domain) by FIGNL1 would substantially destabilize the filament because the N-domain binds between adjacent protomers (fig. S17). The proposed mechanism suggests that FIGNL1 could also act on RAD51 bound to other proteins—including nucleosomes, as shown recently—therefore acting as a general RAD51 regulator (*54*). This is

distinct from other antirecombinases such as RAD54, which is a DNA translocase and dissociates RAD51 from dsDNA only (*55*, *56*). FIGNL1's distinctive mechanism in dissociating RAD51 from chromatin defines its critical roles in cell viability.

REFERENCES AND NOTES

1. P. Baumann, F. E. Benson, S. C. West, *Cell* **87**, 757–766 (1996).
2. F. E. Benson, A. Stasiak, S. C. West, *EMBO J.* **13**, 5764–5771 (1994).
3. Y. Sun, T. J. McCorvie, L. A. Yates, X. Zhang, *Cell. Mol. Life Sci.* **77**, 3–18 (2020).
4. D. K. Bishop, *Cell* **79**, 1081–1092 (1994).
5. A. Carver, X. Zhang, *Semin. Cell Dev. Biol.* **113**, 3–13 (2021).
6. Y. W. Chan, S. C. West, *Cell Cycle* **17**, 2101–2109 (2018).
7. A. Piazza, W. D. Wright, W.-D. Heyer, *Cell* **170**, 760–773.e15 (2017).
8. K. Schlacher, H. Wu, M. Jasin, *Cancer Cell* **22**, 106–116 (2012).
9. S. Tye, G. E. Ronson, J. R. Morris, *Semin. Cell Dev. Biol.* **113**, 14–26 (2021).
10. H. L. Klein, *DNA Repair* **7**, 686–693 (2008).
11. R. B. Jensen, A. Carreira, S. C. Kowalczykowski, *Nature* **467**, 678–683 (2010).
12. L. A. Greenhough *et al*., *Nature* **619**, 650–657 (2023).
13. Y. Rawal *et al*., *Nature* **619**, 640–649 (2023).
14. E. Antony *et al*., *Mol. Cell* **35**, 105–115 (2009).
15. J. Simandlova *et al*., *J. Biol. Chem.* **288**, 34168–34180 (2013).
16. J. D. Ward *et al*., *Mol. Cell* **37**, 259–272 (2010).
17. M. Ito *et al*., *Nat. Commun.* **14**, 6857 (2023).
18. J. Yuan, J. Chen, *Proc. Natl. Acad. Sci. U.S.A.* **110**, 10640–10645 (2013).
19. Q. Zhang *et al*., *Nucleic Acids Res.* **51**, 8606–8622 (2023).
20. K. Matsuzaki, A. Shinohara, M. Shinohara, *Nucleic Acids Res.* **52**, 5774–5791 (2024).
21. J. B. Fernandes *et al*., *PLOS Genet.* **14**, e1007317 (2018).
22. Z. Zhou *et al*., *Cell Rep.* **42**, 112907 (2023).
23. C. Stok *et al*., *Cell Rep.* **42**, 112668 (2023).
24. E. Pinedo-Carpio *et al*., *Sci. Adv.* **9**, eadf4082 (2023).
25. J. D. Tischler *et al*., *Nat. Commun.* **15**, 866 (2024).
26. K. Matsuzaki, S. Kondo, T. Ishikawa, A. Shinohara, *Nat. Commun.* **10**, 1407 (2019).
27. T. Cupido, N. H. Jones, M. J. Grasso, R. Pisa, T. M. Kapoor, *Nat. Struct. Mol. Biol.* **28**, 388–397 (2021).
28. C. Richardson, J. M. Stark, M. Ommundsen, M. Jasin, *Oncogene* **23**, 546–553 (2004).
29. A. Zainu *et al*., bioRxiv 541096 [Preprint] (2023).
30. M. R. G. Taylor *et al*., *Cell* **162**, 271–286 (2015).
31. D. Branzei, B. Szakal, *Curr. Opin. Genet. Dev.* **71**, 27–33 (2021).
32. J. Jumper *et al*., *Nature* **596**, 583–589 (2021).
33. M. Mirdita *et al*., *Nat. Methods* **19**, 679–682 (2022).
34. L. Pellegrini *et al*., *Nature* **420**, 287–293 (2002).
35. Y. Kwon *et al*., *Nat. Commun.* **14**, 432 (2023).
36. M. H. Dunlop *et al*., *J. Biol. Chem.* **286**, 37328–37334 (2011).
37. M. J. Landrum *et al*., *Nucleic Acids Res.* **46** (D1), D1062–D1067 (2018).
38. J. G. Tate *et al*., *Nucleic Acids Res.* **47**, D941–D947 (2019).
39. J. Cheng *et al*., *Science* **381**, eadg7492 (2023).
40. H. Tordai *et al*., *Sci. Data* **11**, 495 (2024).
41. N. Monroe, H. Han, P. S. Shen, W. I. Sundquist, C. P. Hill, *eLife* **6**, e24487 (2017).
42. C. R. Sandate, A. Szyk, E. A. Zehr, G. C. Lander, A. Roll-Mecak, *Nat. Struct. Mol. Biol.* **26**, 671–678 (2019).
43. J. S. Lewis *et al*., *Nature* **606**, 1007–1014 (2022).
44. J. Wald *et al*., *Nature* **609**, 630–639 (2022).
45. G. Pintilie *et al*., *Nat. Methods* **17**, 328–334 (2020).
46. E. R. Jenkinson, J. P. J. Chong, *Proc. Natl. Acad. Sci. U.S.A.* **103**, 7613–7618 (2006).
47. E. A. Zehr, A. Szyk, E. Szczesna, A. Roll-Mecak, *Dev. Cell* **52**, 118–131.e6 (2020).
48. Z. Li, E. I. Golub, R. Gupta, C. M. Radding, *Proc. Natl. Acad. Sci. U.S.A.* **94**, 11221–11226 (1997).
49. E. Zehr *et al*., *Nat. Struct. Mol. Biol.* **24**, 717–725 (2017).
50. M. Su *et al*., *Sci. Adv.* **3**, e1700325 (2017).
51. H. Han, N. Monroe, W. I. Sundquist, P. S. Shen, C. P. Hill, *eLife* **6**, e31324 (2017).
52. C. Alfieri, L. Chang, D. Barford, *Nature* **559**, 274–278 (2018).
53. Q. Ye *et al*., *EMBO J.* **36**, 2419–2434 (2017).
54. T. Shioi *et al*., *Nature* **628**, 212–220 (2024).
55. P. P. Shah *et al*., *Mol. Cell* **39**, 862–872 (2010).
56. J. Essers *et al*., *Cell* **89**, 195–204 (1997).

ACKNOWLEDGMENTS

Initial screening of electron microscopy grids was carried out at Imperial College London Centre for Structural Biology. We acknowledge Diamond Light Source for access and support of the cryo-EM facilities at the UK national eBIC, proposal EM19865, funded by the Wellcome Trust and MRC, and London Consortium for high-resolution cryo-EM (LonCEM), funded by the Wellcome Trust. We thank N. Jones and T. Kapoor for discussions and the gift of ASPIR-1. We thank members of the Zhang and Jasin laboratories for their helpful insights and discussions. **Funding:** This work was funded by Breast Cancer Now and a Wellcome Trust Investigator Award (210658/Z/18/Z) and a Wellcome Trust Discovery Award (227769/Z/23/Z) to X.Z. and Starr Cancer Consortium award I13-0055 and NIH R35 CA253174 to M.J. **Author contributions:** A.C., T.-Y.Y., M.J., and X.Z. designed the project. Cryo-EM sample preparation, image processing, and structure determination was performed by A.C. and L.A.Y. Protein construct cloning, mutagenesis, and purification was performed by A.C., with contributions from K.L. and L.A.Y. In vitro assays were performed by A.C. and L.A.Y., with contributions from K.L. All cellular work was carried out by T.-Y.Y., with assistance from T.W. Mouse studies were carried out by R.W. Bioinformatic analysis was performed by L.A.Y.; A.C. and X.Z. wrote the initial manuscript, with contributions from L.A.Y., T.-Y.Y., and M.J. Edits to the manuscript were carried out by all authors. **Competing interest:** Authors declare that they have no competing interests. **Data and materials availability:** All the structural data have been deposited in Worldwide Protein Data Bank (wwPDB) with access codes EMDB-18946, PDB code 8R64. The cell lines generated for this study are available from M.J. under a materials transfer agreement with the Memorial Sloan Kettering Cancer Center, New York, USA. Transfer of cell lines may be subject to third-party obligations. All other data are available in the main text or the supplementary materials.

SUPPLEMENTARY MATERIALS

science.org/doi/10.1126/science.adr7920
Materials and Methods
Figs. S1 to S17
Tables S1 and S2
References (*57*–*72*)
MDAR Reproducibility Checklist

Submitted 16 July 2024; accepted 20 November 2024
Published online 5 December 2024
10.1126/science.adr7920

NONLINEAR PHONONICS

Photo-induced chirality in a nonchiral crystal

Z. Zeng[1,2], M. Först[1], M. Fechner[1], M. Buzzi[1], E. B. Amuah[1], C. Putzke[1], P. J. W. Moll[1], D. Prabhakaran[2], P. G. Radaelli[2], A. Cavalleri[1,2]*

Chirality, a pervasive form of symmetry, is intimately connected to the physical properties of solids, as well as the chemical and biological activity of molecular systems. However, inducing chirality in a nonchiral material is challenging because this requires that all mirrors and all roto-inversions be simultaneously broken. Here, we show that chirality of either handedness can be induced in the nonchiral piezoelectric material boron phosphate (BPO_4) by irradiation with terahertz pulses. Resonant excitation of either one of two orthogonal, degenerate vibrational modes determines the sign of the induced chiral order parameter. The optical activity of the photo-induced phases is comparable to the static value of prototypical chiral α-quartz. Our findings offer new prospects for the control of out-of-equilibrium quantum phenomena in complex materials.

An object is defined as chiral if its mirror image cannot be superimposed onto itself through any combination of rotations or translations. In crystalline systems, the structural chirality is predetermined by the lattice structure during the formation process (*1*), making it challenging to manipulate the handedness of the system after growth. For example, the chiral crystal α-quartz (*2*) can exist in either right- or left-handed structures (space group $P3_121$ and $P3_221$, respectively), characterized by atomic spirals of opposite handedness within the unit cell (Fig. 1A). Once formed, chiral crystals of opposite handedness cannot be switched into each other without melting and recrystallization of the material (*3*, *4*).

Antiferrochirals are a distinct class of achiral systems in which the unit cell comprises chiral fragments with opposite handedness (*5*). The overall system remains achiral due to the degeneracy between the left- and right-handed structures, resembling racemic crystals (*6*). One notable feature of these systems is their potential to develop chirality under external perturbations that can uncompensate the staggered chiral fragments.

Inducing chirality in achiral systems by nonlinear phononics

Boron phosphate (BPO_4, space group $I\bar{4}$) is an example of an antiferrochiral material. Its equilibrium lattice and the left- and right-handed chiral substructures are sketched in Fig. 1B (*7*). The displacement of the atomic structure along the coordinates of B-symmetry modes (with amplitude Q_B) lifts the degeneracy between the local structures of opposite handedness, resulting in a ferrichiral state. Figure 2A highlights this behavior, where the shaded atomic motions along the B-mode coordinates enhance and reduce the amplitudes of the left- and

[1]Max Planck Institute for the Structure and Dynamics of Matter, Hamburg, Germany. [2]Department of Physics, Clarendon Laboratory, University of Oxford, Oxford, UK.
*Corresponding author. Email: andrea.cavalleri@mpsd.mpg.de

right-handed local chiral structures, respectively. As a result, the handedness of the ferrichiral state can be controlled by the direction of the phonon displacement (*8*), i.e., the sign of its amplitude Q_B, providing an opportunity to rationally design the chirality in these systems by structural engineering.

This effect is not easily stimulated with external fields because it is necessary to couple to a specific lattice mode that needs to be displaced in a specific direction. This is achieved transiently through nonlinear phononics (*9*–*17*), an effective approach to coherently control the atomic structure with light. This concept provides a new basis for the rational design of crystal structures and symmetries with light, inducing desirable functional properties at high speed. In one specific type of nonlinear phononic interaction, the square of a selectively driven, infrared-active terahertz-frequency phonon mode, Q_{IR}, couples linearly to a second mode, Q_2, inducing a rectified, displacive force along the normal mode coordinate Q_2. This rectified force induces a transient crystal structure not accessible at equilibrium (*18*–*22*).

In BPO_4, a displacive force on the B-symmetry phonon modes that control chirality can be achieved by driving either of the degenerate infrared-active E-symmetry phonon modes, polarized along the *a* and *b* axes, respectively. According to the lowest-order coupling term of the form $U = -\alpha Q_{E,a}^2 Q_B + \alpha Q_{E,b}^2 Q_B$ (*23*), the coherent drive of phonon mode $Q_{E,a}$ by a resonant terahertz-frequency field exerts a rectified force onto Q_B in the positive direction, leading to a positive transient displacement of the lattice along the B-mode coordinates away from equilibrium (Fig. 2B). Conversely, if the orthogonal mode $Q_{E,b}$ is resonantly driven, the transient displacement along Q_B changes direction due to the opposite sign in the coupling term (Fig. 2C). Therefore, the system can be driven into either one of the two opposite chiral states by controlling the polarization of the terahertz-frequency excitation pulse.

This effect can be simulated for BPO_4 through two coupled equations of motion for the resonantly driven doubly degenerate mode $Q_{E,a/b}$ and the set of four anharmonically coupled B-symmetry modes $Q_{B,i}$ (i = 1...4), taking the form

$$\frac{\partial^2}{\partial t^2} Q_{E,a/b}(t) + 2\gamma_{E,a/b} \frac{\partial}{\partial t} Q_{E,a/b}(t) + \omega_{E,a/b}^2 Q_{E,a/b}(t) = Z_{E,a/b}^* E(t) \quad (1)$$

$$\frac{\partial^2}{\partial t^2} Q_{B,i}(t) + 2\gamma_{B,i} \frac{\partial}{\partial t} Q_{B,i}(t) + \omega_{B,i}^2 Q_{B,i}(t) = \pm\alpha Q_{E,a/b}^2 \quad (2)$$

Where $\gamma_{E,a/b}$ and $\gamma_{B,i}$ are the damping coefficients, $\omega_{E,a/b}$ and $\omega_{B,i}$ the frequencies of the phonon modes, and $Z_{E,a/b}^*$ is the effective charge that couples the infrared-active $Q_{E,a/b}$ modes to the pulsed terahertz electric field $E(t) = E_0 \sin(\omega_{B,i}\, t) e^{-\frac{t^2}{2\sigma^2}}$. The sign of the force on the B-symmetry modes (right side of Eq. 2) depends on whether the E-symmetry mode is excited along the *a* or the *b* axis. We used ab initio calculations to determine all the relevant phonon parameters used in these equations. These calculations predict that transient displacement of the crystal along the four B-symmetry phonons drives the system into a chiral state, which is determined by the linear superposition of these modes. The induced chirality can be quantified by calculating an electric toroidal monopole as the order parameter (*24*) or by following a recently introduced geometrical approach (*23*, *25*).

Dynamics of chirality and optical activity

The displacement causes two optical effects on a time-delayed probe pulse, optical activity, which relates to the wanted induced chirality, and induced birefringence due to the breaking of the fourfold symmetry (–4) of the crystal, which can be subtracted from the total optical signal to reveal the optical activity. Figure 3, A and B, shows the time-dependent changes of each of these properties (optical activity and induced birefringence) for excitation of the mode $Q_{E,a}$ along the *a* axis, as calculated from the transient lattice structure and taking into account the B-mode–dependent changes in the diagonal and off-diagonal elements of the optical permittivity. The latter were determined using an ab initio density functional theory approach (*23*).

The optical activity alone generates a characteristic polarization rotation that is independent of the incident polarization of the probe light in the *a*–*b* plane (*26*, *27*) (Fig. 3A, inset). Conversely, the birefringence introduces a modulation of the polarization rotation response with a fourfold symmetry with respect to the incident probe polarization [Fig. 3B, inset, and (*23*)] without changing the average value of the signal over all incident probe polarizations. The total polarization rotation signal follows the form

$$\theta(\varphi) = A_1\rho + A_2 \sin(4\varphi - \phi)(\Delta n)^2 \quad (3)$$

where φ is the relative angle between the pump and the probe polarization, ϕ is the angle between

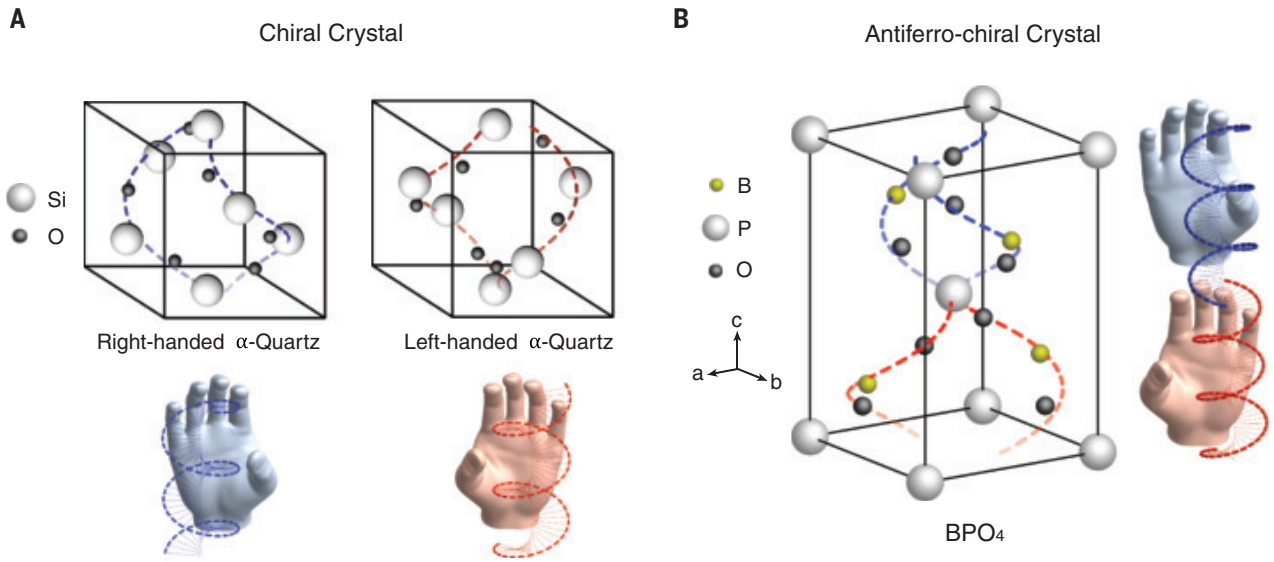

Fig. 1. Chirality in the solid state. (**A**) The prototypical chiral crystal α-quartz exists in left- and right-handed configurations that are determined by the spiral atomic structure formed during the growth process. (**B**) The unit cell of the antiferrochiral crystal BPO_4 is composed of chiral substructures of opposite handedness. The degeneracy of these left- and right-handed structures makes the overall system achiral.

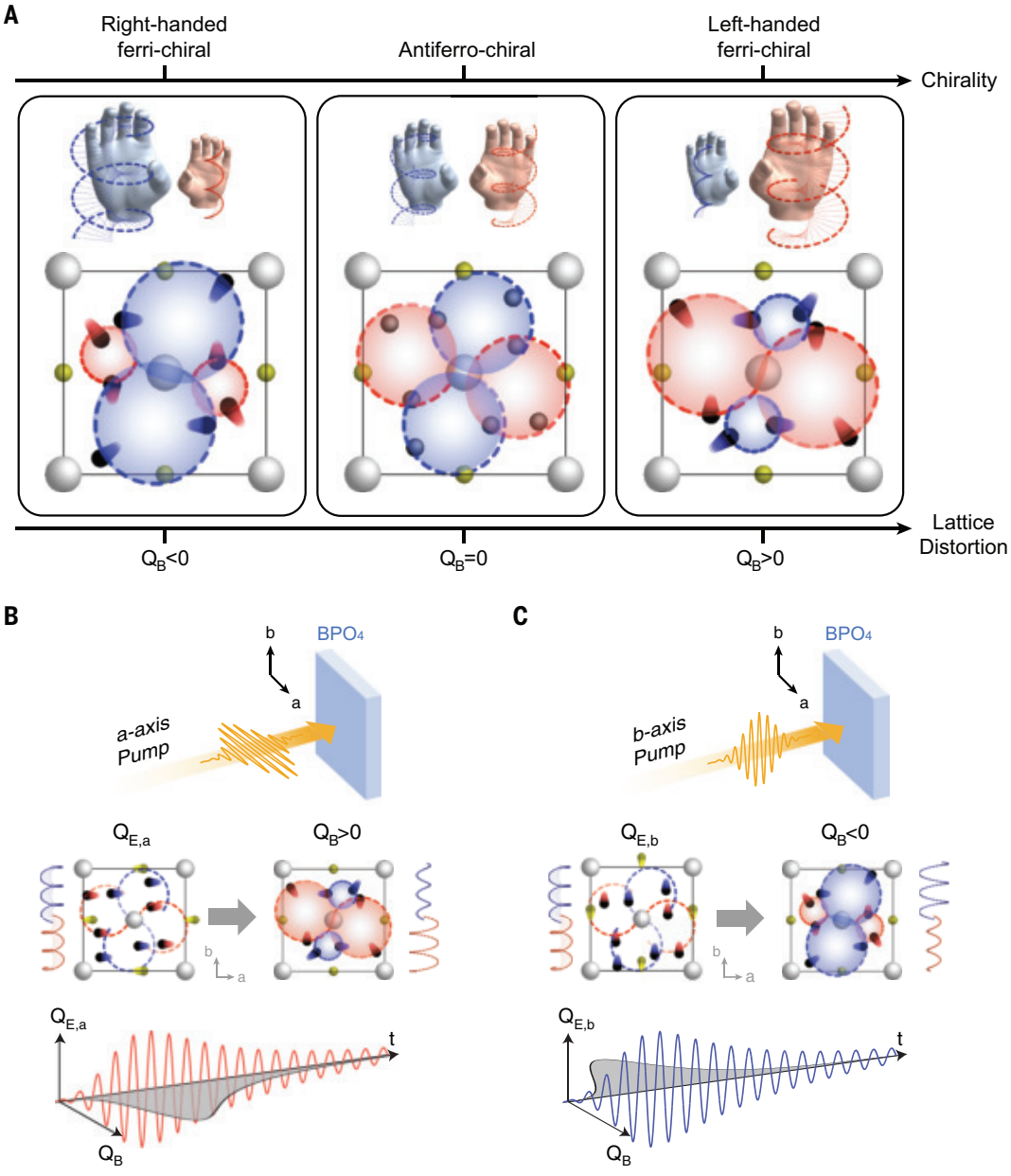

Fig. 2. Light-induced chirality in antiferrochiral BPO_4. (**A**) The atomic displacements in BPO_4 along B-symmetry phonons lift the degeneracy between the local structures of left and right handedness, driving the system from the antiferrochiral to a ferrichiral state. The phonon displacement in the opposite direction induces chirality of opposite handedness. (**B**) A terahertz pump with electric field polarization along the *a* axis induces coherent oscillations of the mode $Q_{E,a}$ about its equilibrium position. A positive transient displacement along the B-mode coordinates is induced through nonlinear phonon coupling, driving the system into the nonequilibrium ferrichiral state with left handedness. (**C**) Exciting the doubly degenerate E-symmetry phonon along the *b* axis induces coherent oscillations of the $Q_{E,b}$ mode about its equilibrium position. A negative transient displacement along the Q_B mode coordinates is induced through nonlinear phonon coupling, driving the system into a ferrichiral state with right handedness.

the pump polarization and the optical axis of the transient birefringence, ρ is the rotary power proportional to the optical activity, and Δn is the birefringence-induced difference in refractive index. The overall time-dependent polarization rotation signal, calculated as a function of the incident polarization, is shown for a terahertz pump with a peak electric field of 5 MV/cm (Fig. 3C).

When the polarization of the pump is oriented along the *b* axis to excite the mode $Q_{E,b}$, the induced displacement of the B-symmetry modes changes direction. Therefore, both the optical activity and the induced birefringence are reversed (Fig. 3, D and E), resulting in a sign change of the overall polarization rotation signal compared with the excitation along the *a* axis (Fig. 3F).

Experimental results

Experimental validation of these predictions was obtained using the optical setup sketched in Fig. 4A. The BPO_4 sample, held at room temperature, was excited by 19-THz center frequency pulses of 3 THz full width at half maximum, with an excitation fluence of up to 5.0 mJ/cm^2 and a corresponding peak electric field of 5.1 MV/cm. These pulses were linearly polarized along either the *a* or the *b* axis, resonantly driving each degenerate E-symmetry phonon mode at its 18.9-THz transverse-optical frequency (*23*).

A time-dependent rotation of the probe polarization was induced by phonon excitation with a pump polarized along the crystal *a* axis (Fig. 4B). At each probe polarization angle, we found a sudden onset of a rotation around time zero, followed by a decay lasting a few picoseconds, far longer than the 200-fs duration of the excitation pulse. The signal displayed a 90° periodicity with the incident probe polarization due to the transient birefringence discussed above.

Because of the modulation induced by the birefringence averaging to zero over all of the probe polarizations (*28*, *29*), the transient optical activity can be extracted by averaging the signal over all the incident probe polarizations at each time delay (Fig. 4C). The result shows a finite and positive signal, providing clear evidence for a nonequilibrium chiral state. Its lifetime follows the excitation and decay of the resonantly driven optical phonon.

We further rotated the pump polarization by 90° to resonantly drive the E-symmetry phonon

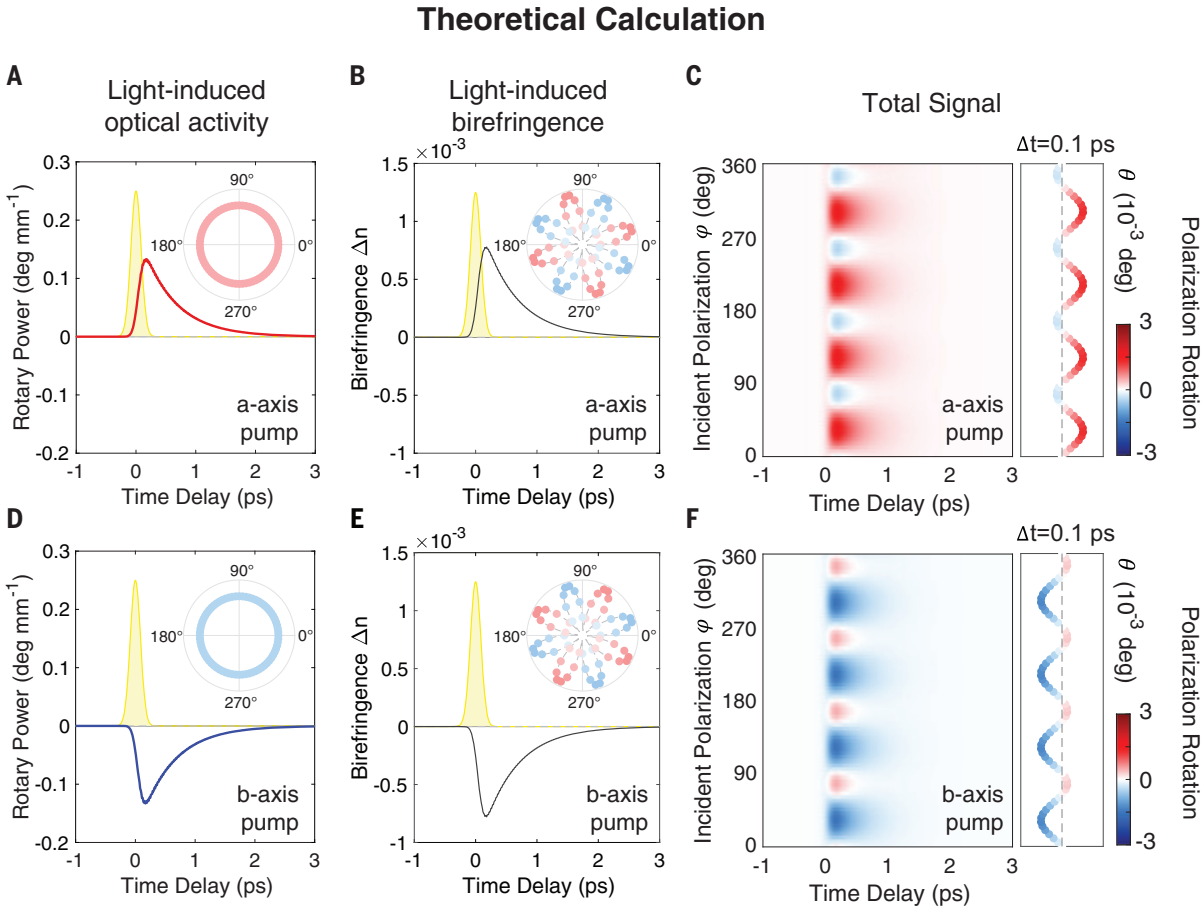

Fig. 3. Theoretical calculations of the light-induced chiral state. (**A**) Light-induced optical activity for the *a*-axis pump as a function of pump-probe time delay. The yellow-shaded area is the temporal profile of the excitation pulse. Inset shows the corresponding amplitude of the polarization rotation signal as a function of probe incident polarization. (**B**) Light-induced birefringence for the same *a*-axis pump as a function of pump-probe time delay. Inset shows the corresponding amplitude modulation of the polarization rotation signal as a function of probe incident polarization. (**C**) The resulting total polarization rotation signal for the *a*-axis pump as a function of probe incident polarization and pump-probe time delay. The signal at a fixed time delay of +0.1 ps is shown on the right. (**D**) Same as (A) but for excitation along the *b* axis. (**E**) Same as (B) but for excitation along the *b* axis. (**F**) Same as (C) but for excitation along the *b* axis. For all calculations, we used a 19-THz pump pulse of 5 MV/cm peak electric field.

along the BPO_4 crystal *b* axis. The corresponding time-dependent polarization rotation, again as a function of the incident probe polarization, and the corresponding optical activity are shown in Fig. 4, D and E. As predicted, the signals reversed sign, showing opposite handedness of the light-induced ferrichiral state compared with the *a*-axis excitation.

Further characterization of the light-induced chiral state validates the predicted nonlinear phononic mechanism. Figure 5A shows the rotary power as a function of the peak electric fields of the 19-THz excitation pulse, exhibiting a quadratic field dependence and a sign reversal for the two different pump polarizations. This behavior is consistent with the nonlinear phonon interaction potential $U = -\alpha Q_{E,a}^2 Q_B + \alpha Q_{E,b}^2 Q_B$. In addition, the magnitude of the nonequilibrium rotary power was resonantly enhanced when the excitation pulses were tuned to the 18.9-THz transverse optical frequency of the doubly degenerate E-symmetry phonon (Fig. 5B). We estimated the magnitude of the light-induced optical activity in BPO_4 at resonance by comparing the nonequilibrium rotary power with the static value of α-quartz (6.8°/mm), a commonly used material for polarization rotation in optics (*30*). For the pump fluence available in the experiment, and assuming that the chiral state is induced only within the extinction depth δ of the excitation pulses (*23*), the light-induced rotary power of BPO_4 is comparable to the equilibrium value of α-quartz.

Concluding remarks

Extension of this approach to ferrichiral systems may enable ultrafast switching with the nonlinear phononic protocol discussed here. Applications to ultrafast memory devices would follow, as well as to more sophisticated optoelectronic platforms powered by light and connected to the handedness of matter. More broadly, the emergence of chirality on the ultrafast time scale, together with the ability to switch between chirality of opposite handedness, offers exciting opportunities for exploring new phenomena in out-of-equilibrium physics of complex matter, especially in topological (*31*–*33*) and correlated systems (*34*, *35*), where handedness plays an important role.

REFERENCES AND NOTES

1. B. L. Feringa, R. A. Van Delden, *Angew. Chem. Int. Ed.* **38**, 3418–3438 (1999).
2. Y. Le Page, G. Donnay, *Acta Crystallogr. B* **32**, 2456–2459 (1976).
3. T. Matsuura, H. Koshima, *J. Photochem. Photobiol. Photochem. Rev.* **6**, 7–24 (2005).
4. N. Kumar, S. N. Guin, K. Manna, C. Shekhar, C. Felser, *Chem. Rev.* **121**, 2780–2815 (2021).
5. Y. Wang *et al.*, *J. Am. Chem. Soc.* **145**, 17443–17460 (2023).
6. T. O. Yeates, S. B. Kent, *Annu. Rev. Biophys.* **41**, 41–61 (2012).
7. Z. Li *et al.*, *Chem. Mater.* **16**, 2906–2908 (2004).
8. C. P. Romao, D. M. Juraschek, *ACS Nano* **18**, 29550–29557 (2024).

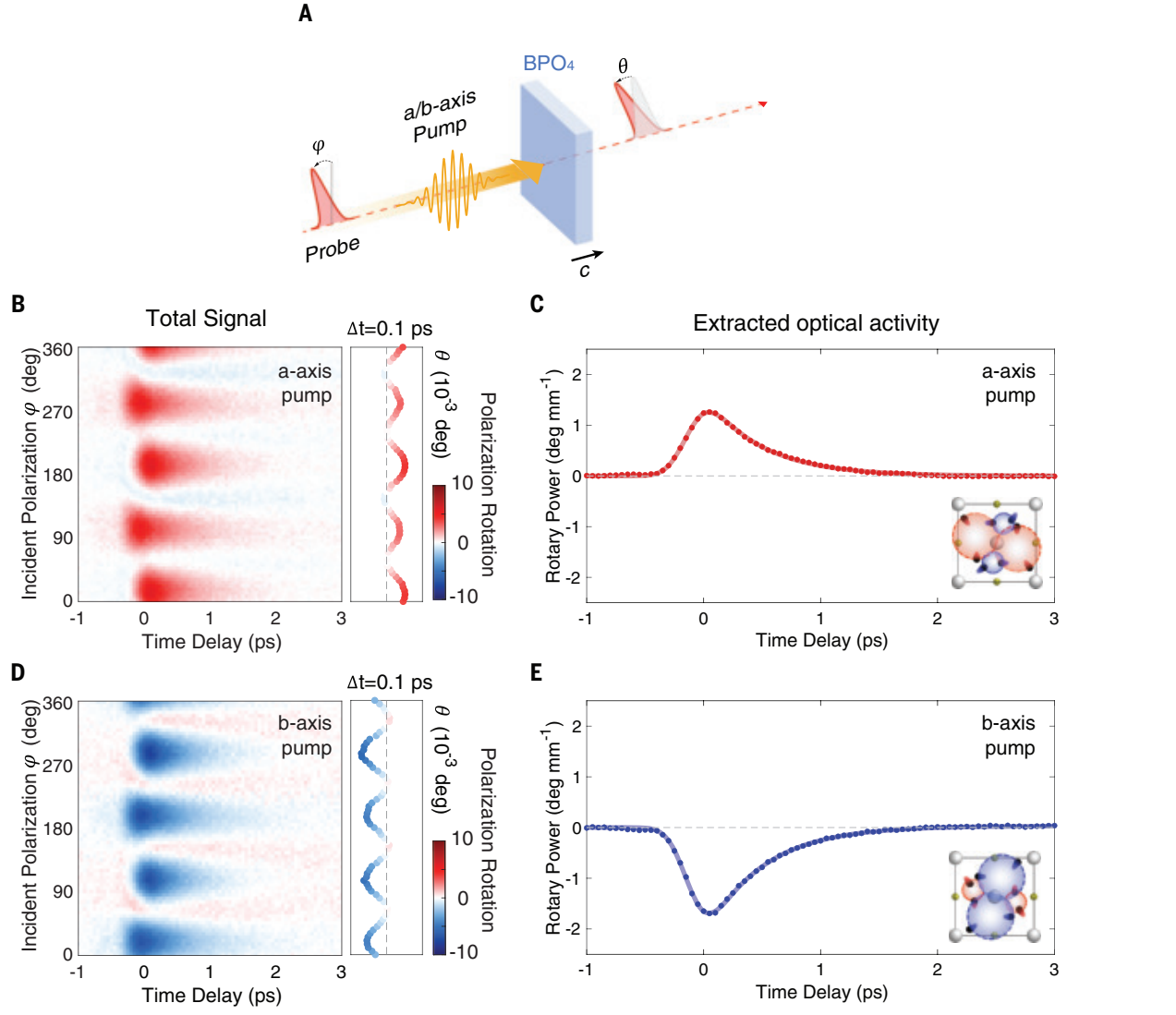

Fig. 4. Time-resolved polarization rotation measurements. (**A**) Schematic of the pump-probe experiment. A linearly polarized terahertz pulse, polarized along either the *a* or *b* axis, drives the BPO_4 crystal into chiral states. A time-delayed near-infrared pulse probes the state by the measurement of its polarization rotation, which is carried out as a function of the probe incident polarization. (**B**) Time delay–dependent polarization rotation signal for *a*-axis excitation as a function of probe incident polarization. The signal at a fixed time delay of +0.1 ps is shown on the right. (**C**) Time delay–dependent rotary power, proportional to the optical activity, extracted from the data shown in (B) and considering the finite extinction depth δ of the excitation pulses. (**D**) Same as (B) but for *b*-axis excitation. (**E**) Same as (C) but for *b*-axis excitation.

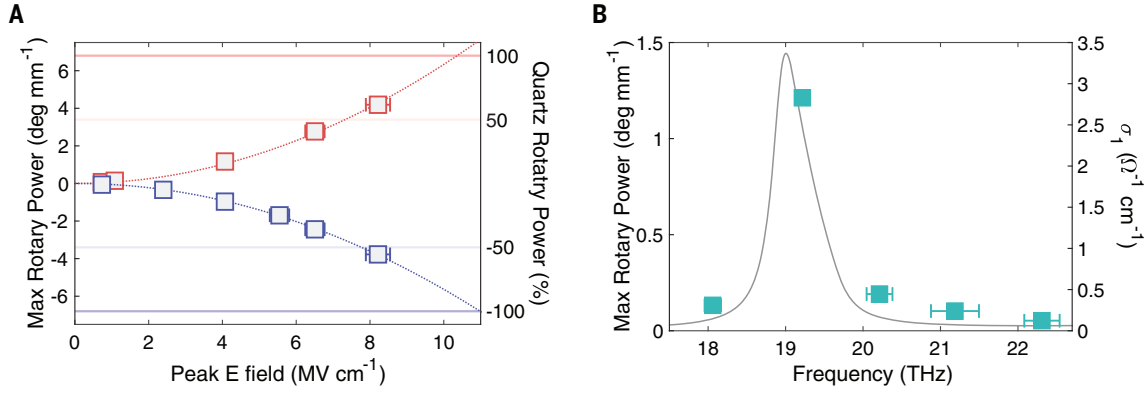

Fig. 5. Characterization of the light-induced chiral states. (**A**) The rotary power of the transient state as a function of the terahertz pulse peak electric field for a-axis–polarized (red) and b-axis–polarized (blue) excitation. (**B**) Maximum of rotary power at fixed peak electric field of 5.1 MV/cm as a function of the center frequency of the excitation pulse. The horizontal error bars are the 1σ confidence interval of the pump center frequency. Gray curve indicates the real part of the optical conductivity.

9. M. Först *et al*., *Nat. Phys.* **7**, 854–856 (2011).
10. P. G. Radaelli, *Phys. Rev. B* **97**, 085145 (2018).
11. X. Li *et al*., *Science* **364**, 1079–1082 (2019).
12. A. Stupakiewicz *et al*., *Nat. Phys.* **17**, 489–492 (2021).
13. A. S. Disa, T. F. Nova, A. Cavalleri, *Nat. Phys.* **17**, 1087–1092 (2021).
14. J. Luo *et al*., *Science* **382**, 698–702 (2023).
15. M. Fechner *et al*., *Nat. Mater.* **23**, 363–368 (2024).
16. M. Basini *et al*., *Nature* **628**, 534–539 (2024).
17. C. S. Davies *et al*., *Nature* **628**, 540–544 (2024).
18. D. Fausti *et al*., *Science* **331**, 189–191 (2011).
19. R. Mankowsky *et al*., *Nature* **516**, 71–73 (2014).
20. R. Mankowsky, A. von Hoegen, M. Först, A. Cavalleri, *Phys. Rev. Lett.* **118**, 197601 (2017).
21. T. F. Nova, A. S. Disa, M. Fechner, A. Cavalleri, *Science* **364**, 1075–1079 (2019).
22. A. S. Disa *et al*., *Nat. Phys.* **16**, 937–941 (2020).
23. Materials, methods, and additional information are available in the supplementary materials.
24. R. Oiwa, H. Kusunose, *Phys. Rev. Lett.* **129**, 116401 (2022).
25. G. H. Fecher, J. Kübler, C. Felser, *Materials* **15**, 5812 (2022).
26. F. Arago, *Sur une modification remarquable qu'éprouvent les rayons lumineux dans leur passage à travers certains corps diaphanes, et sur quelques autres nouveaux phénomènes d'optiques: Lu le 11 août 1811* (Firmin-Didot, 1812).
27. J.-B. Biot, *Mémoire sur un nouveau genre d'oscillation que les molécules de la lumiere éprouvent en traversant certains cristaux* (Chez Firmin Didot, 1814).
28. C. Rockstuhl, C. Menzel, T. Paul, F. Lederer, *Phys. Rev. B Condens. Matter Mater. Phys.* **79**, 035321 (2009).
29. M. Kuwata-Gonokami *et al*., *Phys. Rev. Lett.* **95**, 227401 (2005).
30. M. De Vido *et al*., *Opt. Mater. Express* **9**, 2708–2715 (2019).
31. A. Zyuzin, A. Burkov, *Phys. Rev. B Condens. Matter Mater. Phys.* **86**, 115133 (2012).
32. H. B. Nielsen, M. Ninomiya, *Phys. Lett. B* **130**, 389–396 (1983).
33. N. Ong, S. Liang, *Nat. Rev. Phys.* **3**, 394–404 (2021).
34. J. Ishioka *et al*., *Phys. Rev. Lett.* **105**, 176401 (2010).
35. S.-Y. Xu *et al*., *Nature* **578**, 545–549 (2020).

ACKNOWLEDGMENTS

We thank X. Deng and N. Taherian for help with the sample preparation and the optical setup, D. Nicoletti for help with the Fourier transform infrared characterization, X. Wang for help with the implementation of the optical activity calculations, P. Licht for technical assistance, and J. Harms for help with graphics. **Funding:** This work was supported by the Cluster of Excellence "CUI: Advanced Imaging of Matter" of the Deutsche Forschungsgemeinschaft (DFG) (EXC 2056, project ID 390715994). **Author contributions:** A.C. and Z.Z. conceived the project. Z.Z. and M.Fö. designed and performed the experiments with help from M.B. and E.B.A. P.D. grew the BPO_4 sample. C.P. and P.J.W.M. prepared the sample for the optical measurements. M.Fe. performed the DFT calculations and the simulations of the nonlinear phonon dynamics. Z.Z. analyzed the data with the help from M.Fö., M.Fe., M.B., and P.G.R. Z.Z., M.Fö., and A.C. wrote the manuscript with contributions from all other authors. **Competing interests:** The authors declare no competing interests. **Data and materials availability:** The data supporting the findings of this study are provided in the main text or the supplementary materials.

SUPPLEMENTARY MATERIALS

science.org/doi/10.1126/science.adr4713
Materials and Methods
Supplementary Text
Figs. S1 to S8
Tables S1 to S5
References (*36*–*48*)

Submitted 2 July 2024; accepted 22 November 2024
10.1126/science.adr4713

SCIENCE SHAPING TOMORROW

AAAS | ANNUAL MEETING
Boston, MA | February 13–15, 2025

Join us in Boston for the 2025 AAAS Annual Meeting, February 13-15!

SEE INSIDE FOR DETAILS:

Plenary Sessions | Topical and Special Lectures
Scientific Sessions | ***Science*** Breakthrough Sessions
Workshops | Registration Information

aaas.org/meetings | #AAASmtg

AMERICAN ASSOCIATION FOR THE ADVANCEMENT OF SCIENCE

Join us in Boston, MA for the 2025 AAAS Annual Meeting

REGISTER TODAY TO SHAPE THE SCIENCE OF TOMORROW!

Meeting will feature invited lectures and panels of accomplished speakers:

PLENARY SESSIONS

AAAS Presidential Address: Science Shaping Tomorrow

Presented by Northeastern University

WILLIE E. MAY, Morgan State University

A Vision for American Science & Technology

Presented by Arizona State University

Moderator: **ALISON SNYDER**
Axios

Speakers:

FRANCE CÓRDOVA
Science Philanthropy Alliance

DARÍO GIL
IBM Research and National Science Board

SUDIP PARIKH
American Association for the Advancement of Science

KELVIN DROEGEMEIER
University of Illinois, Urbana-Champaign

MARCIA MCNUTT
National Academies of Sciences, Engineering, and Medicine

Investing to Shape Tomorrow's Science

Moderator: **HOLDEN THORP**
Science Family of Journals

Speakers:

MONICA BERTAGNOLLI
U.S. National Institutes of Health

MARIA LEPTIN
European Research Council

CHARLOTTE DEANE
UK Research and Innovation

DOROTHY NGILA
National Research Foundation, South Africa

We thank the sponsors and supporters of the 2025 AAAS Annual Meeting.

HOST UNIVERSITY:

Northeastern University

Arizona State University

NSF

The George Washington University, Washington, DC

Physicians Formula

Annenberg Public Policy Center, University of Pennsylvania

Georgia Tech School of Public Policy

FIU Florida International University

Tufts University

HFSP Human Frontier Science Program

Physicians Committee for Responsible Medicine

Tulane University School of Science & Engineering

AIP

Get in touch with us about sponsorship and exhibit opportunities in Boston!

Topical and Special Lecturers

The Future of Voting

JUAN GILBERT
University of Florida

Psychedelic Science: What Just Happened?

IMRAN KHAN
UC Berkeley Center for the Science of Psychedelics

Seeing the Unknown: Advanced Techniques for Communicating Uncertainty in Data

LACE PADILLA
Northeastern University

Accelerating Universe, Astrophysics, Dark Energy

ADAM RIESS
Nobel Laureate
Johns Hopkins University

Life at the Interface of Science + Engineering

PHILLIP A. SHARP
Nobel Laureate
Massachusetts Institute of Technology

Jones Lecture: Nutritional Inheritance: How Early-Life Nutrient Provisions Shape Development and Disease Risk

MONICA DUS
University of Michigan, Ann Arbor

McGovern Lecture: Would Enhancing Spatial Thinking Enrich STEM Education?

NORA S. NEWCOMBE
Temple University

Sarton Lecture: Visualizing Space/Time/Matter in Physics, Film and History

PETER GALISON
Harvard University

Enjoy a free entry to the Museum of Science with your AAAS conference badge on Thursday, February 13.

Deluxe registrants, join us on Saturday, February 15, as we wrap up the conference at the museum with indoor lightning, a robotic dog, and a special planetarium screening, exploring the intersection of science and religion, courtesy of the museum and AAAS Dialogue on Science, Ethics and Religion.

Multi-disciplinary Scientific Sessions

Highlighting the importance of integrating science and technology efforts, the 2025 AAAS Annual Meeting will feature multidisciplinary research — research that breaks through walls to advance science more efficiently and effectively.

Climate Change | **Artificial Intelligence** | **Science Communication**

Science Policy | **Food Security** | **Public Health** | **Workforce Development**

Diversity, Equity, and Inclusion | **International Collaboration**

- A Roadmap for State-Level Responsible AI Governance
- After the Genome: What Comes Next and Are We Ready?
- Aging and Ailing Behind Bars in the United States
- AI Governance: From Principle to Practice
- AI in the Era of Climate Change: Solution or Problem?
- An Internet of Cell Images Available to Everyone
- Bioinspired Soft Robotics: Embodied Intelligence
- Building a Resilient Food System for Healthy People and Planet
- Building Trust: Rethinking the Social Contract Between Science and Society
- Can AI and Robotics Create Job Opportunities for People with Disabilities?
- Can Nonprofits Rectify the Failure to Develop Drugs for Diseases of Poverty?
- Climate Extremes: Global, Health, and Community Impacts
- Community Science and AI: Opportunities, Challenges, Ethics, and Policies
- Computing Is Eating the World: Will Saving the Planet Destroy It?
- COVID-19's Lasting Impacts on K-12 Teachers, Students, and Classrooms
- Cultivating Science Policy Partnerships for Equity, Visibility, and Impact
- Dark and Quiet Skies: Why Everyone Should Care
- Data-Driven Evidence-Based Strategies to Advance Health Equity
- Do Microplastics in Agricultural Ecosystems Threaten Food Supply?
- Doing DEI: Advancing Transformative SEA Changes to Achieve Scientific Excellence
- Elusive Scientific Integrity Nirvana in the Executive Branch
- Empowering Interaction: Human-in-the-Loop in the Tactile Internet
- Enhancing Risk Governance for Emerging Biotechnologies
- Family Planning & Fertility Worldwide: Advancements in Global Data and Modeling
- Food Security in Megacities of the Future
- Fostering Equity and Inclusion in Climate Education Through Children's Media
- Fostering Justice-Centered Science Education Together with Students and Teachers
- From Waste to Taste : Demonstrating the Role of Upcycling in Food Systems Today
- Gene Editing for Rare Diseases: Accessibility of Personalized Medicines
- Global Teams Cooperating on Climate Change and Clean Energy Research
- How Can Public/Open Access Achieve Equity for Authors and Readers?
- How Science Can Shape a Healthier Future for Low- and Middle-Income Countries
- Hubble, Webb, and Beyond: New Complementary Strategies for Space Telescopes
- Innovations in Intervention: Local Approaches to Addressing the Climate Crisis
- Mainstreaming Natural Capital Approaches in Policy and Finance Mechanisms
- Mammal Mummies, Microbes, and Blue-Eyed Scallops Foretell Antarctica's Future
- Marine Ecosystem-Based Management Implementation and Performance

- Mitochondrial Transplantation: Opportunities and Challenges
- Monitoring Diverse Ecosystems Over Time: Shared Data and Future Projections
- Multidisciplinary Roadmap of Regenerative Medicine to Disease Prevention
- Nature's Prescription: How Urban Nature, Biodiversity, and Health Are Linked
- New Insights Into Suicide Prevention
- Open Framing Case Studies in Inclusive and Equitable Public Participation Design
- Plant Phenomics: Catalyzing a Paradigm Shift in Biology to Bolster Food Security
- Policymakers' Unmet Desire to Collaborate with Scientists
- Political and Partisanship Effects on Public Health
- Preparing Future Scientists and Engineers to Solve Complex Global Challenges
- Preparing Students in Mathematics for Tomorrow's Science
- Prevention Is Better Than Cure: Toward Scientific Wellness
- Protecting the Moon for Astronomy
- Research on Research Security: How Science Should Inform Federal Policy
- Responding to SDGs with Tech-Oriented Heritage Prevention and Cooperation
- Responsible AI and Machine Learning for Future Health Care
- Revealing Untold Stories: How Technology Facilitates Gendered Reproductive Care
- Rising Tides, Emerging Challenges: Shaping Sustainable Coastal Futures
- Risks From AI to the Economy and Society
- Role of Bias and Diversity in AI Interpretation of Medical Images
- Sacred Mountains, Sacred Bones: Science and Indigenous Cultures
- Scary Science: Risk, Danger, and Public Communication
- Science Engagement with Faith Perspectives in Informal Science Learning
- Science for the Public and Policy: Oppenheimer, Bates, and Carson
- Science to Support Transformation of the Global Financial System
- Scientific Advice During Emergencies: Leveraging Research for Decision Support
- Social Technologies: Why We Can't Live with Them or Without Them
- Software Liability in a Landscape of Emerging Technologies
- The ABCs of 123s
- The Carbon We Have: Solutions for a Sustainable and Circular Bioeconomy
- The Ethics and Policy of Neural Interfaces: Maximizing Benefit, Minimizing Risk
- The Microbiome: A New Frontier in Human Health
- The Plans for Multicultural Settlements in Space
- The Power of Diverse Partnerships to Increase Inclusive Pathways Into STEM
- The Science of Human Language: Insights for and from AI
- The Science, Practice, and Regulation of Artificial Intelligence
- The Three-Legged Stool of Public Trust in Science
- The Value of History and Philosophy of Science for a Strong Scientific Ecosystem
- Toward a Carbon-Free Energy Future: The Nuclear Option
- Towards Actionable Science and Technology Diplomacy
- Treating the Transgender Child: Science and Ethics
- Trends in and Consequences of (Dis)Trust in Science
- Trusting AI Solutions for Pressing Societal Challenges
- UN Plastic Treaty: The Science-Diplomacy Nexus and Where to Go from Here
- Using AI to Stabilize and Protect the Power Grid
- Using Artificial Intelligence to Facilitate Science Learning Opportunities
- Utilizing Policy for Science Literacy Development
- Voice-Based AI for Medicine: Practices for Ethical Interventions at Scale
- What Big Data Can (and Can't!) Tell Us About How Language Works
- What Good Are Forests?

Science | Breakthrough Sessions

Every year, *Science* reflects on what's happened in the past 12 months to identify the most important STEMM developments. The 2024 Breakthrough of the Year is:

Lenacapavir for Long-Lasting HIV Prevention

THE RUNNERS-UP INCLUDE:

- Flowing Mantle Waves Shape the Continents, a Compelling Addendum to the Theory of Plate Tectonics
- Multicellularity Origin Came Much Earlier for Ancient Eukaryotes
- Altermagnetic Discovery: A New Type of Permanently Magnetic Material
- An Evolutionary Surprise: New Nitrogen-Fixing Organelle
- Ultraprecise RNA Pesticides
- JWST Probes the Cosmic Dawn
- Ancient DNA Reveals Ancestral Lineage and How Their Societies Functioned
- Immune Cells Fight Autoimmune Disease
- Starship Sticks the Landing: Mechanical Arms Catch Rocket Booster Back at its Launch Pad

Join sessions focused on these advances at the AAAS Annual Meeting in Boston, February 12-15!

AAAS is proud to honor its award recipients: 2025 AAAS Awards Breakfast, AAAS Kavli Science Journalism Awards and Reception, SEA Change Awards Ceremony and Reception, Shirley M. Malcom Breakfast for STEMM Equity.

See the online program for details regarding how to attend.

WORKSHOPS

Learn how to communicate your STEMM work with advocacy, equity and inclusion in mind.

- Be Green, Be Seen: Act to Advance Sustainability in Science and our Career
- Be Your Own Character: Develop a Unique Voice and Story to Bring Science to Life
- Bringing Human Rights Into STEM Education
- Bringing Science and Technology to Life With Short-Form Video
- Communicating Science to Gen Alpha Through Storytelling
- Communicating Science to Policymakers
- Equitable Community-Engaged Research: A Win for Science, Social Impact and Funding
- Everything but the Tenure Track: Exploring Career Opportunities for Bio-Ph.D.s

- How To: Inclusive STEM Programs for Neurodiverse Undergraduate/Graduate Students
- Metamorphosis of the Postdoc: Overcoming the Tenure-Track Transition Barrier
- Navigating Your Career Pivot: Opportunities in Science Nonprofits
- Public Policy Engagement After the Presidential Election
- Science Communication and Education at the Intersection of Genetics and Justice
- Science Policy for the People: Opportunities for Scientists to Get Involved
- Science Policy on Capitol Hill: Insider's Look on How Decisions Are Made
- Shaping Science Through Slides: Magic Lantern Shows as Scientific Storytelling
- Supporting STEM Advancement for Diverse Students: Best Practices
- The Art of Listening: Using Improvisation to Enhance Science Communication
- The Mental Health Crisis in STEM: Strengthening Institutional Capacity in Faculty
- Training Scientists to Communicate with Policymakers: New Tools and Approaches
- Using Community-Based Participatory Research to Enhance Scientific Impact
- What Would You Do? Responding to Threats to Scientific Freedom

Sci-Mic Stage Can't make it to the conference this year? Catch interviews on the Sci-Mic Chats, streaming live from the Expo.

Postdoc Talks

Sessions about current scientific projects and initiatives

- Impact of Satellites, STEM Education Assessment and Food Waste Policy
- Conversational Agents, Auditory System and Neuroplasticity, and Plastics in the Ocean
- Brain Function, Restorative Sleep, and Influences on Pain
- Wearable Sensors, Conservation, and Wound Healing
- Climate Resilience, Collaborative Map Building, Improving Rainfall Forecasting, and Sewer Design
- User Privacy, AI's Electoral Influence, and Environmental Justice

E-poster Presentations

Presented by GT School of Public Policy

Watch as talented undergraduate and graduate students showcase their innovative research and communication skills.

This exciting event highlights the importance of making science accessible and engaging for all.

Find out more at:
meetings.aaas.org/e-posters

#AAASmtg Registrants!
Create your schedule at the conference here:

AAAS EXPO

See meeting program for additional events taking place in the Expo, including:

Coffee Breaks
Presented by:
Annenberg Public Policy Center, University of Pennsylvania

Happy Hours
Friday and Saturday, 3 PM-5 PM

Friday and Swaturday, 9 AM, 11 AM, and 12:30 PM

AAAS would like to thank the volunteers who have given their time and energy in making this event possible:

- AAAS board of directors
- The Annual Meeting program committee
- AAAS section leadership
- Session reviewers
- E-poster judges
- Session organizers and coordinators

See the full list of 2025 reviewers by visiting meetings.aaas.org/reviewers.

Join us in **Boston, MA, February 13-15**. Register for the 2025 AAAS Annual Meeting through January 22 for discounted advance registration rates (see below). Standard rates will apply thereafter.

Be sure to check the online program to see the access level for the sessions you are interested in. Visit **aaas.org/meetings** for more information.

Basic Access	Advance Deluxe Access
+ Plenaries + Workshops + Sci-Mic Stage + Expo & Events	+ Basic Access Programming + Topical Lectures + Scientific Sessions + Science Breakthroughs + E-Posters + Postdoc Talks

	AAAS MEMBER	NON-MEMBER
General Attendee	$355	$500
Postdoc	$155	$300
Retired Professional	$285	$415
Student	$75	$110

CONNECT WITH US! | #AAASmtg

aaas.org/meetings @AAASmeetings /AAAS.Science /AAAS

By **Luke Childress**

A bite of expertise

In front of me was a sandwich. On the other side of that sandwich was my state's director of public health. What was a second-year Ph.D. student doing in this situation? Despite the fear and excitement that left me feeling like I was riding a unicycle on the edge of a canyon, I did my best to appear easygoing and professional. This lunch had been my idea, after all. I had been struggling to approach the more experienced and prominent scientists I worked with, and I had thought asking them to lunch might offer a way in. I planned to follow specific talking points to avoid any awkward silences, but instead I found myself ad-libbing everything. Would this lunch be an embarrassing dead end rather than the opening I was hoping for?

I had recently joined a group full of world-class investigators—an exciting environment to be a trainee in, but also pretty intimidating. I felt compelled to make the most of the great wealth of knowledge around me. But the days were chock-full of bench work, meetings, and closed office doors. Asking basic questions in group meetings or requesting investigators' time for a discussion felt almost impossible. How was I supposed to make inroads without being obnoxious?

Eventually, I began to notice something: When lunch time came around, the busyness subsided, the conference room was empty, and I often spotted investigators eating in their offices. Holding important meetings or conducting lab work with a mouthful of turkey sandwich was frowned on, but it was quite common to sit down with someone and have a conversation over a meal. It occurred to me that offering lunch could be an acceptable way to connect with a busy principal scientist.

"Offering lunch could be an acceptable way to connect with a busy principal scientist."

I decided to test out my theory, with the state official as my first attempt. I had seen him speak on several occasions—my research institute adjoined the laboratories he ran—and I found his vision for public health inspiring. I seriously doubted he would have the time to meet with a graduate student. Still, I figured I had nothing to lose. So, when I passed him in the hallway one day, I stopped him, introduced myself, and asked whether he would be willing to have lunch with me some time. I worried I would come across as a bother and that I was overstepping some unspoken social rule. But to my surprise, he didn't hesitate. "Of course," he answered.

The lunch lasted a little less than an hour, but it had an enduring impact on me. Despite the awkward small talk I inflicted on him, we found we had many common interests and intellectual passions. He shared that when he had been in grad school, he had also struggled to connect with midcareer professionals. We exchanged contacts for future correspondence, and I left invigorated and full of insights. Something about sitting down for lunch with him made everybody seem a little less godlike and a little more human. It gave me faith in my ability to fit in around accomplished scientists. And all I had done was ask.

With the confidence born of this experience, I made a mental list of people to invite to lunch and worked through it, week by week. I explained I was a student who wanted to learn about their professional experiences. I generally asked in person, often suggested a restaurant to reduce friction in the interaction, and always offered to pay (though the more senior invitees usually insisted on footing the bill). And no matter how preoccupied they seemed, few people have been unwilling to offer me an hour of their time over the pretense of a meal. I've lunched with my thesis committee members, the head of my division, postdocs, lab mates, and collaborating scientists. Each time, it got easier to ask good questions and make a genuine connection. By the time our plates were empty, we've often gone from professional topics to more intimate personal conversations.

In my final year of graduate school, I now have a wealth of lunchtime mentors whom I feel comfortable approaching for advice or references. For the next stage of my career, I'm already looking into the tastiest bistros nearby. ■

Luke Childress is a Ph.D. student at the University of Arkansas for Medical Sciences. Send your career story to SciCareerEditor@aaas.org.

ILLUSTRATION: ROBERT NEUBECKER

Who's the top employer for 2024?

Science 2024 TOP EMPLOYER

Science Careers' annual survey reveals the top companies in biotech & pharma voted on by *Science* readers.

Explore these highly-rated employers in our new interactive experience:
sciencecareers.org/topemployers

CALL FOR PAPERS

SPJ
SCIENCE PARTNER JOURNALS

Energy Material Advances

Energy Material Advances is an online-only, Open Access journal published in affiliation with **Beijing Institute of Technology (BIT)** and distributed by the **American Association for the Advancement of Science (AAAS)**. The journal publishes research articles, review articles, short communications, perspectives, and editorials. *Energy Material Advances* covers multiple fields from cutting-edge material to energy science, investigating theoretical, technological as well as engineering aspects.

Submit your research to *Energy Material Advances* today!

Learn more at **spj.science.org/energymatadv**

The Science Partner Journal (SPJ) program was established by the American Association for the Advancement of Science (AAAS), the nonprofit publisher of the *Science* family of journals. The SPJ program features high-quality, online-only, Open Access publications produced in collaboration with international research institutions, foundations, funders and societies. Through these collaborations, AAAS furthers its mission to communicate science broadly and for the benefit of all people by providing top-tier international research organizations with the technology, visibility, and publishing expertise that AAAS is uniquely positioned to offer as the world's largest general science membership society.

Visit us at: **spj.science.org**

@SPJournals **@SPJournals and @EnergyMatAdv** **@SPJournals** **OPEN ACCESS**

ARTICLE PROCESSING CHARGES CURRENTLY WAIVED FOR ALL ACCEPTED ARTICLES